

REPORT DOCUMENTATION PAGE				Form Approved OMB No. 0704-0188	
<p>The public reporting burden for this collection of information is estimated to average 1 hour per response, including the time for reviewing instructions, searching existing data sources, gathering and maintaining the data needed, and completing and reviewing the collection of information. Send comments regarding this burden estimate or any other aspect of this collection of information, including suggestions for reducing the burden, to the Department of Defense, Executive Service Directorate (0704-0188). Respondents should be aware that notwithstanding any other provision of law, no person shall be subject to any penalty for failing to comply with a collection of information if it does not display a currently valid OMB control number.</p> <p>PLEASE DO NOT RETURN YOUR FORM TO THE ABOVE ORGANIZATION.</p>					
1. REPORT DATE (DD-MM-YYYY) 03-29-2017		2. REPORT TYPE Ph.D Dissertation		3. DATES COVERED (From - To) Sep 2013 - Sep 2016	
4. TITLE AND SUBTITLE Sesquinarines, Magnetics and Atmospheres: Studies of the Terrestrial Moons and Exoplanets				5a. CONTRACT NUMBER N/A	
				5b. GRANT NUMBER	
				5c. PROGRAM ELEMENT NUMBER	
				5d. PROJECT NUMBER	
				5e. TASK NUMBER	
6. AUTHOR(S) Nayak, Michael				5f. WORK UNIT NUMBER	
7. PERFORMING ORGANIZATION NAME(S) AND ADDRESS(ES) Air Force Institute of Technology, Wright-Patterson AFB OH				8. PERFORMING ORGANIZATION REPORT NUMBER	
9. SPONSORING/MONITORING AGENCY NAME(S) AND ADDRESS(ES) Air Force Institute of Technology, Wright-Patterson AFB OH				10. SPONSOR/MONITOR'S ACRONYM(S) AFIT/CIP	
				11. SPONSOR/MONITOR'S REPORT NUMBER(S)	
12. DISTRIBUTION/AVAILABILITY STATEMENT DISTRIBUTION STATEMENT A. Approved for public release. Distribution is unlimited					
13. SUPPLEMENTARY NOTES					
14. ABSTRACT <p>The surface brightness of Deimos, groove patterns on Phobos, crustal magnetic anomalies on the Moon and the composition of exoplanet atmospheres represent some of the most interesting and puzzling questions in planetary science. Why is Deimos significantly brighter and smoother than its partner moon Phobos? What is the origin of the crater chain "grooves" on Phobos? Are the magnetic anomalies in the lunar South Pole-Aitken basin a remnant of the basin's formation, or do they owe their existence to a primordial period of lunar dynamo activity? And finally, as visible wavelength telescopes are designed and tested for space-based exoplanet detections, can we use observed albedo spectra to determine radius, gravity, cloud pressure heights and atmospheric compositions for these planets? I use dynamical modeling, magnetic inversions and Markov Chain Monte Carlo retrievals to address these questions.</p>					
15. SUBJECT TERMS <p>Exoplanets, NASA, satellite, constellation, Guidance, Navigation, Control, Attitude Determination, Planetary Science, Impact physics, Mars, Moon, magnetic anomalies, Phobos, Deimos</p>					
16. SECURITY CLASSIFICATION OF:			17. LIMITATION OF ABSTRACT	18. NUMBER OF PAGES	19a. NAME OF RESPONSIBLE PERSON
a. REPORT	b. ABSTRACT	c. THIS PAGE			MICHAEL NAYAK
(U)	(U)	(U)	UU	208	19b. TELEPHONE NUMBER (Include area code) 808-891-7727



Peer Reviewed

Title:

Sesquinaries, Magnetism and Atmospheres: Studies of the Terrestrial Moons and Exoplaets

Author:

[Nayak, Michael](#)

Acceptance Date:

2016

Series:

[UC Santa Cruz Electronic Theses and Dissertations](#)

Degree:

Ph.D., [Earth Science](#)[UC Santa Cruz](#)

Advisor(s):

[Garrick-Bethell, Ian](#)

Committee:

[Nimmo, Francis](#), [Asphaug, Erik](#), [Worden, Simon P](#), [Fortney, Jonathan J](#)

Permalink:

<http://escholarship.org/uc/item/2h1600hk>

Abstract:

Copyright Information:



Copyright 2016 by the article author(s). This work is made available under the terms of the Creative Commons Attribution-NonCommercial-ShareAlike4.0 license, <http://creativecommons.org/licenses/by-nc-sa/4.0/>



eScholarship
University of California

eScholarship provides open access, scholarly publishing services to the University of California and delivers a dynamic research platform to scholars worldwide.

UNIVERSITY OF CALIFORNIA
SANTA CRUZ

**SESQUINARIES, MAGNETICS AND ATMOSPHERES:
STUDIES OF THE TERRESTRIAL MOONS AND EXOPLANETS**

A dissertation submitted in partial satisfaction
of the requirements for the degree of

DOCTOR OF PHILOSOPHY

in

EARTH SCIENCES

by

Michael Nayak

December 2016

The Dissertation of Michael Nayak
is approved:

Professor Francis Nimmo, chair

Professor Ian Garrick-Bethell

Dr. Simon P. Worden

Professor Erik Asphaug

Professor Jonathan Fortney

Tyrus Miller
Vice Provost and Dean of Graduate Studies

Copyright © by
Michael Nayak
2016

Table of Contents

List of Figures	vi
Abstract	x
Acknowledgements	xii
Chapter 1 Introduction	1
Chapter 2 Sesquinarries: A Case Study of Deimos	4
2.1 Abstract	4
2.2 Introduction	5
2.3 Methods	7
2.3.1 Coordinate Transformations	8
2.3.1.1 Planet Centered Inertial (PCI) frame	8
2.3.1.2 Planet Centered Planet Fixed (PCPF) frame	8
2.3.1.3 Topocentric Horizon Frame (also SEZ: South-East-Zenith frame) ..	9
2.3.2 Impact Model: Generating 2-D Streamlines	11
2.3.3 Creating 3-D Velocity Streamlines	13
2.3.4 Planetary System Model	14
2.4 Results	18
2.5 Mass Transfer between Martian Satellites	21
2.5.1. Comparison with Background Flux	23
2.6. Discussion	29
2.6.1. Importance of Inter-Moon Mass Transfer and Reaccretion	29
2.6.2 The Spectral Dichotomy of Phobos	30
2.6.3 Primary Versus Secondary Impact Morphology	31
2.6.4 Surface smoothness, Brightness and Impact gardening	32
2.7 Figures	34
Chapter 3 Sesquinarries: A Case Study of Phobos	39
3.1 Abstract	39
3.2 Introduction	40
3.3 Methods	43
3.3.1. Mars Gravity System Integrator	43
3.3.2. Outbound Ejecta Velocity Distribution	43
3.3.3. Mass-Velocity Distribution	45
3.4. Results	46
3.4.1. Primordial versus modern orbit	46

3.4.2. Nature of reimpacting ejecta	47
3.4.3. Grid Search Varying the Primary Crater Location	50
3.4.4. Tracing catenae back to a source crater	52
3.4.5. Changing the Z-Model Ejection Angle.....	53
3.5. Discussion	53
3.6. Figures.....	57
Chapter 4 Magnetics: A Case Study of the Lunar South Pole-Aitken Basin.....	66
4.1 Abstract	66
4.2 Introduction.....	67
4.3 Methods.....	69
4.3.1 Data Sources	69
4.3.2 Data Processing and Anomaly Identification	70
4.3.3 Inversion Algorithm 1: Defined Dipoles, Constant Magnetization	72
4.3.4 Inversion Algorithm 2: Gridded Dipoles, Variable Magnetization	73
4.3.5 Uncertainty Estimation for Magnetization Directions	74
4.3.5.1 Time variable contributions	74
4.3.5.2 Non-uniform magnetization directions	77
4.3.5.3 Source body geometry	78
4.4 Results.....	81
4.4.1 Regression Results	81
4.4.2 Comparison with other magnetic paleopoles	87
4.5 Discussion	89
4.5.1 Paleopole directions	89
4.5.2 Magnetization by Impact Processes.....	89
4.5.2.1 TRM in an impact-produced field.....	90
4.5.2.2 SRM in an impact-produced field.....	90
4.5.3 Magnetized South Pole-Aitken basin ejecta or volcanic bodies?	92
4.5.4 Possible Explanations for Diverse Magnetic Field Directions	94
4.5.4.1 Non-axially aligned dipoles and impact-induced dynamos	94
4.5.4.2 Secular Variation	95
4.5.4.3 True Polar Wander over long timescales	95
4.5.4.4 True Polar Wander due to SPA formation.....	96
4.6 Conclusion	99
4.7 Figures.....	101
Chapter 5 Phase-Dependent Atmospheric Retrievals on Gas Giant Planets in Reflected Light.....	140
5.1 Abstract	140
5.2 Introduction.....	141
5.3 Background.....	144
5.3.1 Albedo Model	144
5.3.2 MCMC Methodology	146
5.3.3 Test Cases: Synthetic HD 99492c (Planet A) and HD 192310c.....	149

5.4 Results.....	151
5.4.1 Retrieved best-fit spectra by MCMC	151
5.4.2 Inferring Phase-Dependent Relationships from Posterior Probability Distributions.....	152
5.5 Discussion	155
5.5.1 Methane and Radius Retrieval	156
5.5.2 The impact of a known phase angle.....	156
5.5.3 Applying an intersection criterion to multiple observations.....	157
5.6 Conclusions.....	161
5.7 Figures.....	164
Chapter 6 Bibliography	181

List of Figures

Figure 2.1. Illustration of the relationship between the Planet-Centered Inertial (PCI) and Planet-Centered Planet-Fixed (PCPF) frames.....	34
Figure 2.2. Illustration of the relationship between the Planet-Centered Planet Fixed (PCPF) frame and the South-East-Zenith (SEZ) frames.....	35
Figure 2.3. The fate of Deimos ejecta from Voltaire as a function of orbital geometry and ejection velocity from Voltaire.	35
Figure 2.4. Impact Velocity at Phobos and Deimos vs. particle ejection velocity from Voltaire.	36
Figure 2.5. Impact velocity at Phobos and Deimos vs. duration of particle flight.. ...	36
Figure 2.6. Impact flight path angle (FPA) at Phobos and Deimos versus the impact velocities on the respective bodies.....	37
Figure 2.7. Number of particles still flying and impacts to Phobos and Deimos with time.	37
Figure 2.8. Total mass faster than ejection velocities and mass ejected per velocity bin.	38
Figure 3.1. Reaccretion map for the Stickney impact in Phobos modern and primordial orbits.....	57
Figure 3.2. The evolution of catenae with increasing velocity of ejection from Phobos.....	58
Figure 3.3. Impact vs. ejection velocity for sesquinary impactors.	59
Figure 3.4. Visualization of the orbital history of randomly selected particles.....	59
Figure 3.5. Catenae orientations change from vertical to horizontal depending on the latitude of the primary impact.....	60
Figure 3.6. Tracing an observed catena back to its source crater.	60
Figure 3.7. Impact of primary crater size on resultant catenae.....	61
Figure 3.8. Impact of primary crater longitude (southern hemisphere) on resultant catenae.....	62
Figure 3.9. Impact of primary crater longitude (northern hemisphere) on resultant catenae.....	64
Figure 3.10. Comparing resultant catenae with azimuths of ejecta release.....	64
Figure 3.11. Impact of primary crater latitude (southern hemisphere) on resultant catenae.....	65
Figure 3.12. Variation of resultant catenae with Z-number (ejection angle).....	65
Figure 4.1. Lunar South Pole-Aitken basin study areas.....	101
Figure 4.2. Overview of all datasets used for SPA areas 1-5..	102
Figure 4.3. Overview of all datasets used for SPA areas 6-10.	103

Figure 4.4. Magnetic field maps and histograms of field strengths for the Mare Imbrium region in the lunar wake.....	104
Figure 4.5. Error estimation due to time variable (non-crustal) magnetic fields.....	104
Figure 4.6. RMS error map for the magnetization direction for area 1 (whole-sphere Mollweide projection).....	105
Figure 4.7. Error estimation due to uncertainty in source body geometry..	105
Figure 4.8. Area 1 best fit results for both inversion algorithms..	106
Figure 4.9. Area 2 best fit results with both inversion algorithms.....	107
Figure 4.10. Area 3 best fit results with both inversion algorithms.....	107
Figure 4.11. Area 4 best fit results with both inversion algorithms.....	108
Figure 4.12. Area 5 best fit results with both inversion algorithms.....	108
Figure 4.13. Area 6 best fit results with both inversion algorithms.....	109
Figure 4.14. Area 7 best fit results with both inversion algorithms.....	109
Figure 4.15. Area 8 best fit results with both inversion algorithms.....	110
Figure 4.16. Area 9 best fit results with both inversion algorithms.....	110
Figure 4.17. Area 10 best fit results with both inversion algorithms.....	111
Figure 4.18. RMS error map for the magnetization direction for all datasets for SPA study areas 1-5, obtained using the DD-CM algorithm..	112
Figure 4.19. RMS error map for the magnetization direction for all datasets for SPA study areas 6-10, obtained using the DD-CM algorithm..	113
Figure 4.20. Best-fit magnetization directions for study areas defined in Figure 1, for all datasets.....	114
Figure 4.21. SPA magnetic paleopoles.....	115
Figure 4.22. Paleopoles from SPA anomalies compared with other published paleopoles from other anomalies.....	116
Figure 4.23. Area 1 best fit results, day 123, 2009.....	117
Figure 4.24. Area 1 best fit results, day 61, 1999.....	118
Figure 4.25. Area 1 best fit results, day 142, 1999.....	118
Figure 4.26. Area 2 best fit results, day 69, 2009.....	119
Figure 4.27. Area 2 best fit results, day 96, 2009.....	119
Figure 4.28. Area 2 best fit results, day 33, 1999.....	120
Figure 4.29. Area 3 best fit results, day 69, 2009.....	120
Figure 4.30. Area 3 best fit results, day 96, 2009.....	121
Figure 4.31. Area 3 best fit results, day 61, 1999.....	121
Figure 4.32. Area 4 best fit results, day 151, 2009.....	122
Figure 4.33. Area 4 best fit results, day 115, 1999.....	122
Figure 4.34. Area 4 best fit results, day 142, 1999.....	123
Figure 4.35. Area 5 best fit results, day 96, 2009.....	123
Figure 4.36. Area 5 best fit results, day 151, 2009.....	124
Figure 4.37. Area 5 best fit results, day 142, 1999.....	124
Figure 4.38. Area 6 best fit results, day 96, 2009.....	125
Figure 4.39. Area 6 best fit results, day 33, 1999.....	125
Figure 4.40. Area 6 best fit results, day 115, 1999.....	126
Figure 4.41. Area 6 best fit results, day 142, 1999.....	126

Figure 4.42. Area 7 best fit results, day 96, 2009.	127
Figure 4.43. Area 7 best fit results, day 33, 1999.	127
Figure 4.44. Area 7 best fit results, day 115, 1999.	128
Figure 4.45. Area 8 best fit results, day 96, 2009.	128
Figure 4.46. Area 8 best fit results, day 151, 2009.	129
Figure 4.47. Area 8 best fit results, day 61, 1999.	129
Figure 4.48. Area 8 best fit results, day 142, 1999.	130
Figure 4.49. Area 9 best fit results, day 96, 2009.	130
Figure 4.50. Area 9 best fit results, day 61, 1999.	131
Figure 4.51. Area 9 best fit results, day 88, 1999.	131
Figure 4.52. Area 9 best fit results, day 115, 1999.	132
Figure 4.53. Area 9 best fit results, day 142, 1999.	132
Figure 4.54. Area 10 best fit results, day 151, 2009.	133
Figure 4.55. Area 10 best fit results, day 61, 1999.	133
Figure 4.56. Area 10 best fit results, day 88, 1999.	134
Figure 4.57. Area 10 best fit results, day 142, 1999.	134
Figure 4.58. For Area 1, source model obtained with GD-VM algorithm	135
Figure 4.59. For Area 2, source model obtained with GD-VM algorithm..	135
Figure 4.60. For Area 3, source model obtained with GD-VM algorithm..	136
Figure 4.61. For Area 4, source model obtained with GD-VM algorithm..	136
Figure 4.62. For Area 5, source model obtained with GD-VM algorithm..	137
Figure 4.63. For Area 6, source model obtained with GD-VM algorithm..	137
Figure 4.64. For Area 7, source model obtained with GD-VM algorithm..	138
Figure 4.65. For Area 8, source model obtained with GD-VM algorithm..	138
Figure 4.66. For Area 9, source model obtained with GD-VM algorithm..	139
Figure 4.67. For Area 10, source model obtained with GD-VM algorithm..	139
Figure 5.1. Illustration of the degenerate relationship between decreasing planet phase and increasing planet radius, in yielding an equivalent scattered flux.	164
Figure 5.2. Illustrative representation of two-layer cloud model employed.....	164
Figure 5.3. Candidate target planets favorable for characterization by WFIRST. ...	165
Figure 5.4. Model noise-free contrast spectra for Planet A and HD 192310c (50x metallicity), for a spectral resolution of $R = 70$	165
Figure 5.5. Contrast spectra for Planet A at SNR values of 5 and 20.....	166
Figure 5.6. Contrast spectra for HD 192310c generated at metallicity values of 1x, 10x and 50x that of the Sun. T.	166
Figure 5.7. Best-fit contrast spectra for Planet A at SNR = 10 and varying phase angles: 30°, 60°, 90° and 120°.	167
Figure 5.8. Best-fit contrast spectra for HD 192310c at a metallicity of 1x solar and varying SNR and phase angle.	168
Figure 5.9. Best-fit contrast spectra for HD 192310c at a metallicity of 10x solar and varying SNR and phase angle	169
Figure 5.10. Best-fit contrast spectra for HD 192310c at a metallicity of 50x solar and varying SNR and phase angle	170

Figure 5.11. Posterior probability distribution plot for all eleven parameters retrieved by the MCMC algorithm for Planet A at SNR = 10 and phase angle 60°	171
Figure 5.12. Highlight of pertinent parameter relationships with planet phase angle, excerpted from Figure 5.11.....	172
Figure 5.13. Relationship of planet radius with changing planet phase angle, for Planet A, for an SNR of 20 and a truth phase angle of 30°, 60°, 90° and 120° ..	172
Figure 5.14. Summary of all results for Planet A test case.....	173
Figure 5.15. Summary of all results for the HD 192310c test case with 1x metallicity of the Sun.....	173
Figure 5.16. Summary of all results for the HD 192310c test case with 10x metallicity of the Sun.....	174
Figure 5.17. Summary of all results for the HD 192310c test case with 50x metallicity of the Sun.....	174
Figure 5.18. Results for the 10x metallicity case of HD 192310c, at SNR = 20, for an unbounded and bounded phase angle case.....	175
Figure 5.19. Illustration of the intersection criterion for surface gravity and planet radius.....	175
Figure 5.20. Improvement in 68% confidence interval ranges for methane abundance, surface gravity, planet radius and two-cloud top pressures	176
Figure 5.21. Improvement in 68% confidence intervals for an intersection criterion applied to three randomly chosen phase-varying observations of Planet A and HD 192310c, 10x metallicity case, compared to a randomly chosen single observation.....	177
Figure 5.22. SNR versus phase angle relationships with respect to methane abundance.....	178
Figure 5.23. SNR versus phase angle relationships with respect to surface gravity.....	178
Figure 5.24. SNR versus phase angle relationships with respect to planet radius....	179
Figure 5.25. SNR versus phase angle relationships with respect to inferred phase angle.....	179
Figure 5.26. SNR versus phase angle relationships with respect to the pressure at the top of the bottom cloud.....	180
Figure 5.27. SNR versus phase angle relationships with respect to the pressure at the top of the top cloud.....	180

Abstract

Sesquinarries, Magnetism and Atmospheres: Studies of the Terrestrial Moons and Exoplanets

by

Michael Nayak

The surface brightness of Deimos, groove patterns on Phobos, crustal magnetic anomalies on the Moon and the composition of exoplanet atmospheres represent some of the most interesting and puzzling questions in planetary science. Why is Deimos significantly brighter and smoother than its partner moon Phobos? What is the origin of the crater chain “grooves” on Phobos? Are the magnetic anomalies in the lunar South Pole-Aitken basin a remnant of the basin’s formation, or do they owe their existence to a primordial period of lunar dynamo activity? And finally, as visible wavelength telescopes are designed and tested for space-based exoplanet detections, can we use observed albedo spectra to determine radius, gravity, cloud pressure heights and atmospheric compositions for these planets? I use dynamical modeling, magnetic inversions and Markov Chain Monte Carlo retrievals to address these questions. Major findings include 1) the likelihood of isotropic redistribution of reaccumulated ejected material on Deimos, 2) the creation of hemispherical catenae from the creation of primary craters on Phobos, which match the locations and geomorphology of several existing grooves well, 3) the first

directional magnetic survey of South Pole-Aitken basin anomalies, and a larger than expected diversity in recovered paleopole directions, and 4) the critical importance of considering the effects of planet phase in exoplanet atmosphere retrievals; changing planet phase, when combined with low signal-to-noise observations, can cause several orders of magnitude of uncertainty in atmospheric methane composition and cloud pressure height, among others.

Acknowledgements

Science and religion are two windows that people look through, trying to understand the big universe outside, trying to understand why we are here. The two windows give different views, but both look out at the same universe. Both views are one-sided, neither is complete. Both leave out essential features of the real world. And both are worthy of respect.

- Freeman Dyson, theoretical physicist and mathematician, Princeton.

I would like to gratefully acknowledge financial support under and awarded by the Department of Defense, National Defense Science and Engineering Graduate (NDSEG) Fellowship, 32 CFR 168a, with supplementary support provided by Red Sky Research, LLC. Computational support was provided by the NASA Ames Mission Design Division (Code RD) for research contained in Chapters 2 and 3, through a contract with the University of California Santa Cruz University Affiliated Research Center (UARC). The Planetary Systems Branch (Code SST), NASA Ames Research Center, provided supercomputer access and computational resources for the work in Chapter 5.

I owe a huge debt of gratitude to Dr. Pete Worden, Dr. Steve Zornetzer, Dr. Alan Weston (NASA), and Col. Carol Welsch, Lt. Col Joe Nance and Lt. Col Brian Bracy (USAF), for enabling my unconventional departure from the beaten path onto this PhD adventure. From you, I've learned that a good leader is always willing to be a mentor... even if that means supporting a harebrained idea or two.

I would like to acknowledge both large and small contributions from my research collaborators and co-authors: Francis Nimmo, Jonathan Fortney, Ian

Garrick-Bethell and Tyler Robinson (UC Santa Cruz), Doug Hemingway (UC Berkeley), Mark Marley and Roxana Lupu (NASA Ames), Nikole Lewis (Space Telescope Science Institute), Bogdan Udrea (Embry-Riddle Aeronautical University) and Erik Asphaug (Arizona State).

In no particular order, I would also like to thank Grace Persico, Elizabeth Hyde, Dr. Christopher McKay, David Mauro, Bethany Nagid, Jenna Scarpelli, Jennifer Fish, Christina Doolittle, Ana Martínez-Fernández, Gisela Muñoz, Jeannette van den Bosch and Kay Nayak.

Finally and most importantly, none of this would be possible without the grace and blessing of the Lord. The odds have been impossible; I certainly couldn't have beaten them by myself.

The text of this dissertation includes modified reprints of previously published material. Chapter 2 is a slightly modified version of *Nayak et al.* (2015); the first co-author (Nimmo) supervised the research; the second co-author (Udrea) supported the research and helped design the simulation reference frames; the text of this paper is used with the permission of all co-authors. Chapter 3 is a slightly modified version of *Nayak and Asphaug* (2016); the co-author (Asphaug) supervised the research; the text of this paper is used with permission from Asphaug. Chapter 4 is a slightly modified version of *Nayak et al.* (2016); the first co-author (Garrick-Bethell) supervised the research; the second co-author (Hemingway) supported the research, performed the GD-VM regression calculations and provided access to the Lunar Magnetism Analysis Tool (LMAT) code; the text of this paper is used with the permission of all

co-authors. Chapter 5 is a slightly modified version of *Nayak et al., in prep* (2016). The first co-author (Lupu) provided full-phase retrieval code and supercomputer setup assistance; the second and third co-authors (Marley and Fortney) supervised the research at NASA Ames and UC Santa Cruz respectively; the fourth co-author (Robinson) provided the instrument-specific noise model and the fifth co-author (Lewis) provided phase-varying albedo models for the multiple exoplanets and metallicities used in the study. The text of this paper is used with the permission of all co-authors.

The views expressed in this dissertation are those of the author and do not reflect the official policy or position of the United States Air Force, Department of Defense, NASA or the U.S. Government.

Chapter 1

Introduction

The exponential increase in computational capabilities, in the realm of both individual computing and supercomputing, has enabled a large jump in simulation capability for planetary scientists. This is especially evident in the three subfields explored in this dissertation – ejecta dynamics, magnetic inversions and broad-scale retrievals of gas giant atmospheric properties – allowing this work a complexity and level of insight that might not have been possible even ten years ago. This work may be divided into three general partitions. In order, I inquire after geophysical puzzles related to the moons of Mars (sesquinaries, Chapters 2 and 3), magnetic anomalies on Earth’s moon (magnetics, Chapter 4) and finally, atmospheric retrievals for inferring properties of gas giant planets beyond our solar system (exoplanets, Chapter 5).

The first puzzle explored here concerns the physical appearance and geological features noted on both of Mars’ tiny moons, Phobos and Deimos. Deimos is smoother and brighter than its inner counterpart, while Phobos bears several mysterious “groove”-like marks on its surface. The dichotomy in appearance and groove structure, while first noted in the *Viking* lander era almost fifty years ago, has to date not been fully resolved. By using multiple simulations with thousands of test particles, I make the case that “sesquinaries” may have a significant role to play. In

Chapter 2, I consider **Mars' outer moon Deimos**. By modeling sesquinary impact cratering from the impact that formed its largest crater, Voltaire, it is found that sesquinary ejecta globally resurface Deimos near-isotropically, erasing the previous geological record. I conclude that dating the surface of Deimos is likely more challenging than previously suspected. In Chapter 3, I consider **Mars' inner moon Phobos**. Simulations of just-escaping sesquinary ejecta show persistent reaccretions in low-velocity chain-like clusters similar to catenae on Ganymede and Callisto. The morphological similarity to linear pitted chains on Phobos suggests a link to the long-debated mysterious grooves on Phobos; I conclude that these catenae present the missing piece to families of grooves that do not fit well to a tidal model for groove origin as Phobos spirals toward Mars.

The second puzzle explored in this work pivots to magnetics, but still with a sesquinary flavor. Chapter 4 considers **Earth's Moon**. Despite having no global magnetic field, the Moon still exhibits anomalous localized crustal magnetic fields. The origin of these fields is still mysterious, particularly in the large lunar South Pole-Aitken basin. Inverse regression techniques applied to magnetic anomalies in this region show diverse paleopoles that imply geophysically improbable amounts of true polar wander. A number of possible formation hypotheses are explored, including long and short timescale true polar wander and subsurface dikes magnetized during an ancient period of lunar dynamo activity. Continuing the thread from Chapters 2 and 3, it is found that secondary ejecta from sesquinary impactors, reaccreting as the Moon experienced large changes in its moments of inertia in the aftermath of the

South Pole impact, might also be another plausible explanation for the large paleopole variations observed.

For my fourth and final study (Chapter 5), I pivot to the detection of **extrasolar planets (exoplanets)**. The atmospheric and physical properties of these gas giants are explored; I use parallelized Markov Chain Monte Carlo (MCMC) techniques to perform atmospheric retrievals on future targets of optical wavelength imaging, and retrieve properties such as methane abundance, planet radius, planet gravity and cloud properties. The inverse recovery of spectral signatures of exoplanet coronagraph targets, in the visible wavelength regimes explored here, bear particular application to the planning phase of an upcoming NASA direct-imaging exoplanet mission (WFIRST).

In summary, this dissertation aims to 1) expand studies of sesquinary impacts and help quantify their geophysical importance; 2) present implications inferred from diverse paleopoles from lunar magnetic anomalies, and 3) implement retrieval techniques to study the atmospheres of gas giant planets in solar systems beyond our own.

Chapter 2

Sesquinaries: A Case Study of Deimos

This chapter is a modified reprint of M. Nayak, F. Nimmo and B. Udre (2016), Effects of Mass Transfer between Martian Satellites on Surface Geology, Icarus 267, pp. 220-231, DOI: 10.1016/j.icarus.2015.12.026.

2.1 Abstract

Impacts on planetary bodies can lead to both prompt secondary craters and projectiles that reimpact the target body or nearby companions after an extended period, producing so-called “sesquinary” craters. This chapter examines sesquinary cratering on the moons of Mars. By modeling the impact that formed Voltaire, the largest crater on the surface of Deimos, the orbital evolution of resulting high-velocity ejecta across 500 years is explored using four-body physics and particle tracking.

The bulk of mass transfer to Phobos occurs in the first 10^2 years after impact, while reaccretion of ejecta to Deimos is predicted to continue out to a 10^4 year timescale, in agreement with [Soter, 1971]. Relative orbital geometry between Phobos and Deimos plays a significant role; depending on the relative true longitude, mass transfer between the moons can change by a factor of five. Of the ejecta with a

velocity range capable of reaching Phobos, 25 - 42% by mass reaccretes to Deimos and 12 - 21% impacts Phobos. Ejecta mass transferred to Mars is <10%.

It is found here that the characteristic impact velocity of sesquinaries on Deimos is an order of magnitude smaller than those of background (heliocentric) hypervelocity impactors and will likely result in different crater morphologies. The time-averaged flux of Deimos material to Phobos can be as high as 11% of the background (heliocentric) direct-to-Phobos impactor flux. This relatively minor contribution suggests that spectrally red terrain on Phobos [*Murchie and Erard, 1996*] is not caused by Deimos material. However the high-velocity ejecta mass reaccreted to Deimos from a Voltaire-sized impact is comparable to the expected background mass accumulated on Deimos between Voltaire-size events. Considering that the high-velocity ejecta contains only 0.5% of the total mass sent into orbit, sesquinary ejecta from a Voltaire-sized impact could feasibly resurface large parts of the moon, erasing the previous geological record. Dating the surface of Deimos may be more challenging than previously suspected.

2.2 Introduction

Several features about the surface geology on the moons of Mars remain poorly understood. The grooves on Phobos, which do not exist on Deimos, have received the most attention [*Thomas, 1979; Weidenschilling, 1979; Horstman and Melosh, 1989*], and theories for their formation continue to be proposed to this day [*Murray et al., 2006; Hamelin, 2011; Basilevsky et al., 2014; Asphaug et al., 2015b*;

Nayak and Asphaug, 2015, 2016; Wilson and Head, 2015]. However this is far from the only mystery. Though both moons are heavily cratered, with saturated surfaces and fine-grained regolith from impact debris accumulation [*Thomas, 1979; Lunine et al., 1982*], a large portion of ejecta produced on Deimos is retained in the form of crater fill of ~5 m depth [*Thomas and Veverka, 1980b*], a phenomenon not noted on Phobos. This difference is still unexplained [*Lee, 2009*]. The surface of Deimos is also significantly smoother and brighter than Phobos, likely a result of crater fill [*Veverka, 1978; Thomas, 1993; Thomas et al., 1996*].

Phobos also exhibits two distinct spectral units, one of “redder” origin and one of “bluer” origin, possibly stemming from a compositional difference [*Murchie and Erard, 1996; Lee, 2009*]. The bluer unit is associated with the Stickney crater and an origin from depth. The redder unit associated with the surface and small craters; it is spectrally similar to D-type asteroids, but also to Deimos [*Murchie and Erard, 1993, 1996*]. It has been proposed that the red unit is a wide-spread shallow layer superimposed on a blue base [*Murchie and Erard, 1996*], for which there are four possible causes [*Britt and Pieters, 1988; Murchie et al., 1991*]: 1) accretion of D-asteroid material onto blue Phobos material; 2) optical alteration of the bluer unit; 3) accretion of ejecta from Martian basin impacts and subsequent space weathering or 4) Phobos is an inherently heterogeneous rubble pile and the red/blue units are end-member compositions. One aim of this study is to investigate the possibility that the red veneer on top of the base blue unit may be ejecta accreted from Deimos rather than Mars.

Previous work has established that impact ejecta can reimpact the target body or nearby companions after an extended period, creating so-called “sesquinary” impact morphology. Examples of sesquinary studies in the literature include Earth’s Moon [Gladman *et al.*, 1995], Io [Alvarellos *et al.*, 2008], Ganymede [Alvarellos *et al.*, 2002], Europa [Zahnle *et al.*, 2008] and Pluto [Bierhaus and Dones, 2014]. For Mars, previous work suggests ejecta released at slightly greater than the satellite’s escape velocity could remain in the system and subsequently reimpact at low relative velocities [Soter, 1971, 1972]. Possible evidence for this was noted in analysis of Viking images [Veverka and Duxbury, 1977], however the efficiency of this process was previously unknown [Thomas, 1979]. This chapter reports on the distribution of impact velocities and geometries from inter-moon mass transfer trajectories, and present conclusions on the role and importance of sesquinary mass transfer between the Martian moons.

2.3 Methods

Voltaire, the largest confirmed crater on Deimos, has a diameter of 3 km [Thomas, 1979; Thomas and Veverka, 1980a]. By modeling the orbital evolution of ejecta from the Voltaire-forming impact, we aim to characterize an end-member case of mass transfer from Deimos to other Martian system bodies.

To model the streamlines ejected by the Voltaire impact, we use a simplified form of Maxwell’s Z-model [Maxwell and Seifert, 1974; Maxwell, 1977; Roddy, 1977]. First, coordinate transformations necessary to use surface-centered Z-model

streamlines in a Mars-centered simulation are detailed. Three planet-based frames are used, explained below.

2.3.1 Coordinate Transformations

2.3.1.1 Planet Centered Inertial (PCI) frame

The origin of the PCI frame is the center of the body: Mars, Deimos or Phobos. The positive x-axis points toward the vernal equinox, the positive z-axis extends through the North Pole of the planet and the y-axis completes the right hand system. In this definition, the North Pole is that pole of rotation that lies on the north side of the invariable plane of the solar system [Archinal *et al.*, 2010]. The planetary system model described in Section 2.3.4 is placed with reference to the Mars Centered Inertial (MCI) frame.

2.3.1.2 Planet Centered Planet Fixed (PCPF) frame

Like the PCI frame, the origin of the PCPF frame is also the center of the body, and shares its z-axis definition. However, the x-axis extends through the intersection between the planet's equator and its prime meridian, with the y-axis completing the right hand system.

Figure 2.1 illustrates the relationship between the PCI and PCPF frames. PCI can be rotated into the PCPF frame around the z-axis with the rotation matrix:

$${}^{PCPF}R^{PCI} = \begin{bmatrix} \cos w & \sin w & 0 \\ -\sin w & \cos w & 0 \\ 0 & 0 & 1 \end{bmatrix} \quad (2.1)$$

where w is the angle of rotation.

2.3.1.3 Topocentric Horizon Frame (also SEZ: South-East-Zenith frame)

The topocentric horizon frame is adapted from the South-East-Zenith (SEZ) frame as defined by [Vallado, 2013]; the two are referred to interchangeably here. The definition of the Topocentric Horizontal frame assumes a sphere centered at the center of mass of Deimos and tangent to the origin of the frame, which is the center of the impact site (Voltaire). The x-axis is aligned with the meridian that passes through the center of Voltaire and points south. The y-axis is defined such that the x-y plane is tangent to the surface of Deimos at the center of Voltaire and points along the local latitude circle. Completing the right-handed system, the z-axis points radially outward from the impact site towards the “local” zenith. The local horizon forms the fundamental plane for this system, i.e., the plane defined by the south and east axes. It should be noted that there is a subtle difference between the definition of the impact site’s latitude by geodetic or astronomical standards [Vallado, 2013]; these become identical by imposing the assumption of a perfectly spherical impacted body (Deimos). The low gravitational acceleration at the surface of Deimos has a negligible effect on the speed of the ejecta, so the assumption of a uniform spherical geometry is justified.

Figure 2.2 illustrates the relationship between SEZ and PCPF. ε_{ej} is the elevation angle of the ejection velocity vector from the horizontal, defined as $0 \leq \varepsilon_{ej} \leq 90^\circ$. From the Z-model formulation (see Section 2.3.2), $\varepsilon_{ej} = 35.4^\circ$. β_{ej} is the azimuth of the ejection velocity vector and is measured from the North, positive clockwise as viewed from above the site such that $0 \leq \beta_{ej} \leq 360^\circ$, and is sampled

at 11 positions across this range separated by 30° . The streamlines defined in Z-model frame can be rotated into SEZ using the relationships:

$$\begin{aligned} v_{South} &= v_r \cos(180^\circ - \beta_{ej}) \\ v_{East} &= v_r \sin(180^\circ - \beta_{ej}) \end{aligned} \quad (2.2)$$

where v_r is defined by Equation 2.7. Subsequently two rotation matrices, the first around the y-axis and the second around the z-axis, are required to rotate the SEZ frame into the PCPF frame (specifically, the Voltaire SEZ frame into the Deimos-Centered Deimos-Fixed frame). The rotation matrices are:

$${}^{DCDF}R^{SEZ} = \begin{bmatrix} \cos \lambda_i & -\sin \lambda_i & 0 \\ \sin \lambda_i & \cos \lambda_i & 0 \\ 0 & 0 & 1 \end{bmatrix} \begin{bmatrix} \sin \varphi_i & 0 & \cos \varphi_i \\ 0 & 1 & 0 \\ -\cos \varphi_i & 0 & \sin \varphi_i \end{bmatrix} \quad (2.3)$$

where φ_i and λ_i are illustrated in Figure 2.2. Finally, the DCDF velocity coordinates are converted to MCI. By manipulating the basic kinematic equation for the position vector of an ejected particle in the DCDF frame, \vec{r}_e^{DCDF} , in terms of the known \vec{v}_e^{DCDF} :

$$\vec{v}_{ej}^{MCI} = \frac{d}{dt} \vec{r}_D^{MCI} + \vec{v}_{ej}^{DCDF} + {}^{MCI}\omega^{DCDF} \times \vec{r}_i^{DCDF} \quad (2.4)$$

Now $\frac{d}{dt} \vec{r}_D^{MCI} = \vec{v}_D^{MCI}$, where \vec{v}_D^{MCI} is the velocity vector of Deimos in the MCI frame. This is determined from Deimos ephemerides. ${}^{MCI}\omega^{DCDF}$ is the angular rate of the DCDF frame with respect to MCI; this is the rotation rate of Deimos. \vec{r}_i^{DCDF} is the position of the impact site in DCDF coordinates.

Following a similar process, for the impact of ejecta with Phobos the process is reversed to obtain the velocity vector at impact in the Phobos Centered Phobos-Fixed (PhCPhF) frame. With similar notation as used above this relation is:

$$\vec{v}_{ej}^{PhCPhF} = \vec{v}_{ej}^{MCI} - \vec{v}_{Ph}^{MCI} - {}^{MCI}\omega^{PhCPhF} \times \vec{r}_i^{PhCPhF} \quad (2.5)$$

The validity of these equations has been checked with MICE, a commercial level interface created by JPL/Caltech to SPICE ephemeris information from NASA's Navigation and Ancillary Information Facility (naif.jpl.nasa.gov) [Acton *et al.*, 2002].

2.3.2 Impact Model: Generating 2-D Streamlines

To model the streamlines ejected by the Voltaire impact, we use a simplified form of Maxwell's Z-model [Maxwell and Seifert, 1974; Maxwell, 1977; Roddy, 1977]. Though limited by its neglect of interactions across streamlines, the Z-model reasonably approximates several experimentally observed features [Melosh, 1989; Richardson *et al.*, 2007]. The limitations of a Z-model implementation are discussed at length by [Barnhart and Nimmo, 2011]. This application is only concerned with ejecta streamlines that escape Deimos, and is unaffected by the details of cratering flow beneath the ground plane, surface material mixing during ejection or direct retention and emplacement of deposits. Therefore it provides a suitable level of insight into an outbound velocity distribution; approximations made by the Z-model are unlikely to alter our qualitative results.

The formulation of [Barnhart and Nimmo, 2011] is adopted here, who use $Z = 2.71$ for a Mars application. When tested against numerical computations, $Z = 2.7$ represents surface explosion cratering flow well [Melosh, 1989]. All streamlines are

ejected at a constant angle of 35.4° from the horizontal, set according to the relation [Maxwell, 1977]:

$$\varepsilon_{ej} = \tan^{-1}(Z - 2) \quad (2.6)$$

Outbound radial (v_r) and vertical (v_z) ejection velocities vary inversely with distance from the center of the crater r [Maxwell, 1977] as:

$$v_r = \alpha / r^Z \quad (2.7)$$

$$v_z = (Z - 2)v_r \quad (2.8)$$

where g_D denotes the acceleration due to gravity for Deimos (0.003 m/s^2) and:

$$\alpha = \sqrt{\frac{g_D R_t^{2Z+1}}{4Z(Z-2)}} \quad (2.9)$$

Using a final crater radius $R_f = 1500 \text{ m}$ for Voltaire [Veverka, 1978], the transient crater radius is calculated as $R_t = 0.65 R_f$ [Barnhart and Nimmo, 2011]. For the analysis presented here the number of streamlines (n) has been chosen to yield a suitably dense streamline distribution with velocities greater than the Deimos escape velocity. Setting $R_{min} = 0$ and varying $R_{min} \leq r \leq R_t$, $n = 600$ streamlines evenly spaced in radius are generated within the Voltaire crater. Converting streamlines into axisymmetric coordinates [cf. Barnhart and Nimmo, 2011, Fig 1], the radial and vertical coordinates are extracted as:

$$r = R_i \sin \theta (1 - \cos \theta)^{\frac{1}{Z-2}} \quad (2.10)$$

$$z = R_i \cos \theta (1 - \cos \theta)^{\frac{1}{Z-2}} \quad (2.11)$$

where θ is the angle from the vertical $\{\theta \mid \theta \in 0 : \pi/2\}$ and:

$$R_i = \frac{R_f - R_{min}}{n} \quad (2.12)$$

2.3.3 Creating 3-D Velocity Streamlines

The 2-D axisymmetrical distribution is now used to create an approximation to a 3-D excavation. The fate of the ejecta particle (reaccretion to Deimos, impact to Phobos, impact to Mars or escape) can vary greatly depending on the azimuth of the streamline. To rotate around the azimuthal direction, we define the Topocentric Horizon frame (Section 2.3.1.3), adapted from the South-East-Zenith (SEZ) frame [Vallado, 2013]. The azimuth of the ejection velocity vector β is measured from the north, clockwise as viewed from above the impact site. A 30° span is selected as a compromise between computational efficiency and sampling a variety of azimuths across the possible solution space, such that $\beta \mid \beta \in (0: \pi/6: 2\pi)$ for a total of 11 possible azimuths. This yields a three-dimensional outbound velocity distribution tied to Voltaire. For use with the Mars gravity system integrator, these coordinates are then rotated into the Mars Centered Inertial (MCI) frame; details of coordinate transformations through the Deimos-Centered Deimos-Fixed (DCDF) and Deimos-Centered Inertial (DCI) frames were presented in Section 2.3.1.3.

Finally, this work is specifically interested in those streamlines that have sufficient velocity to reach the orbit of Phobos. Since both moons lie in the same orbital plane [Cazenave *et al.*, 1980], the minimum velocity at Deimos to reach Phobos can be analytically calculated with the Hohmann transfer [Section 6.3, Curtis, 2013]. Particles begin to cross the orbit of Phobos at velocities above 500 m/s, so we set the lower bound on velocities of interest at 400 m/s. From Deimos, the minimum

velocity to escape the gravitational well of Mars is analytically approximated as [Eqn 2.80, *Curtis*, 2013]:

$$v_{esc} = \sqrt{2\mu/r_{Deimos}} \quad (2.13)$$

where r_{Deimos} is the distance from Deimos to Mars and μ is the product of the gravitational constant and the mass of Mars. From Equation 2.13, $v_{esc} = 1.91$ km/s; we set the upper bound on velocities of interest at 2 km/s. Therefore, velocity streamlines in the range $\{v \mid v \in 400 : 2000 \text{ m/s}\}$ are examined. Nineteen of 600 streamlines fall within this range; rotated around 11 azimuthal positions, this creates a 209-streamline distribution. While this work focuses on ejecta with sufficient velocity to reach Phobos (~ 400 m/s), note that the majority of ejecta launched from Deimos at lesser velocities will ultimately re-impact Deimos.

2.3.4 Planetary System Model

This section details the formulation of the planetary model. Centered at the primary, the Mars gravity system is modeled with 12 x 12 gravity harmonics from the NASA Planetary Data System [pds-geosciences.wustl.edu] [*Murchie*, 2010]. The effects of permanent solid tides are included, truncated to the size of the gravity field. The present-day orbit of Deimos is likely similar to its primordial orbit [*Burns*, 1978; *Lambeck*, 1979]; the 500-year orbits of Phobos and Deimos are generated analytically from modern-day mean orbital parameters [ssd.jpl.nasa.gov, Table 2.1]. A subset of streamlines was run against high-precision orbits generated for Phobos and Deimos [*Genova and Folkner, personal communication, 2015*]; results were not found to

differ substantially from those run against the analytical orbits. In the interest of computational speed, the analytical formulation is adopted hereafter.

Table 2.1. Mean Orbital Parameters and Constants for Phobos and Deimos

	Deimos	Phobos
Semi-major axis	23485 km	9389.8 km
Eccentricity	0.00115571	0.0164255
Inclination	1.79 deg	1.09 deg
Right Ascension of Ascending Node	148.0 deg	319.9 deg
Argument of Periapsis	123.3 deg	270.7 deg
Mean longitude ¹	109.7 deg	190.6 deg
Rate of mean longitude	0.00330049 deg/s	0.0130317 deg/s
Mean radius	6.2 km	11.3 km
Acceleration due to gravity	0.003 m/s ²	0.0057 m/s ²
Escape velocity	5.56 m/s	11.39 m/s
Hill sphere radius	16.5 km	21.5 km

Due to its proximity to Mars, the orbit of Deimos is primarily influenced by Mars’ oblateness; the third-body effect from the Sun or other planetary bodies such as Jupiter is negligible [Burns, 1972]. Ejecta released from the orbits of Deimos will follow a similar pattern; we therefore neglect these third-body effects. Similarly, solar radiation pressure is a second-order effect when compared to solar gravity perturbations [Klacka, 2002; Farnocchia et al., 2014]; we neglect this effect as well. However for complete understanding of orbital evolution within the Martian system we include third-body perturbation effects from Phobos and Deimos, making the physics of our model a four-body problem.

It is assumed that any particle that enters the Hill sphere (Table 2.1) of either moon will be captured by it². Due to its irregularly triaxial shape, Deimos has an

¹ Mean longitude is calculated with reference to a mean epoch coordinate system: The mean equator-mean equinox coordinate system is evaluated at the epoch of the object. The starting epoch is arbitrary due to our evaluation of the orbital dynamics at multiple relative geometry configurations between Mars, Phobos and Deimos that encompass all possible geometries between the bodies.

uneven gravity field that causes the escape velocity to be lower at the sub-Mars and anti-Mars points [Davis *et al.*, 1981]. Ejecta in the 4-6 m/s range will see the largest variation in range [Thomas, 1993]; since the slowest particle we consider is ejected at ≥ 400 m/s and the escape velocity varies on the order of cm/s, it may be safely assumed that the escape velocity at Voltaire equals the average escape speed over Deimos.

Finally the impact of relative orbital geometry is considered. Though an analytical formulation has been used to consider similar problems in the past [Soter, 1971; Dobrovolskis and Burns, 1980; Thomas, 1998], this approach may be insufficient for a full understanding of ejecta dynamics. Phobos is closer to Mars than any other planetary satellite, and is the only moon with an orbital period less than the rotational period of its primary body [Burns, 1972]. The flux of material impacting Phobos can vary drastically between inferior and superior conjunctions between Phobos and Deimos. The difference in the true longitude between Deimos and Phobos can (and does, see Figure 2.3) change the outcome of a Phobos collision to a Mars collision, or vice versa. Therefore, though the orbits of Phobos and Deimos are generated analytically, all propagation in this work is ephemeris-centered.

Deimos has an orbital period of 30.3 hours, and Phobos 7.5 hours. To evaluate the fate of ejecta across the range of possible Mars-Deimos orbital geometries, this orbit is discretized into 28 geometry configurations (GCs), evenly spaced in one-hour

² To test the validity of using the Hill sphere as an impact boundary, we selected 100 Phobos impact trajectories at random and integrated them with an impact boundary of 13 km, the longest semi-major axis of Phobos [Murchie *et al.*, 2003]; 98/100 trajectories were still found to impact. Therefore, our qualitative results are not affected by the use of the Hill sphere as an impact boundary.

increments from the Deimos apoapsis. In this time period, Phobos completes nearly four orbits of Mars, allowing for discretization of the range of possible Mars-Phobos-Deimos orbital geometries as well. At each GC, 209 streamlines are released and propagated, for a total of 5,852 streamlines, thereby ensuring a robust capture of the impacting process despite variations in orbital positions and conjunction geometries.

Estimates for lifetime of ejecta in the Martian system range from 10^2 to 10^4 years [Soter, 1971; Davis *et al.*, 1981]. Each streamline is integrated in the Mars gravity system for $t_{\max} = 500$ years, stopping sooner only in the event of a planetary body collision or departure from the Mars gravitational sphere of influence. This length of integration balances computational feasibility with permitting a statistically significant number of ejected particles to impact or escape. As shall be shown, the uncertainty introduced by doing so does not affect our conclusions. It also permits the use of a Runge-Kutta integrator without excessive approximations to the perturbed Hamiltonian [Leimkuhler and Reich, 2004]. A seventh-order Runge-Kutta integrator with eighth-order error control is used for all orbit propagations. The maximum permitted relative error is 10^{-10} . The Tisserand parameter is used to evaluate the performance of the integrator, according to which:

$$\frac{1}{a} + 2\sqrt{a(1 - e^2)}\cos i \cong \text{constant} \quad (2.14)$$

where a , e and i are the semi-major axis, eccentricity and inclination of the orbit. The differences in the Tisserand parameter for an individual particle are no greater than 10^{-5} , i.e., at most, a 0.001% change across the integration period.

2.4 Results

Figure 2.3 plots the fate of 5,852 massless ejecta particles in the Martian gravity system across 500 years as a function of the orbital geometry and Voltaire ejection velocity. The number of reaccretions to Deimos and particles still flying are relatively constant, with minor fluctuations. However, if the Voltaire impact occurs when Deimos is near periapsis, a spike in Mars impacts and a corresponding drop in particles escaping the system are noted. This is, in fact, due to the difference in true longitude between Phobos and Deimos at the time of ejecta launch; depending on the relative conjunctive geometry, the mass flux from Deimos to Phobos can be up to 500% higher.

It is surprising to note that there is more mass flux from Deimos to Phobos as opposed to Mars; intuitively, one would expect that most mass ejected from Deimos would either reaccrete or spiral down to Mars. Because greater mass is released at lower ejection velocities [*O’Keefe and Ahrens*, 1985], these results suggest impacts on Deimos may have an effect on Phobos' geology; we shall attempt to estimate the magnitude of that effect in Section 2.5.

For impacts with Mars, Phobos or Deimos, impact velocity is calculated with reference to the Planet-Centered Planet Fixed frame (Section 2.3.1.3) in question. The variation of impact speeds at Phobos and Deimos is charted across 28 GCs (Figure 2.4). For Phobos, regardless of orbital location at the time of ejecta release, impact velocity scales linearly with particle ejection velocity. Faster particles impact with higher speeds, in some cases up to 4 km/s (though still not as high as ~20 km/s

expected for heliocentric impactors). On Deimos, however, impacts above 1 km/s are relatively rare. Almost no high-velocity (>1 km/s) impacts are noted from near-apoapsis positions. 81% of impacts are clustered in the 0.4-0.8 km/s region, implying that low-velocity reaccretions to Deimos are relatively common.

Next, the relationship between impact velocities and the time to impact is examined. No significant acceleration effect with time or particular links to orbital geometry are noted (Figure 2.5). However, the contrast between the two bodies is again evident. On Phobos, the majority of impacts occur in less than 100 years; subsequent impacts become less frequent as time increases. This implies that the 500-year timescale selected is adequate to capture the majority of Deimos-to-Phobos material transfer. On Deimos, however, impacts continue to build, with the flux of impacts remaining relatively constant even at the end of the 500-year timescale. Therefore, it seems that while the majority of mass transfer to Phobos occurs early on, reaccretions to Deimos likely continue out to the 10^4 year timescale hypothesized by Soter (1971). This also makes it likely that a large number of the particles still flying at the end of the 500-year simulation will end up reaccreting to Deimos. As a consequence, it is unlikely that increasing the computation time will qualitatively change our conclusions.

The flight path angle (FPA) is the angle between the incoming velocity vector and the position vector defined by the surface of the planet, and can be calculated as [Curtis, 2013]:

$$\tan \Upsilon = \frac{\pi}{2} - \frac{e \sin \Phi}{1 + e \cos \Phi} \quad (2.15)$$

where e is the eccentricity of the impact trajectory and Φ is the true anomaly.

The relationship between impact velocity and FPA reinforces the rarity of high-speed reaccretion events on Deimos (Figure 2.6). On Phobos, the frequency distribution of impactor velocities and flight path angles suggests that impacts created by Deimos ejecta can vary from oblique, classically secondary impacts to direct cratering events.

Finally, investigating the likelihood of continuing collisions beyond the chosen 500-year timeframe tests the fidelity of these results. Figure 2.7 shows time curves for particles still flying and particles impacting Phobos or Deimos. As expected, Phobos impacts taper off with time, and the total number of Phobos impacts (y) fits well ($R^2 > 0.995$) to a logarithmic distribution defined by $y = 178.4 \ln(t/t_0)$, where t is time in years and the time constant t_0 is ~ 10.46 years. Deimos impacts continue to increase and fit well ($R^2 > 0.995$) to a distribution defined by $y = 469 \ln(t/t_0)$, where the time constant t_0 is ~ 47.9 years. Interestingly, the ratio between the time constants for Phobos and Deimos are similar to the ratio of their orbital periods.

Reaccretions to Deimos are therefore expected to continue, but for how long? The shape of the graph for particles still in flight is in a logarithmic decrease; when extrapolated (Figure 2.7, far right) it takes approximately 10,000 years for the number of particles still in flight to drop below 10% of the total number of particles generated. This result agrees well with predictions made by Soter (1971). However, a word of caution is appropriate here. Soter and this study both neglect effects of solar

radiation pressure. While a second-order effect on the 500-year timescale, it can play a significant role across longer time periods, and could decrease the time to impact [Klacka, 2002]. Based on this, conclusions drawn here are not expected to change qualitatively with an increase in propagation time and corresponding decrease in number of particles still flying.

By analyzing the Martian system within the framework of an analytical restricted three-body problem, previous work finds that essentially all ejecta from either Phobos or Deimos will be reaccreted to the moon of origin [Soter, 1971; Dobrovolskis and Burns, 1980]. Differing results in this work suggest that the four-body ephemerides formulation is critical to full understanding of the orbital dynamics.

2.5 Mass Transfer between Martian Satellites

To investigate the geologic impact of mass transfer between Phobos and Deimos, it is desired to convolve the probability distributions from Figure 2.3 with an appropriate mass-velocity distribution. Advanced scaling laws developed from numerical methods exist [e.g. *Leinhardt and Stewart*, 2012], but given the uncertainties associated with several key parameters, a more transparent and simpler approach is preferred. For gravity-dominated cratering the volume ejected faster than a given velocity is [*Holsapple*, 1993; *Housen and Holsapple*, 2011]:

$$V = R^3 C_{ej} \left(\frac{v_{ej}}{\sqrt{gR}} \right)^{-\nu} \quad (2.16)$$

where v_{ej} is the ejection velocity (from Figure 2.3) and R is the final radius of Voltaire.

A sand-like surface is well represented by $\nu = 1.2$ [Melosh, 1989]. Experimental results that determine mass-velocity distributions for impacts into granular targets find $C_{ej} = 0.25$ [Hermalyn and Schultz, 2013]. Their results correlate well to the literature; Andrews (1975), Cintala et al (1999) and Stöffler et al. (1975) find C_{ej} values between 0.25 and 0.36. We adopt $C_{ej} = 0.3$ and $\nu = 1.2$. For Phobos' density $\rho = 1.9$ g/cc [Avanesov et al., 1989; Rosenblatt et al., 2008; Schmedemann et al., 2014] is used. From (2.16), the mass ejected within each velocity bin is calculated (Figure 2.8). In total, 3×10^9 kg is ejected from Deimos between 400-2000 m/s.

Using Equation 2.16 and the acceleration due to gravity of Deimos (0.003 ms^{-2}), the total mass excavated faster than escape velocity is 6.1×10^{11} kg; 0.5% of this total is therefore ejected in the 400-2000 m/s velocity range. Of this 0.5%, what percentage reaches Phobos? From integrating the mass delivered per velocity bin (Figure 2.8) and averaging it across impacts at all GCs (Figure 2.3), approximately 3.5×10^8 kg impacts Phobos. This is 12% of the total mass released in the 400-2000 m/s range. This is also 21% of the mass not still in orbit at the end of the simulation (“still flying”, Figure 2.3). If all this mass were to ultimately impact Phobos, the total impacting mass would be 6×10^8 kg, the likely maximum value. Therefore, 12-21% of the mass that *can* reach Phobos *does* end up on Phobos on a 10^4 -year timescale.

The same analysis yields 7.2×10^8 kg impacting Deimos, which is 25% of the total mass released in the 400-2000 m/s range and 42% of the mass in this range not

still flying. This yields an upper bound of 1.2×10^9 kg impacting Deimos. Ejecta launched at lower velocities than 400 m/s cannot reach Phobos and will mostly re-impact Deimos. Mars only receives 5-9% of ejecta in the 400-2000 m/s range. The remaining ejecta escapes the Mars system into heliocentric space.

2.5.1. Comparison with Background Flux

We seek to place the sesquinary mass flux into perspective by comparing it to the estimated background mass flux from meteoroidal impacts. The exact flux of small meteoritic bodies at Mars orbit is not known, so a formulation dependent on a characteristic timescale is derived below, which eliminates the Mars mass flux quantity. Brown et al (2002) use data from geostationary satellites around the Earth to estimate a power law relationship between the number of objects colliding with the Earth per year (N) with diameters of at least D , of the form:

$$\log N = c_0 - d_0 \log D \quad (2.17)$$

where $c_0 = 1.568 \pm 0.03$, $d_0 = 2.70 \pm 0.08$. Assuming the same power law distribution for Martian system bodies, for $N = N_{planet}$ this can be reformulated as:

$$N_{planet}(d > D) = C_{planet} D^{-d_0} \quad (2.18)$$

where $C_{planet} = 10^{c_0}$. As will be shown, the value of this constant does not matter for the analysis in this work. Assuming spherical impactors with diameter D and density ρ_i , the incremental number of impactors dN per year results in a mass flux increment of:

$$dM = \frac{1}{6} \rho_i \pi D^3 dN \quad (2.19)$$

kg per year. Differentiating Equation 2.18, substituting into Equation 2.19 and integrating to $D_{max} = D$, the mass accumulated by a generic planetary body in kg/yr from asteroidal flux is:

$$M_{planet}(d > D) = C_{planet} \left[\frac{d_0}{3-d_0} \right] \left[\frac{\pi \rho_i}{6} \right] D^{3-d_0} \quad (2.20)$$

where $d_0 < 3$. Zahnle et al (2003) derive a relationship for the impact rate of a satellite compared to its planet. Applied to the Mars system, this is:

$$N_{Pho}(d > D) = N_{mars} f_{Pho} \quad (2.21)$$

where D is the diameter of the largest impactor incident to Phobos and:

$$f_{Pho} = \frac{R_{Pho}^2}{R_{mars} a_{Pho}} \quad (2.22)$$

where a is the distance from Mars. The resulting values are 5×10^{-7} and 4×10^{-6} for Deimos and Phobos respectively. Combining Equations 2.18 and 2.21 for Phobos:

$$C_{Pho} = \frac{f_{Pho}}{D_{st}^{-d_0}} N_{mars}^{st} \quad (2.23)$$

where N_{mars}^{st} signifies $N_{mars}(d > D_{st})$. The assumption here is that Stickney is the largest impact to have occurred on Phobos over its history and the diameter of the Stickney-forming impactor is D_{st} . Substituting Equation 2.23 into Equation 2.18, and applying 2.18 to N_{mars}^{st} :

$$M_{Pho}(d > D_{st}) = C_{mars} f_{Pho} \left[\frac{d_0}{3-d_0} \right] \left[\frac{\pi \rho_i}{6} \right] D_{st}^{3-d_0} \quad (2.24)$$

Next, we define a characteristic timescale τ defined such that τ years elapse between Voltaire-size collisions on Deimos. From (2.21) and the definition of N :

$$\tau = 1/N_{Dei} = 1/(f_{Dei} N_{mars}^{vol}) \quad (2.25)$$

where N_{mars}^{vol} is $N_{mars}(d > D_{voltaire})$ for Deimos. Expanding this according to Equation 2.18:

$$\tau = 1/(f_{Dei} C_{mars} D_{vol}^{-d_0}) \quad (2.26)$$

Across τ years, combining Equations 2.24 and 2.26, the poorly known (and, on long timescales, time-variable) annual mass flux delivered to Mars represented by C_{mars} cancels. The total mass accreted by Phobos due to background impacts on a Voltaire timescale is:

$$m_{Pho,acc} = \tau M_{Pho} = \frac{f_{Pho}}{f_{Dei}} \left[\frac{d_0}{3-d_0} \right] \left[\frac{\pi \rho_i}{6} \right] \frac{D_{st}^{3-d_0}}{D_{vol}^{-d_0}} \quad (2.27)$$

Equation 2.27 is only dependent on the diameter of the impactors and the slope of the size-frequency distribution. For Phobos, the largest crater is Stickney, with a 170-m likely impactor size [Asphaug and Melosh, 1993]. For Deimos, the Voltaire impactor diameter is estimated from gravity-dominated scaling relations, rearranged from *Cintala and Grieve* (1998) and *Schmidt and Housen* (1987) and similar to *Zahnle et al* (2003):

$$D_{vol} = \left(0.862 D_t \left(\frac{\rho_D}{\rho_i} \right)^{\frac{1}{3}} V_i^{-0.44} g_D^{0.22} \right)^{1.2821} \quad (2.28)$$

where the subscript i denotes the impactor that created Voltaire, subscript d denotes Deimos, units are CGS and D_t is the diameter of the Voltaire transient crater, taken to be 1.95 km. Asphaug and Melosh (1993) assume an impact of 3 km/s for the Stickney impact; assuming the same impact velocity and impactor density, (2.28) yields a Voltaire impactor diameter of 25 m. From Equation 2.27, for an asteroid-type impact ($\rho_i=2.6$ g/cc; *Barnhart and Nimmo* (2011)), the mass accreted by Phobos from

solar system impactors between Voltaire-scale impacts is approximately 2.9×10^9 kg; it would be less if the impactor were assumed to have the lower characteristic density of Phobos. Comparing this to the 3.5×10^8 kg that impacts Phobos during every Voltaire impact, the fraction of Deimos material delivered to Phobos (F) represents, on average, 0.12 of the material accreted to Phobos from direct solar system impactor flux.

Using a similar derivation for Deimos, it is found that only 2×10^8 kg is accreted to Deimos by solar system impactors between Voltaire-size events. Deimos receives less material than Phobos because the focusing factor (Equation 2.21) is smaller. This flux is exceeded greatly by the reaccreted mass ejected during a Voltaire-size impact; for ejecta with velocities 400-2000 m/s, $F = 3.6$, where F is the fraction of Deimos material delivered to Phobos. However this velocity range is only 0.5% of the total mass thrown into orbit. Ejecta with velocity < 400 m/s has insufficient velocity to reach Phobos (or Mars) and will likely reaccrete to Deimos. Thus, the true value of F across all ejecta is likely ~ 700 for Deimos. In other words, on Deimos, mass reaccreted during a Voltaire-size impact greatly exceeds mass naturally accreted from solar system impactors. However, sesquinarities from a large impact on Deimos provide only a minor contribution to the flux at Phobos.

As a reality check, the applicability of Equation 2.17 to Mars system impacts is calculated. The frequency of a Voltaire-sized impact is $\tau = 1/N_{dei}$ years, or 134 Ma. The issue of the apparent age of Voltaire is discussed further below. Using Equation 2.26, the ratio of the timescale for a Voltaire-forming impact on Deimos to a

Stickney-forming impact on Phobos is 0.049. Therefore, the frequency of a Stickney-sized impact is approximately every 2.7 Ga, which seems quite reasonable.

As an additional check, the mass flux to Mars is estimated from studies in the literature. *Chappaz et al* (2011) find that the mass flux from Mars to Phobos can be estimated at $0.25 \mu\text{g}/\text{m}^3/\text{yr}$ or $0.2 \text{ kg}/\text{yr}$ across the inner moon's surface area assuming a mixing depth of 0.5 m. The mass flux of solar system projectiles to Phobos is numerically found to be $k = 40\text{-}2400$ times greater than the flux from Mars ejecta, with a Monte Carlo preferred value of $k = 195$ [*Ramsley and Head*, 2013]. The preferred value yields a mass flux at Phobos of $38.5 \text{ kg}/\text{yr}$ from asteroids, comets and meteoroids. At this rate, across 134 Ma, Phobos accumulates $5.2 \times 10^9 \text{ kg}$ from direct impacts, within a factor of two of the $2.9 \times 10^9 \text{ kg}$ derived above.

While independent of Mars' meteoroidal flux, the results are admittedly susceptible to the assumed size of the Voltaire impactor. The size of Stickney implies that the gravity regime approximation is likely appropriate. However the short timescale derived for the Voltaire impact implies that it may be deeper in the strength regime than initially assumed. If true, the Voltaire impactor would have to be larger than 25 m, which would reduce quantitative estimates of F , the fraction of Deimos' mass flux with respect to the solar system impactor mass flux.

Assuming that the impactor was incident at a 45° angle [*Melosh*, 1989; *Holsapple*, 1993], the diameter of an impactor for strength-dominated cratering may be estimated by rearranging Equation 1.17 from *Zahnle et al* (2008) to yield:

$$D_{vol} = 1.027 \left(\frac{Y}{V_t^2} \frac{D_t^3}{\rho_i} \right)^{\frac{1}{3}} \quad (2.29)$$

where Y represents the dynamic strength of the body; other variables are as in Equation 2.28. *Melosh* (1989) uses a value of $Y = 2$ MPa, the observed yield stress at crater collapse, to estimate the gravity/strength transition on the Earth and the Moon. Adopting this value in Equation 2.29, the diameter of the Voltaire impactor is 88 m. However, the value of Y is uncertain; for the low-density Deimos, it is unlikely that the yield strength is as high as 2 MPa. For an order of magnitude change in Y ranging from 0.2 to 20 MPa, the diameter of the impactor varies from 40 to 190 m.

Is strength or gravity scaling more appropriate for modeling the Voltaire impact? Gravity can be a factor on solar system bodies as small as 400 m [*Love and Ahrens*, 1996]. Phobos and Deimos have similar compositions, bulk densities and accelerations due to gravity [*Davis et al.*, 1981; *Szeto*, 1983], and several arguments for modeling cratering on Phobos in the gravity-dominated regime are detailed in *Asphaug and Melosh* (1993) and *Asphaug et al* (2015a). Finally, while some authors have used the wide distribution of ejecta on Deimos to surmise that strength-scaling may be appropriate for Deimos [*Lee et al.*, 1986], we suggest that this global distribution could instead be a function of the large amount of mass reaccreted over 500yr timescales (Section 2.3). However, even if the Voltaire impact is in the strength regime, this would not change our qualitative results, i.e., 1) that the sesquinary mass transfer is a relatively small fraction of meteoroidal impacts to Phobos, and 2) that the mass reaccreted to Deimos from large Deimos impacts exceeds the meteoroidal mass

flux to Deimos. For instance, increasing the diameter of the Voltaire impactor to 88 m, the qualitative results become $F = 0.004$ for Phobos and $F = 24$ for Deimos across all ejecta velocities. Therefore, uncertainty on where the Voltaire impact lies in the gravity/strength regime does not affect our qualitative conclusions.

2.6. Discussion

2.6.1. Importance of Inter-Moon Mass Transfer and Reaccretion

The central result of this work concerns the relative mass transfer during impacts on Deimos. It has been found that a Voltaire-sized impact on Deimos does transfer mass from Deimos to Phobos, with sufficient velocity to create primary crater morphology, discussed further below. When viewed with reference to the solar system impactor flux, the sesquinary mass transfer is not significant, and is likely in the 10% range. However, compared to the 25 ppm of Mars material in Phobos regolith estimated by *Chappaz et al* (2011), one out of ten particles originating from Deimos is a large number and is of interest to Phobos lander mission concepts [e.g. *Udrea et al.*, 2015, 2016].

While the placement of Voltaire within the strength-gravity domain can cause some uncertainty in impactor size, it has been shown that the total ejecta mass reaccreted to Deimos is likely to greatly exceed the background mass flux to Deimos ($F > 20$). A Voltaire-sized impact could therefore feasibly resurface large parts of the moon, erasing the previous geological record. Dating the surface of Deimos may be

more challenging than previously suspected; the surface age may better represent the age of either Voltaire or the similarly sized Swift crater. Further, an 11-km concavity on the southern end of Deimos is hypothesized to be a possible impact scar from an ancient, very large collision [Lee *et al.*, 1986; Thomas, 1993; Thomas *et al.*, 1996]. If true, this would have resulted in the transfer of significant sesquinary mass transfer to Phobos, and a complete resurfacing of Deimos's surface.

2.6.2 The Spectral Dichotomy of Phobos

Phobos exhibits two distinct spectral units, one of “redder” origin and one of “bluer” origin, a distinction that likely stems from a compositional difference [Rivkin *et al.*, 2002; Lee, 2009]. It has been proposed that the red unit is a wide-spread shallow layer superimposed on a blue base that is perhaps more representative of Phobos composition at depth [Murchie and Erard, 1996; Murchie *et al.*, 2008]. Possible mechanisms for the superimposition of red material were briefly outlined in Section 2.1 [Britt and Pieters, 1988]. These include the hypothesis that the spectrally red “veneer” may be ejecta accreted from Deimos rather than Mars, as suggested by, e.g., Smith *et al* (2015).

Presented results for the distribution of low-velocity, oblique-angle impacts (Figure 2.6) support the existence of trajectories that could, in theory, deposit a “veneer” of red Deimos material across Phobos's surface. However, the inter-moon mass flux is relatively small compared to the solar system impactor flux, which likely has a greater effect on the global surface geology, particularly in the 100+ Ma since the last Voltaire-sized impact. Therefore it is believed to be unlikely that the red

veneer of Phobos is of Deimos origin. Recent spectral analysis by *Thomas et al* (2011) supports this finding with evidence of subsequent impacts penetrating the blue unit near Stickney to reveal redder material. This observation casts doubt on the idea that the blue unit may be representative of Phobos at depth [*Basilevsky et al.*, 2014]. Ultimately, sample return from both Phobos and Deimos will conclusively establish which spectral unit is representative of depth; results from this work suggest that the surface unit is unlikely to originate from Deimos.

2.6.3 Primary Versus Secondary Impact Morphology

Due to the dearth of classic secondary impact features such as radial crater chains or herringbones, it has been concluded that few, if any Phobos craters are secondary in origin [*Thomas*, 1979; *Thomas and Veverka*, 1980a]. A similar conclusion was reached for Deimos. A limit of 10 m/s on maximum re-impact velocity was proposed by *Thomas* (1998) and continues to be used in analysis of Phobos' geology [*Murray et al.*, 2006; *Schmedemann et al.*, 2014; *Smith et al.*, 2015]. However, every sesquinary impact studied here occurs at speeds above 100 m/s. Though still orders of magnitude below heliocentric impactor velocities, Figure 2.6 shows several high-velocity, high-FPA particles that could create craters indistinguishable from primary impact craters on Deimos, and particularly on Phobos.

On Deimos, over 80% of impacts cluster in the 0.6 ± 0.2 km/s region, implying that the majority of reaccretions are low velocity (subsonic). However for Phobos sesquinary particles can arrive with either subsonic or supersonic impact

velocities. One would therefore predict a wide range in the resulting crater morphology; a comprehensive image survey of Phobos may be able to distinguish between the different crater morphologies. Several low-velocity, low-FPA particles incident to Phobos have been found here, which could create classic oblique or chained secondary impact morphology; a Phobos image survey by *Smith et al* (2015) finds several craters and deposits likely originating from such low-velocity impacts.

The escape speed from Mars at Phobos' orbit is 3 km/s, which is exceeded by the fastest sesquinary impacts (Figure 2.4). These impacts can create ejecta of their own that may subsequently be lost from the Mars system. Mass loss from Phobos is one possible explanation for why outlines of ejecta blankets are not conspicuous on Phobos [*Lee et al.*, 1986]. Additional simulations of Phobos-centered ejecta dynamics are presented in Chapter 3 and confirm this hypothesis.

2.6.4 Surface smoothness, Brightness and Impact gardening

Very little ejecta escapes large bodies (e.g. Earth), with the majority redeposited locally as a continuous ejecta blanket. Most ejecta escape from very small bodies (e.g. Phoebe [*Burns et al.*, 1996]), never to be reaccreted. Ejecta dynamics on Deimos present an interesting bridge between these two regimes, with sesquinary effects appearing to be important. Ejecta escapes but is then reaccreted on a timescale of up to hundreds of years, resulting in a global, near-isotropic redistribution of sesquinary ejecta.

For a Voltaire-sized impact, almost all of the ejecta material launched at velocities < 400 m/s will ultimately reaccrete to Deimos [Soter, 1972; Thomas *et al.*, 1996]. From equation (2.16) above this represents 6.1×10^{11} kg, or about 0.5m thickness of material distributed evenly over the entire surface. We estimate that the Voltaire and Swift impacts together could have added on the order of 1 m of fresh regolith or crater fill to Deimos. It has been suggested that the smoother and brighter surface of Deimos is due to crater fill of 5-7 m depth [Veverka, 1978; Thomas, 1979, 1993; Thomas *et al.*, 1996]. Given our estimate, it is suggested that reaccreting sesquinary mass provides at least a partial explanation for the origin of this crater fill material.

The impact velocity distributions (Figure 2.4) also suggest a tertiary ejecta effect. Though most sesquinary impacts to Deimos are relatively low speed (< 1 km/s), these are still significantly higher than the escape velocity of Deimos (5.5 m/s, Table 2.1) and could potentially launch additional ejecta in their turn (see below). Similarly, ejecta from Deimos can impact Phobos with enough mass and speed to create craters and excavate Phobos mass, which could then enter Mars orbit.

On Deimos, sesquinary impacts represent a large mass flux relative to the background flux and have \sim km/s impact velocities (Figure 2.2). The result is likely to be the production of further suborbital, ballistically emplaced ejecta. This mechanism could contribute to the smooth appearance of the Deimos surface. Energy and momentum transfer from reaccretion impacts might even set off downslope movement noted on Deimos [Thomas and Veverka, 1980b], though admittedly the

efficiency of the impacts at initiating this process is unknown and should be constrained in the future.

The possibility of sesquinary impact gardening makes the evolution of regolith in between major collision events a complex process on both Martian moons. Determining the exact nature of Deimos material mixed with Phobos regolith is one of the primary science objectives of lander concepts in development for Phobos [Udrea *et al.*, 2015, 2016]. The methods applied in this work are further applicable to understanding regolith development and dust belts on small bodies within planetary gravitational wells, such as the Saturnian moons of Tethys, Calypso and Telesto.

2.7 Figures

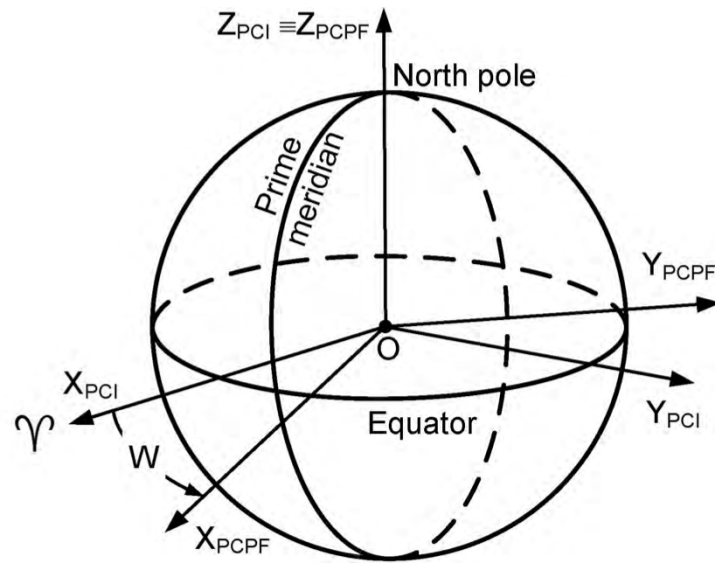


Figure 2.1. Illustration of the relationship between the Planet-Centered Inertial (PCI) and Planet-Centered Planet-Fixed (PCPF) frames.

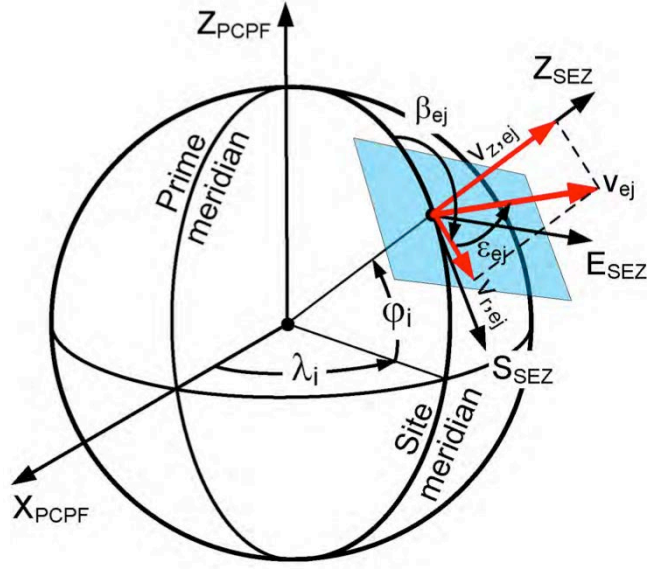


Figure 2.2. Illustration of the relationship between the Planet-Centered Planet Fixed (PCPF) frame and the South-East-Zenith (SEZ) frames. The fundamental plane is highlighted (blue).

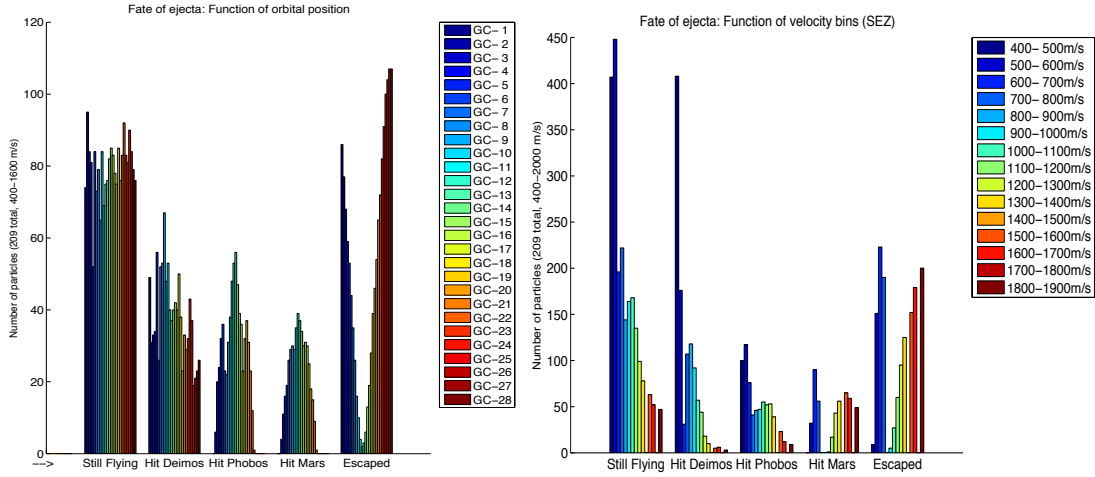


Figure 2.3. The fate of Deimos ejecta from Voltaire as a function of (Left) Orbital Geometry and (Right) Ejection Velocity from Voltaire. GC-1 is near-apoapsis; GC-14 is near-periapsis. Note that the difference in the Deimos-Phobos angle is the important quantity with regard to ejecta fate (see text).

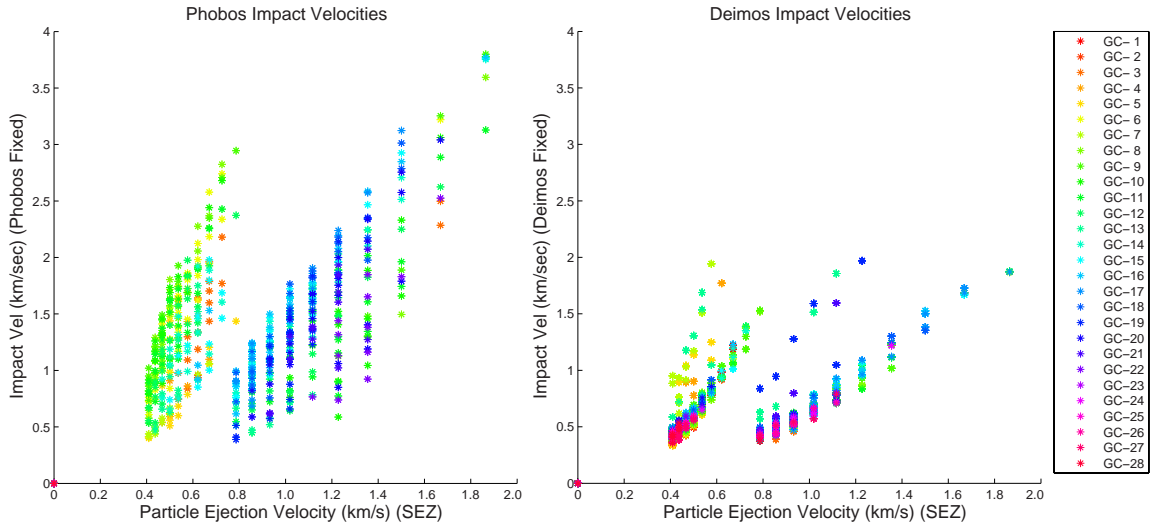


Figure 2.4. (Left) Impact Velocity at Phobos and (Right) Impact Velocity at Deimos versus particle ejection velocity from Voltaire. While Phobos exhibits several high-velocity impacts, high-velocity impacts at Deimos are relatively rare and are primarily clustered below 1 km/s (compare to ~ 20 km/s heliocentric impactor velocity). The discontinuity at 700 m/s in both graphs is due to an increase in impacts to Mars at that velocity range for certain Deimos-Phobos orbital geometries (Figure 2.3).

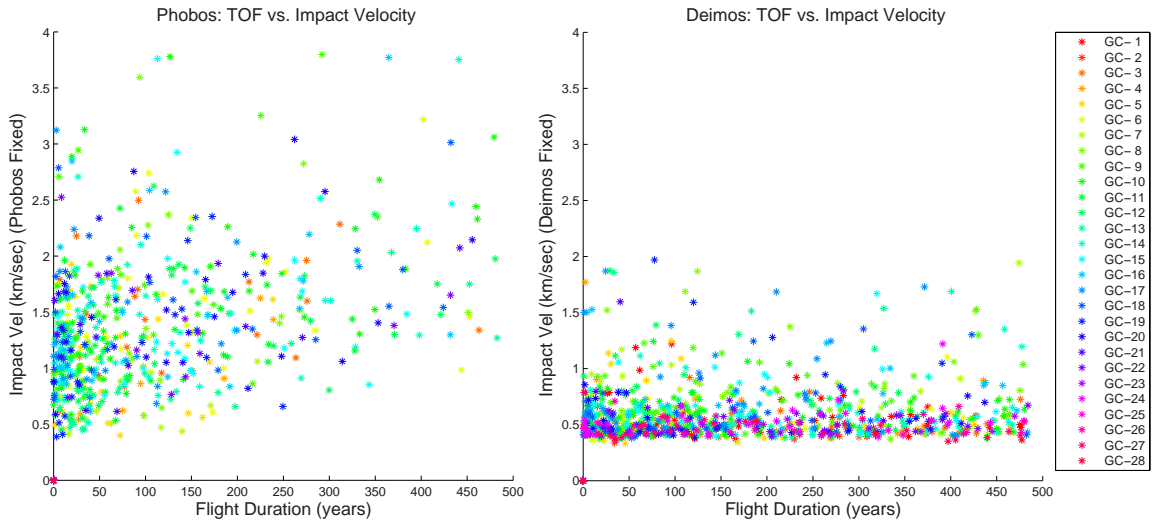


Figure 2.5. (Left) Impact velocity at Phobos and (Right) Impact velocity at Deimos versus duration of particle flight. While impacts to Phobos are frequent in the first 100 years post impact, they begin to taper off toward the end of the examined duration; impacts to Deimos, on the other hand, continue at a relatively constant pace, implying that while 500 years captures the bulk of Phobos mass transfer, reaccretions to Deimos will likely continue to the 10^4 year timescale [Soter, 1971; Davis *et al.*, 1981].

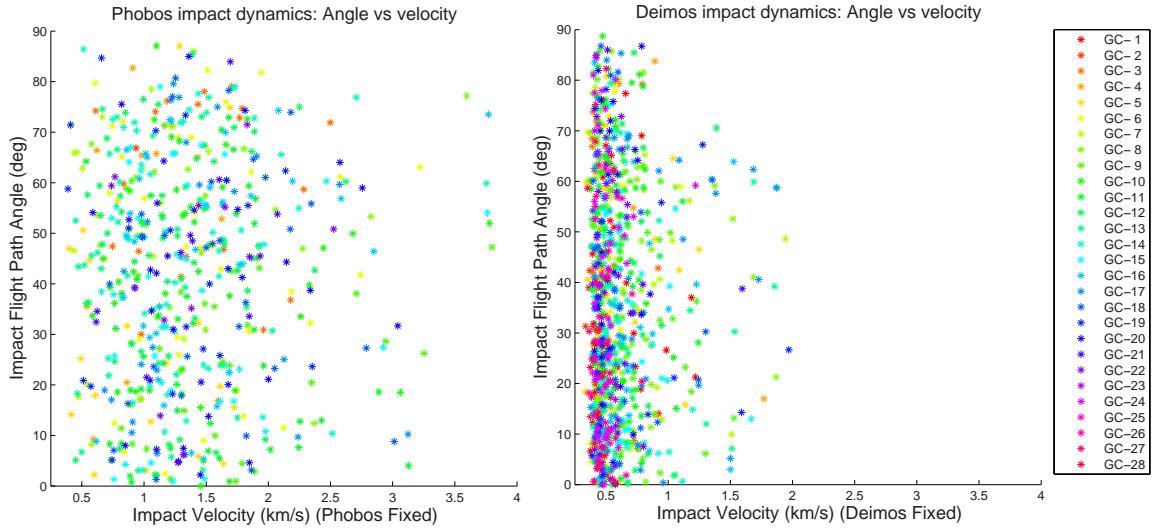


Figure 2.6. (Left) Impact flight path angle (FPA) at Phobos and (Right) Impact FPA at Deimos versus the impact velocities on the respective bodies. Apart from reinforcing the fact that Deimos impacts are primarily low-velocity, we also see a wide distribution in flight path angles. There are several low-velocity, low-FPA impacts that should create oblique or secondary crater morphology, and several high-velocity, high-FPA impacts that will exhibit direct or primary crater morphology.

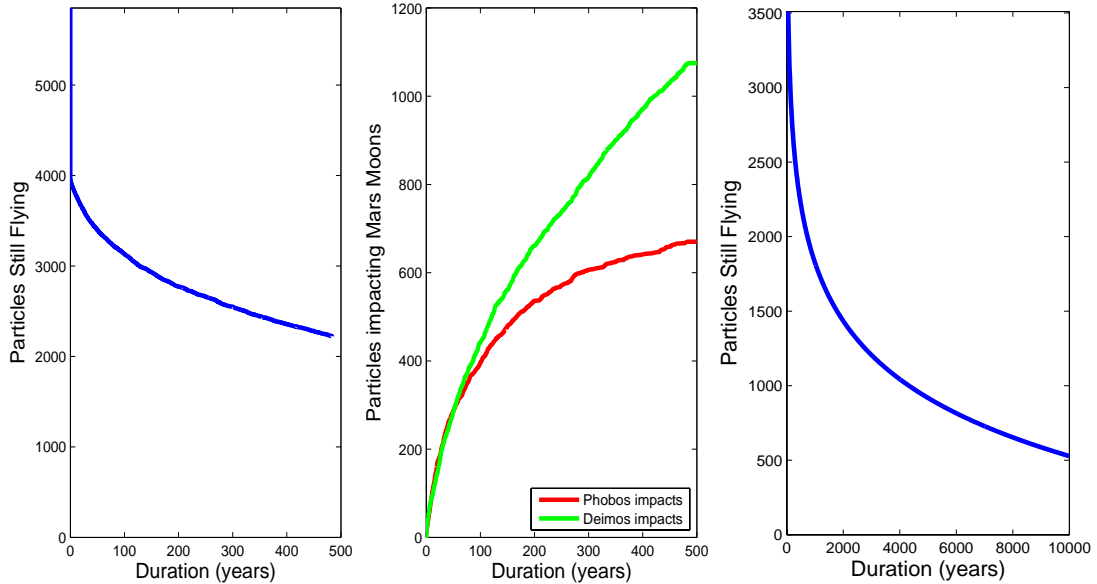


Figure 2.7. Number of (Left) particles still flying and (middle) impacts to Phobos and Deimos with time. The curves are well behaved, with no unexpected jumps. Impacts to Phobos can be seen to be tapering off, while reaccretions to Deimos continue to rise. These are expected to continue until no more particles are still flying. (Right) Extrapolation of the logarithmic decrease in the left plot. The decrease fits well ($R^2 > 0.995$) to a logarithmic distribution defined by $y = -563\ln(t/t_0)$, where $t_0 \sim 25,000$ years. Using this curve, it takes 10,000 years for the particles still flying to drop below 500, agreeing with Soter (1971).

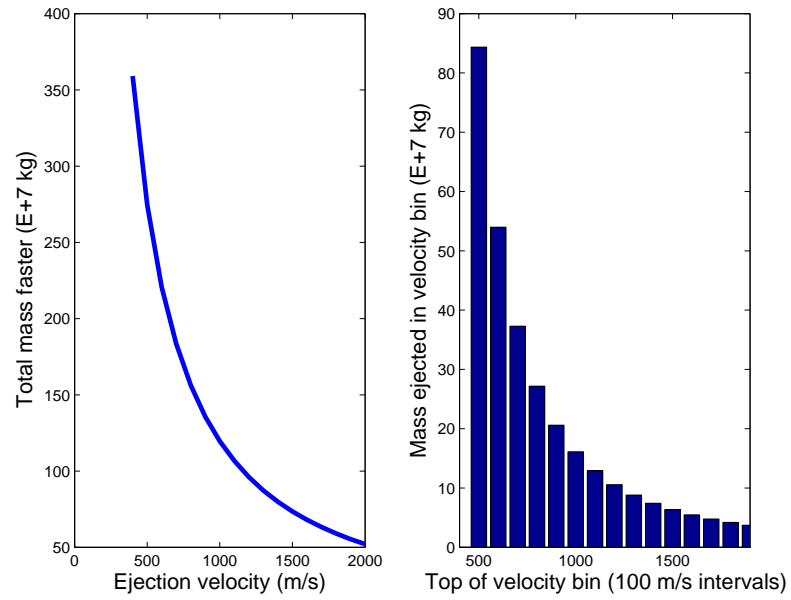


Figure 2.8. (Left) Total mass faster than ejection velocities (Equation 2.16). (Right) Mass ejected per velocity bin in tens of millions of kg. Velocity bins correspond to Figure 2.3.

Chapter 3

Sesquinaries: A Case Study of Phobos

This chapter is a modified reprint of Nayak and Asphaug (2016), Sesquinary Catenae on the Martian Satellite Phobos from Reaccretion of Escaping Ejecta, Nature Communications, DOI: 10.1038/ncomms12591.

3.1 Abstract

The Martian satellite Phobos is crisscrossed by linear grooves and crater chains whose origin is unexplained. Anomalous grooves are relatively young and crosscut tidally predicted stress fields as Phobos spirals toward Mars. In this chapter, we report strong correspondence between these anomalous features and reaccretion patterns of sesquinary ejecta from impacts on Phobos. Escaping ejecta persistently imprint Phobos with linear, low-velocity crater chains (catenae) that match the geometry and morphology of prominent features that do not fit the tidal model. This work proves these cannot be older than Phobos' current orbit inside Mars' Roche limit. Distinctive reimpact patterns allow sesquinary craters to be traced back to their source, for the first time across any planetary body, creating a novel way to probe planetary surface characteristics. For example, it is shown that catena-producing craters likely formed in the gravity regime, providing constraints on the ejecta velocity field and knowledge of source crater material properties.

3.2 Introduction

Ejecta escaping from an impact on a natural satellite often goes into orbit about the primary and can reimpact the satellite or its companions after an extended period. These ‘sesquinary’ impacts [Zahnle *et al.*, 2008] are slower than primary impacts, but faster than the satellite escape velocity. Because they spend time in orbit they do not simply radiate from their primary crater like secondary craters; nonetheless their close dynamical association with the satellite can give them a unique geometrical distribution. Like secondary craters, sesquinary craters are probes of the primary ejection process, but are also bound to the dynamics of the planet-satellite system. Unlike secondaries, to date no sesquinary crater has been traced back to its primary.

Phobos, the $26 \times 22 \times 18$ km battered moon of Mars, is covered in parallel linear features whose orientation is, for the most part, aligned with de-orbiting tidal stresses as Phobos spirals closer to Mars. As the tidal bulge grows, surface stresses increase and cause striations [Soter and Harris, 1977; Asphaug *et al.*, 2015b]. However, many of Phobos’ linear features do not align with any interpretation of tidal stress, giving rise to alternative models such as impact fractures related to the formation of Stickney [Fujiwara, 1991], the largest crater on Phobos, ejecta from Mars basin formation [Murray and Heggie, 2014], pitted regolith from bouncing boulders [Wilson and Head, 2015] and drainages opening up into a fractured substrate [Horstman and Melosh, 1989]. Even with recent improvements incorporating two-layer tidal stresses

from orbital decay [Asphaug *et al.*, 2015b], a subset of prominent hemispherical crater chains crosscut predicted stress fields and bear a closer resemblance to distal secondary crater chains on the Moon, except there is no apparent source crater. They also resemble the tidal catenae on Ganymede and Callisto that are the result of cometary disruption inside the Roche limit of Jupiter [Melosh and Schenk, 1993]. We propose these features on Phobos are a novel kind of structure intermediate between these two phenomena, which we call “sesquinary catenae”.

We classify four kinds of satellite impacts. A primary impact is by a bolide from outside the planet's sphere of influence; these are generally the fastest. A secondary impact is by a fragment ejected from a primary crater; these are the slowest cratering events, no faster than a fraction of the satellite's escape velocity v_{esc} . Such craters radiate from the primary and form linear chains and clumps. A sesquinary impact is formed by crater ejecta that escape but remains in orbit in the system; its impact velocity is intermediate between v_{esc} and the orbital velocity v_{orb} . When the satellite is far from the planet, sesquinary can produce primary-like crater morphology. Intermediate between sesquinary and secondary is the so-called dosquinary, where the ejecta reimpacts after spending only a few orbits aloft. These can be thought of as the slowest possible sesquinary, but not quite secondaries, since the gravitational influence is primarily that of the planet. These are limited to satellites that orbit close to the planet.

Sesquinary/dosquinary from Phobos are especially interesting for three reasons: First, the escape velocity v_{esc} is of order $\sim 10 \text{ ms}^{-1}$, hundreds of times slower

than its orbital velocity $v_{\text{orb}} \sim 2.2 \text{ km s}^{-1}$. The slowest escaping ejecta, which comprise the major mass fraction, cannot stray far from the satellite. Second, the escaping ejecta are subject to powerful orbital and tidal distortion, since the current semimajor axis $a \sim 2.77 R_{\text{Mars}}$ is significantly inside the classical Roche limit $R_{\text{roche}} \sim 3.19 R_{\text{Mars}}$ [Witasse *et al.*, 2014]. Third, as shall be shown, the timescale for reaccretion is so short that ejected particles can be reaccreted before they have time to disperse. This leads to the curious geomorphic phenomenon of sesquinary catenae, each linked to a particular source crater on Phobos, and sets these features apart from crater chains on bodies beyond deep planetary gravity wells of planets, such as asteroids Eros [Buczkowski *et al.*, 2008], Gaspra and Steins [Marchi *et al.*, 2010]. Analytical formulations have been used to study the dynamics of escaping and reaccreting ejecta [Soter, 1971; Burns, 1972; Dobrovolskis and Burns, 1980], but to precisely predict sesquinary reimpact locations an ephemerides formulation is required, as in Chapter 2. Similar to that approach, multiple orbital configurations around Mars are considered to evaluate variations in Mars-Phobos orbital geometry and inferior or superior conjunctions with Deimos at the time of the primary ejecta-producing impact. Since the significant percentage of mass escaping Phobos is ejected slower than 100 ms^{-1} (92%, Section 3.3), the component ejected with velocities from $v_{\text{esc}} \sim 11 \text{ ms}^{-1}$ to 100 ms^{-1} is tracked in precise detail. Planetocentric latitude and longitude of each impact location are then extracted from the evolution model.

3.3 Methods

3.3.1. Mars Gravity System Integrator

Ejecta are integrated in an ephemeris-centered frame for an arbitrarily chosen primary impact epoch, incorporating solar third body perturbations and a 20×20 Mars gravity harmonic model [Murchie, 2010]. As described in greater detail in Chapter 2, our model accounts for changes in the rotation and longitude rate of Phobos, precession of the argument of periapsis and longitude of the ascending node, and its non-spherical shape (triaxial ellipsoid with semi-major axes of $13 \times 11.4 \times 9.1$ km [Murchie *et al.*, 2003]). Integration time is capped at 10 years to permit use of a 7th-order Runge-Kutta integrator without excessive approximations to the perturbed Hamiltonian [Leimkuhler and Reich, 2004].

3.3.2. Outbound Ejecta Velocity Distribution

For the ejected material, streamlines ejected by a primary impact on Phobos are modeled using an axisymmetric Z-model formulation [Maxwell, 1977; Roddy, 1977]. Though limited by its neglect of interactions across streamlines, the Z-model reasonably approximates several experimentally observed features [Melosh, 1989; Barnhart and Nimmo, 2011]. The limitations of a Z-model implementation are discussed at length in [Barnhart and Nimmo, 2011]. As in Chapter 2, this application is only concerned with ejecta streamlines that escape Phobos, and is unaffected by the details of cratering flow beneath the ground plane, surface material mixing during ejection or direct retention and emplacement of deposits [Nayak *et al.*, 2016b].

Therefore the Z-model provides a suitable level of insight into an outbound velocity distribution; approximations made are unlikely to alter quantitative results. Hydrocode studies of the Stickney impact (~10 km diameter) find $Z = 3.5$ to suitably represent cratering flow [Asphaug and Melosh, 1993], adopted here. All streamlines are ejected at a constant angle set according to Equation 2.6 [Maxwell, 1977]; for $Z = 3.5$, this angle is 56.3° , measured from the horizontal (Figure 2.1 and 2.2).

Outbound radial (v_r) and vertical (v_z) ejection velocities vary inversely with distance from the center of the crater r as in Equations 2.7 and 2.8 [Maxwell, 1977], using the acceleration due to gravity g on Phobos as 0.0057 ms^{-2} . The cratering flow is ultimately dependent on the transient crater radius, calculated as $R_t = 0.65 R_f$, where R_f is the final radius of the crater [Barnhart and Nimmo, 2011]. For example, the Stickney primary impact is simulated in this work using a final radius of 5.05 km [Veverka and Duxbury, 1977] and a transient crater radius of 3.28 km. The number of streamlines n is chosen to yield a suitably dense distribution of velocities greater than the Phobos escape velocity. Setting $R_{\min} = 0$ and varying $R_{\min} \leq r \leq R_t$, n streamlines evenly spaced in radius are generated within a crater of choice. Streamlines may then be converted to axisymmetric coordinates; radial and vertical coordinates are defined by Equations 2.10 and 2.11 [Barnhart and Nimmo, 2011].

The Z-model yields a 2D axisymmetrical velocity distribution; similar to Chapter 2, this is then rotated around the azimuthal direction at $5\text{-}30^\circ$ azimuth (β) intervals to create a 3D velocity distribution. This three-dimensional outbound velocity distribution is tied to the crater being studied, in the Topocentric Horizon

frame, adapted from the South-East-Zenith (SEZ) frame [Vallado, 2013] (Figure 2.1 and 2.2). This frame is centered at the crater, with the x-axis pointing south and aligned with the meridian passing through the crater. The x-y plane is tangent to the surface and points along the local latitude circle. Completing the right-handed system, the z-axis points radially outward from the impact site towards the “local” zenith [Nayak *et al.*, 2016b]. For use with the Mars gravity system integrator, these coordinates are then rotated into the Mars Centered Inertial (MCI) frame through the Phobos Centered Phobos Fixed (PCPF) and Phobos Centered Inertial (PCI) frames respectively. Details of coordinate transformations may be found in Chapter 2.

ε_{ej} is the elevation angle of the ejection velocity vector; from the Z-model $\varepsilon_{ej} = 56.3^\circ$. β_{ej} is the azimuth of the ejection velocity vector and is measured from the north, positive clockwise as viewed from above the site such that $0 \leq \beta_{ej} \leq 2\pi$, and varies from $\beta \mid \beta \in [0: \pi/6: 2\pi)$ for a total of 13 possible azimuths to $\beta \mid \beta \in [0: \pi/36: 2\pi)$ for a total of 71 possible azimuths (specific details are shown in figure captions below).

3.3.3. Mass-Velocity Distribution

For gravity-dominated cratering, volume ejected faster than a given velocity is given by Equation 2.16, where v_{ej} is the ejection velocity and R is the final radius of the crater [Holsapple, 1993; Morrison *et al.*, 2009]. For the coefficients in Equation 2.16, a sand-like surface is well represented [Melosh, 1989] by $\nu = 1.2$, and mass-velocity distributions from experimental impacts into granular targets [Housen and

Holsapple, 2011] find $C_{ej} = 0.25$, a value that correlates well to other published values between 0.25 and 0.36 [*Andrews, 1975; Stöffler et al., 1975; Cintala et al., 1999*]. We adopt $C_{ej} = 0.3$ and $\nu = 1.2$. Using Equation (2.16) and a Phobos density of 1.9 g/cc [*Avanesov et al., 1989; Rosenblatt et al., 2008*], the mass ejected within each velocity bin is calculated. For the Stickney impact, of the 1.5×10^{13} kg ejected faster than the Phobos escape velocity, only 1.2×10^{12} kg (8%) is ejected faster than 100 ms^{-1} . Similarly, with 2.72×10^{12} kg ejected faster than 30 ms^{-1} , 80% of ejecta mass with sufficient velocity to escape Phobos leaves between $11.3\text{-}30 \text{ ms}^{-1}$. Numbers are nearly identical for craters down to 1 km diameter formed in the gravity regime.

3.4. Results

3.4.1. Primordial versus modern orbit

We find that a majority of the mass ejected from Phobos at low velocity ($<100 \text{ ms}^{-1}$) reaccumulates; the rest impacts Mars or leaves the system. A minor fraction ($<1\%$) impacts Deimos at randomized locations. This work first characterizes Stickney, the largest crater on Phobos, which either formed geologically recently or when Phobos was in a more distant orbit close to the synchronous line [*Burns, 1978; Cazenave et al., 1980; Yoder, 1982*]. Figure 3.1(a) shows the reimpact map for Stickney had it occurred in Phobos' present orbit, with a mean reaccumulation time of ~ 22 hours where $a \sim 2.77 R_{\text{Mars}}$. Catenaes from Stickney are clearly distinguishable. Figure 3.1(b) shows the reimpact map for a primordial $a = 6R_{\text{Mars}}$ [*Yoder, 1982*]. Here, with a mean reaccumulation time of ~ 32 years and max of 88 years, individual reaccumulated particles

have lost their geometrical association due to the much longer flight time. A study of sesquinarries originating from Deimos finds that ejecta particles reaccrete over ~500 years and do not form crater chains [Nayak *et al.*, 2016b]. Therefore, for Phobos' modern orbit inside the Roche limit, reimpacts are not only more frequent than in a primordial orbit, but occur over shorter timescales (days) and are recognizably coherent, forming chains.

3.4.2. Nature of reimpacting ejecta

The pattern of reimpacts as pictured against increasing ejection velocity (Figure 3.2) shows that the catenae originate from very low-velocity particles just above the escape velocity of Phobos. At ejection velocities of $< 25 \text{ ms}^{-1}$, nearly all reimpacts cluster in catenae-like patterns; above 30 ms^{-1} , a few times v_{esc} , reimpacts are less correlated to catenae-like structures. Studying the reimpact velocities (Figure 3.3), we find that they are correspondingly higher than v_{esc} [Davis *et al.*, 1981; Thomas, 1998] but sufficiently low that craters produced are expected to morphologically resemble secondary craters. In addition, though the mean reaccretion time for all Phobos-impacting particles is ~22 hours, the large majority of catenae-forming impacts occur in ~6-14 hours.

As such, these are a special case of sesquinary impacts (dosquinarries). Although the impactors temporarily escape the gravitational influence of Phobos, they exhibit behavior that may be best described as intermediate between a secondary

and traditional sesquinary impactor. Since 80% of the total mass that escapes Phobos during an impact is ejected at speeds of $<30 \text{ ms}^{-1}$ (Section 3.3), this mass influx is a mechanism capable of significant impact to the surface geology; for detailed characterization of catena production this work now focuses on $10\text{-}30 \text{ ms}^{-1}$ streamlines.

Next, we attempt to establish if the catenae are a frequent phenomenon by searching for a lower limit of impact crater diameter that results in the creation of catenae-like structures. We generate $<30 \text{ ms}^{-1}$ reimpact maps for ejecta from primary craters of 1-km, 3-km and 5-km in diameter (Stickney: $\sim 10 \text{ km}$ diameter). As seen in Figure 3.7, catenae are predicted to form as a byproduct of sesquinary impact from primary craters at least as small as 1-km in diameter, and likely smaller. The saturated (at least down to 300 m craters [Veverka and Duxbury, 1977]) surface of Phobos suggests that the creation of low-velocity, clustered linear impact structures from sesquinary ejecta is a relatively frequent process; catena formation is approximately as frequent as gravity-regime crater formation, where most of the escaping ejecta mass is just barely escaping ($<30 \text{ ms}^{-1}$). This suggests that linear chains of low-velocity impact structures are a relatively frequent process on modern Phobos, each correlated with a source crater.

It is interesting to note that a kilometer-sized crater in the strength regime would create faster ejecta, consequently producing less reaccreting ejecta [Asphaug and Melosh, 1993] and few (if any) crater chains. This analysis therefore allows one to probe the dynamics of crater ejecta in a way not done before, for instance proving

that catena-producing craters formed in the gravity regime (in deep regolith) and are likely not much older than Phobos' current orbit (< 50 Ma). Figure 3.4 illustrates how orbital ejecta lingering in the vicinity of the Phobos orbit can be swallowed up in hemispherical patterns that lead to chain or catena-like reaccretion patterns (e.g. Figure 3.1). Tracing the precise orbital history of multiple particles shows that ejected particles transition from the gravitational influence of Phobos to Mars for a period of between 1-5 orbits before subsequent impact, reaccreting before they have time to disperse. The mean reaccretion time of ~ 22 hours is ~ 3 times the orbital period of Phobos; for $< 100 \text{ ms}^{-1}$ impact velocity events, the mean reaccretion time is ~ 6 -14 hours, or ~ 1 -2 times the orbital period of Phobos.

The higher the ejection velocity (Figure 3.3), the higher the corresponding scatter is in the locations of reaccretion (Figure 3.2). This correlates to longer flight times and greater interactions with Mars-dominated gravity, as opposed to the low-velocity impactors, which escape Phobos-centered gravity but do not stray far from the orbit of the satellite before reimpact. Low-velocity impactors creating the catena appear to be dosquinary in nature, i.e., intermediate between typical secondary and sesquinary impactor behavior.

Given a low-velocity ejection bracket (11 - 30 ms^{-1} , Figure 3.5), the azimuth of ejection controls the length and coherence of the catenae. From the ejection azimuths for reaccreting particles, it can be seen that different azimuths result in different “sections” of the catena being formed (shape legend, Figure 3.5). The formation of an axisymmetric cone, with ejecta along every outbound azimuth, is of course an

idealized case. In reality, depending on the geometry of the primary crater formation (and resulting streamlines), catenae may range from highly focused to “patchy”. If no particle is ejected between the azimuths of (say) 30° - 45° , there will be a corresponding “gap” in the catena. The location of this gap can be inferred from the respective shape legends. Inversely, given a suspected catena on Phobos, this makes it possible to infer the properties of the primary impact.

3.4.3. Grid Search Varying the Primary Crater Location

Good correlation exists between models of tidal stresses induced by the orbital decay of Phobos toward Mars and several groove families, but cannot match a number of grooves across the surface [Asphaug *et al.*, 2015b]. Can the observed catenae detailed in this work account for these misfit grooves? Even among this subset of grooves, a wide variety of orientations are seen [Hurford and Asphaug, 2015]. To determine if sesquinary catenae can be responsible for all these varied orientations, we investigate the effect of ejecta originating from sources other than Stickney.

An equidistant longitudinal and latitudinal grid is now created, ranging from 90° N to 90° S in 30° increments and 180° W to 180° E in 90° increments, for a total of 35 grid points. This span accounts for variations between the leading and trailing apex of Phobos, as well as the sub- and anti-Mars points. Since it has already been shown that the size of the origin crater has no effect on the geometry of the resulting

reaccretions, the velocity distribution from a 3-km diameter crater is chosen as the standard distribution and “released” from each grid point.

The results presented in this chapter show that the longitude of the primary crater has no effect on reaccreting catenae for impacts in both the southern hemisphere (Figure 3.8) and northern hemisphere (Figure 3.9). In these figures, note that we have restricted ourselves to showing results for $\beta \mid \beta \in [\pi: \pi/36: 2\pi)$ for clarity; results are mirrored for $\beta \mid \beta \in [0: \pi/36: \pi)$. This can be seen by comparing the panels of Figure 3.11, the reimpact map for the Stickney impact.

While longitude of the primary crater has little effect, the latitudinal location of the primary impact has a direct relation to the orientation of the catenae. Figure 3.5 shows catenae resulting from primary impacts at 0° , 30° , 60° and 85° N latitude. An interesting pattern emerges: polar primary impacts create horizontal catenae, while vertical chains result from equatorial primary impacts. These results are mirrored in the southern hemisphere (Figure 3.11). The range of possible catenae orientations, from horizontal to vertical, show that low-velocity sesquinary impactors could indeed match the orientation of those grooves that do not fit a tidal evolution origin. Orientations are mirrored across primary impacts to either hemisphere, which can be seen by comparing Figure 3.5 (northern hemisphere) to Figure 3.11 (southern hemisphere). From the variation between orbital geometries at the time of the primary impact, the location of the catenae can shift longitudinally, depending on the location of the primary impact along Phobos’s orbit around Mars.

3.4.4. Tracing catenae back to a source crater

Based on the relationships of reaccreting catenae to a primary crater location, we can now match a catena to its source crater, not previously done for any planetary body. In doing so we can constrain the ejecta velocity field and provide knowledge of the material properties in the region of the source crater. For our case study, we choose one of the more prominent Phobos catenae, shown in Figure 3.6(a). Previously studied in the literature [*Veverka and Duxbury, 1977*] and hemispheric in extent, it is not obviously correlated with Stickney or any other crater, is morphologically similar to cratering expected for ejecta colliding at just above $\sim v_{\text{esc}}$ and crosscuts the predicted stress field for tidal grooves [*Asphaug et al., 2015b; Hurford and Asphaug, 2015*]. This makes it a suitable test of the hypothesis that sesquinary catenae can match those grooves that do not fit tidal models.

In comparing to Figure 3.5(d), the highlighted catena is similar to reimpacts predicted for a near-polar primary source crater, narrowing the grid search to above 60° N. Sesquinary ejecta emanating from an impact at the 2.6-km diameter crater Grildrig (81° N, 196° W) is modeled, and a very close match to the observed catena is found (Figure 3.6). This test case shows that reimpacting slow co-orbital ejecta can explain previously mysterious features not well explained by any previously proposed mechanism. These ejecta would be proximal to the crater on a 'normal-gravity' body like the Moon, but on Phobos, they get pulled apart into strands before re-impact a matter of orbits later.

3.4.5. Changing the Z-Model Ejection Angle

Equation 2.6 fixes the ejection angle for the velocity distribution: in this final subsection, it is investigated whether this affects the outcome of the simulations presented above. Figure 3.12. shows the reaccretion map for a simulation in which the ejection angle of the outbound ejecta is allowed to stochastically vary between $\varepsilon_{ej} = 45^\circ$ and $\varepsilon_{ej} = 65^\circ$, i.e., for Z-model numbers between $3 \leq Z \leq 4.14$. This is overplotted on top of results for a simulation which uses our standard values of $\varepsilon_{ej} = 56.3^\circ$ and $Z = 3.5$. The similarity between the results shows that changing ejection angle or Z number does not change the qualitative results presented; catena-like formations are still expected. However, the ejection angle may represent a constraint on the crater ejection mechanism; varying the Z-number may further improve the fit of our modeled catena to, for example, ejecta from the Grildrig crater.

3.5. Discussion

The results presented in this chapter support Grildrig's formation in the gravity regime and in deep regolith. Grildrig does show raised rims corresponding to gravity-regime production, is reasonably fresh, and of suitable diameter to produce the observed catena. When loose material is ejected at velocities just exceeding escape velocity, self-gravity of the material becomes a factor and leads to clump formation, as seen from asteroid family and binary formation simulations [*Durda et al.*, 2007; *Walsh et al.*, 2008]. This is how an impact to deep regolith can release large

ejecta fragments, which would then become sesquinary impactors. This is also why the catenae do not have cleanly-discriminated crater forms, but rather clumpy streamers of interconnected features.

The rim of Grildrig shows craters similar in size to the catena in its vicinity; it is likely that reimpacting ejecta may have formed some of these. Better image data from a dedicated Phobos mission can enable studies of chronology in the relative sense, i.e., evaluate the hypothesis that craters on the rim of Grildrig are coeval with catena craters associated with sesquinary ejecta from Grildrig. Certainly, if sesquinary ejecta is indeed the source of the indicated crater chain, there is little one can say about crater ages on Phobos from the consideration of sub-km scale crater densities; age estimates from crater counting were previously used [Thomas *et al.*, 1978] as an argument against a tidal origin [Soter and Harris, 1977] for grooves.

In conclusion, catenae on Phobos created by low-velocity sesquinary impactors are persistent across the range of longitudinal, latitudinal, orbital and conjunctive variations, with distinctive resulting geometries. This in turn implies that catena formation is approximately as frequent as gravity-regime crater formation, where most of the escaping ejecta mass is just barely escaping ($<30 \text{ ms}^{-1}$). For such events, the fate according to our model is for material to impact in a linear chain. Based on Figure 3.3, we expect the resulting crater morphology to be similar to secondary craters in nature, consistent with secondary crater chains and catenae noted on the Moon. The direct association of sesquinary catenae with source craters is an important and new kind of planetary data set, leveraging a 1:1 correspondence to

constrain the dynamical and geologic history of Phobos in a novel way. Without applying any morphological criterion, we can say if a catena-like feature on Phobos is a good candidate for a sesquinary origin by asking if it follows the distinct trending direction that it must follow if it were sesquinary (Figure 3.5). Based solely on an inspection of Figure 3.5, initial guesses may be made at the latitude of that feature's possible source crater; a grid search similar to that performed for Grildrig would then narrow possibilities down to one source crater.

Significant craters without corresponding catenae might need to have formed when Phobos was in a more distant orbit, or in strength-controlled impacts with faster ejecta. Conversely, catenae without corresponding source craters may have formed when Phobos was in a different orbital or tidal locking geometry with respect to Mars. The lack of correlation of major catenae with our predictions for Stickney (Figure 3.1) suggest that Stickney formed when Phobos was more distant from Mars [Schmedemann *et al.*, 2014]. For example, long flight times for particles reaccruting to Deimos result in many reimpacts but no catenae on that body [Nayak *et al.*, 2016b]. This does not preclude the possibility of impact craters on Phobos that are uncorrelated Stickney sesquinarities.

Discriminating sesquinary catenae from tidal stress-induced fissures [Asphaug *et al.*, 2015b], or catenae-like features formed from regolith draining into fissures [Horstman and Melosh, 1989], is the next step in Phobos surface science. For example, sesquinary catenae may exhibit raised rims typical of impact craters, whereas catenae-like features formed by regolith draining would not. Similarly, the

walls of drainage pits would stand at the angle of repose, whereas sesquinary craters might be less steep. However, given the generally heterogeneous quality and resolution of Phobos images, and the lack of systematic mapping products applied to the Mars Express data sets [Witasse *et al.*, 2014], discriminating catenae as sesquinary or otherwise solely on the basis of imaging is an expansive task, rendered further difficult by the fact that there may be multiple mechanisms for linear feature formation at play. There is a need for published topographic profiles of Phobos that reliably measures the slopes of Phobos features relative to the satellite's effective gravity (which can vary measurably across the surface of the moon), from which the distinct origin of a particular catena might be distinguished. The creation of these products is ongoing.

Using this, future work will start with systematic and objective geomorphic measurements of the directions, slopes, depths, and the sizes and spacings of linear pits and craters, in order to classify linear features on Phobos objectively (e.g. into secondary ejecta-like streamers versus fissures, etc.), analogous to [Morrison *et al.*, 2009] but applied to modern Phobos data [Witasse *et al.*, 2014]. These classified features will then be compared to model predictions, especially sesquinary catena predictions from fresh-looking source craters in present and geologically recent orbits, groove predictions from the tidal model [Asphaug *et al.*, 2015b] and any other viable mechanisms. This study also has potential implications for other closely bound satellite systems, especially Pluto and Charon, whose tidal locking and close

proximity leads to the possibility of similar short-timescale reaccretions collecting preferentially onto facing hemispheres.

3.6. Figures

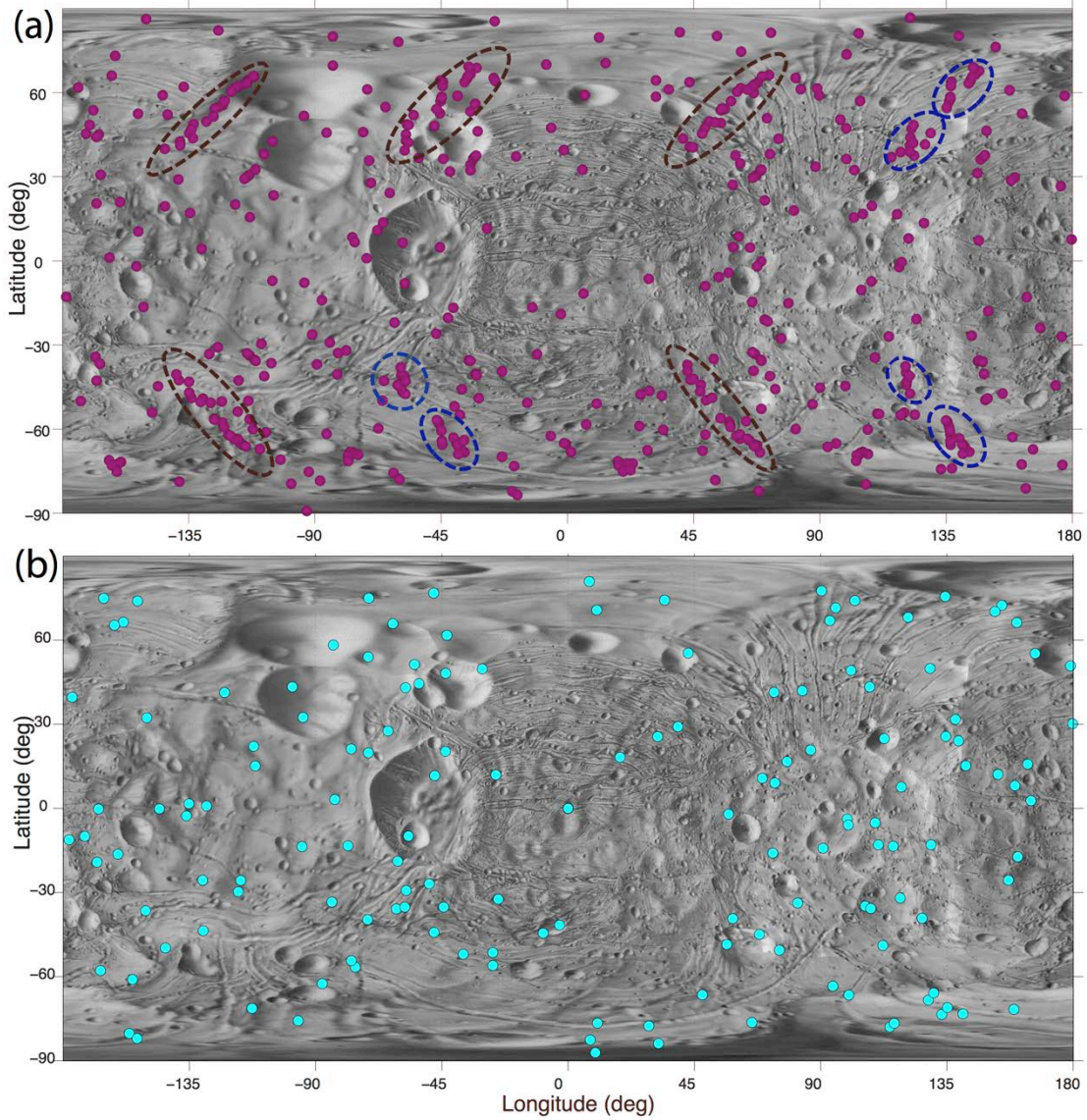


Figure 3.1. Reaccretion map for the Stickney impact in Phobos modern and primordial orbits. (a) Ejecta from Phobos in its modern orbit, $a \sim 2.77R_{\text{mars}}$; multiple linear strings of reimpacts are noted in both hemispheres (brown and blue ellipses). (b) Ejecta from Phobos in its primordial orbit near the Mars synchronous line, $a \sim 6R_{\text{mars}}$; similar reaccretion patterns are not seen. All ejection velocities range from $11\text{-}100 \text{ ms}^{-1}$, azimuth $\beta \in [0: \pi/6: 2\pi)$.

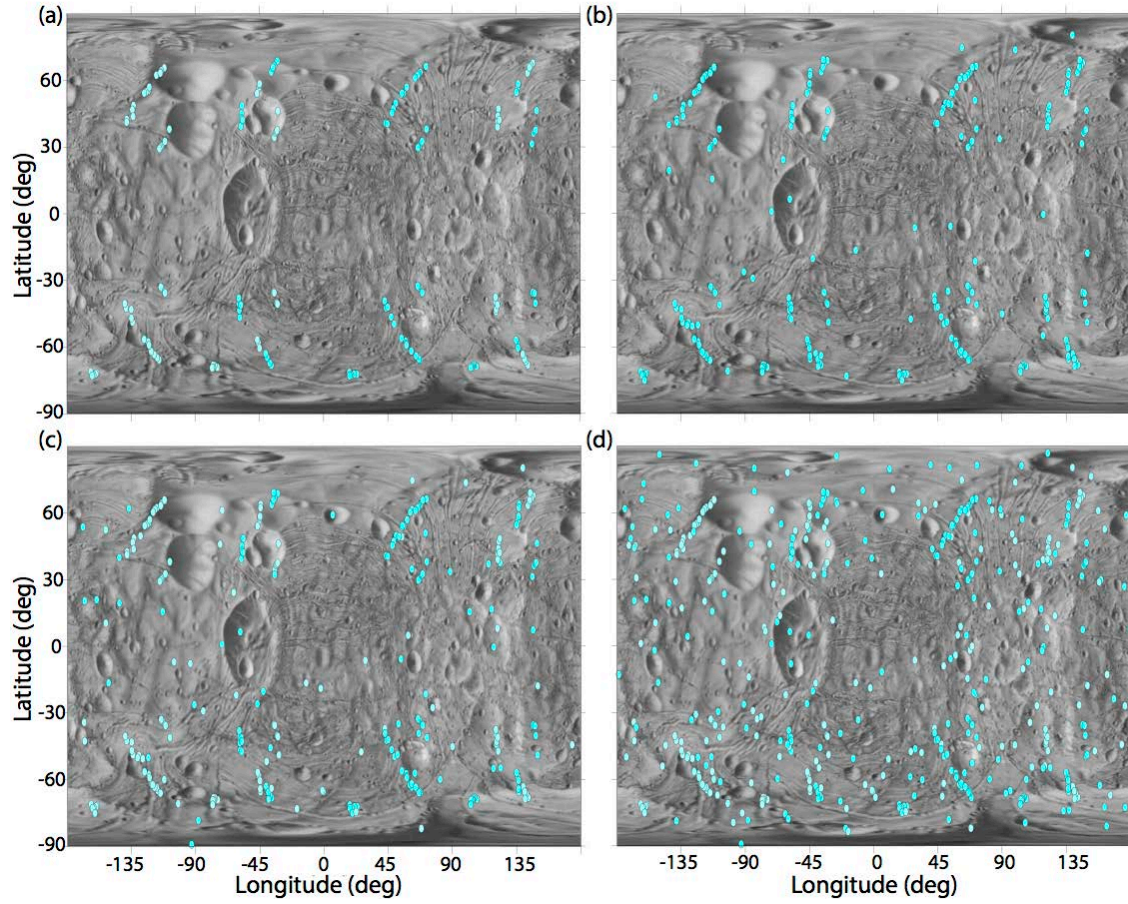


Figure 3.2. The evolution of catenae with increasing velocity of ejection from Phobos. Maps show reimpact locations for sesquinary impactors with ejection velocity greater than Phobos escape velocity and lesser than: (a) 20 ms^{-1} , (b) 25 ms^{-1} , (c) 30 ms^{-1} and (d) 100 ms^{-1} . Catenae-like formations are evident from particles ejected at lower velocities. As ejection velocity increases past 30 ms^{-1} , reimpacts become less correlated to catenae-like structures. The source of the catenae is therefore very low-velocity particles. The primary impact location is Stickney and azimuth $\beta \in [0: \pi/6: 2\pi)$.

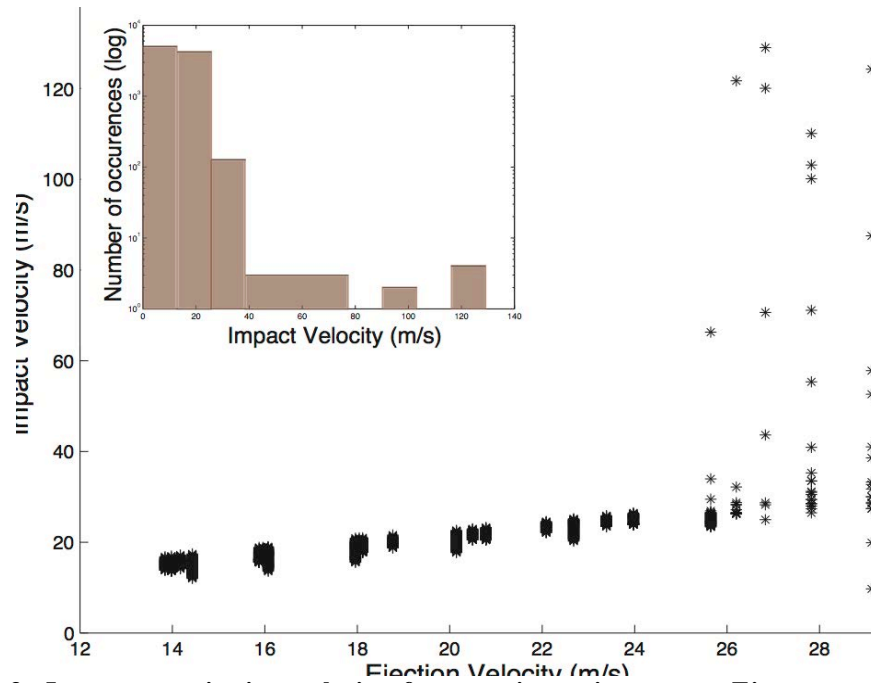


Figure 3.3. Impact vs. ejection velocity for sesquinary impactors. Ejecta corresponds to simulations in all panels of Figure 3.2. The majority of impacts occur at a velocity comparable to their ejection velocity, i.e., between $11\text{-}30\text{ ms}^{-1}$. However a small fraction experience acceleration due to greater interactions with Mars' gravity (inset); these have a correspondingly longer accretion time. Based on these results, sesquinary impact craters are largely expected to have an appearance similar to secondary craters noted in image surveys of Phobos.

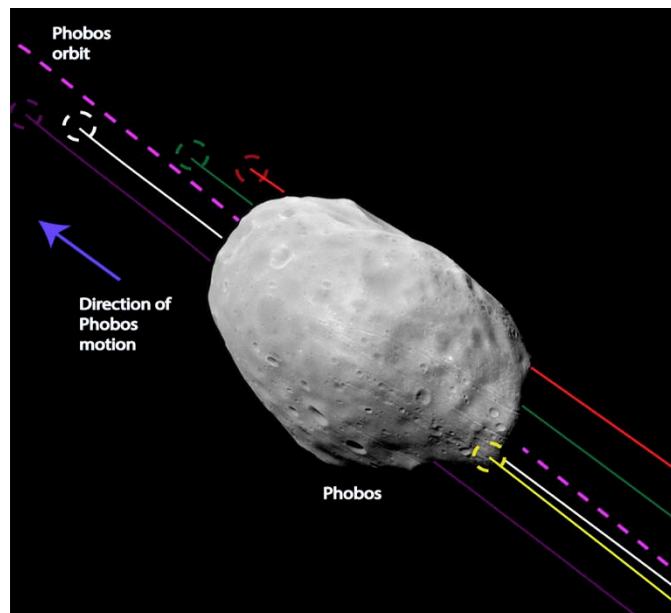


Figure 3.4. Visualization of the orbital history of randomly selected particles. Shown are the trajectories of randomly selected projectiles ejected at $11\text{-}30\text{ ms}^{-1}$, which impact over a relatively short time in a grouped fashion. As Phobos moves along its orbit (toward the top of the figure, dashed pink line), ejected particles in the vicinity of Phobos' orbit (crimson, white, green, red,

yellow lines) are reaccreted to the satellite. Dashed circles represent planetocentric impact points, illustrating how hemispherical catena (see Figure 3.5) may be formed.

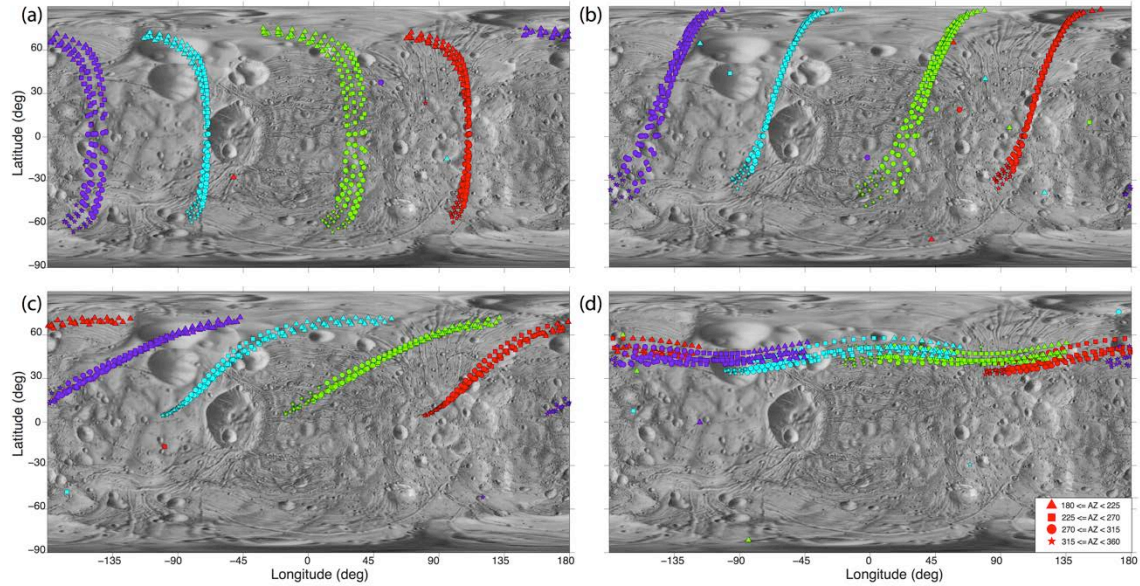


Figure 3.5. Catenae orientations change from vertical to horizontal depending on the latitude of the primary impact. Maps show resultant catenae from primary impacts on Phobos at the prime meridian and (a) 0° N; (b) 30° N; (c) 60° N; (d) 85° N. Resulting orientations are the mirror inverse of those from southern hemisphere impacts (compare to Figure 3.11). Variations with orbital geometry at primary impact can be seen, namely, when Phobos is at Mars periapsis (red), apoapsis (blue), halfway between periapsis and apoapsis along the ascending (purple) and descending node (green). Ejection velocities are 11-30 ms⁻¹; source crater is of 3-km diameter. Shapes denote ejection azimuth (legend); $\beta \in [\pi; \pi/36; 2\pi]$ are shown (compare to Figure 3.10).

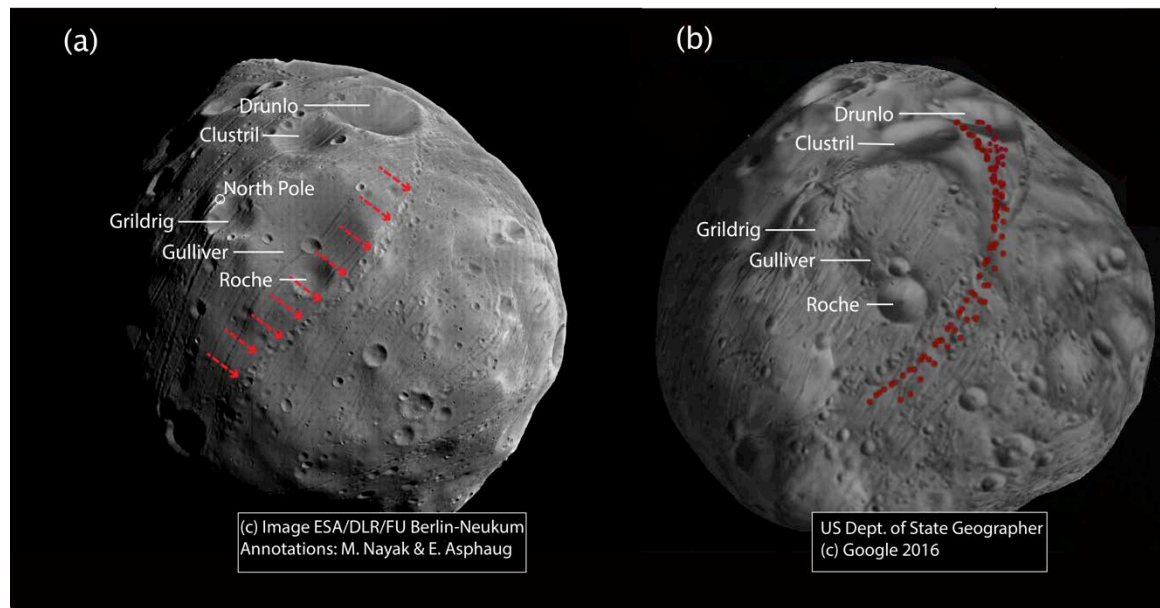


Figure 3.6. Tracing an observed catena back to its source crater. (a) Spacecraft image of Phobos (Photo credit: ESA/Mars Express) showing the observed catena of interest (red arrows); (b)

Reimpact map for a primary impact at Grildrig, azimuth $\beta \in [0: \pi/36: 2\pi)$ rendered in 3D. Relative sizes and orientations between (a) and (b) are similar and may be correlated from labeled craters; Flimnap and Skyresh craters are in shadow in (a). Features underlined in yellow in (b) are on the opposite hemisphere. From the correlation, the highlighted catena likely originates from sesquinary ejecta from Grildrig.

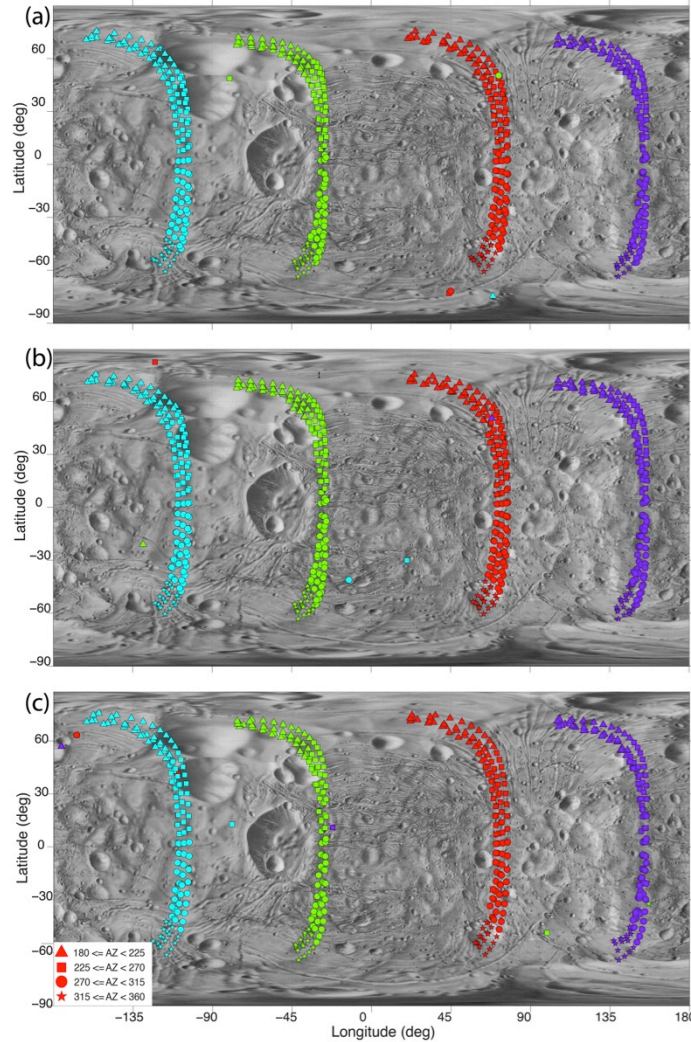


Figure 3.7. Impact of primary crater size on resultant catenae. Maps show resultant catenae from velocity distributions centered at the location of Stickney but with Z-model crater sizes of diameter (a) 5 km; (b) 3 km and (c) 1 km. Reimpacting particles have ejection velocities of 11-30 ms^{-1} ; no change is evident between varying crater sizes in this velocity range. Craters as small as 1 km in diameter appear capable of creating catenae-like structures. Ejection azimuth β is henceforth restricted (compare to Figure 3.10) to $\beta \in [\pi: \pi/36: 2\pi)$; shapes denote ejection azimuth of reaccreted particles (legend, lower left). Changes with orbital geometry configurations at the time of the primary impact are shown, namely, when Phobos is at Mars periapsis (red), apoapsis (blue), halfway between periapsis and apoapsis along the ascending node (purple) and the descending node (green).

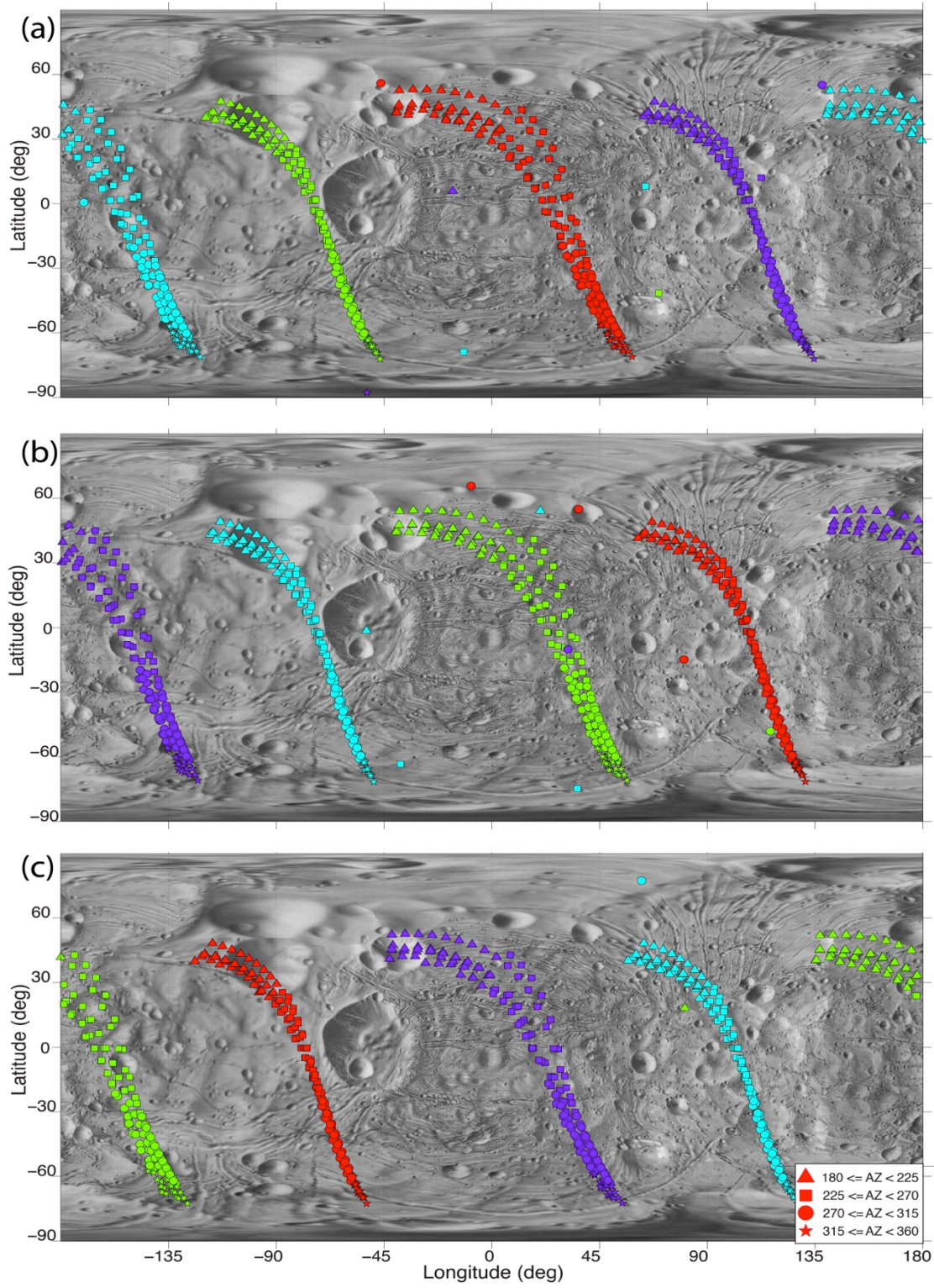


Figure 3.8. Impact of primary crater longitude (southern hemisphere) on resultant catenae. Maps show resultant catenae for a primary impact at latitude 30° S; longitude ranges between (a) 90° W; (b) prime meridian; (c) 180° E. Large changes in primary impact crater longitude

have no effect on the orientation of the resulting catenae and are degenerate with orbital phasing of Phobos around Mars. Reimpacting particles have ejection velocities of $11\text{-}30\text{ ms}^{-1}$ and $\beta \in [\pi: \pi/36: 2\pi)$. Colors and shapes denoting the ejection azimuth are as in Figure 3.7.

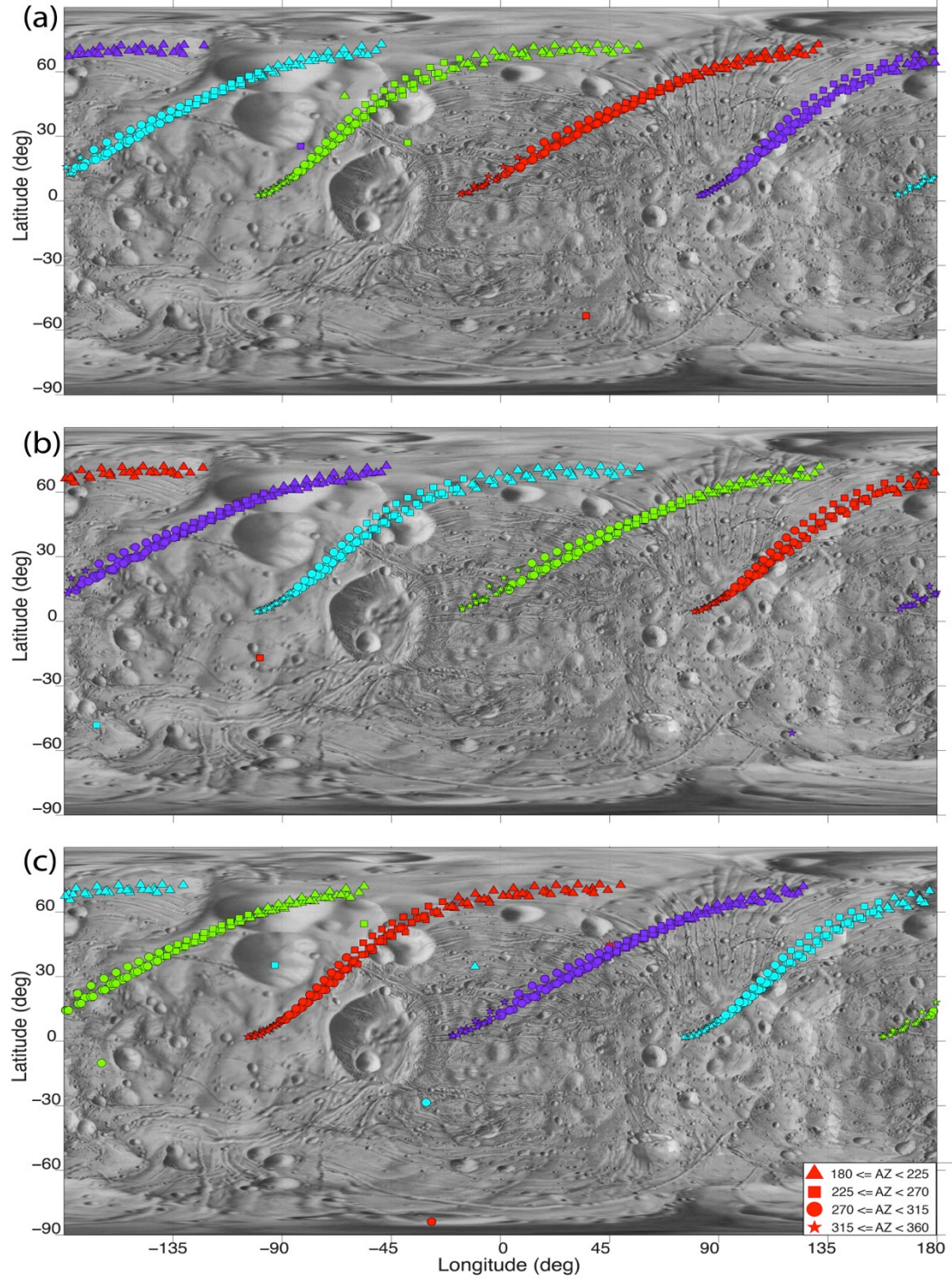


Figure 3.9. Impact of primary crater longitude (northern hemisphere) on resultant catenae. Maps show resultant catenae for a primary impact at latitude 60° N; longitude ranges between (a) 90° W; (b) prime meridian; (c) 180° E. Large changes in primary impact crater longitude have no effect on the orientation of the resulting catenae and are degenerate with orbital phasing of Phobos around Mars. Reimpacting particles have ejection velocities of $11\text{--}30\text{ ms}^{-1}$ and $\beta \in [\pi: \pi/36: 2\pi)$. Colors and shapes denoting the ejection azimuth are as in Figure 3.7.

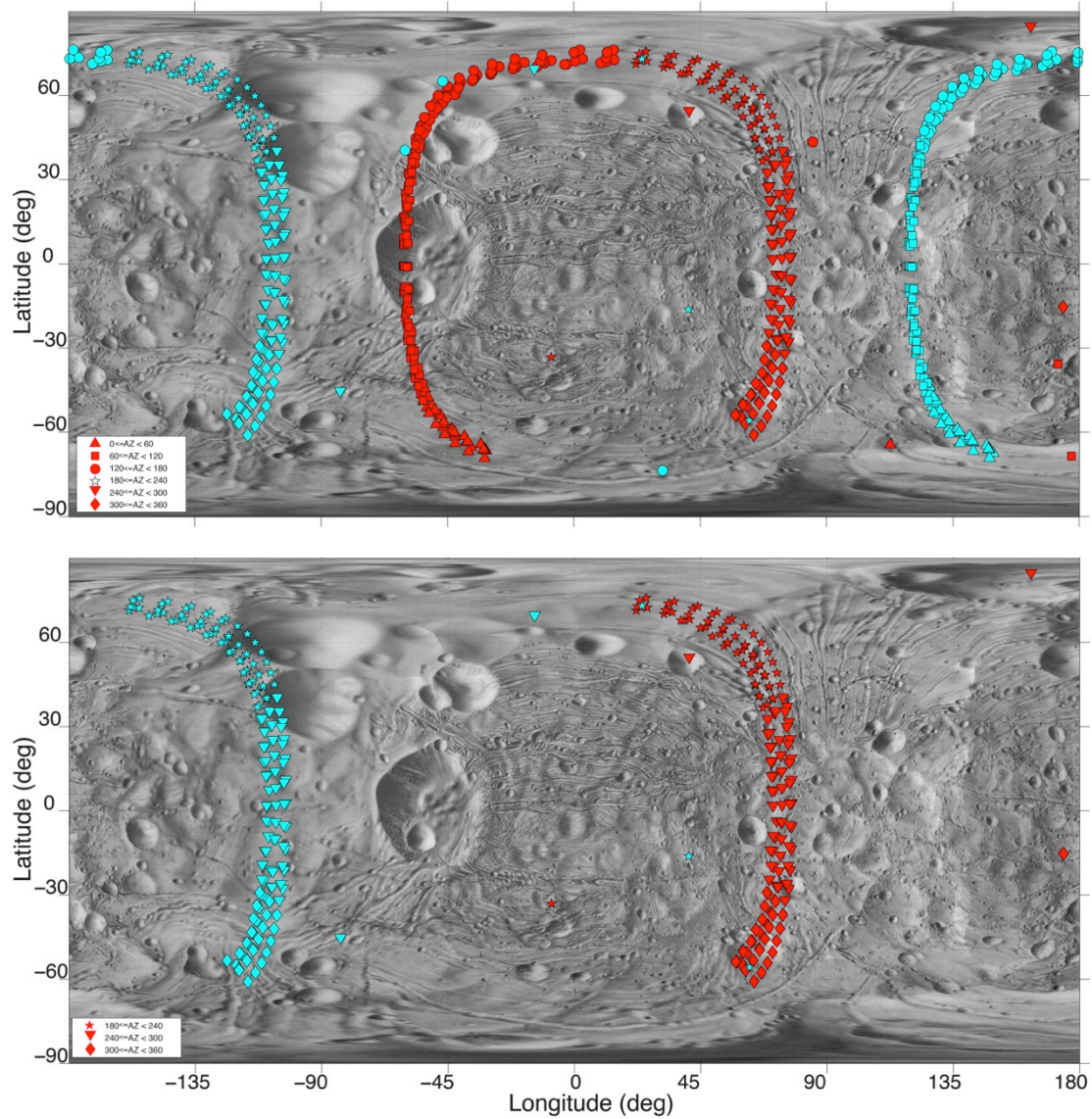


Figure 3.10. Comparing resultant catenae with azimuths of ejecta release. Maps show resultant catenae from the Stickney impact (centered at 1° N, 46° W) from particles with ejection velocities from $11\text{--}30\text{ ms}^{-1}$. Colors are as in Figure 3.7. (Top) Azimuths of ejected particles are $\beta \mid \beta \in [0: \pi/36: 2\pi)$; (bottom) compares catenae for azimuths restricted to $\beta \mid \beta \in [\pi: \pi/36: 2\pi)$. Shapes denoting ejection azimuth are in legends (bottom left) of both panels. Mirroring the catenae in the bottom panel yields the full picture; for clarity in comparing geometry configurations (GCs) we show the subset of azimuths in the bottom subfigure.

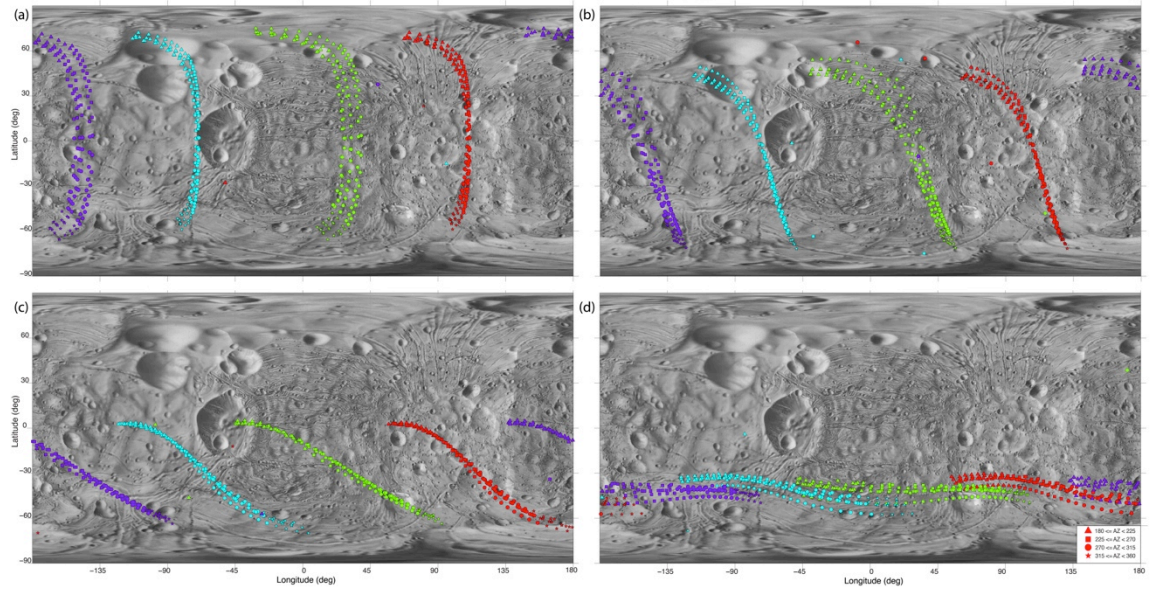


Figure 3.11. Impact of primary crater latitude (southern hemisphere) on resultant catenae. Maps show resultant catenae from primary impacts on Phobos at the prime meridian and (a) 0° S; (b) 30° S; (c) 60° S; (d) 85° S. Catenae orientation can change from near-vertical to horizontal, depending on the latitude of the primary impact, and mirror northern hemisphere impacts (compare to Fig 5). Reimpacting particles have ejection velocities of 11-30 ms⁻¹, $\beta \in [\pi/36: 2\pi]$; colors and azimuth legend as in Figure 3.7.

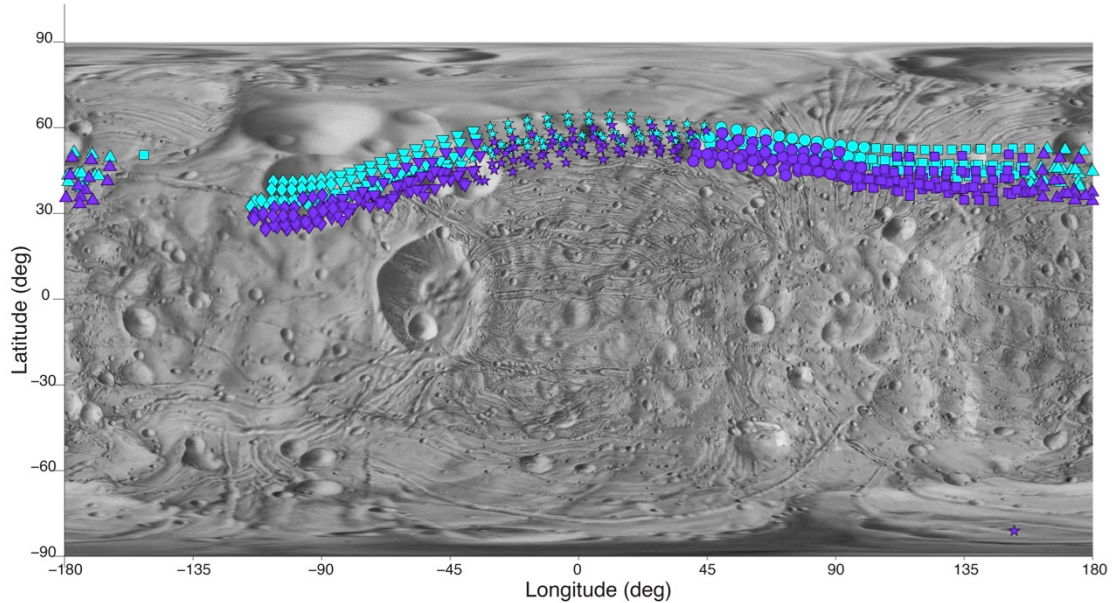


Figure 3.12. Variation of resultant catenae with Z-number (ejection angle). Reaccretion map for ejecta from the Girdrig crater, at Phobos periapsis around Mars, where the ejection angle is held fixed at 56.3° (blue catena) and allowed to vary stochastically between 45° and 65° (purple catena). Highly similar reaccretion patterns between the two methods show that the catena formation mechanism detailed here does not depend on Z-number or ejection angle variations.

Chapter 4

Magnetics: A Case Study of the Lunar South Pole-Aitken Basin

This chapter is a modified reprint of M. Nayak, D. Hemingway and I. Garrick-Bethell (2016), Magnetization in the South Pole-Aitken Basin: Implications for the lunar dynamo and true polar wander, accepted, Icarus.

4.1 Abstract

A number of magnetic anomalies are present along the northern edge of the lunar South Pole-Aitken (SPA) basin. A variety of hypotheses for their formation have been proposed, but an in-depth study of their properties has not been performed. Here we use two different methods to invert for their source body characteristics: one that completely searches a small parameter space of fewer than ten uniform-strength dipoles per anomaly, and another that uses grids of hundreds of dipoles with variable magnetization strengths. Both methods assume uniform magnetization directions at each anomaly and with one exception, produce nearly the same results. We introduce new Monte Carlo methods to quantify errors in our inversions arising from Gaussian time-dependent changes in the external field and the uncertain geometry of the source bodies. We find the errors from uncertainty in source body geometry are almost always higher. We also find a diverse set of magnetization directions around SPA, which we combine with other physical arguments to conclude that the source bodies

were likely magnetized in a dynamo field. Igneous intrusions are a reasonable explanation [Purucker *et al.*, 2012] for the directional variability, since they could be intruded over different magnetic epochs. However the directional variability also implies either surprisingly large amounts of true polar wander or non-axially aligned dynamo fields. We also explore the possibility that true polar wander caused by the SPA impact could allow iron-rich SPA ejecta to record a diverse set of magnetic field directions. Some of this material may have also become “sesquinary” ejecta and re-impacted across the Moon on 10^4 - 10^6 year timescales to capture such changes. No completely satisfactory answer emerges, except that the dipole-axis of the lunar dynamo may have been variable in direction.

4.2 Introduction

The South Pole-Aitken (SPA) Basin is the Moon’s largest and oldest well-defined basin [Garrick-Bethell and Zuber, 2009]. It is also the site of the largest grouping of magnetic anomalies on the Moon [Purucker, 2008]. Initially discovered by the Apollo 15 subsatellite [Coleman *et al.*, 1972], the origin of these features remains unknown. Across the last 20 years, three dominant hypotheses for their formation have emerged. The first is that ejecta from the Imbrium and Serenitatis basins has accumulated at their antipodes, which fall within the SPA basin (Hood and Huang, 1991; Lin *et al.*, 1998; black crosses in Figure 1). This antipodal ejecta then attains a remanent magnetization from either a dynamo field, or a field related to the impact event [Hood and Artemieva, 2008]. The second hypothesis is that the

anomalies arise from subsurface dikes that cooled in a dynamo field [Purucker *et al.*, 2012]. The third is that iron-rich material derived from the SPA impactor cooled in a dynamo field [Wieczorek *et al.*, 2012]. Determining which, if any of these hypotheses are true, would have implications for understanding the nature and history of the lunar dynamo.

Despite the importance of these anomalies in understanding lunar magnetism, no detailed studies of the source body characteristics have been performed. Purucker *et al.* (2012) modeled one of the anomalies within SPA as a series of vertically magnetized dikes, and estimated their magnetization strength. Global studies of lunar magnetic anomalies have neglected the SPA region [Arkani-Hamed and Boutin, 2014; Takahashi *et al.*, 2014], because of the complicated field structure in the region. Using a method they refer to as surface vector mapping, Tsunakawa *et al.* (2014) calculated the statistics of the declination of the field over the anomalies at SPA. Based on the distribution of declinations, they found evidence that the source bodies are horizontally elongated in the east-west direction. While they also estimated the magnetization direction and magnetic paleopole from the anomaly centered on the Leibnitz crater within SPA, they did not estimate the source body characteristics of any of the larger magnetic anomalies that characterize the region.

Here, we will show that many individual anomalies can be identified within SPA. We use software that can readily generate and compare magnetic field maps from all available observations, helping us avoid spurious or poorly defined magnetic anomalies that may have complicated other efforts to study the region. Comparisons

with a spherical harmonic model of the magnetic field [Purucker and Nicholas, 2010] provide a further test of consistency. We will show that the source body magnetization directions offer a key test for their formation hypotheses, and we make a substantial effort to characterize the uncertainty in these directions. The paper is organized as follows: Section 4.3 presents our methods, including uncertainty estimation, Section 4.4 presents our results, and in Section 4.5, we discuss possible origins of the observed diversity in magnetization directions. We consider an impact versus dynamo origin for these anomalies, secular variation, dynamos misaligned with the lunar spin axis, and both long and short-timescale true polar wander. Finally, Section 4.6 contains our conclusions.

4.3 Methods

4.3.1 Data Sources

We use magnetometer data from two independent sources: Lunar Prospector (LP-MAG) and SELENE/Kaguya (K-MAG). The Lunar Prospector fluxgate magnetometer measured the vector magnetic field at up to 18 Hz and transmitted its measurements at a reduced resolution of 9 Hz. Level 1B LP-MAG data are obtained from the NASA Planetary Data System (ppi.pds.nasa.gov). The SELENE/Kaguya spacecraft used a tri-axial fluxgate magnetometer with a sampling rate up to 32 Hz. K-MAG magnetometer data are obtained from the SELENE data archives (12db.selene.darts.isas.jaxa.jp). The cadence of measurements used in this study is 0.2

Hz for LP-MAG and 0.25 Hz for K-MAG. Topography data are from the Lunar Orbiter Laser Altimeter (LOLA) [Smith *et al.*, 2010] (pds-geosciences.wustl.edu).

To best capture the Moon's crustal field, all data used for analysis were collected in either the lunar wake or while the Moon was in the Earth's magnetotail (wake/tail), avoiding distortions caused by the solar wind noted by [Kurata *et al.*, 2005; Halekas *et al.*, 2008]. Tail datasets specifically exclude epochs during which plasma sheet disturbances were noted [Halekas *et al.*, 2012]. Consecutive orbits are $\sim 1^\circ$ in longitude apart. At 0.2 Hz, successive magnetometer measurements are separated by ~ 8 km in the latitudinal direction. All data used in this study are from the final months of Lunar Prospector in 1999 and Kaguya in 2009, when measurements were taken at observation altitudes below 50 km.

4.3.2 Data Processing and Anomaly Identification

Details on the generation of magnetic field maps used in this paper (e.g. Figure 4.8) are after Hemingway and Garrick-Bethell (2012), summarized here for completeness. After subtracting the background field (taken to be the mean field across each orbit segment spanning the region of interest), the remaining fields are assumed to be due to crustal sources. Data from consecutive orbits are combined and fit to square meshes using Delaunay triangulation, with a grid spacing of $0.25^\circ \times 0.25^\circ$ (7.6 km x 7.6 km equatorial). This spacing is finer than the spacing between observations (e.g., ~ 8 km latitude, ~ 30 km longitude for LP-MAG), ensuring no loss of signal variation during grid generation. Orbit segments that visually appear

distorted by transient magnetic noise, despite these efforts, are discarded. Gaps in spacecraft coverage, if any, can be seen in magnetic field maps, as the spacecraft measurement locations are shown in all figures (e.g. Figure 4.8, white points).

To analyze the northern SPA region, we divide the strongest magnetic anomalies into ten study areas (Figure 4.1). We choose anomalies whose Kaguya and LP magnetic field maps are consistent with maps from a spherical harmonic model of the field [Purucker and Nicholas, 2010], which can be seen by comparing Figure 4.1b and 1c. Anomalies that were not consistent with this model or showed artifacts of external disturbances were not used. Areas 1 and 2 encompass two approximately linear and perpendicular magnetic features; in their vicinity is Area 3, also in proximity to the Van de Graaff crater [Dyal *et al.*, 1974]. Area 1 is very similar to the area modeled by Purucker *et al.* (2012). Together, we refer to Areas 1-3 as the northwestern cluster. Area 9 is to the southwest of these areas and is associated with the “swirl” albedo anomalies at Mare Ingenii [Blewett *et al.*, 2011; Kramer *et al.*, 2011]. Area 4 is an isolated anomaly to the southeast of areas 1-3. Areas 5-8 are east-west trending linear features found to the east of these study areas, and together we refer to them as the eastern stripes. The anomalies at areas 1 and 8 appear connected in some maps of the magnetic field (Purucker *et al.* 2012). Finally, we also define area 10, interesting because it falls outside the basin’s outer topographic rim [Garrick-Bethell and Zuber, 2009].

We divide all data in this paper by the day of observation, such that each dataset for a given anomaly is collected at approximately the same altitude. The

datasets may be referenced to the day on which they were collected, e.g., 1999 day 172 (LP-MAG; read as 99172) or 2009 day 123 (K-MAG; read as 09123). Figure 4.2 shows an overview of the total magnetic field maps created for all observation days used for all study areas; Figure 4.23 - Figure 4.57 show details of magnetic inversions for all these areas (see Section 4.3.3 and 4.3.4).

4.3.3 Inversion Algorithm 1: Defined Dipoles, Constant Magnetization

To assess the robustness of our results, we use two different algorithms to invert for source body characteristics. Both are regressions to find the least squared error. The first completely searches a given parameter range using manually placed dipoles as the source bodies. The regression parameter space varies burial depth in km, magnetic dipole moment in Am^2 , magnetic dip (inclination) in degrees downward from the horizontal, and declination in degrees clockwise from north. All dipoles in a given study area are constrained to be at the same depth, moment and direction. Source dipole positions (latitude \forall_s and longitude ϕ_s) are placed manually by the user at locations where the magnetic field strength is greatest according to our maps. We refer to this henceforth as the Defined Dipoles, Constant Magnetization (DD-CM) algorithm. As we will show, the ability to completely search a parameter space at relatively fast computation speeds gives this algorithm some advantages when uncertainties must be estimated.

The depth is allowed to vary between 1 km and 99 km in steps of 0.25 km, and the dipole magnetic moment between 10^{11} Am² and 10^{14} Am² in steps of 2.5×10^{11} Am². Depth solutions are further constrained to be no shallower than the deepest negative topography in a given study area, ensuring that all solutions lie beneath the lunar surface; depth is measured against a reference sphere of 1737.4 km [Smith *et al.*, 2010]. The magnetic inclination is allowed to vary from -90° to +90° in steps of 1° and declination from -180° to +180° in steps of 1°.

For n field measurements inside a given study area, the difference between the model and the data is computed. We minimize the mean of the root mean square (RMS) total error of the east (δB_{east}), north (δB_{north}) and radial (δB_{radial}) component errors, δB_{total} , as:

$$(\delta B_{total})_{RMSS} = \sqrt{\frac{1}{n} \sum_{i=1}^n (\delta B_{east}^2 + \delta B_{north}^2 + \delta B_{radial}^2)} \quad (4.1)$$

This quantity is then ranked in decreasing order of total error to find the best-fit magnetic characteristics.

4.3.4 Inversion Algorithm 2: Gridded Dipoles, Variable

Magnetization

We test the validity of our inversion results using an alternative, more objective approach, at the expense of exploring a much larger parameter space. Instead of placing dipoles manually, we establish a $0.25^\circ \times 0.25^\circ$ grid of dipoles covering the entire study area [Nicholas *et al.*, 2007; Hemingway and Garrick-Bethell, 2012]. All dipoles are again constrained to be at the same depth, inclination

and declination. Unlike the first algorithm, however, the magnetic moment is allowed to vary among the dipoles. This creates a large $n+3$ parameter space, where n is the number of dipoles; Table 4.1 lists the number of gridded dipoles for each study area, which ranges from 320-1408. The solution is then found via a genetic search algorithm that minimizes the RMS error (for details, see Hemingway and Garrick-Bethell (2012)). The algorithm evolves through “generations” to progress toward a better fit (smaller error) to the data. However, the evolutionary nature of the algorithm does not guarantee optimality of the solution. We refer to this henceforth as the Gridded Dipoles, Variable Magnetization (GD-VM) algorithm. The grid of best-fit magnetic moments found by this method, ranging across several orders of magnitude at each anomaly, can be seen in Figure 4.58 - Figure 4.67, which show representative results for each study area.

4.3.5 Uncertainty Estimation for Magnetization Directions

Error in our regressions arises from: 1) time-variable contributions to the measured field due to non-crustal fields or instrument noise, 2) the ideal assumption that all sources are uniformly magnetized in the same direction, and 3) the simplified geometry of our source models, even if the assumption of unidirectional magnetization were completely true.

4.3.5.1 Time variable contributions

One method to account for the first source of error is to report the set of solutions with an RMS error equal to or less than the uncertainty in the magnetic field

measurements [Parker, 1991]. The range of magnetization directions in this set then defines the error in the best-fit direction. The drawback of this method is that the use of the field's uncertainty is arbitrary. For example, at different observation altitudes, the magnitude of the RMS error for the best-fit solution will vary, such that the measurement uncertainty will have a different impact on the size of the set of solutions that represent the error. More importantly, as we show below, the set of allowable solutions suggested by Gaussian measurement noise (or external field oscillations) of a given magnitude is often small compared with the size of the set of solutions contained by an RMS error of equal magnitude. That is, using the uncertainty in the field measurement to define the allowable solution set can overestimate the error in the regression, at least in the case of lunar magnetic field measurements.

To demonstrate this effect, we simulate the effect of Gaussian measurement noise in each of the 45 regressions we perform (Figure 4.2). Before doing so, we first estimate the characteristic noise magnitude. For both LP-MAG and K-MAG, the instrument noise is < 0.1 nT, such that the dominant source of error arises from fluctuations in the interplanetary magnetic field (IMF) rather than the instrument. To estimate a characteristic amplitude of the oscillations in the IMF over the timescale of observation at one magnetic anomaly, while in the wake or magnetotail, one would ideally examine the time-dependent oscillations just prior to flying over the anomaly of interest. However, there is no simple way to separate oscillations arising from small-scale crustal fields and time dependent fields. As a proxy, we can examine the

field variations over the Mare Imbrium region while the Moon is in the wake. Since the Imbrium region is known to have the lowest amount of crustal magnetism anywhere on the Moon [Mitchell *et al.*, 2008; Tsunakawa *et al.*, 2014], observations there are the most likely to represent only the time dependent oscillations. We find that the standard deviations at Imbrium are 0.07 nT and 0.13 nT for two representative days (Figure 4.4). However, to be conservative, we use an order of magnitude higher standard deviation of 1 nT as the representative value. Takahashi *et al.* (2014) make a similar (1 nT) assumption about the magnitude of external field contributions.

Next, to simulate the effect of typical time-dependent fields in our DD-CM regressions, we added random Gaussian noise with a standard deviation of 1 nT to each field component (east, north, radial) for all 45 datasets. An example is shown in Figure 4.5. Note that we are assuming that the noise at each measurement point is uncorrelated with the previous measurement point. Our assumption is only valid if oscillations in the IMF occur on timescales faster than the time between measurements (5 seconds for LP data, and 4 seconds for Kaguya data). Future work will determine the dependence of our error estimates on a variety of correlation timescales, and better determine the actual timescale of IMF oscillations.

For each of the 45 datasets (Figure 4.2), we generated 20 sets of noise-added data. Assuming the best-fit directions are Fisher distributed [Fisher, 1953], their angular standard deviations and Fisher distribution precision parameters k , were then obtained from each set of 20 simulations. The mean k value across all datasets was

then used as the final estimate of the uncertainty from time-dependent fields. The ability to simulate the effect of noise in this manner represents an advantage of the DD-CM method, which has a faster computation time compared to the GD-VM method (see Figure 4.5).

We find that the angular standard deviation in best-fit direction associated with 1 nT noise is always smaller than the set of directions permitted when using an error threshold of 1 nT. For example, the best-fit RMS error for Area 1, 09096 (Figure 4.5) is 2.4 nT, which is already higher than the ~ 1 nT uncertainty in the field (this is true for all anomalies in this study). The set of solutions that are allowed by considering 1 nT additional RMS error (total residual error 3.4 nT) produces $\sim 30^\circ$ of uncertainty in the best-fit magnetization direction (Figure 4.6). In contrast, Figure 4.6 also shows that adding 1 nT Gaussian noise to these data via the above method only produces an angular standard deviation of 5° in the best-fit direction. The smaller size of the effect of simulated Gaussian noise is true in all of our regressions.

4.3.5.2 Non-uniform magnetization directions

The second contribution to error is the non-uniform magnetization directions in the source bodies. However, it is impossible to make any inferences about the magnetization if we permit the infinite number of possible source magnetizations with mixed directions. Therefore we must at least assume that the source is uniformly magnetized. We attempt to mitigate this effect by selecting small, well-defined

anomalies (Figure 4.1). Of course, if non-uniformity dominates the source of error then these regression results are less meaningful.

4.3.5.3 Source body geometry

Finally, we address what is likely the dominant source of uncertainty: the complex geometry of the magnetic source bodies compared to our simplified models. We do this in two ways. The first is to use compute the best-fit magnetization separately for different altitude datasets at each anomaly. Data from different altitudes display a diversity of magnetic field morphologies, as field strength decays with altitude (which ranges in this study from 13-46 km). Hence, each altitude will lead to different choices of dipole locations; for example, compare Figure 4.8 to Figure 4.23 - Figure 4.25. Similarly, the geometries of the best-fit source bodies will also vary. This variability is an advantage, as it allows us to probe the sensitivity of our results to source geometry, with the spread in the best-fit magnetization directions representing the measure of uncertainty. This is analogous to the practice in paleomagnetism of sampling a single rock formation multiple times at different sites [Irving, 1964]. Because each measured direction at each altitude is independently calculated we can also assign a 95% confidence interval to the mean direction [Butler, 1998]. In practice, we combine the results from both the DD-CM and GD-VM algorithms to calculate the final mean and confidence interval, even though the direction measurements for a given day are not strictly independent across the two

algorithms. We also include one best-fit direction obtained from the merged data at all altitudes, using the GD-VM algorithm.

The second way we account for uncertainty due to source body geometry is to explore the range in directions that are returned by displacing the nominal DD-CM algorithm dipoles for all 45 datasets. We calculate the effect of placing dipoles anywhere randomly on a 0.5° -radius circle from their nominal location (Figure 4.7). The value of 0.5° represents the approximate error in longitudinal uncertainty in the anomaly peak field location (orbits are spaced by approximately 1° for a given constant altitude data set). For each data set, we use 100 random placements of dipoles at any location on the defined circles and calculate the 100 best-fit magnetization directions and k values. The k values are then averaged within an area to obtain the uncertainty from source geometry for that area. Again, this represents an advantage of the DD-CM method compared to the GD-VM method, due to the ability to modify model dipole placements and a faster computation time. We will see this advantage manifest when exploring ambiguous regression results for area 2. Finally, we note that for area 4 we use 0.25° -radius circles, due to the close proximity of the model dipoles there.

The dispersions in best-fit directions obtained from our Monte Carlo simulations for time-dependent fields and 0.5° -radius dipole displacements are then combined using their k values, averaged together for each area [Irving, 1964]:

$$1/k_{total} = 1/k_{time-dependent} + 1/k_{source-geometry} \quad (4.2)$$

An angular standard deviation θ_{63} is then estimated by (Irving, 1964):

$$\theta_{63} \approx 81/k^{0.5} \quad (4.3)$$

Finally, it is added to the angular 95% confidence interval obtained from the variable altitude results within a given area.

The following is a summary of our uncertainty estimation methods:

1. Account for time-dependent external field contributions and instrument noise: Perform Monte Carlo simulations for every anomaly and altitude with the addition of 1 nT noise, and obtain mean k for the best-fit directions within an anomaly, using the DD-CM algorithm (Figure 4.5).
2. Account for uncertainty in source geometry: Perform Monte Carlo simulations for every anomaly and altitude while altering the dipole placement, and obtain mean k for the best-fit directions within an anomaly using the DD-CM algorithm (Figure 4.7, Table 4.2).
3. Combine the k values from steps 1 and 2 and obtain the angular standard deviation via equations 2 and 3.
4. Account for uncertainty in source geometry by using variable altitude data, and hence variable dipole placement. Obtain a 95% confidence interval on the mean direction from the combined best-fit directions from the DD-CM and GD-VM algorithms (Table 4.3).
5. Add the angular dispersion from step 3 to the angular 95% confidence interval from step 4 to obtain the total angular uncertainty estimate in the best-fit direction.

4.4 Results

4.4.1 Regression Results

Minimum error magnetization directions are found for each Lunar Prospector and Kaguya dataset, using both the DD-CM (Section 4.3.3) and the GD-VM (Section 4.3.4) algorithms. Table 4.1 compiles the values of these best-fit directions. The best-fit models are shown in Figure 4.8 - Figure 4.17 for study areas 1-10. The figures show 10 representative examples, one for each study area; Figure 4.23 - Figure 4.57 show all results for every dataset listed in Table 4.1. Angular standard deviations and k for the noise-added and dipole displacement simulations are shown in Table 4.2 for all datasets. RMS error maps for all datasets (similar to Figure 4.6) are compiled in Figure 4.18 and Figure 4.19; these illustrate the difference between using an arbitrary uncertainty threshold and the Monte Carlo methods employed in this work.

Figure 4.20 compiles the values of the best-fit directions from the DD-CM and GD-VM algorithms. For the DD-CM algorithm, we show one standard deviation of dispersion from 1 nT noise (Figure 4.20a) and one standard deviation of dispersion from displacing the model dipoles by 0.5° (Figure 4.20b) (see Methods). Overall, we find the error from the uncertainty in source geometry (Figure 4.20b) is usually larger than the error from the effects of time-dependent fields (Figure 4.20a).

Interestingly, we find source geometry errors at areas 2 and 8 are substantially larger than for the other anomalies. The large error in area 2 arises from the existence of two nearly equal local minima in its DD-CM error map, which is not seen at any

other anomaly (see Figure 4.18). The two minima are approximately 110° apart. Small displacements of the dipoles from their nominal locations flip the best-fit solution into the other minimum, producing its large uncertainty ellipses, particularly for day 09096 (Figure 4.20b). One of our four best-fit solutions (day 99033) falls in this secondary minimum. Because area 1 and 2 have slight overlap (Figure 4.1), we tested if the double minima could be a result of area 1 data influencing the regression at area 2. We ran the DD-CM algorithm against data for area 2, but this time excluded spacecraft measurements over area 1. The results are not significantly different; the two minima are still seen for area 2. Using the GD-VM algorithm, one finds the best-fit directions for area 2 are approximately between the two minima found by the DD-CM algorithm (Figure 4.20c), $\sim 60^\circ$ from either one. This difference between the two algorithms is the largest for any area. Further work will be required to better understand the nature of the error space at area 2, and its source body characteristics; we will investigate, for example, oppositely magnetized blocks of magnetization in this region (cf. Parker, 1988).

For area 8, the large error arises largely from the flatness of the error space, instead of the existence of multiple minima (Figure 4.18). In particular, the declination of this nearly equator-pointing magnetization vector is poorly constrained, with results spanning a range of $\sim 100^\circ$ of arc (a result found to be true using either the DD-CM or GD-VM algorithm). Again, without the error maps provided by the DD-CM algorithm, we would not have been able to isolate and understand these sources of uncertainty in areas 2 and 8.

Next, we calculate the mean magnetization strength for all study areas using the best-fit depths and magnetic moments recovered by both the DD-CM and GD-VM algorithm (Table 4.1). For this calculation, the area of the magnetic anomalies is taken as the area across which the magnetic field $B \geq B_{max}/4$, where B_{max} is the peak magnetic field in a given study area. We choose to approximate the thickness of the magnetic material as twice the average of the best-fit magnetic source depths. Most values cluster in the 0.1-0.3 A/m range found by [Purucker *et al.*, 2012], who studied a region similar to area 1. A few isolated datasets at the lowest altitudes show higher magnetizations, but with the exception of area 9, average magnetizations for a particular study area across all datasets are close to the 0.1-0.4 A/m range suggested by [Wieczorek and Weiss, 2010]. Even for area 9, only the GD-VM average magnetization is outside this range.

In most cases the GD-VM algorithm returns higher values for magnetizations than the DD-CM algorithm. This is a result of the shallower depths returned by the GD-VM algorithm, which arise because of the sheet-like nature of the magnetic source, compared to the dipolar model in the DD-CM algorithm. In general the depth of the magnetic source bodies is not well constrained from our results, due to the possibility of non-uniquely trading depth with moment, but ultimately does not factor in to our paleo-directional analysis.

Finally, best-fit paleopoles for all datasets are calculated from the best-fit magnetization directions [Butler, 1998] (Figure 4.21, Table 4.3). The uncertainties derived from the methods described in the Methods section yield a circular error

ellipse for each area that becomes distorted when its paleopole is calculated. Hence we calculate the two different semi-axes of the ellipse along the great circle path from the site to pole (dp) and the semi-axes of the ellipse perpendicular to that path (dm) (Butler, 1998). For area 2, we also show the paleopoles from the two local error minima found in the DD-CM method, particularly because one falls very close to the paleopole for area 1 (within its uncertainty), while the other falls close to the paleopoles from areas 3, 6, and 8 (within the uncertainties of 6 and 8).

Table 4.1. Lunar Prospector (LP) and Kaguya (KG) datasets used for inversions, with best-fit magnetic characteristics found using both the DD-CM and GD-VM algorithms. Mean observational altitude, data day and site latitude and longitude are shown. GD-VM dipoles column indicates the number of gridded dipoles used for the GD-VM simulation. Calculated magnetizations for both algorithms are shown. Highlighted rows correspond to figures shown in the main text (Figure 4.8 - Figure 4.17); corresponding GD-VM dipole maps for these datasets are also shown in Figure 4.58 - Figure 4.67. Best-fit figures for non-highlighted rows may be found in Figure 4.23 - Figure 4.57.

Study Area	Spacecraft	Year	Day	Latitude (deg N)	Longitude (deg E)	Alt (km)	DD-CM algorithm					GD-VM Algorithm				
							Depth (km)	Moment (10 ¹² Am ²)	Inc (deg)	Dec (deg)	Mag (A/m)	Dipoles	Depth (km)	Inc (deg)	Dec (deg)	Mag (A/m)
1	LP-MAG	1999	142	-25	-184	22.4	25	8.4	13	-123	0.12	580	5	18	-128	0.70
	LP-MAG	1999	61	-25	-184	32.3	24	6.4	32	-116	0.09	580	5	22	-128	0.62
	K-MAG	2009	96	-25	-184	39.4	36	11.0	42	-132	0.06	580	26	30	-126	0.12
	K-MAG	2009	123	-25	-184	33	37	6.4	20	-114	0.11	580	14	20	-116	0.24
	Merged											580	6	19	-123	0.42
2	LP-MAG	1999	33	-20	-188	32.8	46	21.0	36	21	0.06	1408	21	11	-71	0.20
	K-MAG	2009	69	-20	-188	44.7	37.5	26.0	29	-129	0.06	1408	39	5	-54	0.10
	K-MAG	2009	96	-20	-188	39.4	40	15.0	26	-135	0.07	1408	38	7	-52	0.11
	K-MAG	2009	123	-20	-188	33	40	20.0	32	-141	0.07	1408	26	7	-53	0.16
	Merged											1408	12	8	-59	0.14
3	LP-MAG	1999	61	-27	-192	32.3	47	19.0	31	1	0.08	432	21	20	3	0.16
	K-MAG	2009	69	-27	-192	44.7	55	62.0	32	-8	0.10	432	27	13	-1	0.16
	K-MAG	2009	96	-27	-192	39.4	49.5	18.0	49	4	0.07	432	23	27	-8	0.13
	K-MAG	2009	123	-27	-192	33	48	17.0	49	2	0.06	432	23	21	2	0.13
	Merged											432	11	25	-8	0.15
4	LP-MAG	1999	115	-33	-183	32.3	28	6.4	-64	-46	0.06	320	24	-55	-56	0.09
	LP-MAG	1999	142	-33	-183	22.4	40.5	12.0	-73	-89	0.07	320	13	-52	-50	0.20
	K-MAG	2009	96	-33	-183	39.4	28	6.2	-69	-23	0.06	320	24	-70	-28	0.08
	K-MAG	2009	151	-33	-183	13.7	23.5	5.7	-82	86	0.06	320	8	-62	-42	0.30
	Merged											320	9	-85	-73	0.17
5	K-MAG	2009	96	-19	-165	39.4	32.5	11.0	-33	-16	0.06	850	24	-23	-23	0.15
	K-MAG	2009	151	-19	-165	13.7	55	34.0	-24	-12	0.12	850	25	-34	-33	0.17
	LP-MAG	1999	142	-19	-165	22.4	46	21.0	-29	-23	0.09	850	26	-30	-33	0.14
	K-MAG	2009	123	-19	-165	33	38.5	7.9	-56	6	0.06	850	28	-36	-25	0.11
	Merged											850	12	-30	-39	0.14
6	LP-MAG	1999	142	-24	-165	22.4	46	23.0	47	-38	0.10	576	23	50	-28	0.16
	LP-MAG	1999	33	-24	-165	32.8	55	33.0	49	24	0.08	576	31	39	53	0.13
	LP-MAG	1999	115	-24	-165	32.3	55	30.0	41	-8	0.08	576	21	47	18	0.16
	K-MAG	2009	96	-24	-165	39.4	46	22.0	49	31	0.07	576	32	31	-21	0.12
	K-MAG	2009	123	-24	-165	33	55	21.0	43	-14	0.08	576	34	38	-25	0.11
7	LP-MAG	1999	33	-27	-165	32.8	55	22.0	35	-160	0.09	341	26	28	-132	0.15
	LP-MAG	1999	115	-27	-165	32.3	41.5	12.0	45	-180	0.07	341	25	38	159	0.12
	K-MAG	2009	96	-27	-165	39.4	24.5	8.0	46	152	0.08	341	21	34	155	0.14
	K-MAG	2009	123	-27	-165	33	37	11.0	40	131	0.07	341	24	34	143	0.12
	Merged											341	14	39	165	0.13
8	K-MAG	2009	123	-31	-164	33	25.5	6.9	2	146	0.05	1100	39	-3	-131	0.08
	LP-MAG	1999	61	-31	-164	32.3	46	21.0	1	-172	0.03	1100	45	3	134	0.06
	K-MAG	2009	151	-31	-164	13.7	25	5.9	-17	138	0.05	1100	13	0	123	0.31
	LP-MAG	1999	142	-31	-164	22.4	55	20.0	-17	-128	0.04	1100	36	-6	-119	0.10
	K-MAG	2009	96	-31	-164	39.4	28	7.8	-1	-162	0.03	1100	46	-3	-132	0.07
9	LP-MAG	1999	61	-36	-198	32.3	29.5	26.0	1	119	0.16	672	7	-4	145	0.52
	LP-MAG	1999	88	-36	-198	32.2	34	37.0	-12	146	0.13	672	9	-11	162	0.43
	LP-MAG	1999	115	-36	-198	32.3	25	30.0	-6	139	0.14	672	7	-8	141	0.49
	LP-MAG	1999	142	-36	-198	22.4	22.5	17.0	-2	144	0.18	672	4	-5	153	0.95
	K-MAG	2009	96	-36	-198	39.4	26	23.0	-5	125	0.16	672	7	-8	141	0.41
10	K-MAG	2009	123	-36	-198	33	23.5	15.0	-5	135	0.19	672	5	-3	143	0.65
	Merged											672	4	-7	146	0.58
	LP-MAG	1999	61	-14	-153	32.3	36	25.0	34	-180	0.05	506	15	15	156	0.20
	LP-MAG	1999	88	-14	-153	32.2	20.5	8.3	32	166	0.10	506	12	11	-167	0.23
	LP-MAG	1999	142	-14	-153	22.4	21	17.0	29	-175	0.06	506	5	14	-174	0.56
10	K-MAG	2009	123	-14	-153	33	19	15.0	21	-172	0.06	506	5	10	-172	0.50
	K-MAG	2009	151	-14	-153	13.7	16	14.0	25	-168	0.07	506	4	10	-155	0.87
	Merged											506	4.5	13	-160	0.47

Table 4.2. Uncertainty estimates for regression results. Minimum RMS error recovered using the DD-CM algorithm for all areas and altitudes, the Fisher distribution precision parameter k , angular standard deviation θ_{63} ($= 81/k^{1/2}$), obtained from Monte Carlo simulations for the effects of time-dependent fields and 0.5° radius displaced dipoles. Altitude-averaged precision parameter k and the 95% confidence interval (α_{95}) are shown for each area. Highlighted rows correspond to figures shown in the main text (Figure 4.8 - Figure 4.17).

Study Area	Spacecraft	Year	Day	Min. RMS error (DD-CM) (nT)	Min. RMS error (GD-VM) (nT)	Noise simulation θ_{63}	Precision parameter k	Displaced dipole simulation θ_{63}	Precision parameter k
1	LP-MAG	1999	142	7.4	3.9	1.6	2526	7.4	120
	LP-MAG	1999	61	5.6	2.2	2.1	1474	7.3	124
	K-MAG	2009	96	2.4	1.1	5.0	264	4.2	381
	K-MAG	2009	123	6.3	2.3	2.9	774	3.8	446
2	LP-MAG	1999	33	5.9	3.1	1.5	3120	4.5	332
	K-MAG	2009	69	3.7	2.3	3.3	620	5.7	203
	K-MAG	2009	96	4.0	2.2	2.1	1542	44.1	3
	K-MAG	2009	123	5.7	3.2	1.7	2318	14.3	32
3	LP-MAG	1999	61	4.1	2.0	3.1	676	5.7	202
	K-MAG	2009	69	3.1	1.6	3.1	674	7.2	128
	K-MAG	2009	96	1.7	0.9	4.3	353	6.1	177
	K-MAG	2009	123	2.8	1.3	5.3	234	6.4	160
4	LP-MAG	1999	115	1.5	1.1	6.4	159	4.7	300
	LP-MAG	1999	142	4.4	2.0	4.2	375	5.3	232
	K-MAG	2009	96	1.1	0.8	7.2	127	5.5	219
	K-MAG	2009	151	8.1	3.7	1.9	1761	8.6	89
5	K-MAG	2009	96	2.0	1.0	5.3	232	3.7	472
	K-MAG	2009	151	9.1	4.0	1.3	3959	3.6	501
	LP-MAG	1999	142	4.6	1.9	2.0	1648	3.3	601
	K-MAG	2009	123	2.2	1.1	5.2	243	4.1	383
6	LP-MAG	1999	142	5.7	3.1	2.4	1150	15.1	29
	LP-MAG	1999	33	3.8	1.6	4.8	288	11.5	50
	LP-MAG	1999	115	3.3	2.0	4.8	283	5.3	234
	K-MAG	2009	96	2.2	1.1	7.8	109	6.9	140
	K-MAG	2009	123	2.7	1.5	4.6	308	4.4	343
7	LP-MAG	1999	33	3.1	1.6	5.0	262	4.6	311
	LP-MAG	1999	115	2.2	1.3	6.0	184	6.3	164
	K-MAG	2009	96	1.5	0.9	8.9	83	8.3	95
	K-MAG	2009	123	2.4	1.4	5.2	244	6.7	147
8	K-MAG	2009	123	2.6	1.7	4.4	347	28.0	8
	LP-MAG	1999	61	2.5	1.5	6.0	184	3.9	443
	K-MAG	2009	151	7.5	3.9	2.4	1121	36.6	5
	LP-MAG	1999	142	4.4	2.6	3.7	476	3.2	625
	K-MAG	2009	96	1.6	1.1	7.2	128	5.3	235
9	LP-MAG	1999	61	6.3	3.2	1.4	3496	4.3	352
	LP-MAG	1999	88	5.6	2.3	1.8	1999	8.1	99
	LP-MAG	1999	115	5.7	2.1	1.9	1837	9.6	71
	LP-MAG	1999	142	9.0	3.5	1.0	6997	8.5	91
	K-MAG	2009	96	4.0	1.5	2.8	853	8.1	101
	K-MAG	2009	123	4.5	1.5	1.8	2004	5.4	228
10	LP-MAG	1999	61	3.0	1.5	3.0	730	7.7	112
	LP-MAG	1999	88	3.2	1.7	7.9	104	11.9	46
	LP-MAG	1999	142	4.7	2.3	2.2	1315	10.2	63
	K-MAG	2009	123	1.9	1.3	3.9	431	7.3	124
	K-MAG	2009	151	8.0	4.2	1.2	4571	15.5	27

Table 4.3. Errors and paleopoles arising from using variable altitude data., The paleolatitude, paleolongitude, and value of k and the 95% confidence ellipse (α_{95}) are obtained by combining the best-fit directions of the DD-CM and GD-VM algorithm best-fit directions. The α_{95} value is added to the mean dispersions in Figure 20a and 20b to obtain the final circular error, also shown. ,The distorted version of this error circle at the paleopole is also shown (Figures 21 and 22): the semi-axis of the ellipse along the great circle path from site to pole (dp) and semi-axis of the ellipse perpendicular to that path (dm).

Area	<i>Altitude averaged</i>		Paleolatitude	Paleolongitude	Final	dp	dm
	k	$\alpha-95$			circular error		
1	58.5	6.8	-34.8	84.2	12.2	7.0	13.1
2	3.3	33.9	8.5	-259.6	41.0	24.0	44.3
3	38.7	8.4	46.9	-194.9	15.7	9.6	17.4
4	27.8	9.9	-51.8	-140.9	16.4	24.5	28.4
5	33.0	9.1	-68.1	-75.5	13.3	8.6	15.1
6	14.5	12.4	38.0	-165.1	19.9	16.6	25.7
7	11.2	16.1	-78.5	-62.0	24.5	18.2	29.9
8	3.2	30.9	54.2	-142.2	37.1	18.7	37.3
9	50.0	5.9	37.0	-247.6	12.6	6.3	12.6
10	25.4	9.2	-83.3	82.9	18.9	10.3	19.8

4.4.2 Comparison with other magnetic paleopoles

In Figure 4.22b-d we show paleopoles from isolated magnetic anomalies studied by Takahashi et al. (2014) and Arkani-Hamed and Boutin (2014), as well as paleopoles inferred from the magnetization of the crust at craters [Arkani-Hamed and Boutin, 2014]. The magnetized crust paleopoles from Arkani-Hamed and Boutin (2014) are the means of the values listed in their Table 2. None of the anomalies studied by these groups were inside SPA. To compare our results with these three datasets, we reverse all of our paleopoles into the same southern hemisphere (Figure 4.22a), as in Takahashi et al. (2014). Here we have dropped the paleopole found from the mean of all data sets at area 2, and only show the paleopoles from the two local error minima in the DD-CM algorithm.

Takahashi et al. (2014) found paleopoles that cluster into two groups, one near the present pole, and another at mid-latitudes. We find a wider dispersion in the distribution of our paleopoles, but we do find some clustering at the present pole (areas 5, 7 and 10), as well some near their mid-latitude cluster (areas 3, 6, and 8). The remaining poles are not easily assigned to either of these clusters. However, overall, the paleopoles we find do seem to avoid longitudes on the farside (the bottom half of the sphere in Figure 4.22a), and latitudes $< 30^\circ$. None of the paleopoles from Arkani-Hamed and Boutin (2014) show obvious correlation with any of the clustering found here or in Takahashi et al. (2014).

Finally, we note that many of the paleopoles are substantially separated by their error ellipses, such that it is unlikely that only one or two paleopoles would be consistent with all of the anomalies, without severely affecting their RMS error values. This can also be visualized by examining the error spaces in Figure 18 and 19; because most anomalies are at similar latitudes and longitudes (most within $\sim 30^\circ$), the diversity in paleopole locations is mostly determined by the diversity in magnetization directions. Hence, the diversity in RMS error minima in Figure 18/19 also graphically illustrates the diversity in paleopole locations.

In the next section, we address possible origins for the dispersion seen in our study, and test some of the hypotheses for anomaly formation.

4.5 Discussion

4.5.1 Paleopole directions

The wide variation in magnetic paleopoles derived from SPA's magnetic anomalies presents a puzzle. In Sections 4.5.1 – 4.5.4, we discuss the implications of the diverse paleopole locations for the formation of these anomalies, the history of true polar wander, and the nature of the lunar dynamo.

4.5.2 Magnetization by Impact Processes

A long-standing hypothesis is that the strongest lunar magnetic anomalies are genetically related to the antipodes of the Imbrium, Orientale, Serenitatis and Crisium basins [Moore *et al.*, 1974; Hood and Williams, 1989; Lin *et al.*, 1998; Hood *et al.*, 2001]. Compression and amplification of the interplanetary magnetic field (IMF) by impact-produced plasma may be strongest at the basin antipode, where impact ejecta may also preferentially collect [Hood and Artemieva, 2008]. The antipodes to the Imbrium and Serenitatis basins are close to our study areas (Figure 4.1), suggesting this process may be responsible for forming the anomalies we have examined here. If true, antipodal ejecta may become magnetized via either thermo-remanent magnetization (TRM) or shock-remanent magnetization (SRM). Below we assess these two possibilities.

4.5.2.1 TRM in an impact-produced field

If the magnetization were produced by a TRM, hot ejecta would cool in the presence of transient IMF-amplified fields that would last, at most, for one day. Assuming a thermal diffusivity of $10^{-6} \text{ m}^2/\text{s}$, the thermal cooling length-scale for one day is ~ 1 meter. Therefore, TRM would be restricted to 1 meter of material. The magnetic moments we find across all SPA study areas range between 10^{13} Am^2 and 10^{14} Am^2 . Using source body horizontal extents from Figure 4.1 (black dashed boxes), depths of ~ 1 m lead to high TRM magnetizations ranging between 10^3 to 10^4 A/m. These values are 3-4 orders of magnitude higher than samples recovered by Apollo missions. Additionally, the top ~ 1 m would have been completely overturned and demagnetized in the time since the antipodal impact ~ 4 billion years ago [Arnold, 1975]. Therefore, TRM from impact-related fields is implausible, in agreement with [Hood and Artemieva, 2008].

4.5.2.2 SRM in an impact-produced field

Alternately, impact shock pressures from the deposition of ejecta at the antipode may create SRM in the ejecta deposit. However, to allow unidirectional SRM to be stably imparted to a large-scale (e.g. $> 4000 \text{ km}^2$ for Areas 1 and 2; $> 30000 \text{ km}^2$ for Areas 5-8) geologic formation, the shock waves must pass through the rock when the entire region is at rest. Shock waves begin propagating through the rock instantly upon impact, yet at that moment the ejecta is still traveling at 2.0-2.4 km/s [Hood and Artemieva, 2008]. Therefore, the ejecta at the antipode will change orientation as it comes to rest, after any SRM has formed, such that the total

remanence of the ejecta deposit will be randomized and nulled. Hood and Artemieva (2008) also rule out SRM in the ejecta, using a different line of reasoning.

It is possible that the underlying rock could be shocked by the impacting ejecta and acquire a unidirectional SRM [*Hood and Artemieva, 2008*]. However, we suggest that there are two problems with this hypothesis. Firstly, one would expect nearly vertical local magnetization if the SRM producing field was compressed by solar wind plasma (see, for example, field lines in Figure 8-9, Hood and Artemieva, 2008). Instead, only one magnetic anomaly, area 4, has a nearly vertical magnetization, and the rest show a preference for low inclinations, if anything (the rest are at least $>33^\circ$ away from the vertical, Figure 4.20).

Secondly, deposition of impact ejecta would take place over a short period of time, over which the ambient field direction is likely to be nearly constant. There are only two basin antipodes within SPA, which implies that the magnetic anomalies should have one of two magnetization directions. Roughly, areas 1-3 (northwest cluster), 4, and 9 are antipodal to Imbrium, while areas 5-8 (eastern stripes), and 10 are antipodal to Serenitatis. First, we consider the five anomalies at the Imbrium antipode. Here we find that areas 1 and 3 have magnetization vectors 109° apart. The magnetization at area 4 is 85° from that at area 1 and 109° from area 3. The magnetization at area 9 (Mare Ingenii) is 76° from area 1, 40° from area 3, and 128° from area 4. All of these separations are well outside the error ellipses. The only two clusters are the directions of areas 1 and 2, and possibly area 3 with the second error minimum obtained at area 2 (here we do not include the extent of the error ellipse of

area 2, which just overlaps with area 9, since that error ellipse is affected by the existence of two error minima). In sum, there are at least four widely separated magnetization directions near the Imbrium antipode, all well separated by their error ellipses. It is plausible the similar directions at areas 1 and 2 suggest this pair was magnetized by deposition of impact ejecta, but it would not explain the magnetization of the other areas.

At the five anomalies at the Serenitatis antipode, areas 5, 7, and 10 have similar directions, as do areas 6 and 8, but the two groups are over $\sim 120^\circ$ apart, and well separated by error ellipses. Therefore, we conclude again that it is not likely that the Serenitatis impact is responsible for magnetizing all of these anomalies.

In sum, the diversity of directions argues against the SRM hypothesis, or at least allows only a subset of the geographically clustered anomalies to be due to SRM. Similar arguments can be applied to ruling out SRM from surface seismic waves. Considering all of the observations above, we conclude that at least some of the magnetic source bodies in SPA were magnetized in a lunar dynamo field, rather than a field associated with impact events.

4.5.3 Magnetized South Pole-Aitken basin ejecta or volcanic bodies?

[*Wieczorek et al.*, 2012] proposed that material from the SPA impactor impact might be the source of many of the SPA basin's magnetic anomalies, and even other anomalies across the Moon. Under this hypothesis, hot iron-enriched material from

the SPA impactor acquired a TRM in a dynamo field. However, if SPA ejecta landed hot and cooled in a dynamo field, the resulting anomalies should all have the same magnetization direction (but see section 4.5.3.4). Instead, the diverse magnetization directions (see section 4.5.1.2, above) suggest that they were magnetized at different epochs.

The last remaining viable hypothesis is that magnetic anomalies in the northern SPA basin formed as a result of magnetized sub-surface dikes [*Purucker et al.*, 2012]. Dikes forming over long time periods would permit different magnetization directions during different magnetic epochs. The cluster of three paleopoles close to the present pole (areas 5, 7 and 10, Figure 4.22a) would suggest a traditional axial-aligned dynamo magnetized these dikes when the Moon was in its present orientation. However, the diversity in paleopoles seen is still enigmatic (see Section 4.5.3). Further, if the dike hypothesis is true, this implies that the dikes near SPA are special in some way, since the nearside of the Moon, covered much more extensively by volcanism (and presumably associated with subsurface dikes), shows no magnetic structures like those at SPA. Andrews-Hanna et al. (2014) reported linear gravity-gradient anomalies that may be dikes, but so far, no obvious correlation between these structures and magnetic anomalies have been found. We note that Gong and Wieczorek (2016) find a correlation between magnetization and gravity anomalies in some locations.

4.5.4 Possible Explanations for Diverse Magnetic Field

Directions

The above arguments suggest the magnetizing fields for many of the SPA anomalies arose from a dynamo. However, they do not offer an obvious explanation for the diversity in field directions. Due to the small size of the lunar core, and the rapid decay of magnetic quadrupole and higher terms as a function of distance, it is likely that the ancient lunar dynamo was dominantly dipolar at the surface [Weiss and Tikoo, 2014]. If the dipole was aligned with the Moon's spin axis, the magnetization directions contain information about the Moon's paleopole. The diverse paleopoles in Figure 4.21 seem to imply large amounts of true polar wander [Goldreich and Toomre, 1969; Runcorn, 1983]. While the diversity in Figure 4.21 is surprising, in comparison with the results of [Arkani-Hamed and Boutin, 2014; Takahashi et al., 2014] (Figure 4.22a), the diversity of paleopoles seen in our findings is still greater. Below we consider some possible explanations for the diverse paleopole locations.

4.5.4.1 Non-axially aligned dipoles and impact-induced dynamos

Currently, our understanding of the nature of the lunar dynamo is limited. Paleomagnetic studies favor a dynamo that existed from approximately 4.2-3.6 Ga ago. Mechanisms for sustaining such a long-lived core dynamo are uncertain, with recent proposals for dynamos driven by mechanical stirring from impacts and precession [Dwyer et al., 2011; Le Bars et al., 2011; Weiss and Tikoo, 2014]. However, it is not known if these dynamos produce the same field organization as the

Earth's dynamo. It may be possible that these exotic dynamos exhibit more variable dipole axis directions, which could explain the diversity of paleopoles seen. Unfortunately, more work modeling small dynamos like that of the Moon is needed before evaluating this hypothesis further.

4.5.4.2 Secular Variation

Another possible origin for the diverse paleopole locations is geomagnetic secular variation of a dynamo that is on average aligned with the lunar spin axis. The Earth's spin axis is presently 11° away from its magnetic dipole axis, and it is plausible that the Moon's ancient dipole axis was also not exactly aligned with its spin axis. It is also possible that secular drift might be larger on a body with a small core such as the Moon. However, some of the paleopole locations at SPA are over $\sim 75^\circ$ apart (after accounting for the possibility of reversals, Figure 4.22a), and over the timescale of magnetic anomaly formation, the mean dipole orientation might average to be aligned with the spin axis. Presently, we have little information available about the lunar dynamo to further evaluate the role of secular variation in explaining the diversity of paleopole directions.

4.5.4.3 True Polar Wander over long timescales

The large amount of polar wander implied by the paleopoles is difficult to reconcile with other geophysical constraints for the orientation history of the Moon. Currently there are two comprehensive studies that derive estimates of the degree of polar wander on the Moon due to long-term changes in the Moon's moments of

inertia [Garrick-Bethell, 2016]. The first uses the shape and gravity of the Moon exterior to large basins to establish the earliest orientation of the Moon [Garrick-Bethell *et al.*, 2014b]. The authors find the present lunar pole has changed by $\sim 36^\circ$ from its earliest axis, but it does not coincide with any of the paleopole clusters we find (Figure 4.22a). The second study uses polar hydrogen deposits as a constraint on the history of polar wander, and infers that up to $\sim 10^\circ$ of paleolatitude change has occurred [Siegler *et al.*, 2016]. They infer large longitude changes, but they cannot produce the large paleopole changes implied by the anomalies studied here. In summary, the limited number of available geophysical models that estimate lunar polar wander cannot produce the diversity and large magnitude of paleopole changes required to explain our observations. Interestingly, we find that all of our paleopoles are $>35^\circ$ from the present equator (Figure 22a, accounting for reversals), which may be due to the difficulty in producing the large required changes in the Moon's moments of inertia.

4.5.4.4 True Polar Wander due to SPA formation

Very large initial changes in the Moon's moments of inertia due to SPA's crater might have produced large amounts of polar wander. Eventually, these changes must have subsided over millions to billions of years, since the gravity signature observed today is muted [Zuber *et al.*, 2013]. If hot material was cooling in the presence of a dynamo field throughout the Moon's reorientation, its magnetization could in principle capture multiple lunar orientations, thereby producing the diversity of paleopole locations. Some of this hot material could be iron-rich material from the

SPA impactor [Wieczorek *et al.*, 2012]. Following impact, the free precession damping time of the Moon is $\sim 2 \times 10^5$ years [Peale, 1976; Williams *et al.*, 2001], assuming a semimajor axis of 30 Earth radii, dissipation quality factor $Q = 50$ and degree-2 love number $k_2 = 0.1$ (which we assume to be representative of the Moon when SPA formed). The length scale for cooling in $\sim 2 \times 10^5$ years is ~ 3 km (assuming a thermal diffusivity of 10^{-6}), which is small compared to the scale of the anomalies we observe, but perhaps not so much as to preclude recording a measurable magnetization.

However, using a simple model for reorientation, we find that density anomalies produced by SPA's crater do not produce paleopoles that overlap with those of its magnetic anomalies. In our model, we replace SPA's gravity potential inside the outer topography rim with values between -3 times the maximum, and +2 times the maximum of the present day potential, in increments of 0.25 times the maximum potential. The inertia tensor and paleopoles were then calculated for each of these cases using the resulting globally calculated degree-2 spherical harmonics (cf. Garrick-Bethell *et al.*, 2014). These positive and negative gravity values represent very different models of SPA's effects, but illustrate the range of paleopoles that are possible. We find the maximum extent of true polar wander from SPA's formation passes close to the paleopoles from areas 7 and 10 (Figure 4.22a, the negative anomaly path approaches the center of SPA as the anomaly size grows, as expected). However, these anomalies are already close to the present pole, and do not need to be explained by polar wander. We do find that the extreme limits of polar wander

approach the error ellipses of areas 5 and 8, such that this process could plausibly explain some of these magnetic paleopoles. Unfortunately, the paleopoles from areas 1, 2, 3, 5, and 9, and to a lesser extent area 6, do not come close to the paleopoles produced by SPA. Thus, cooling of SPA ejecta deposits over short timescales ($\sim 10^5$ years), or even dikes that formed when the Moon resided at any of the SPA-produced paleopoles, cannot fully explain the observed diversity of magnetic paleopoles we find.

There are many unknowns in modeling the paleopoles allowed by SPA's formation. For example, reorientation and magnetic anomaly formation depends on the SPA impact's effect on dynamo operation [Arkani-Hamed and Olson, 2010a, 2010b], the inertia tensor of the Moon just before SPA formation and the length scale (and thereby cooling timescale) of the materials making up the anomalies. Furthermore, the spin vector of the Moon will be freely precessing around its angular momentum vector during over the damping timescale of reorientation. If the dynamo after SPA impact retained its alignment along the Moon's angular momentum vector, this precession could broaden the range of paleopoles permitted (essentially accessing a range of paleopoles around the paleopoles shown in Figure 4.22a, with the range depending on the precession angle). Therefore, we cannot definitively rule out polar wander processes as the origin for some of the diverse paleopole locations at SPA.

A variant of the hypothesis of iron-rich SPA ejecta [Wieczorek *et al.*, 2012] is the cooling of iron-rich “sesquinary” [Zahnle *et al.*, 2008] impactors formed by the SPA impact. Ejected into orbit immediately after impact, studies on various planetary

bodies show that these impactors can return to a body from 10^4 years [Nayak *et al.*, 2016b] to 10^6 years [Gladman *et al.*, 1995] post-impact, at approximately escape velocity [Nayak and Asphaug, 2016]. With reimpacts spread across this timescale, we propose that reaccreting iron-rich material originally from SPA, either still hot from the impact or heating upon re-impact, could record a diverse set of orientations as the Moon reorients in response to moment of inertia changes. Across this timescale, impact locations become random [Nayak *et al.*, 2016a]; such sesquinary magnetism caused by these iron-rich impactors would be widely distributed around the Moon.

4.6 Conclusion

Using two different inversion methods, we find diverse directions of magnetization among magnetic anomalies in the northern SPA basin. The diverse directions help rule out impact-related fields as their only origin. Intrusive bodies, such as the dikes proposed by [Purucker *et al.*, 2012], are a plausible explanation. The diverse paleopole locations could imply large amounts of true polar wander, but true polar wander inferred independently from gravity [Garick-Bethell *et al.*, 2014b] and hydrogen deposits [Sieglar *et al.*, 2016] implies more modest changes in the Moon's orientation. The diverse directions argue against the hypothesis that they all formed from iron-rich SPA ejecta that cooled in a dynamo field [Wieczorek *et al.*, 2012]. A simple gravity anomaly model for large amounts of SPA-produced reorientation fails to explain at least five of the paleopoles observed, but many unknowns remain in modeling this process. Some SPA ejecta may have produced

iron-rich sesquinary impactors that landed across the Moon and recorded orientation changes as they cooled in a dynamo field. A dynamo that was not aligned with the lunar spin axis remains a plausible explanation for all observations, but gaps remain in our ability confirm this hypothesis. The wide variety of viable hypotheses and large number of unknowns highlight the complexity of interpreting the origins of lunar magnetic anomalies and their paleopoles.

4.7 Figures

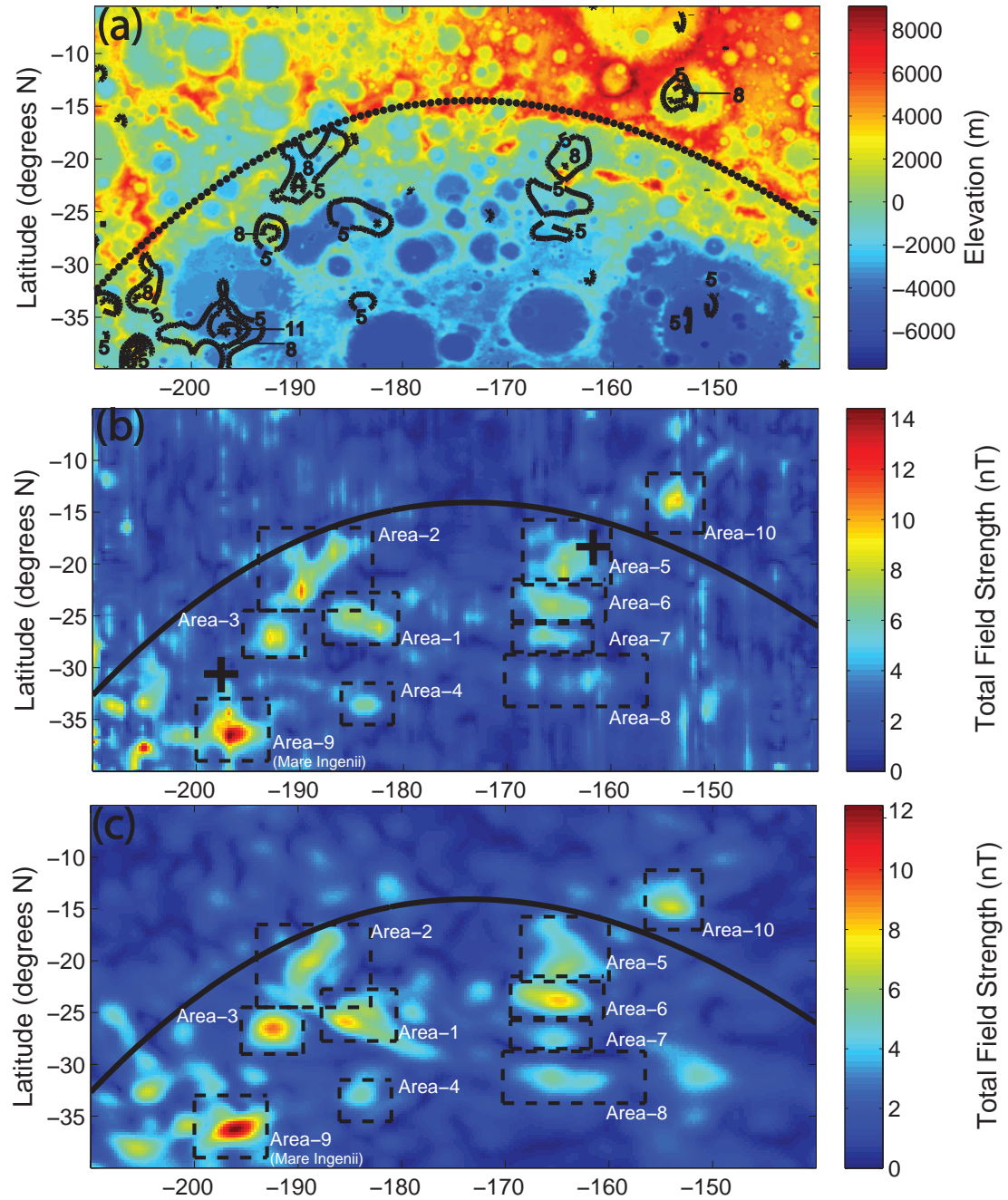


Figure 4.1. Lunar South Pole-Aitken basin study areas. The SPA rim is per Garrick-Bethell and Zuber (2009). (a) Magnetic contours superimposed over LOLA topography data (contours are taken from the map in part b). Contours shown are 5, 8 and 11 nT; (b) Magnetic field map with study areas highlighted (dashed black lines). Magnetic field data are from the Kaguya spacecraft magnetometer measurements taken on day 96 in 2009; at a mean altitude of 39.4 km. Black crosses indicate the location of the Imbrium (west) and Serenitatis (east) basin antipodes. (c) Magnetic field map taken from a spherical harmonic model [Purucker and Nicholas, 2010] for the

SPA region. Study areas are highlighted. We refer to areas 1-3 as the northwestern cluster, and areas 5-8 as the eastern stripes.

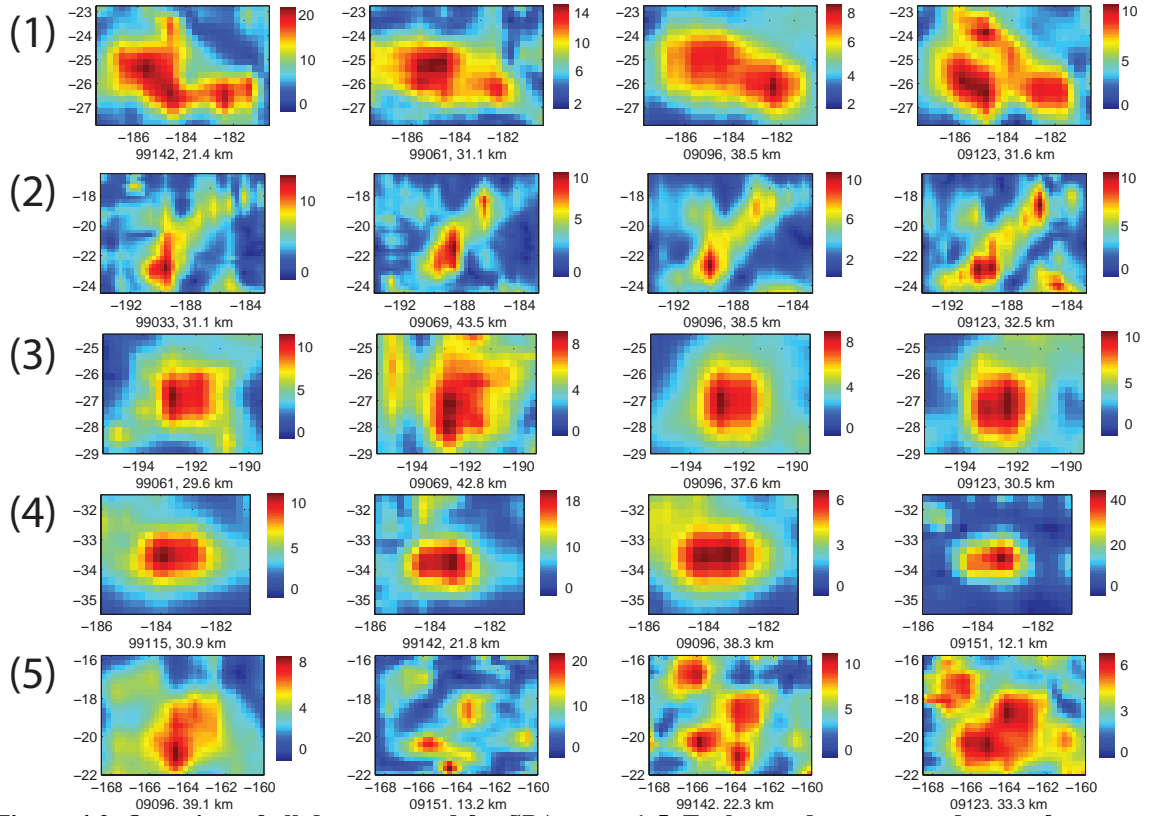


Figure 4.2. Overview of all datasets used for SPA areas 1-5. Each row denotes a study area from Figure 4.1. Mean measurement altitudes are shown. Data collection days may be read in the format YY-DDD, e.g., 09123 is 2009 day 123, and so on.

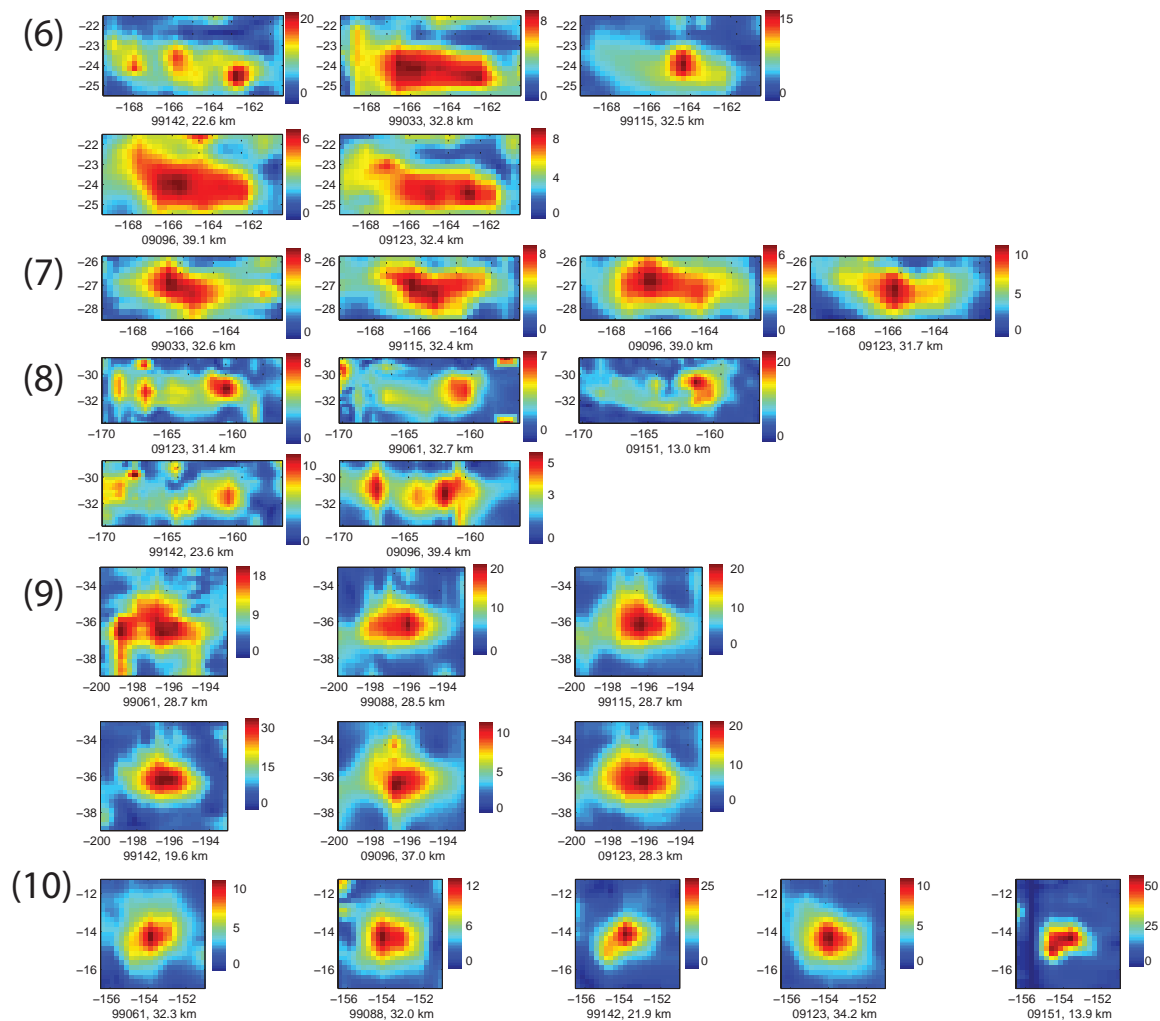


Figure 4.3. Overview of all datasets used for SPA areas 6-10. Each row denotes a study area from Figure 4.1. Mean measurement altitudes are shown. Data collection days may be read in the format YY-DDD, e.g., 09123 is 2009 day 123, and so on.

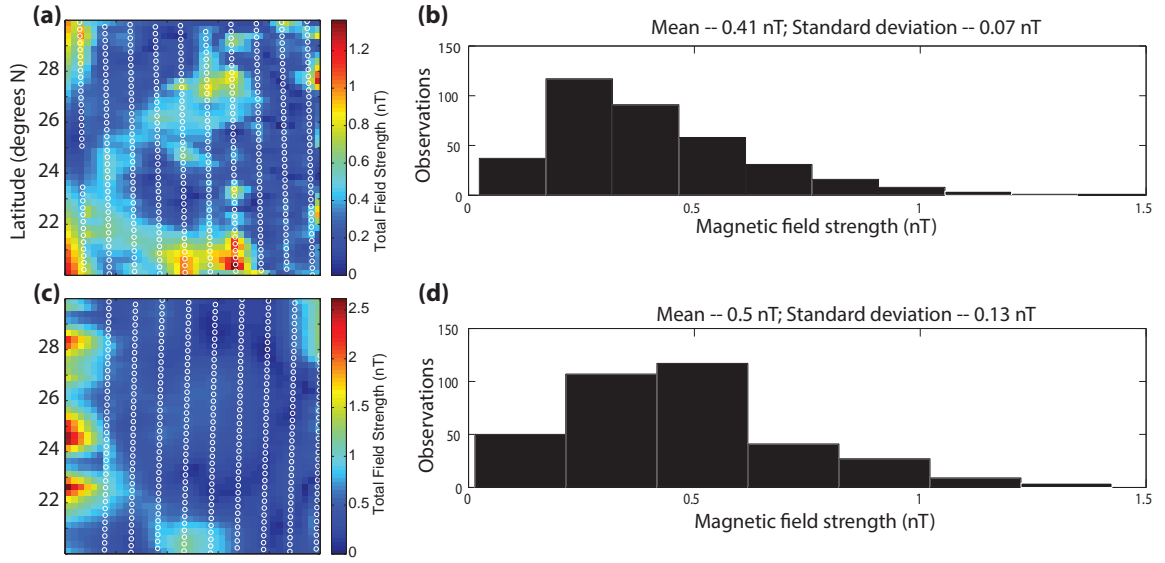


Figure 4.4. Magnetic field maps and histograms of field strengths for the Mare Imbrium region in the lunar wake. Panels (a) and (c) are magnetic field maps of Imbrium representing data from LP-MAG observation days 118 and 131 in 1999 respectively. White dots indicate observation locations. The mean observation altitude is 31.3 km for day 118 and 29.8 km for day 131. Panels (b) and (d) are corresponding histograms of the strength of the total magnetic field.

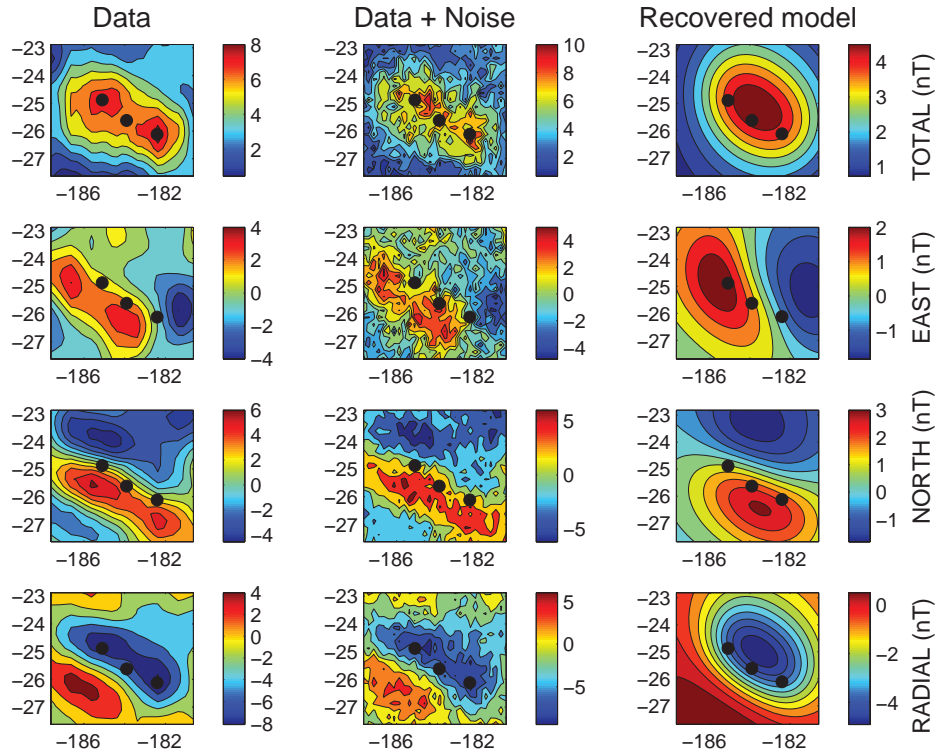


Figure 4.5. Error estimation due to time variable (non-crustal) magnetic fields. Kaguya magnetic field data for area 1, 2009 day 96 (left column), the effect of random noise with a standard deviation of 1 nT added to that data (middle column) and one of our Monte Carlo regressions for

the depth, moment and direction values for data + noise with the DD-CM algorithm (right column). Dipole source geometry is identical to the placement in Figure 4.8 (black dots).

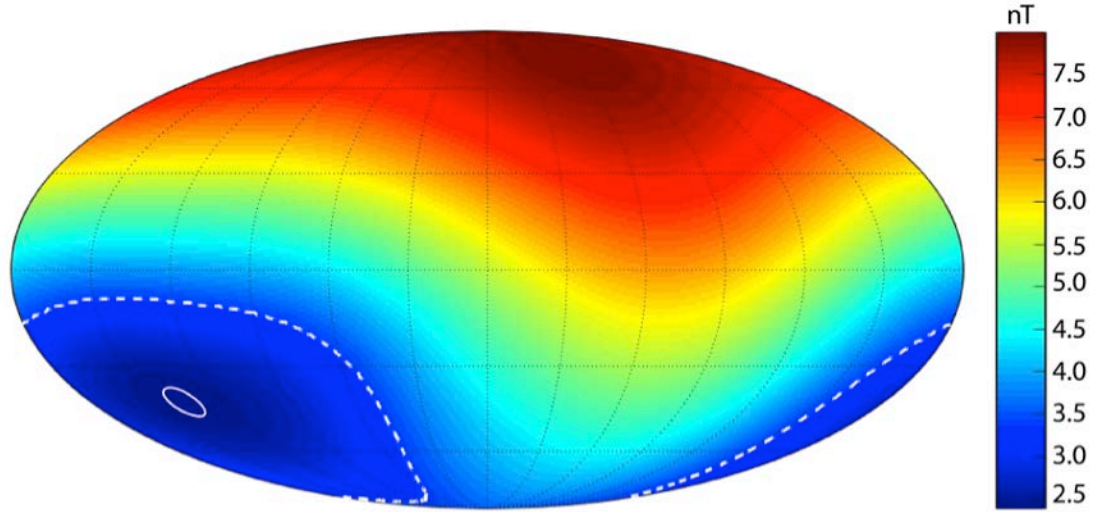


Figure 4.6. RMS error map for the magnetization direction for area 1, 2009 day 96, centered at 0° inclination and 0° declination (whole-sphere Mollweide projection, in which the southern hemisphere is positive inclination). The small white circular contour indicates one angular standard deviation of dispersion, from Monte Carlo simulations of the addition of 1 nT Gaussian noise to observations (Figure 4.5). The larger, outer white dashed contour indicates the minimum error solution plus 1 nT.

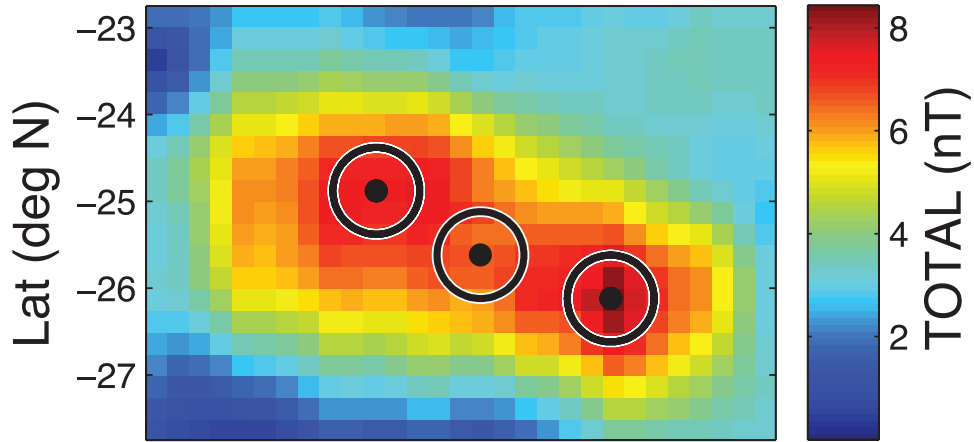


Figure 4.7. Error estimation due to uncertainty in source body geometry. Black points are the nominal dipole locations for a DD-CM regression at area 1. Circles represent the locations of dipoles placed randomly in our Monte Carlo error simulations and are 0.5° in radius. K-MAG total field observations in the lunar wake on 2009 day 96. Compare to Figure 4.8.

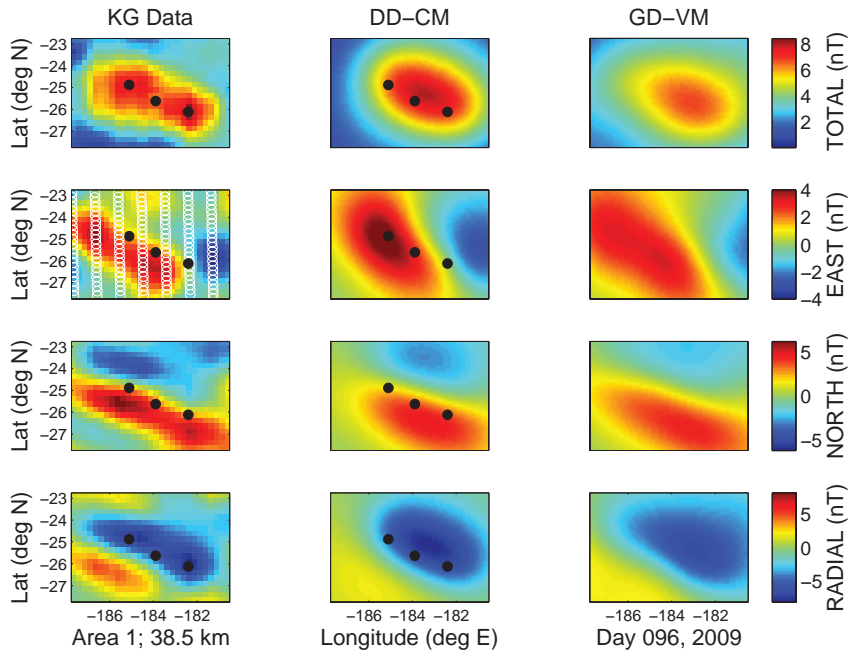


Figure 4.8. Area 1 best fit results for both inversion algorithms. (Left column) K-MAG observations in the lunar wake on 2009 day 96, compared to (Middle column) a grid-based model with variable magnetizations (GD-VM) and (Right column) a model with manually placed dipoles of equal magnetization (DD-CM). Source dipoles in the DD-CM algorithm are approximately located at maxima in the observed total field (black dots). White dots in the east, north and radial panels are locations of spacecraft magnetometer measurements. The mean measurement altitude is shown in Figure 4.2.

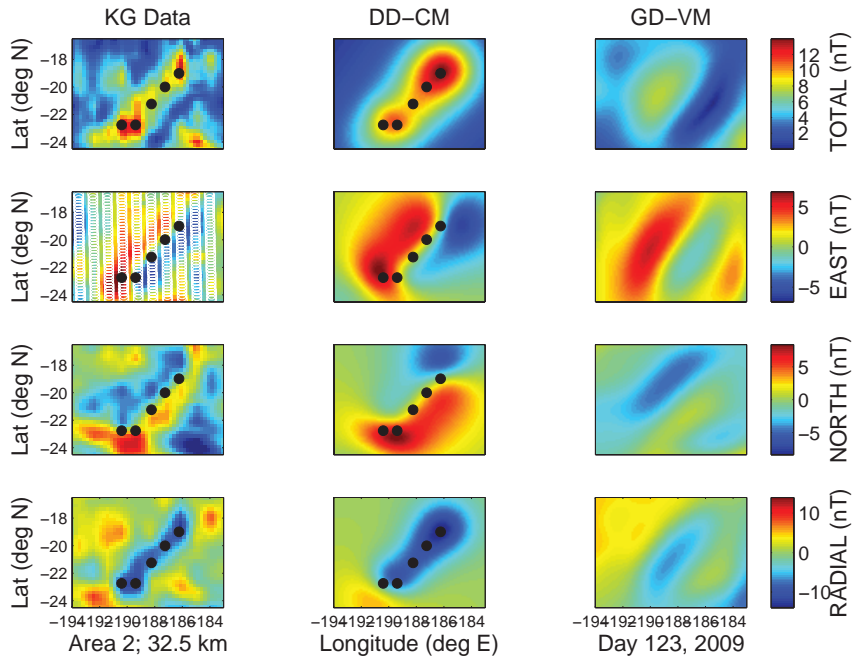


Figure 4.9. Area 2 best fit results with both inversion algorithms. Figure details are as in Figure 4.8, except that magnetometer measurements are taken from K-MAG, 2009 day 123.

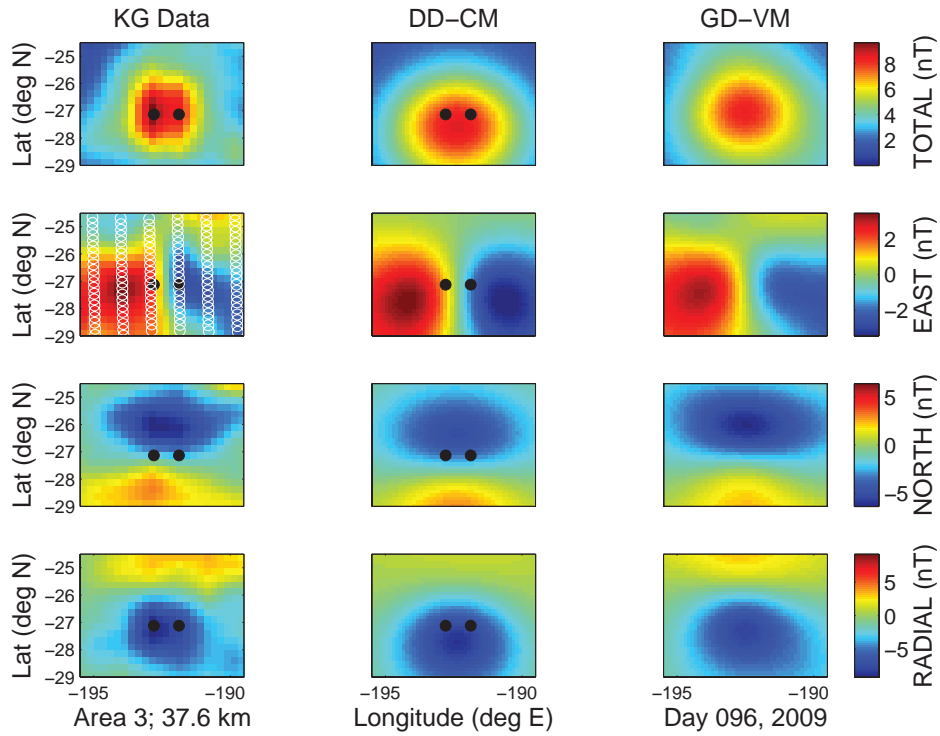


Figure 4.10. Area 3 best fit results with both inversion algorithms. Figure details as in Figure 4.9.

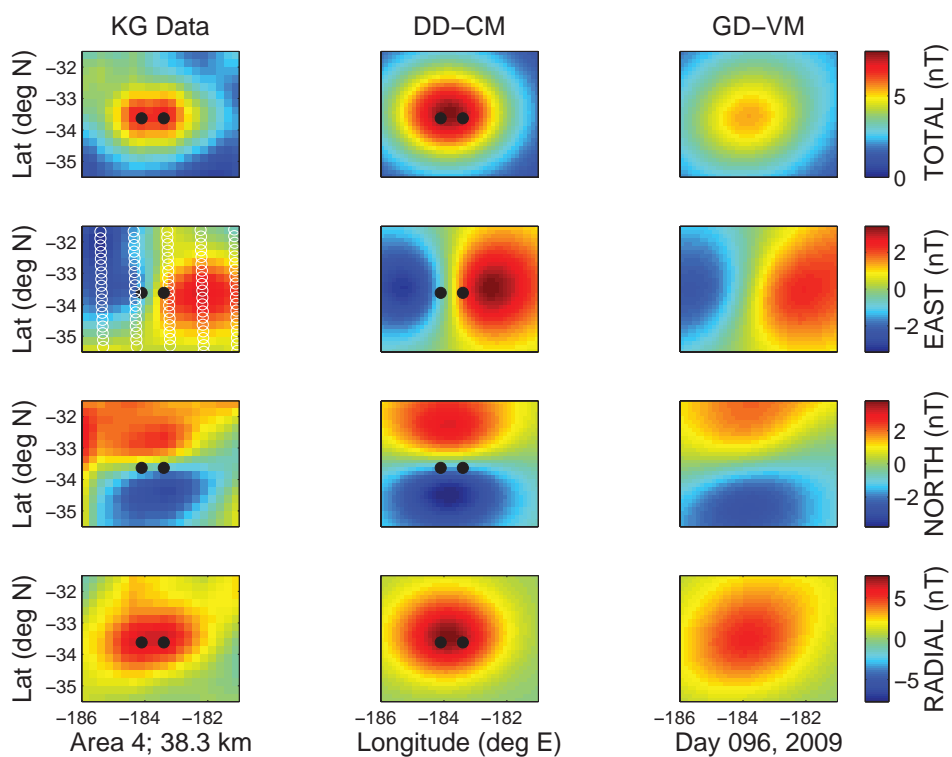


Figure 4.11. Area 4 best fit results with both inversion algorithms. Figure details as in Figure 4.8.

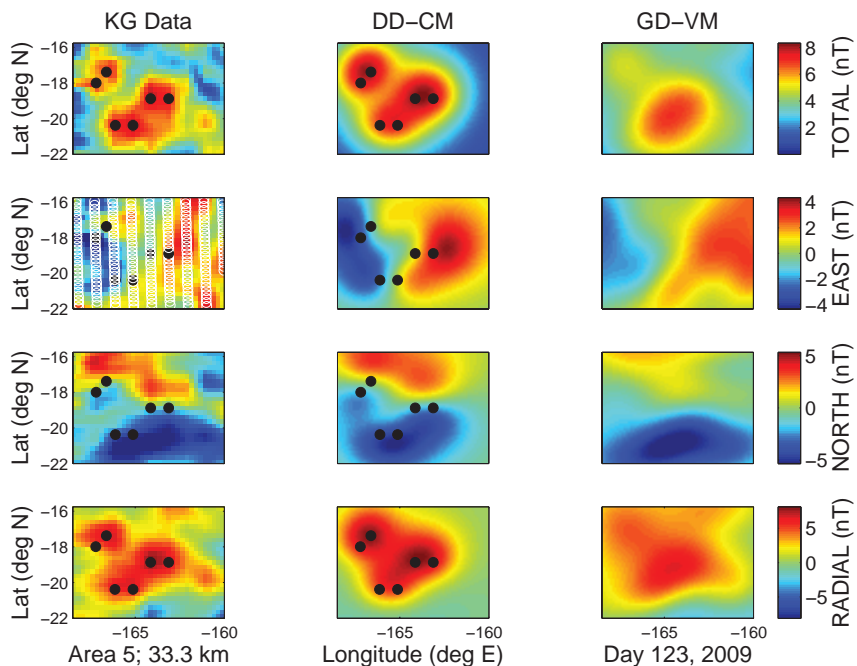


Figure 4.12. Area 5 best fit results with both inversion algorithms. Figure details as in Figure 4.9.

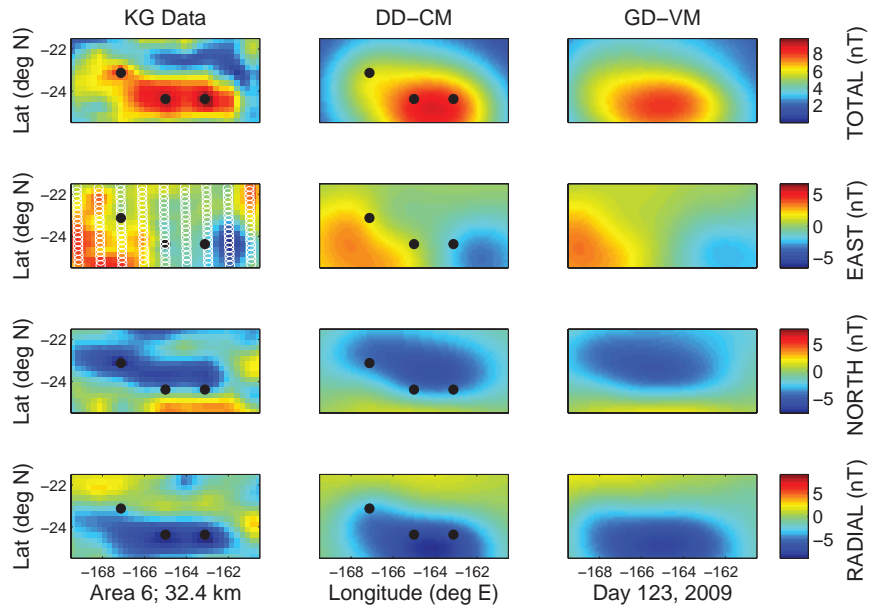


Figure 4.13. Area 6 best fit results with both inversion algorithms. Figure details as in Figure 4.9.

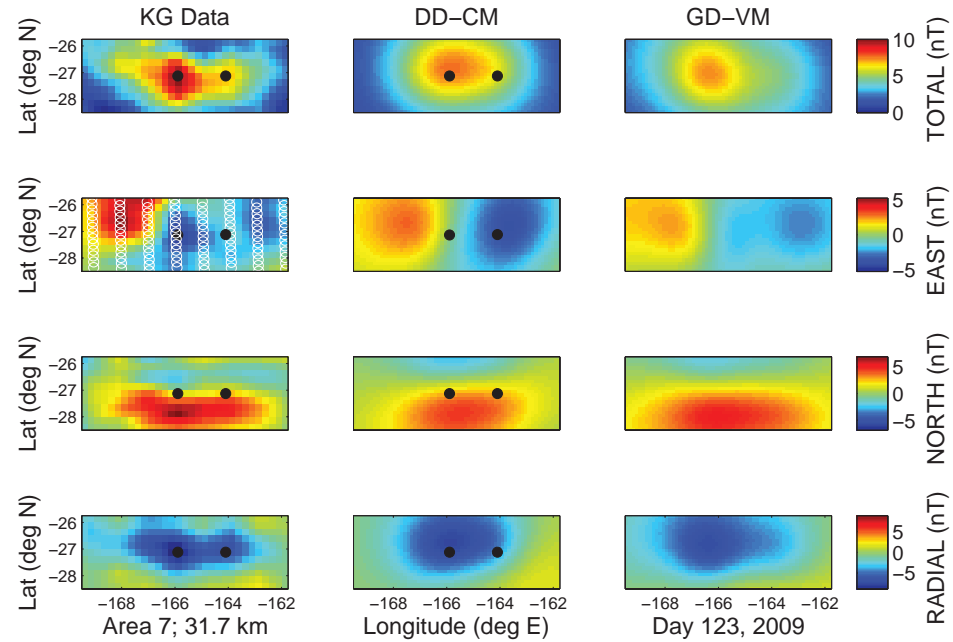


Figure 4.14. Area 7 best fit results with both inversion algorithms. Figure details as in Figure 4.9.

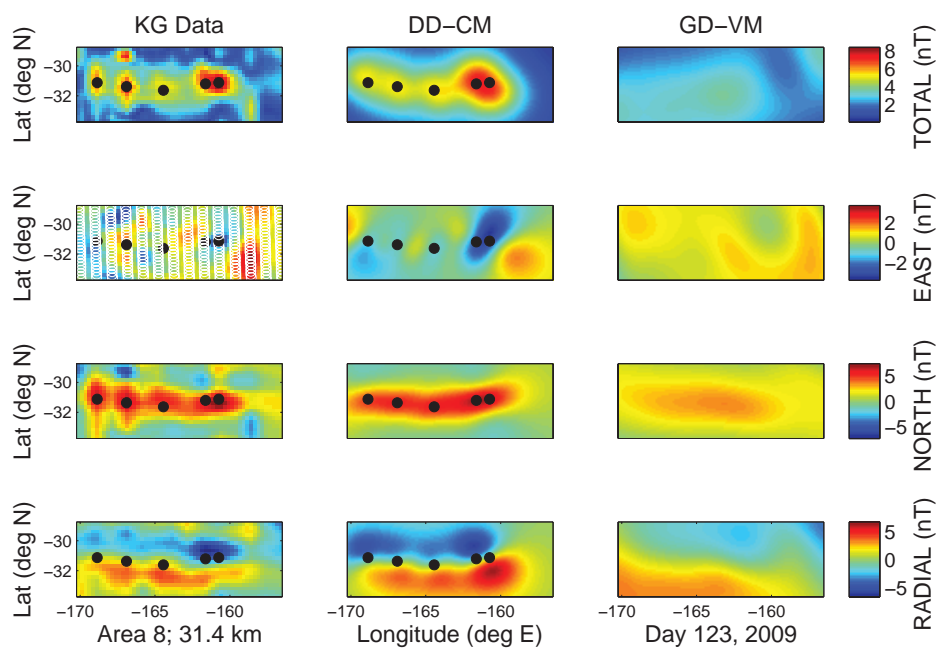


Figure 4.15. Area 8 best fit results with both inversion algorithms. Figure details as in Figure 4.9.

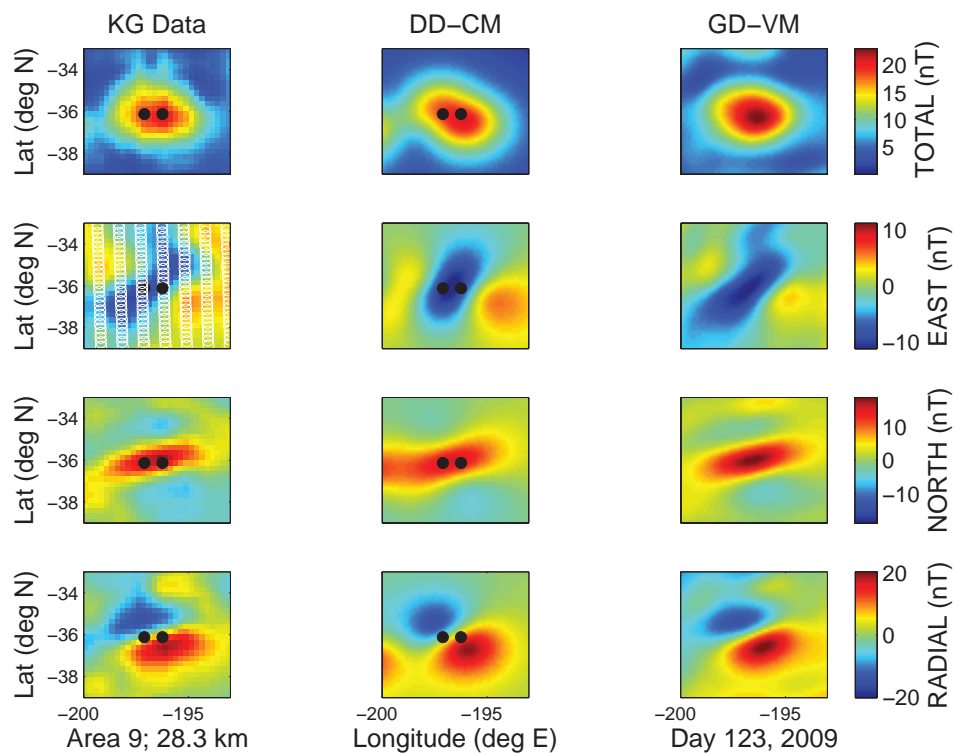


Figure 4.16. Area 9 best fit results with both inversion algorithms. Figure details as in Figure 4.9.

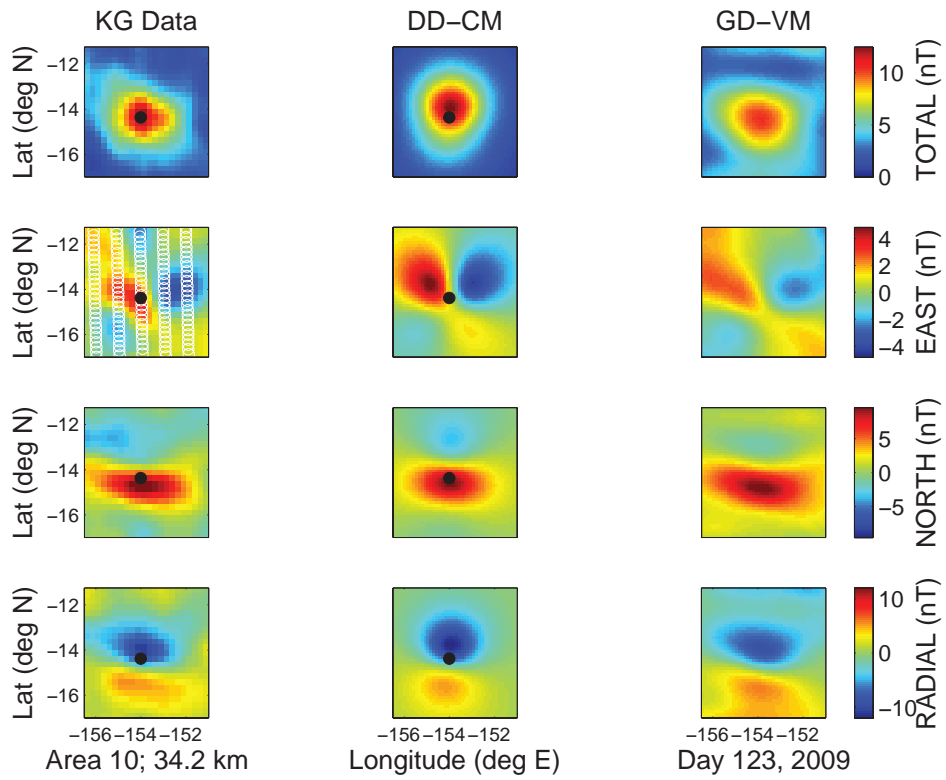


Figure 4.17. Area 10 best fit results with both inversion algorithms. Figure details as in Figure 4.9.

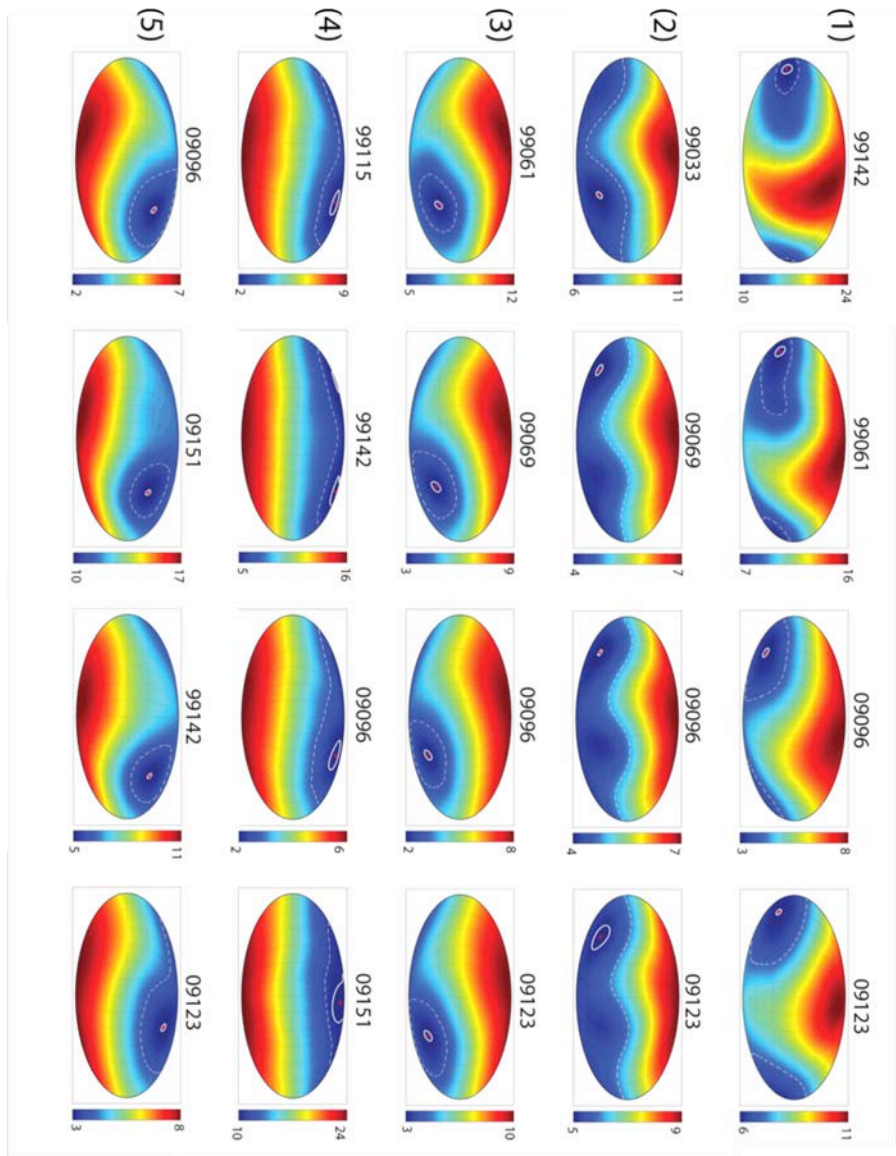


Figure 4.18. RMS error map for the magnetization direction for all datasets for SPA study areas 1-5, obtained using the DD-CM algorithm. Southern hemisphere is positive inclination; the whole-sphere Mollweide projection is centered at 0° inclination and 0° declination. The solid white circular contour indicates one angular standard deviation of dispersion from the best-fit solution (red star, Table 4.1), from Monte Carlo simulations of the addition of 1 nT Gaussian noise to observations in the DD-CM algorithm. The larger, dashed white contour indicates the minimum error solution plus 1 nT, a measure of uncertainty using an arbitrary threshold defined by the measurement uncertainty (not used in our final analysis). The error from Monte Carlo simulations of the effects displacing the nominal dipoles by 0.5° is not shown, and nor is the 95% confidence interval from using different altitude data sets.

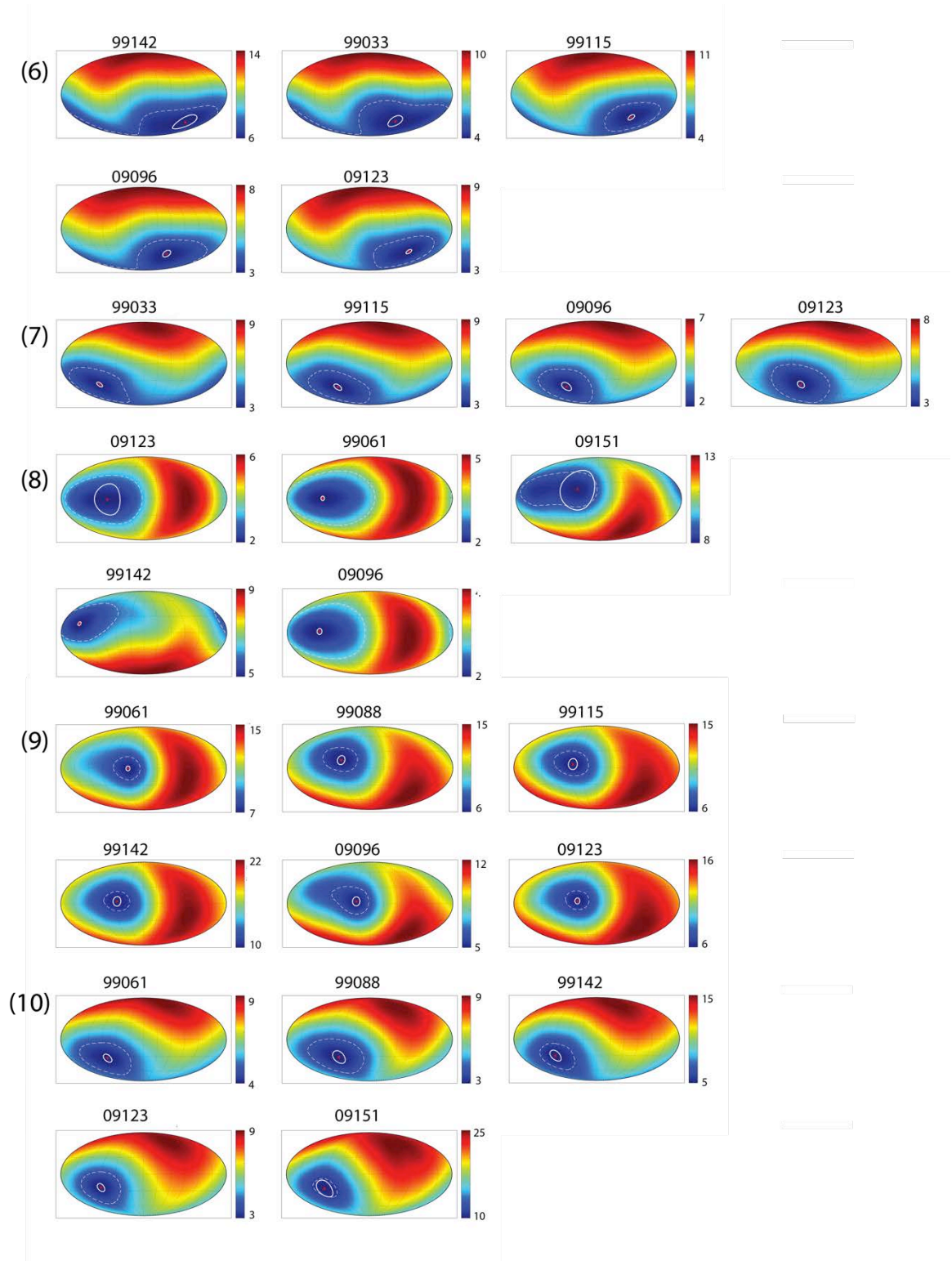


Figure 4.19. RMS error map for the magnetization direction for all datasets for SPA study areas 6-10, obtained using the DD-CM algorithm. Description is as in Figure 4.18.

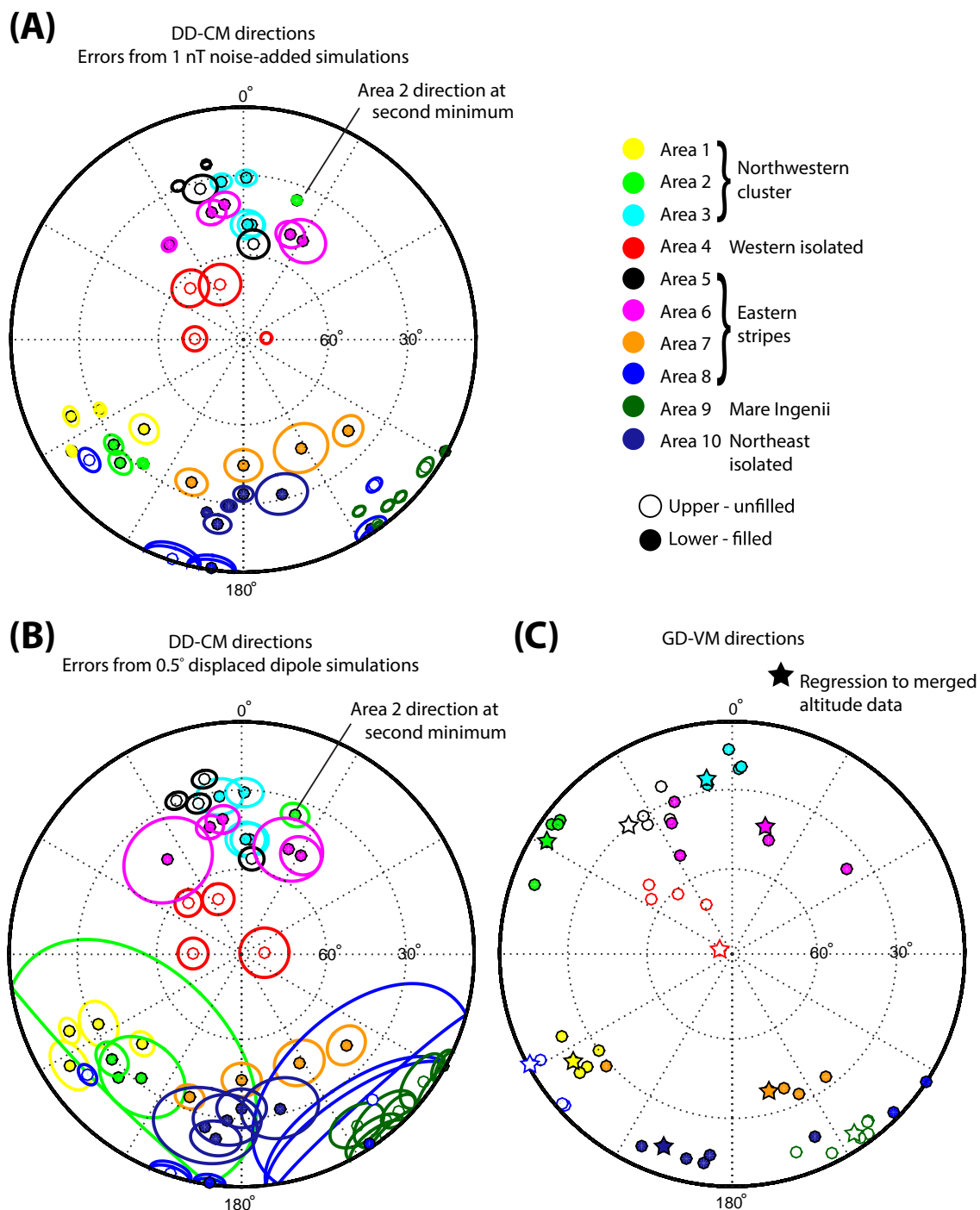


Figure 4.20. Best-fit magnetization directions for study areas defined in Figure 1, for all datasets in Figure 4.2 and Figure 4.3. Directions derived from different altitudes and different spacecraft at the same study area are represented by the same color. Positive inclinations are in the lower

hemisphere (filled circles). (A & B) Results for the DD-CM algorithm. Ellipses in A represent one standard deviation of dispersion from 1 nT noise simulations. Ellipses in B represent one standard deviation of dispersion from simulations of displaced dipoles (0.5°). (C) Results from the GD-VM algorithm, including results from regressions to merging data at all altitudes shown in Figure 4.2 and Figure 4.3, within a given study area (stars).

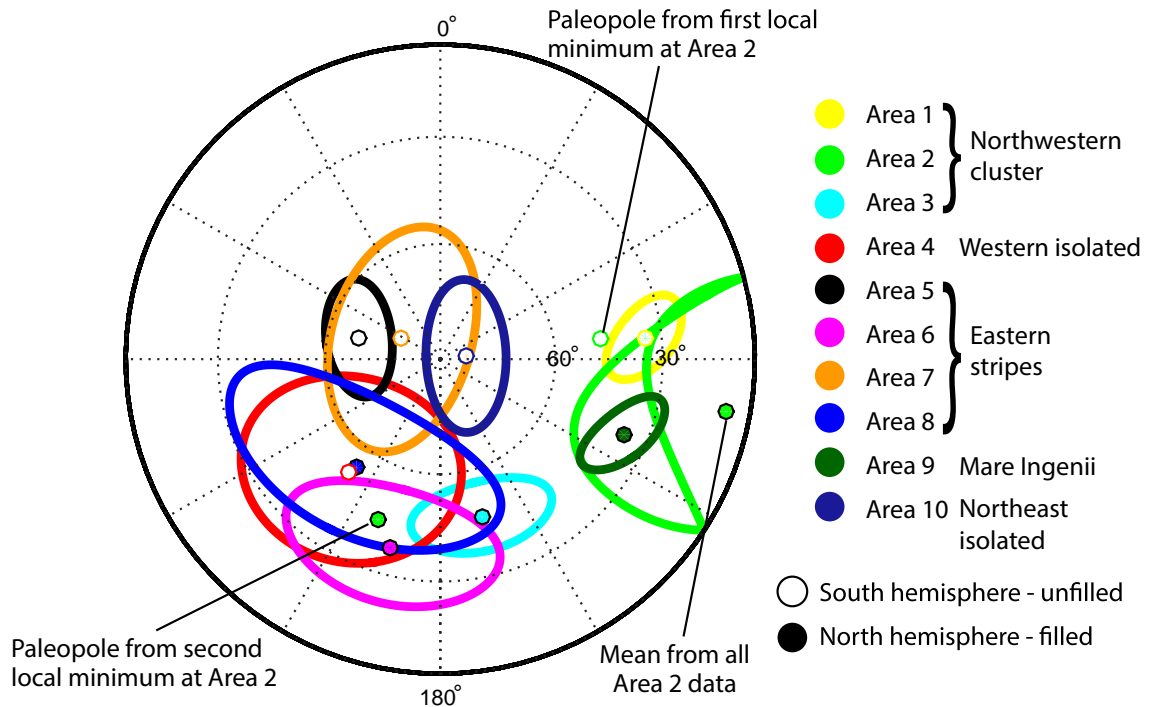


Figure 4.21. SPA magnetic paleopoles. Paleopoles are the mean of the combined results from the DD-CM and GD-VM algorithms, at all directions (altitudes) shown in Figure 4.20. Ellipses represent the 95% confidence interval obtained when calculating the mean direction from the combined DD-CM and GD-VM results, plus the mean of the standard-deviation ellipses in Figure 4.20a, plus the mean of the standard-deviation ellipses in Figure 4.20b (calculated using the Fisher precision parameters k for each). Error ellipses are not calculated for the two different minimum error solutions for area 2 from the DD-CM algorithm.

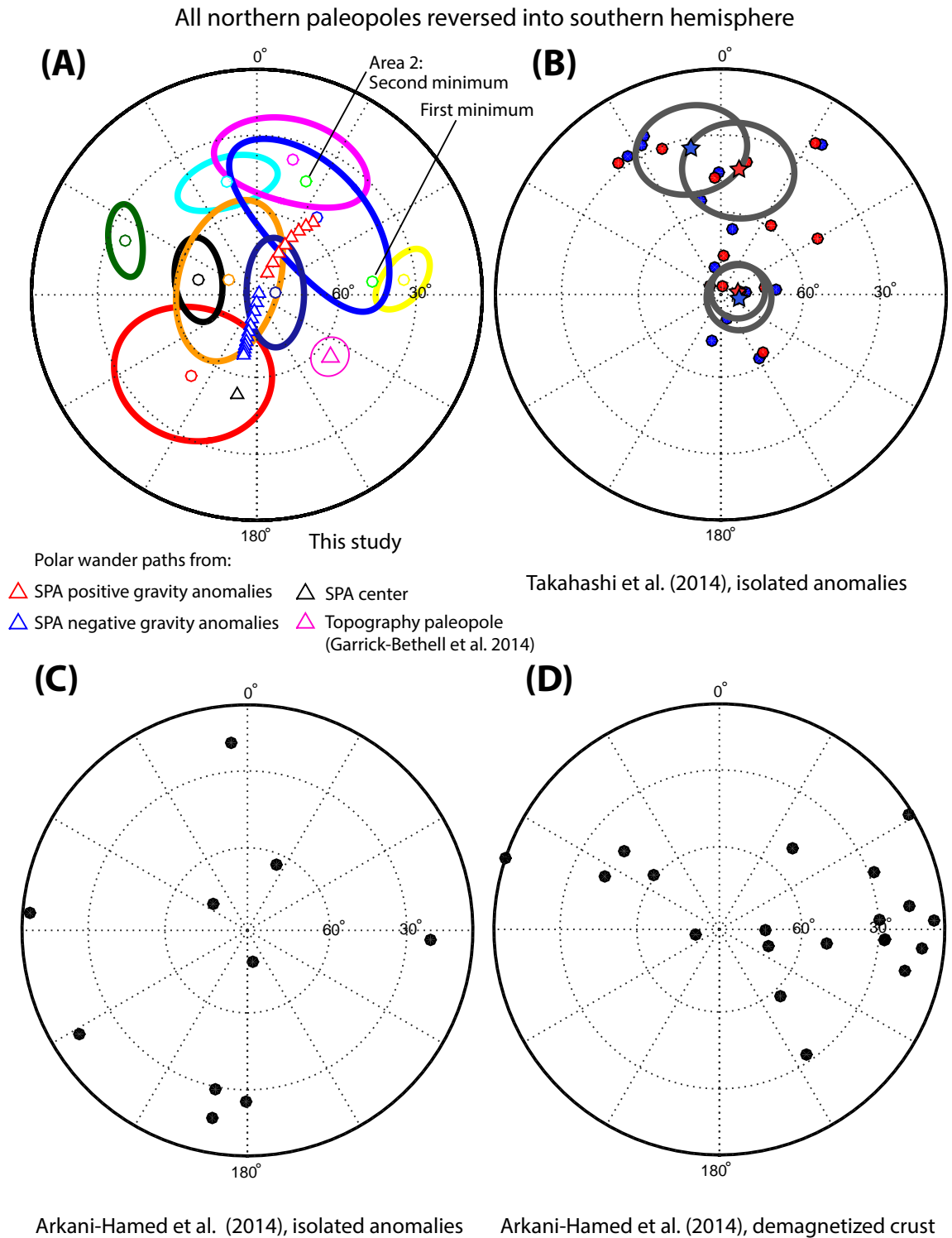


Figure 4.22. Paleopoles from SPA anomalies compared with other published paleopoles from other anomalies. Both figures show the southern hemisphere (all points are southern latitudes). (A) Our results from Figure 4.20, with all northern poles reversed into the southern hemisphere. The mean paleopole obtained from all data at area 2 (see Figure 4.21) has been omitted in this

figure. Red and blue triangles are possible paleopoles for SPA immediately after its formation, assuming an extreme range of density anomaly models; red (blue) points are positive (negative) density anomalies (see Section 4.5.3.4). SPA's center (a limiting paleopole for very negative density models of SPA) is at (-53.2° S, 191° E) (black triangle). The magenta triangle shows the paleopole derived from the tidal component of the Moon's topography, outside of large basins [Garrick-Bethell *et al.*, 2014a]. (B) Paleopoles from the 11 anomalies reported by [Takahashi *et al.*, 2014]. No anomalies are within SPA. Blue (red) points represent inversions from Kaguya (Lunar Prospector) data. In most cases, multiple points represent paleopoles from single sites. Stars represent the means of the two clusters. (C) Paleopoles from 10 isolated anomalies reported by Arkani-Hamed and Boutin (2014). (D) Paleopoles from the crust at 20 impact craters reported by Arkani-Hamed and Boutin (2014).

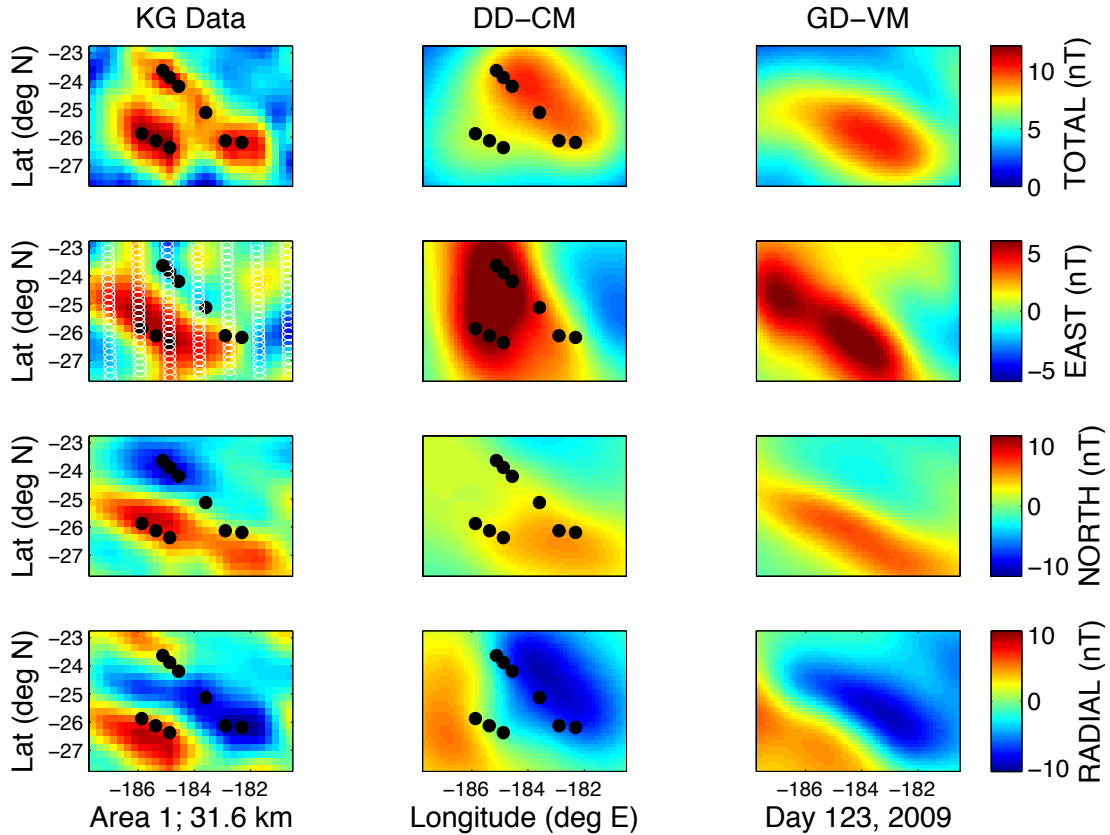


Figure 4.23. Area 1 best fit results, day 123, 2009. Figure details as in Figure 4.9.

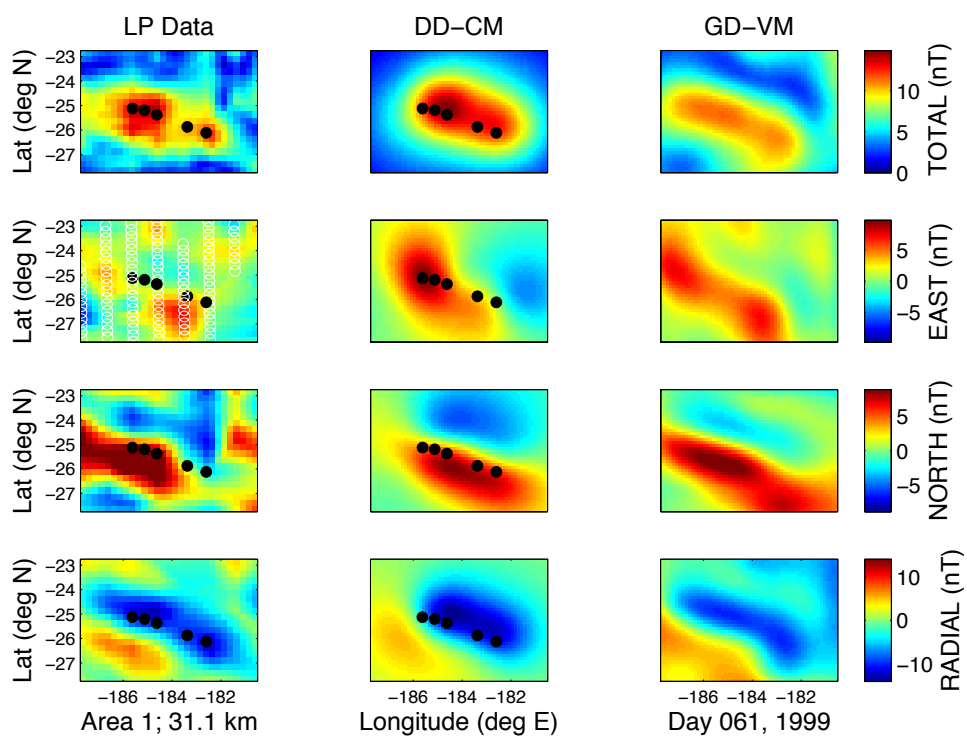


Figure 4.24. Area 1 best fit results, day 61, 1999. Figure details as in Figure 4.9.

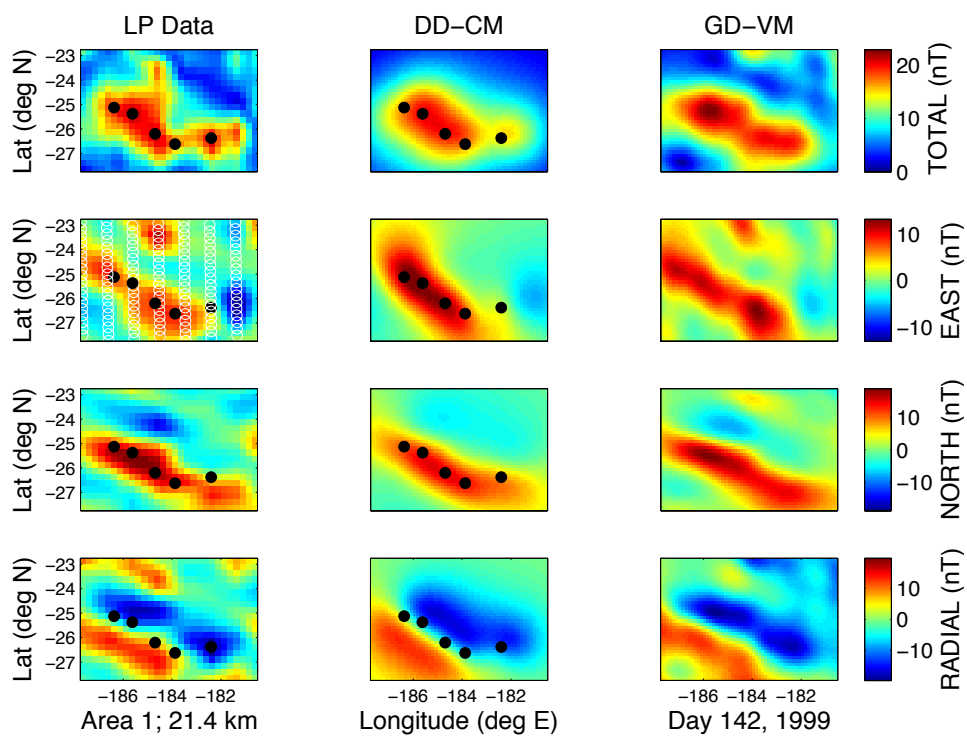
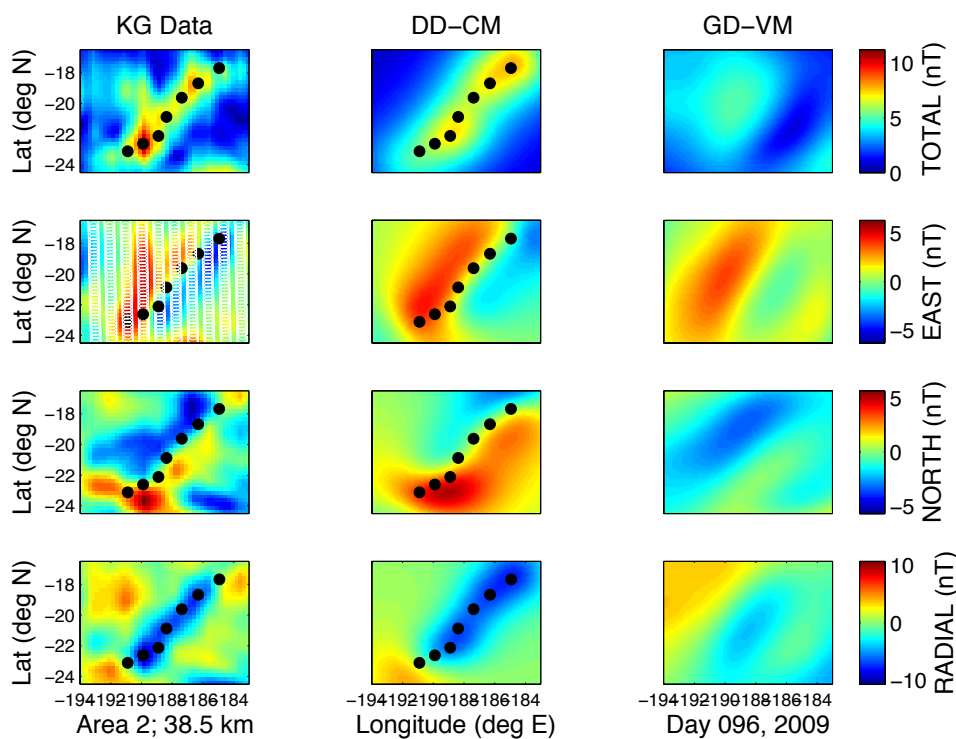
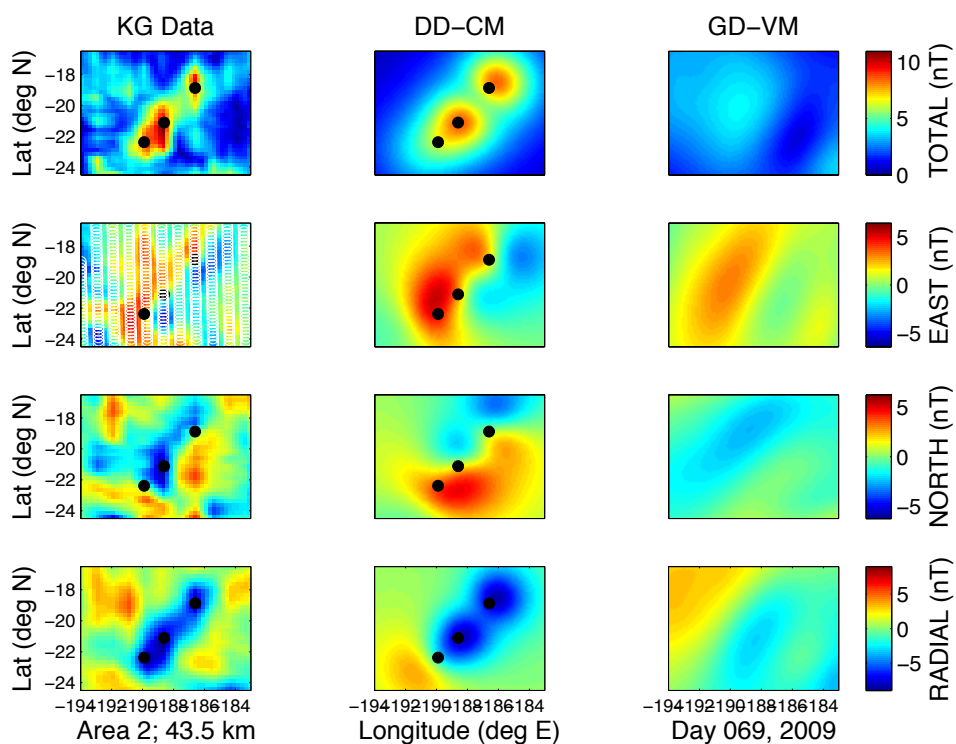


Figure 4.25. Area 1 best fit results, day 142, 1999. Figure details as in Figure 4.9.



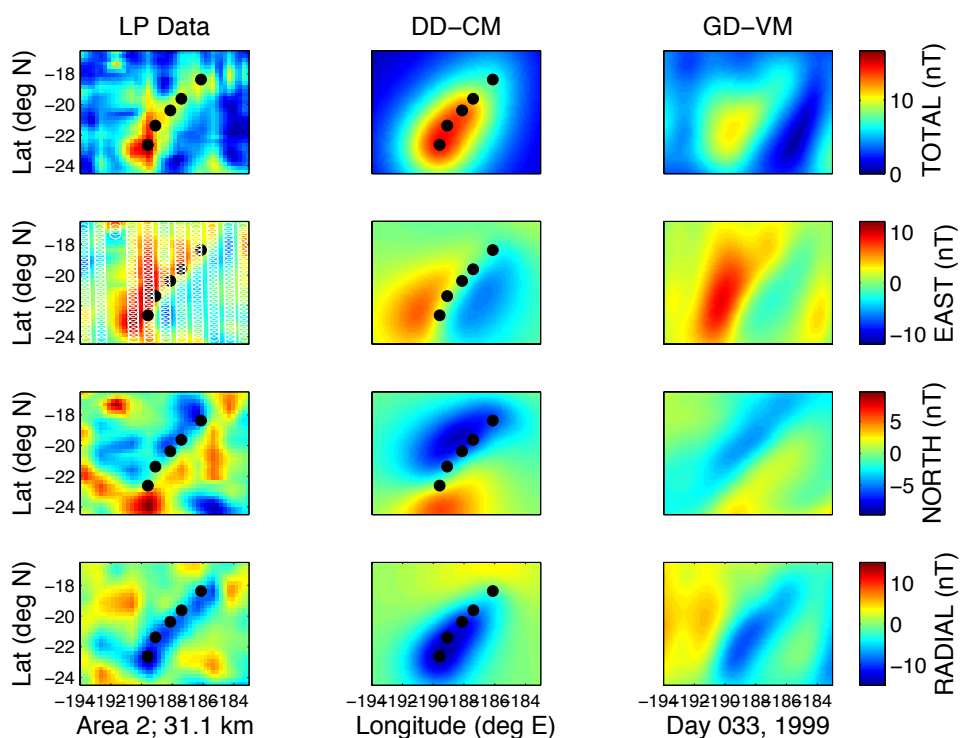


Figure 4.28. Area 2 best fit results, day 33, 1999. Figure details as in Figure 4.9.

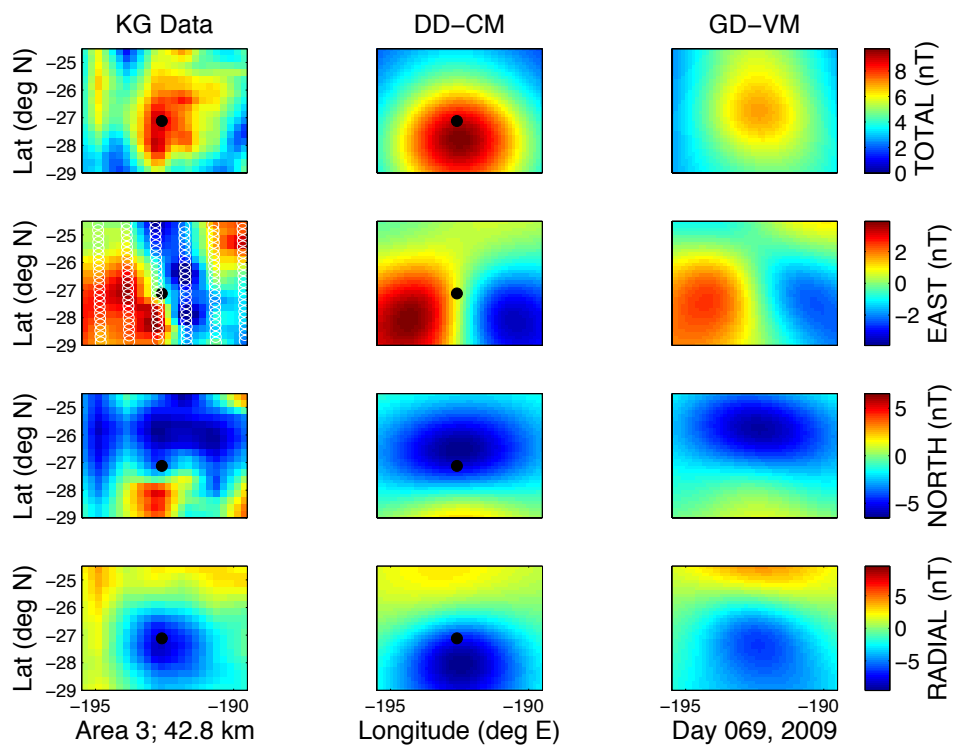


Figure 4.29. Area 3 best fit results, day 69, 2009. Figure details as in Figure 4.9.

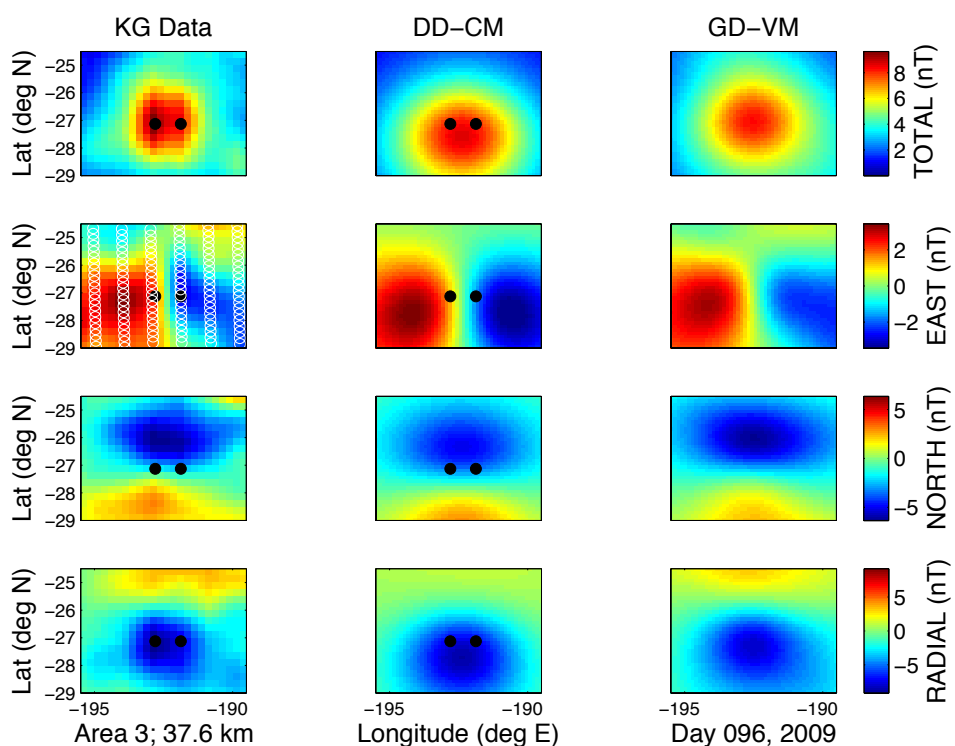


Figure 4.30. Area 3 best fit results, day 96, 2009. Figure details as in Figure 4.9.

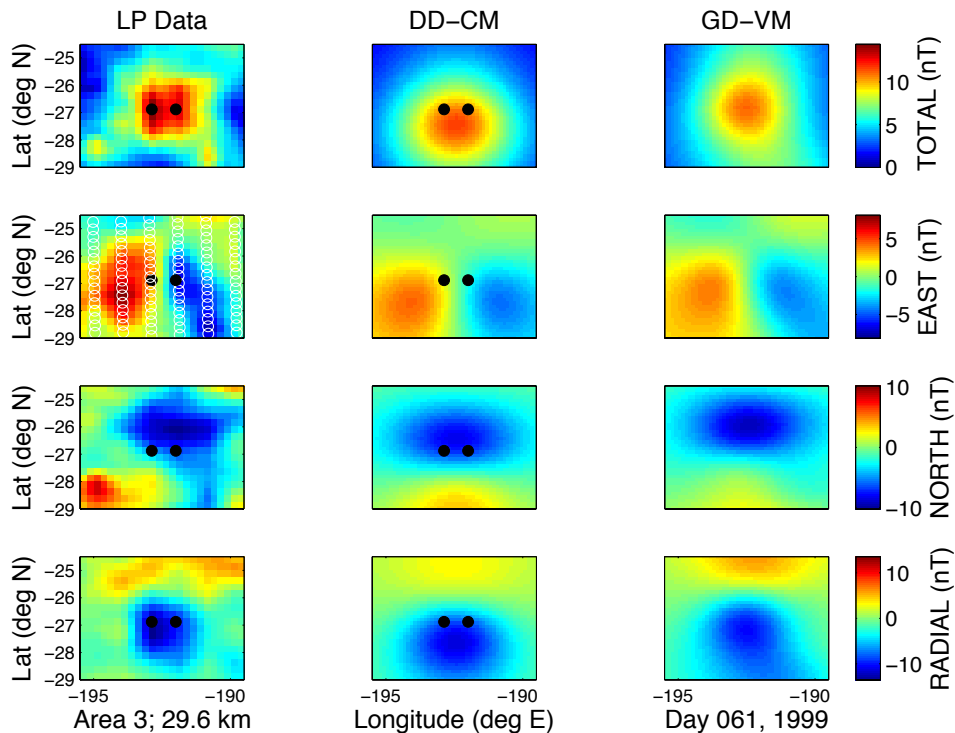


Figure 4.31. Area 3 best fit results, day 61, 1999. Figure details as in Figure 4.9.

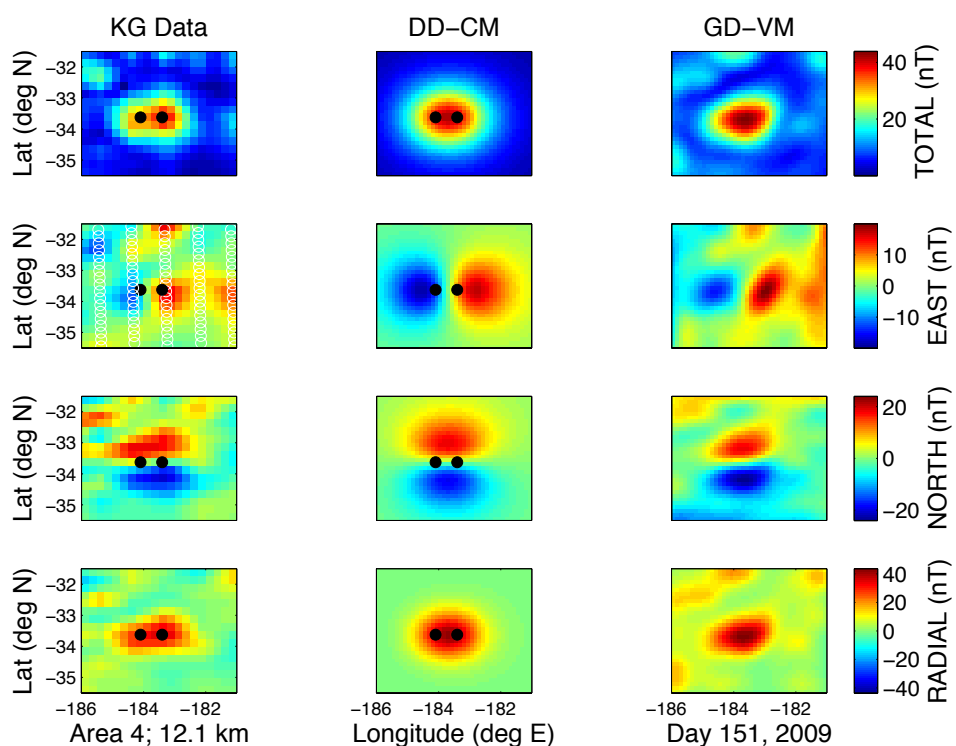


Figure 4.32. Area 4 best fit results, day 151, 2009. Figure details as in Figure 4.9.

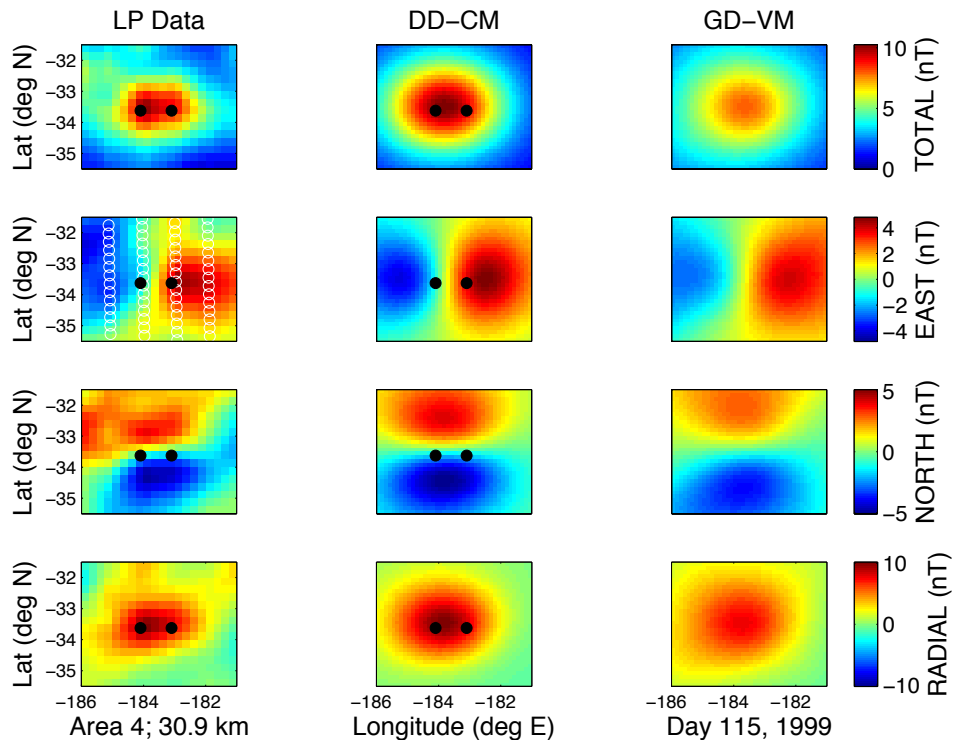


Figure 4.33. Area 4 best fit results, day 115, 1999. Figure details as in Figure 4.9.

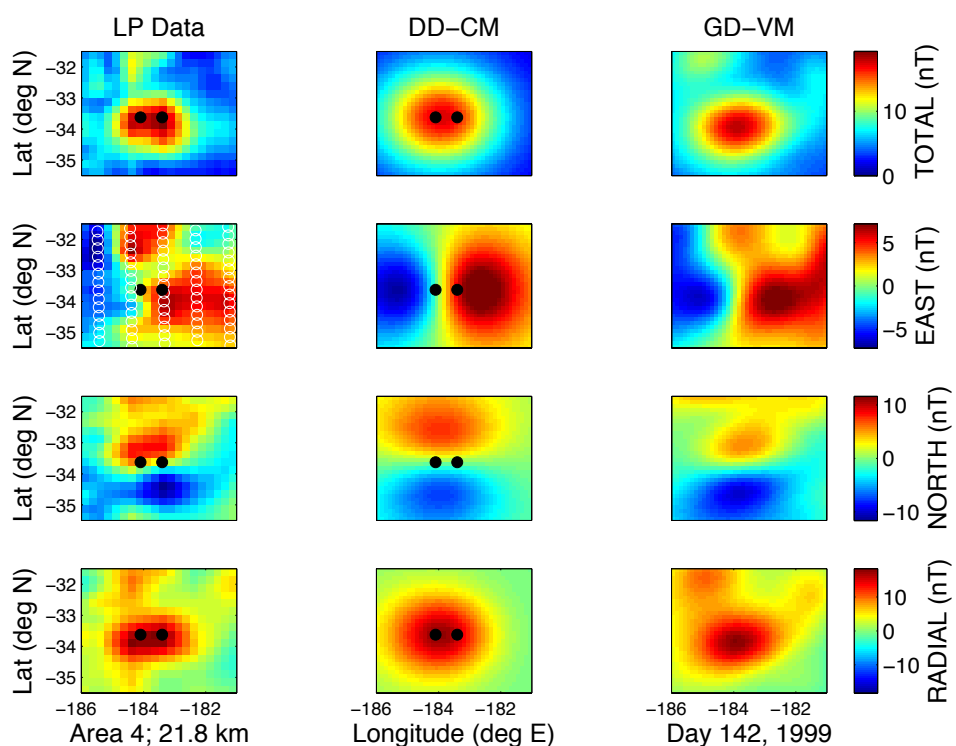


Figure 4.34. Area 4 best fit results, day 142, 1999. Figure details as in Figure 4.9.

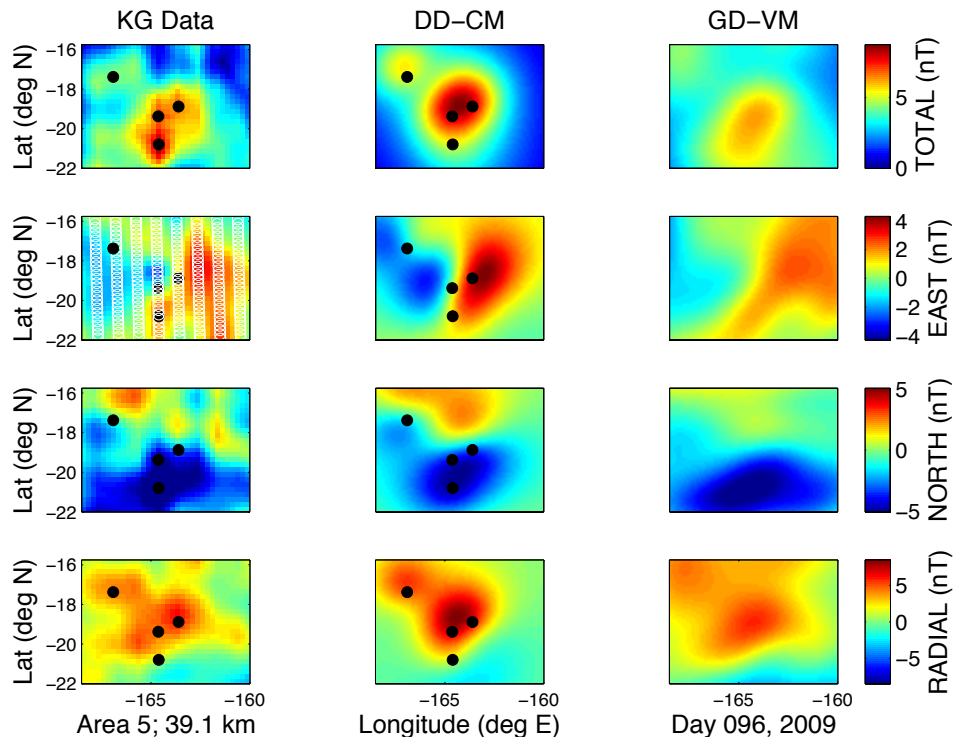


Figure 4.35. Area 5 best fit results, day 96, 2009. Figure details as in Figure 4.9.

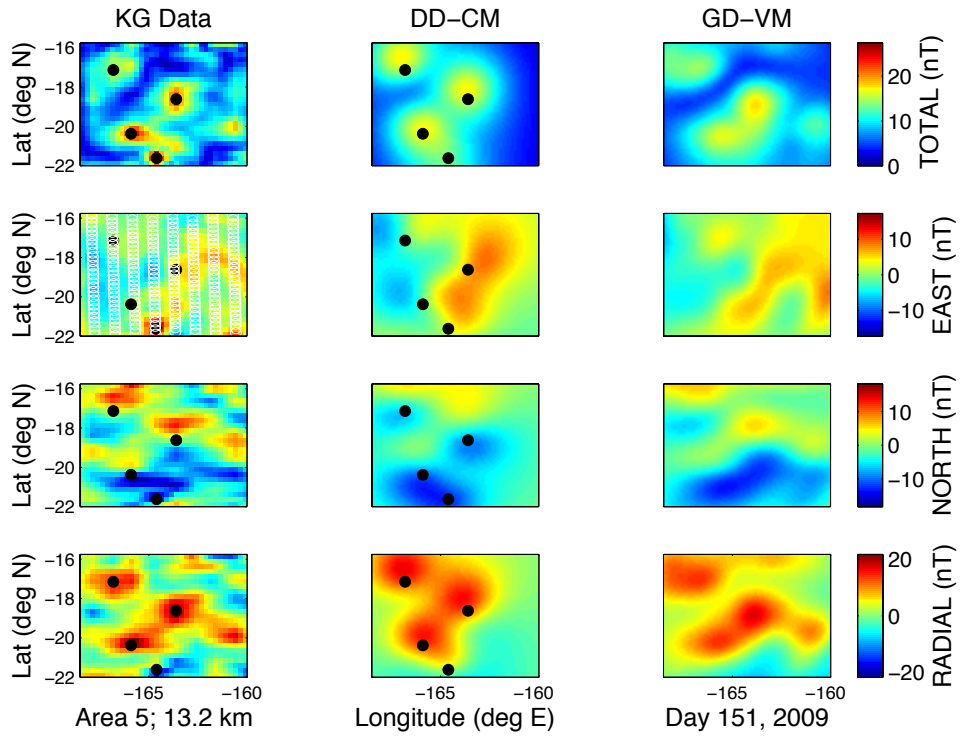


Figure 4.36. Area 5 best fit results, day 151, 2009. Figure details as in Figure 4.9.

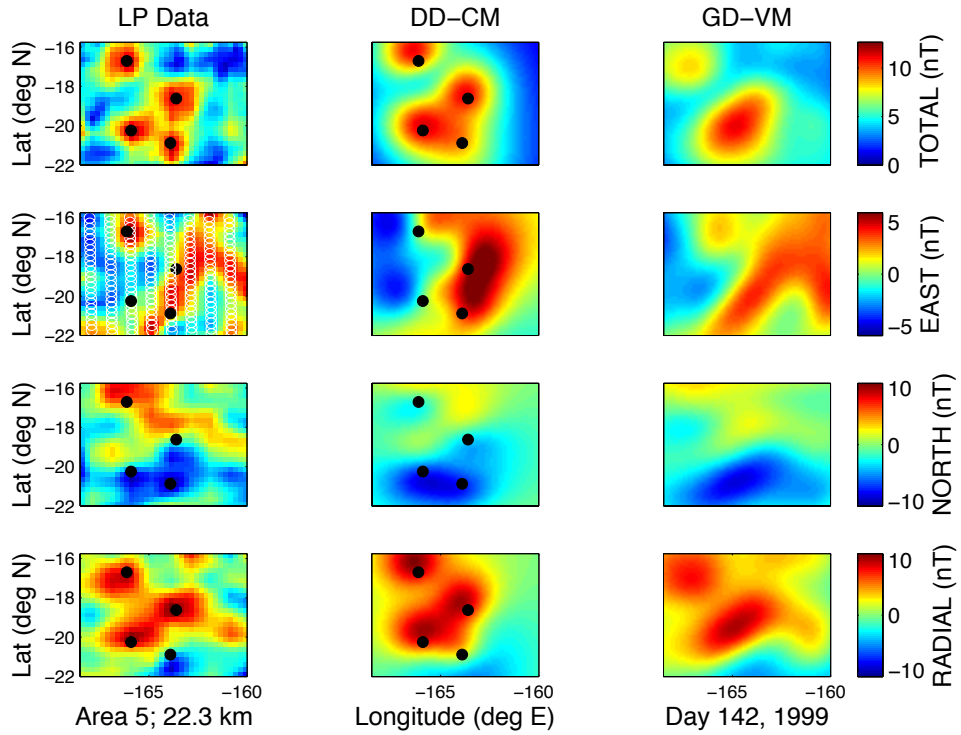


Figure 4.37. Area 5 best fit results, day 142, 1999. Figure details as in Figure 4.9.

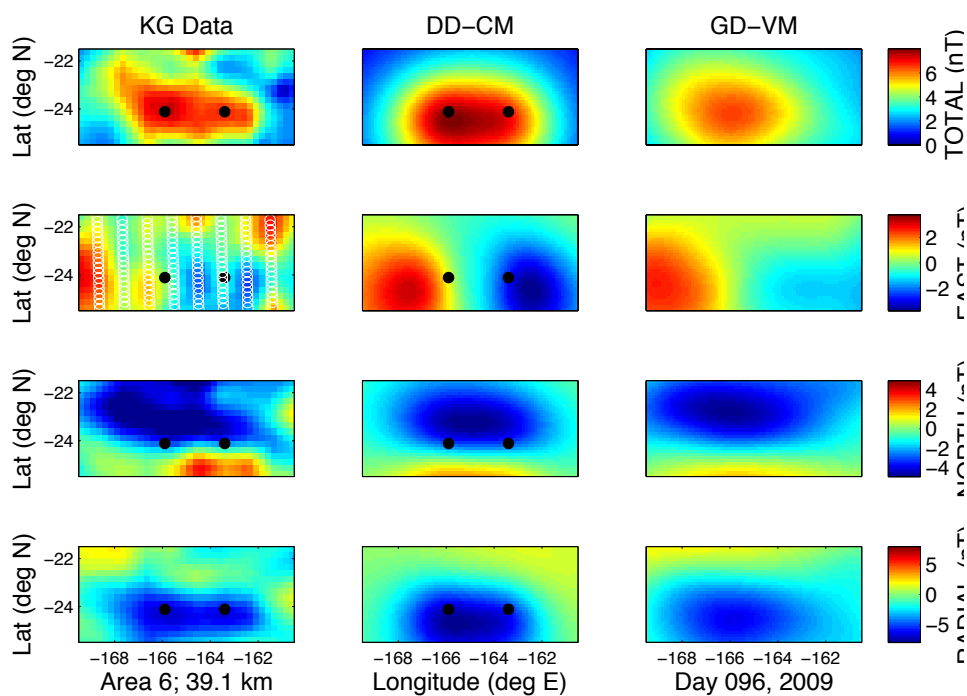


Figure 4.38. Area 6 best fit results, day 96, 2009. Figure details as in Figure 4.9.

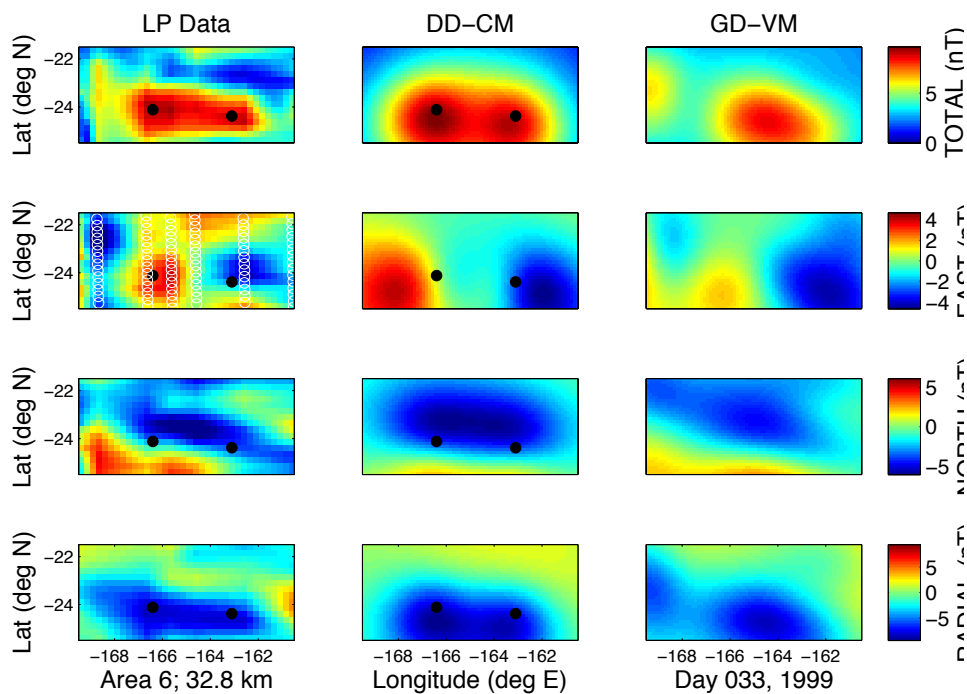


Figure 4.39. Area 6 best fit results, day 33, 1999. Figure details as in Figure 4.9.

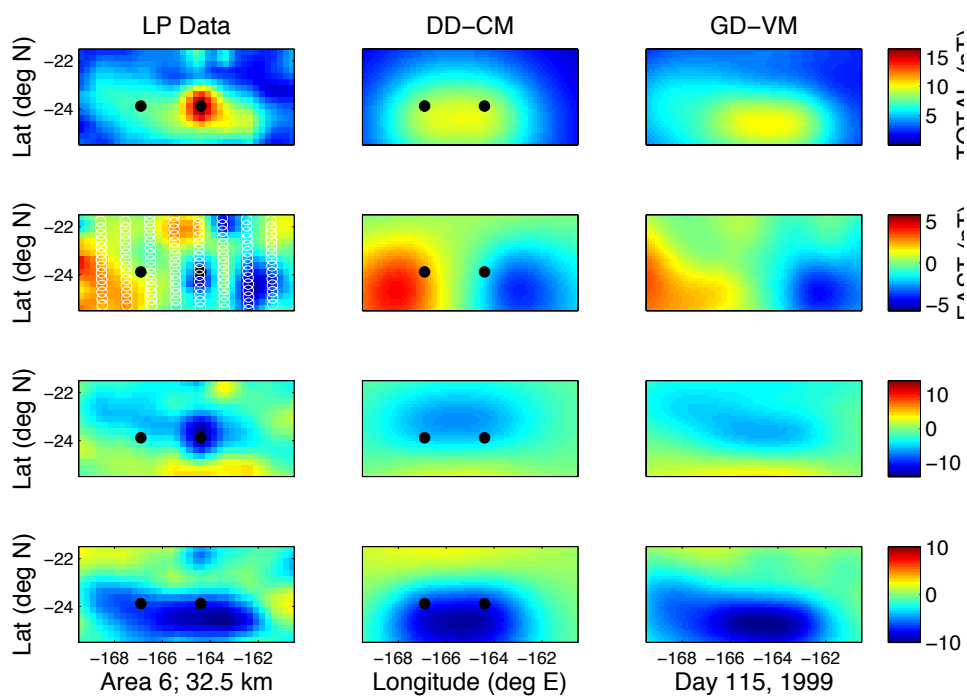


Figure 4.40. Area 6 best fit results, day 115, 1999. Figure details as in Figure 4.9.

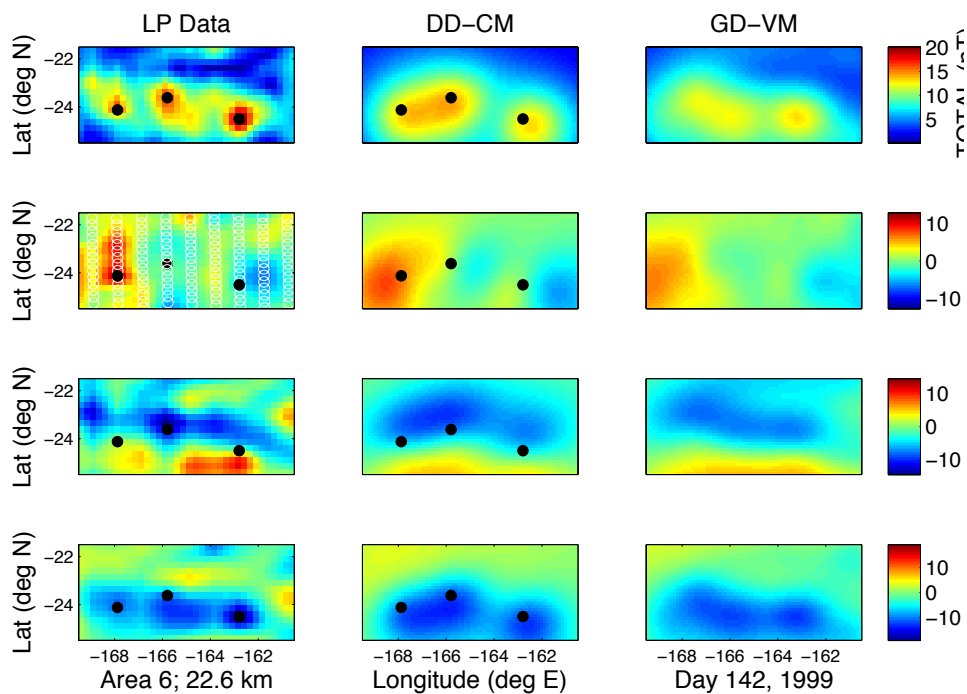


Figure 4.41. Area 6 best fit results, day 142, 1999. Figure details as in Figure 4.9.

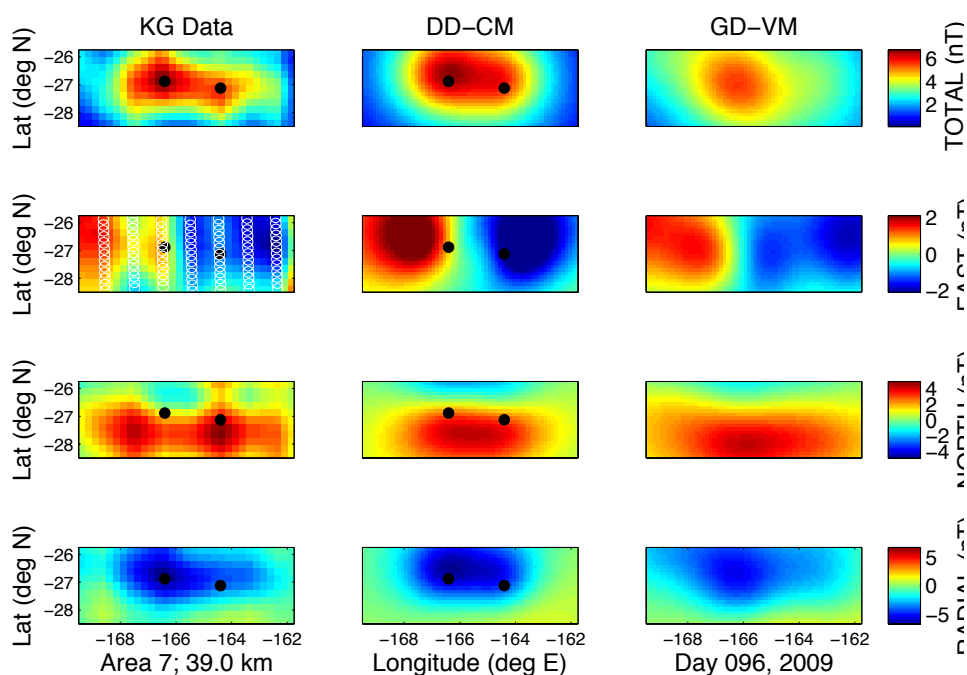


Figure 4.42. Area 7 best fit results, day 96, 2009. Figure details as in Figure 4.9.

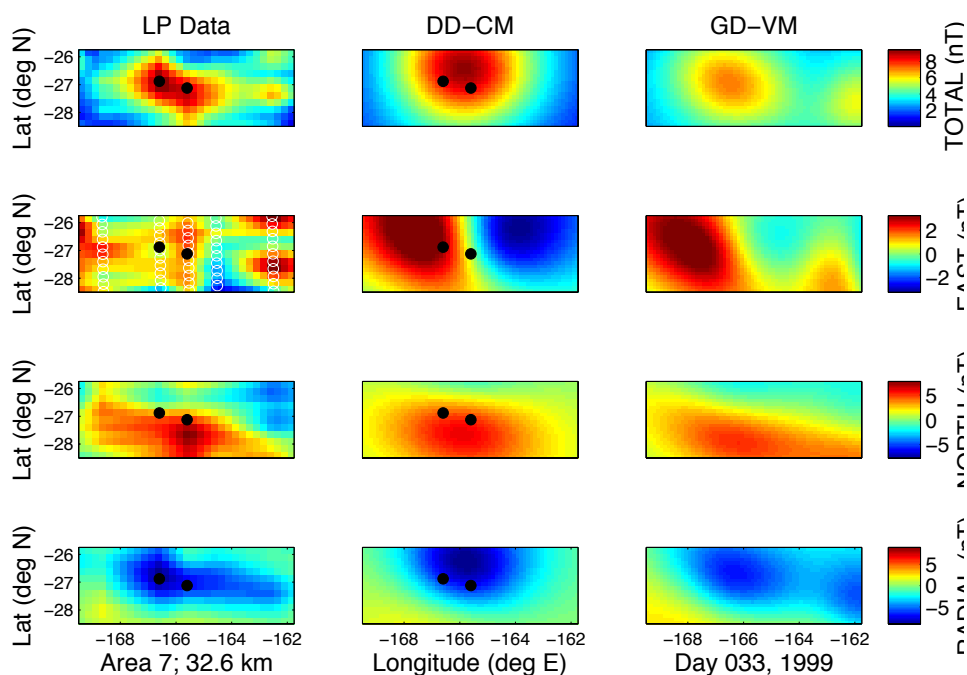


Figure 4.43. Area 7 best fit results, day 33, 1999. Figure details as in Figure 4.9.

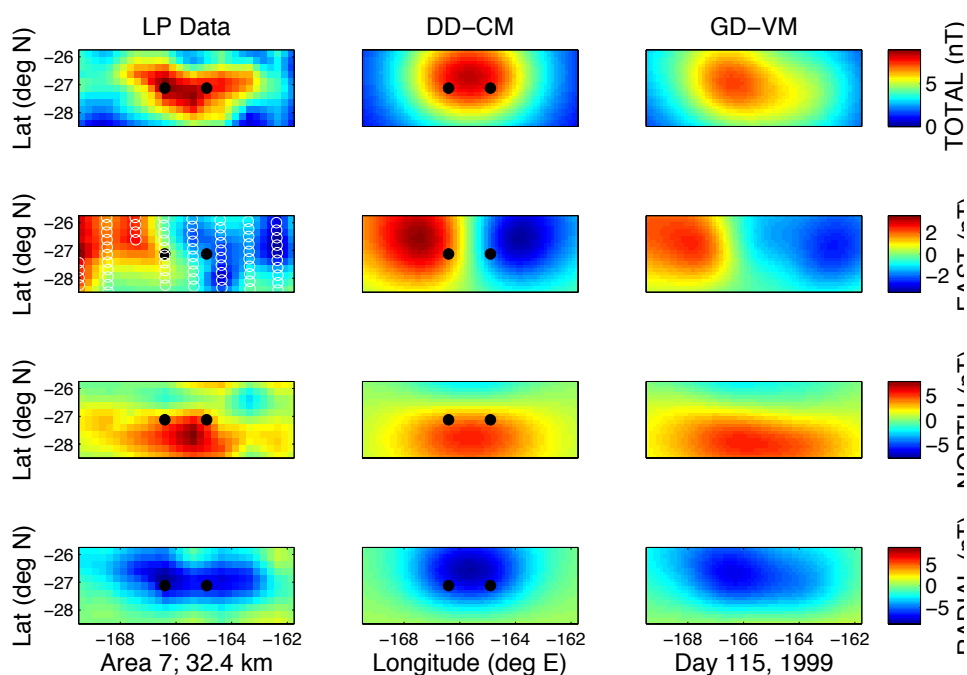


Figure 4.44. Area 7 best fit results, day 115, 1999. Figure details as in Figure 4.9.

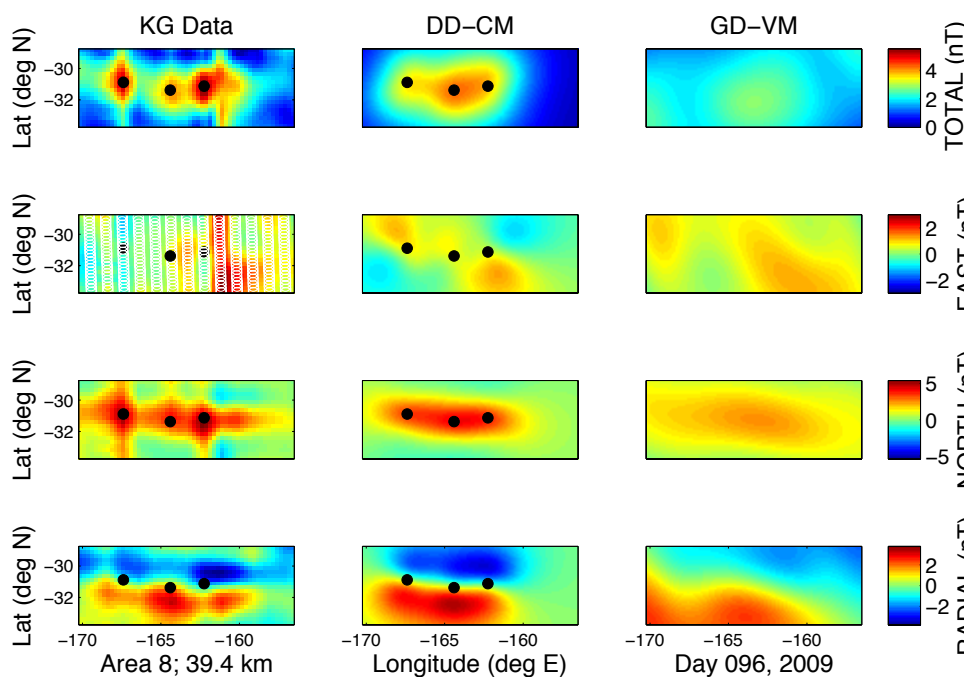


Figure 4.45. Area 8 best fit results, day 96, 2009. Figure details as in Figure 4.9.

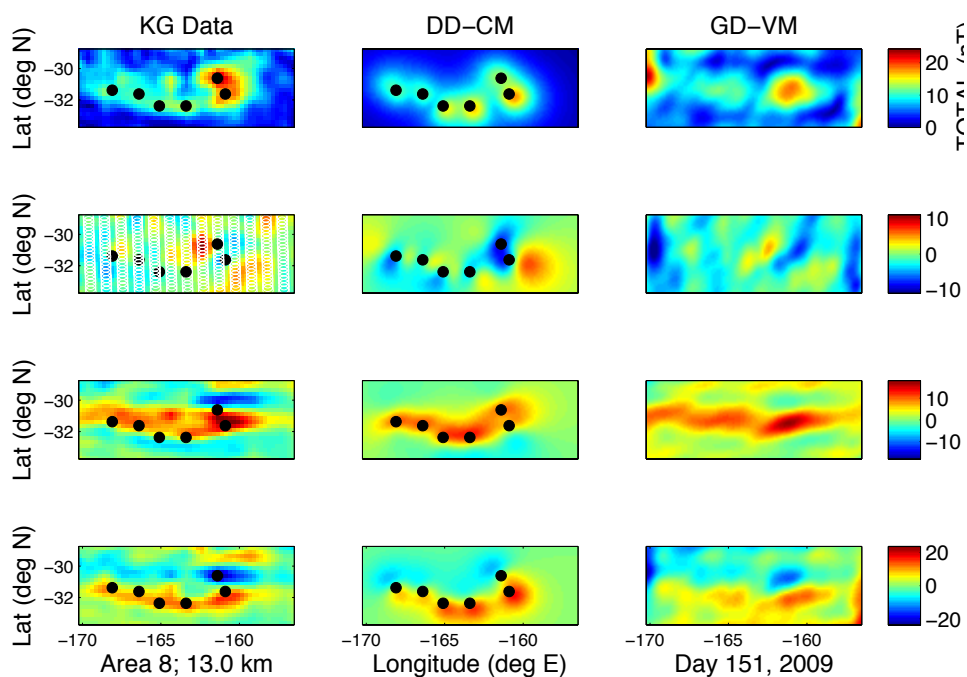


Figure 4.46. Area 8 best fit results, day 151, 2009. Figure details as in Figure 4.9.

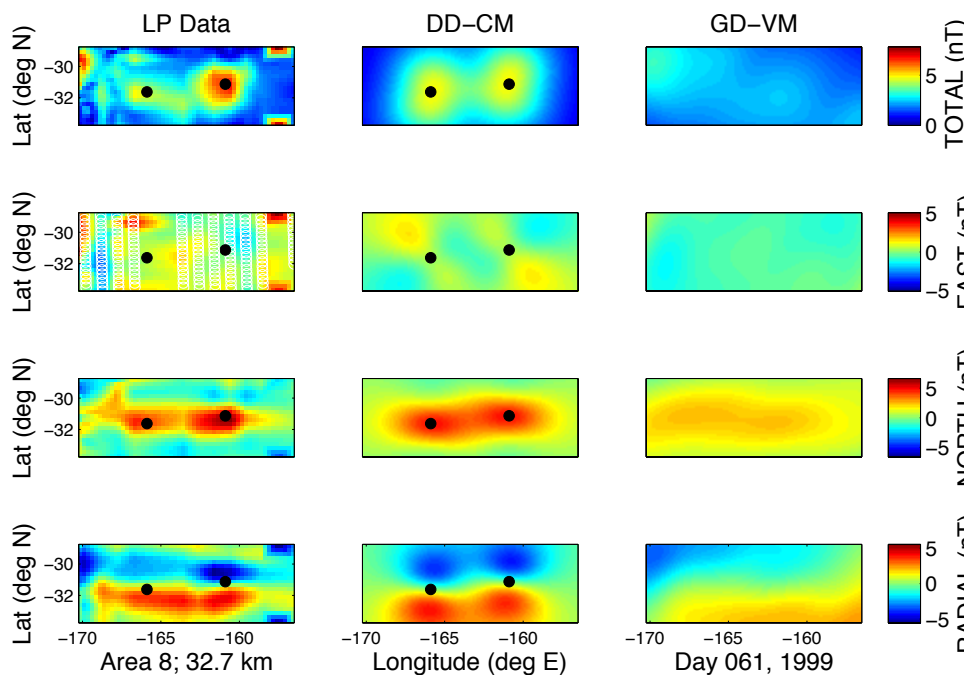


Figure 4.47. Area 8 best fit results, day 61, 1999. Figure details as in Figure 4.9.

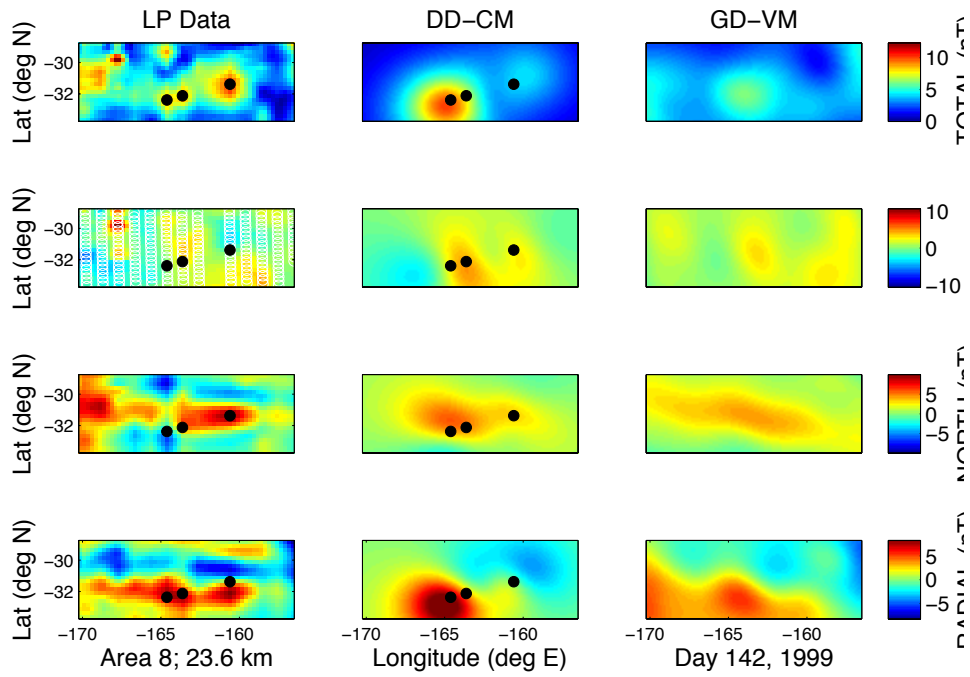


Figure 4.48. Area 8 best fit results, day 142, 1999. Figure details as in Figure 4.9.

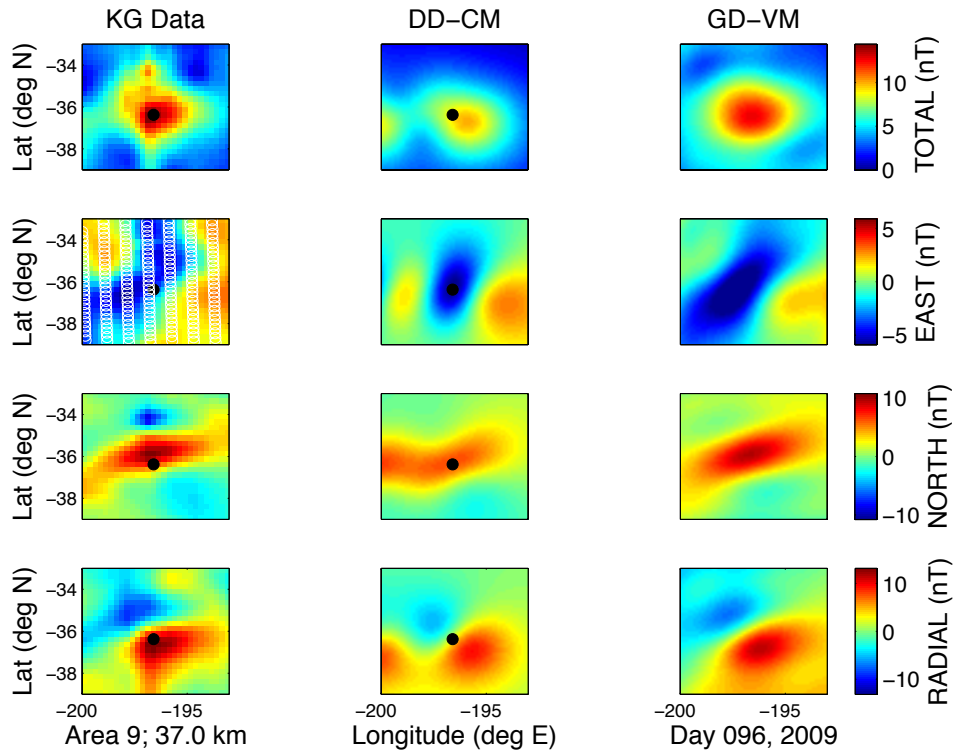


Figure 4.49. Area 9 best fit results, day 96, 2009. Figure details as in Figure 4.9.

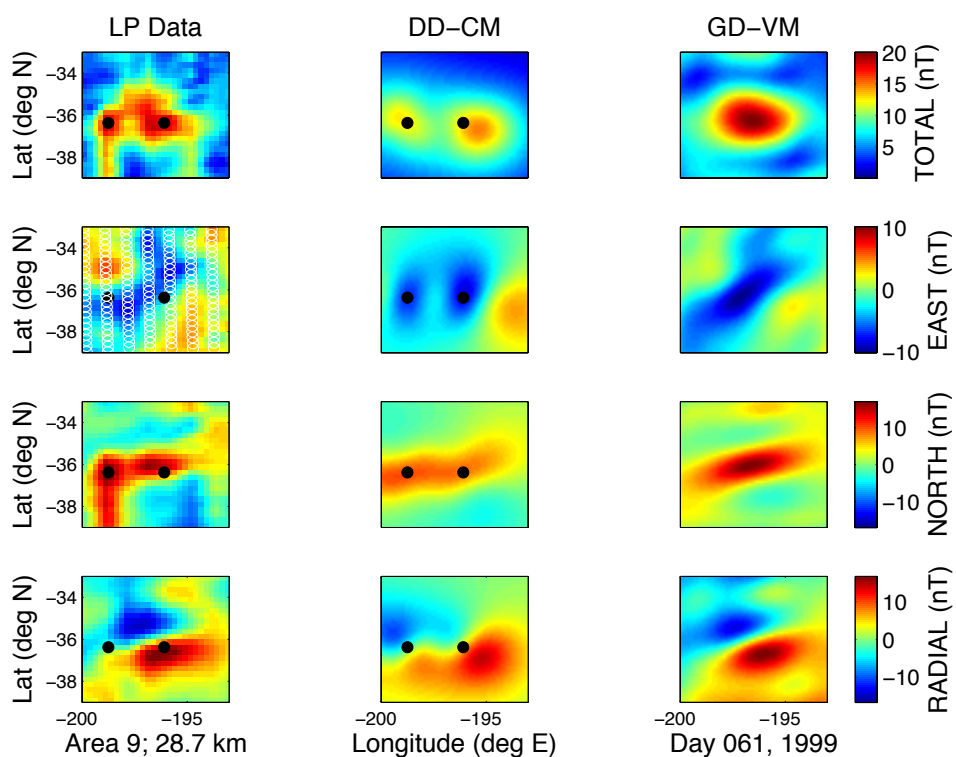


Figure 4.50. Area 9 best fit results, day 61, 1999. Figure details as in Figure 4.9.

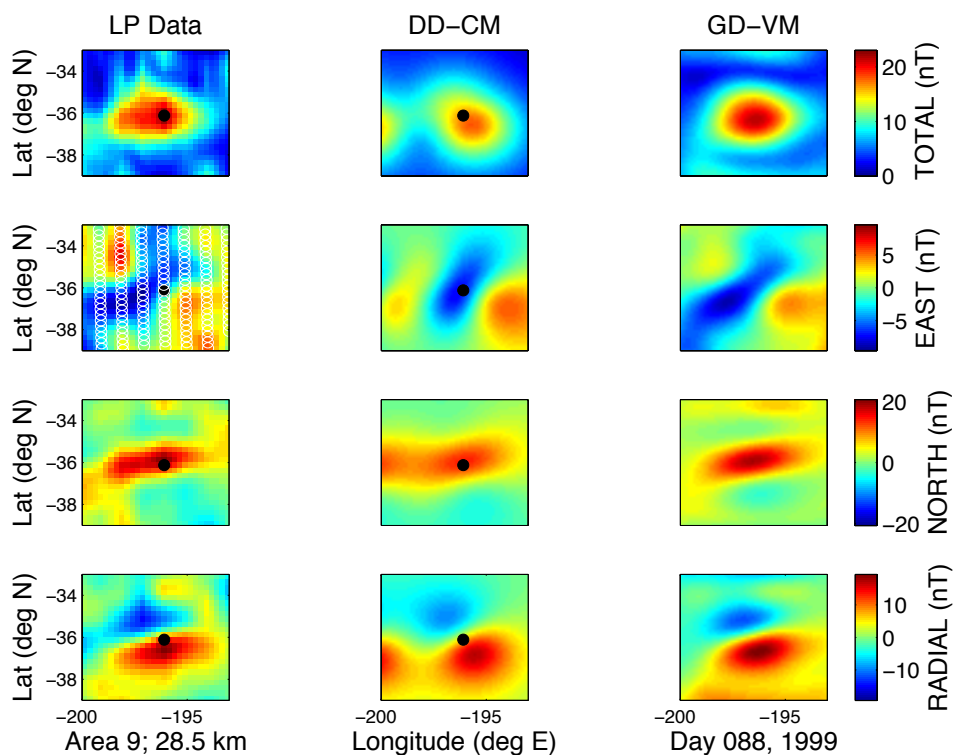


Figure 4.51. Area 9 best fit results, day 88, 1999. Figure details as in Figure 4.9.

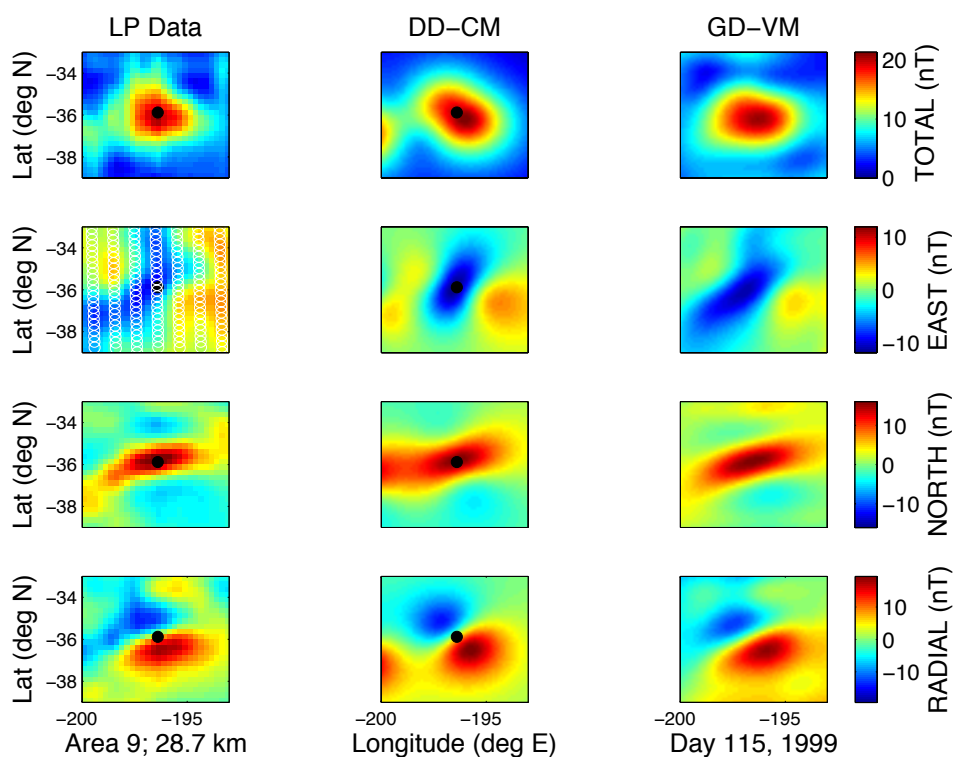


Figure 4.52. Area 9 best fit results, day 115, 1999. Figure details as in Figure 4.9.

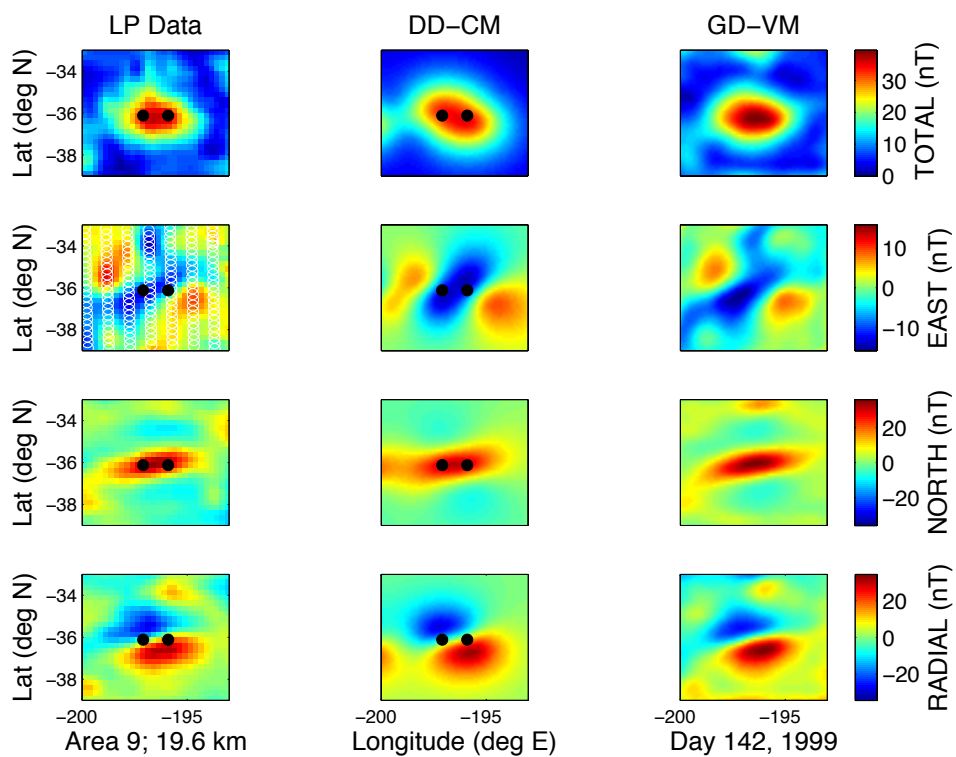


Figure 4.53. Area 9 best fit results, day 142, 1999. Figure details as in Figure 4.9.

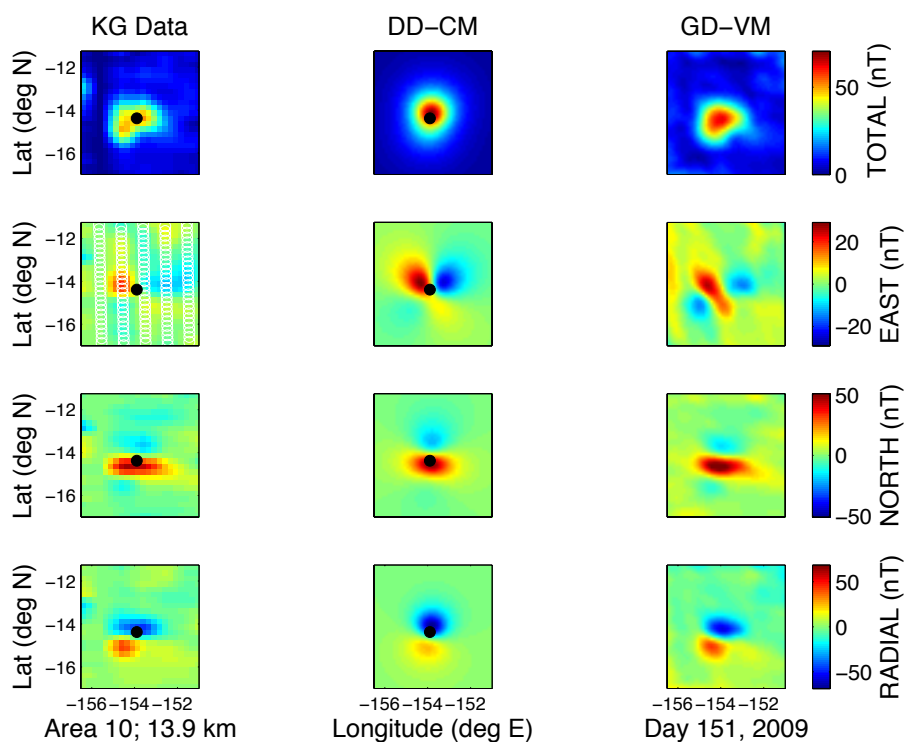


Figure 4.54. Area 10 best fit results, day 151, 2009. Figure details as in Figure 4.9.

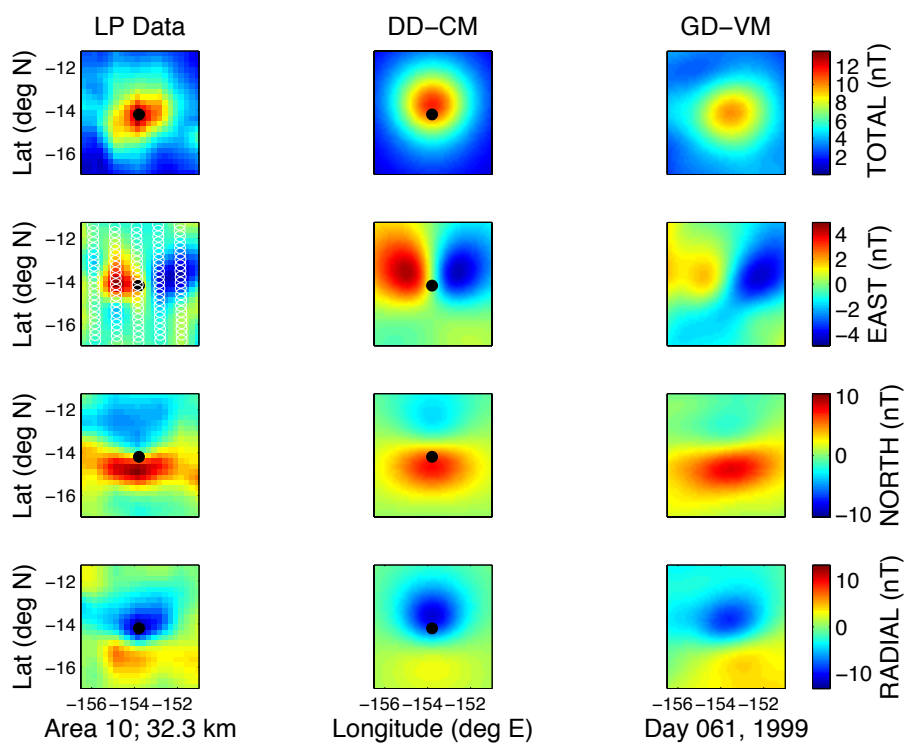


Figure 4.55. Area 10 best fit results, day 61, 1999. Figure details as in Figure 4.9.

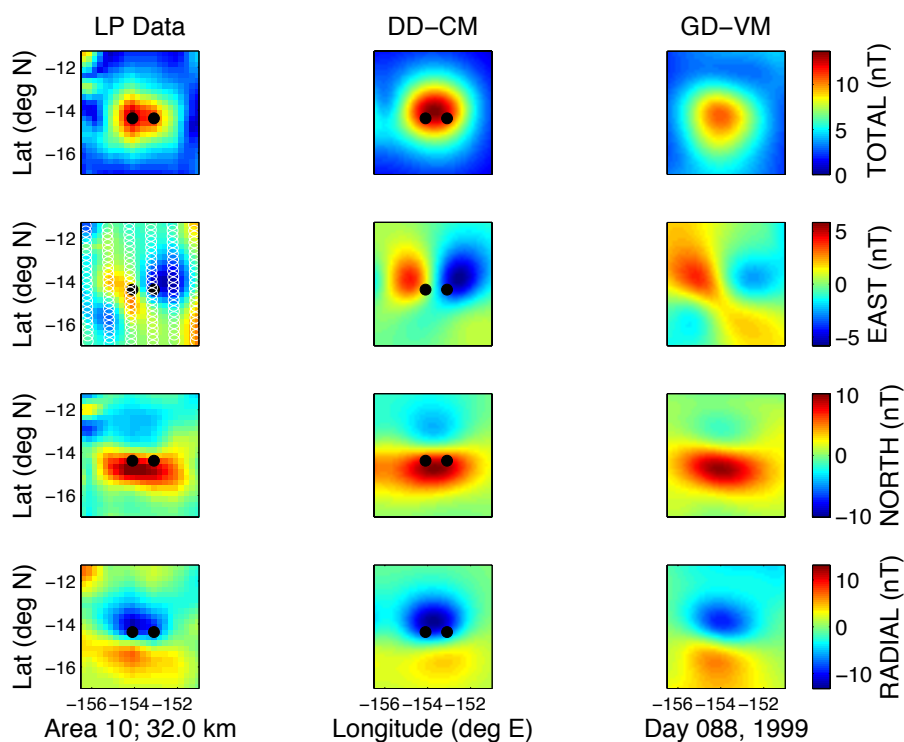


Figure 4.56. Area 10 best fit results, day 88, 1999. Figure details as in Figure 4.9.

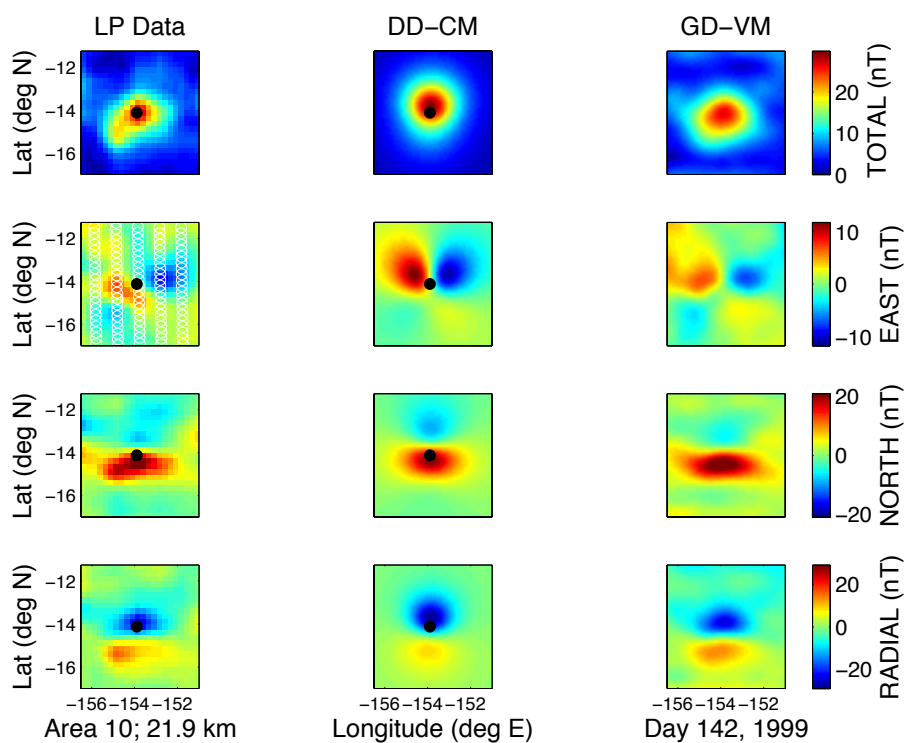


Figure 4.57. Area 10 best fit results, day 142, 1999. Figure details as in Figure 4.9.

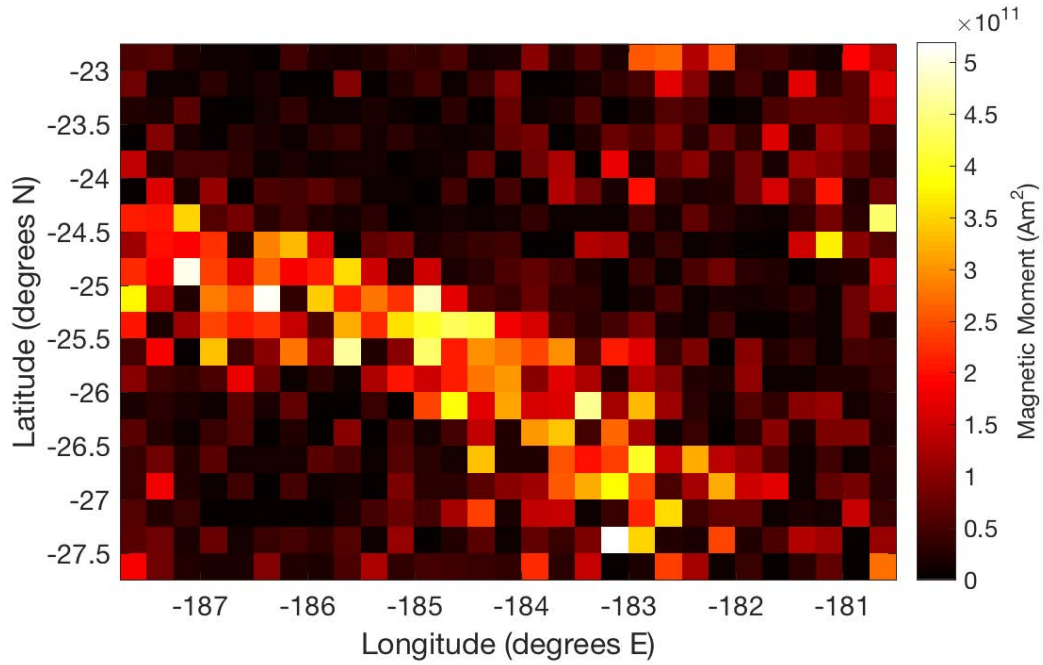


Figure 4.58. For Area 1, source model obtained with GD-VM algorithm [cf. *Hemingway and Garrick-Bethell, 2012*]. Each square represents a single dipoles covering 0.25×0.25 degrees ($\sim 5 \times 10^7 \text{ m}^2$); colors indicate each dipole's total magnetic moment. Number of gridded dipoles is shown in Table 4.1. Dataset is the same as in Figure 4.8.

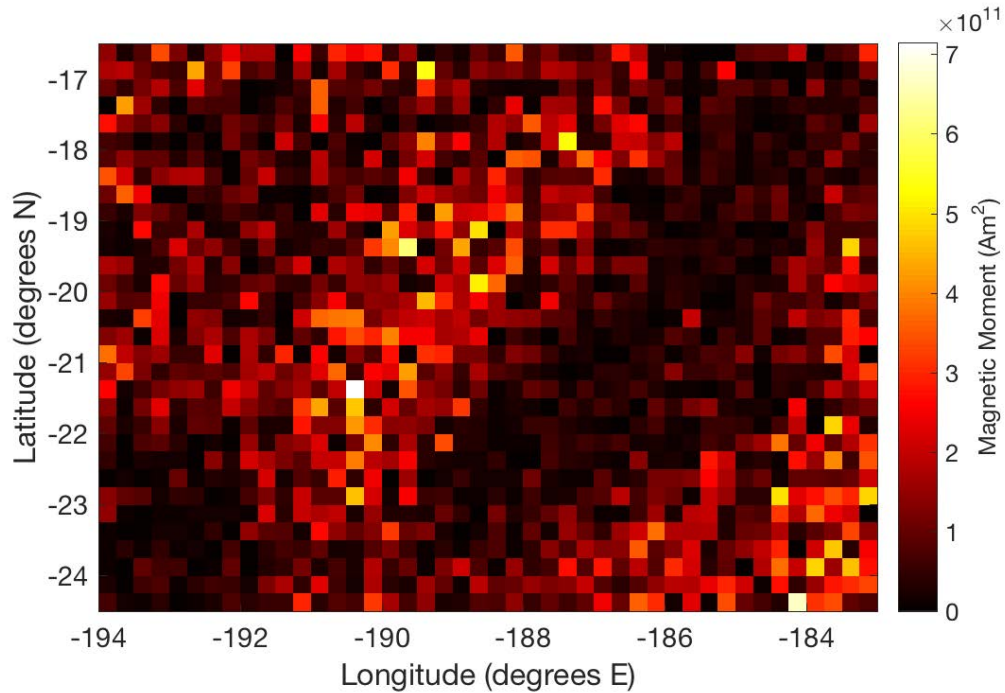


Figure 4.59. For Area 2, source model obtained with GD-VM algorithm. Details are as in Figure 4.58, except that the dataset is the same as in Figure 4.9.

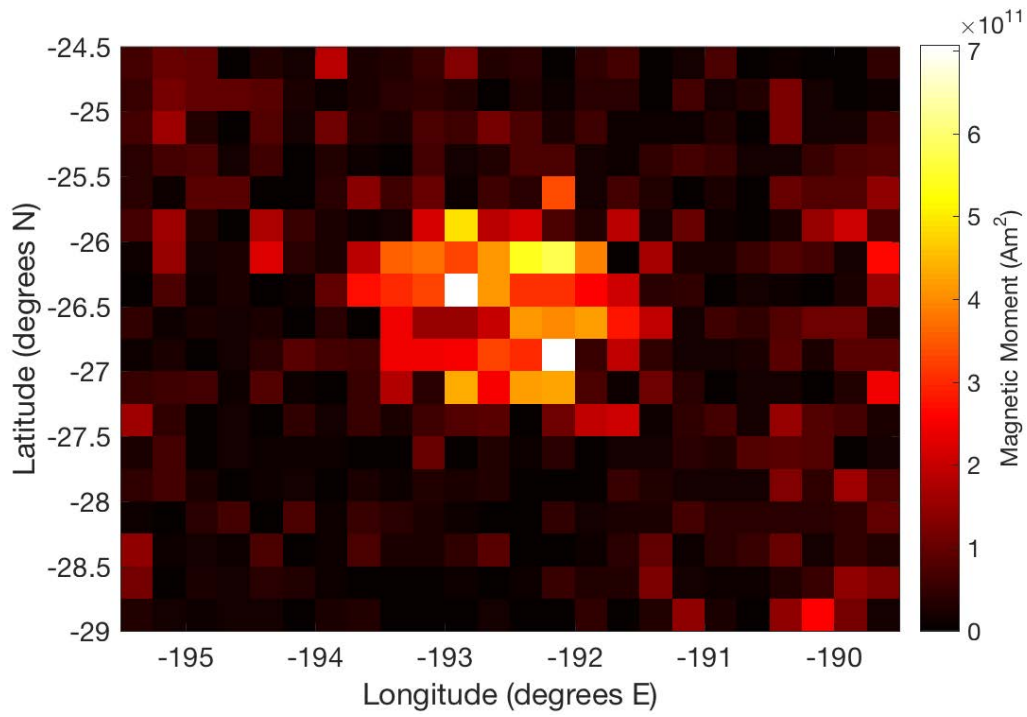


Figure 4.60. For Area 3, source model obtained with GD-VM algorithm. Details are as in Figure 4.58, except that the dataset is the same as in Figure 4.10.

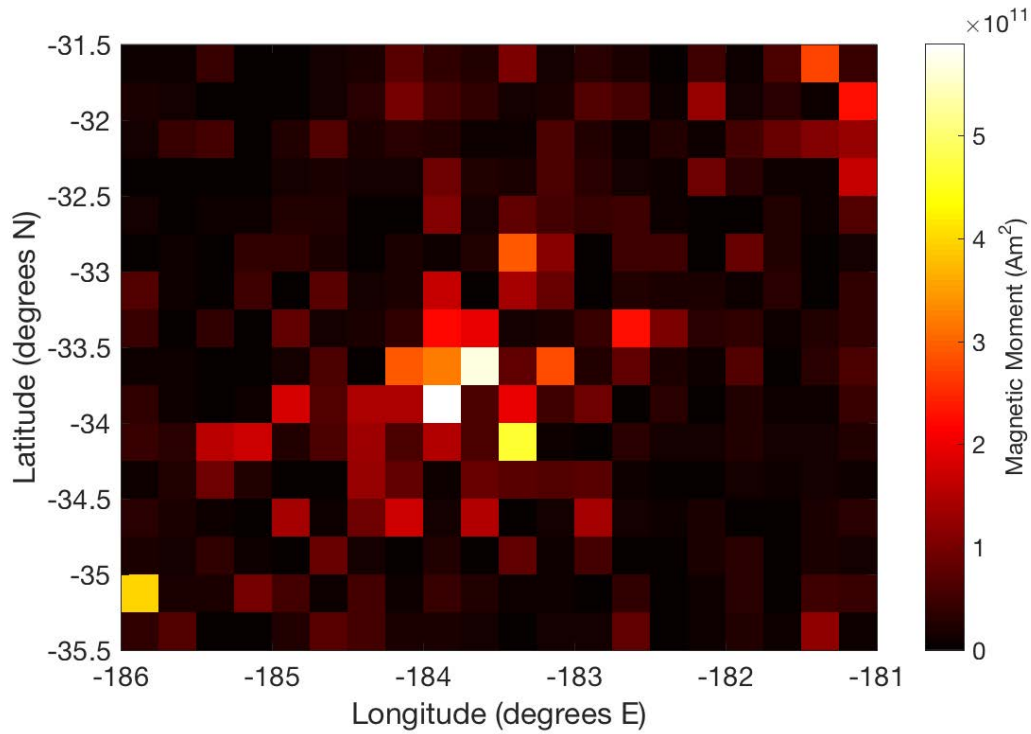


Figure 4.61. For Area 4, source model obtained with GD-VM algorithm. Details are as in Figure 4.58, except that the dataset is the same as in Figure 4.11.

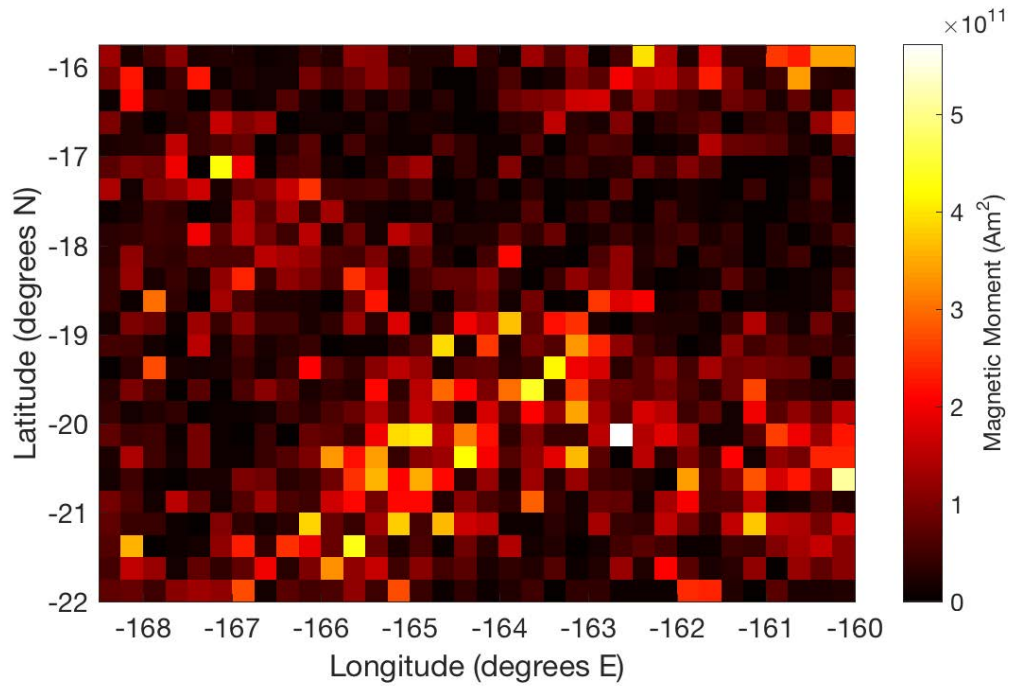


Figure 4.62. For Area 5, source model obtained with GD-VM algorithm. Details are as in Figure 4.58, except that the dataset is the same as in Figure 4.12.

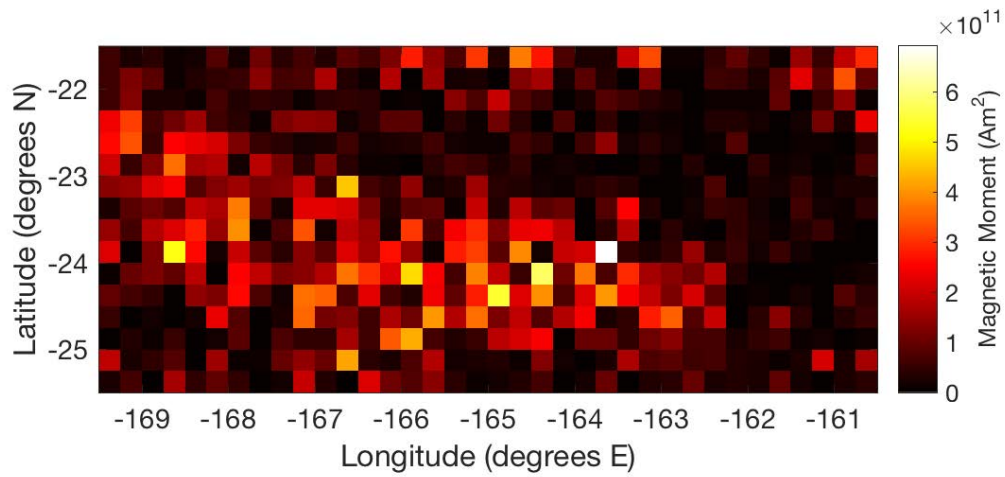


Figure 4.63. For Area 6, source model obtained with GD-VM algorithm. Details are as in Figure 4.58, except that the dataset is the same as in Figure 4.13.

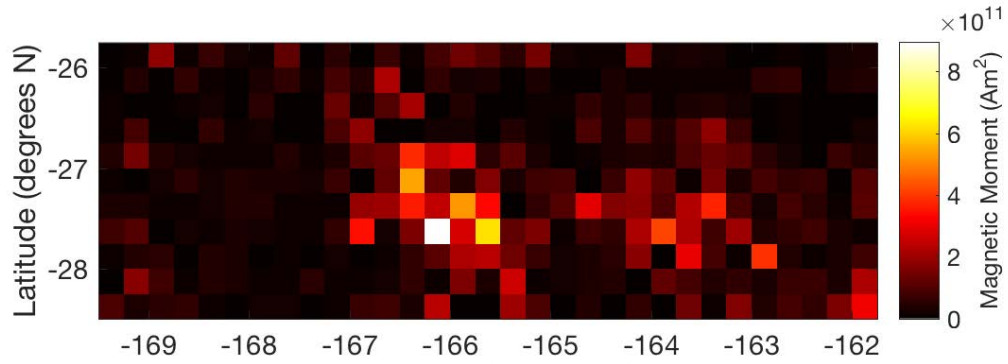


Figure 4.64. For Area 7, source model obtained with GD-VM algorithm. Details are as in Figure 4.58, except that the dataset is the same as in Figure 4.14.

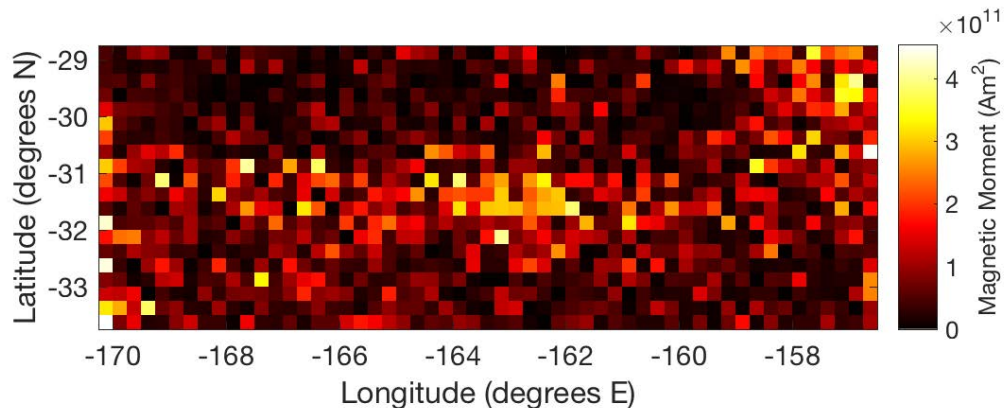


Figure 4.65. For Area 8, source model obtained with GD-VM algorithm. Details are as in Figure 4.58, except that the dataset is the same as in Figure 4.15.

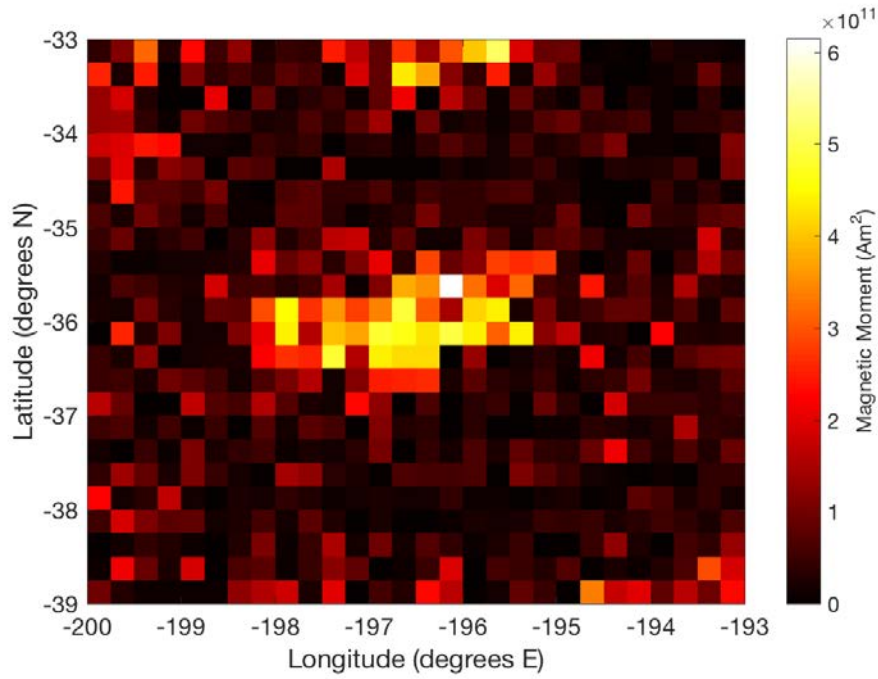


Figure 4.66. For Area 9, source model obtained with GD-VM algorithm. Details are as in Figure 4.58, except that the dataset is the same as in Figure 4.16.

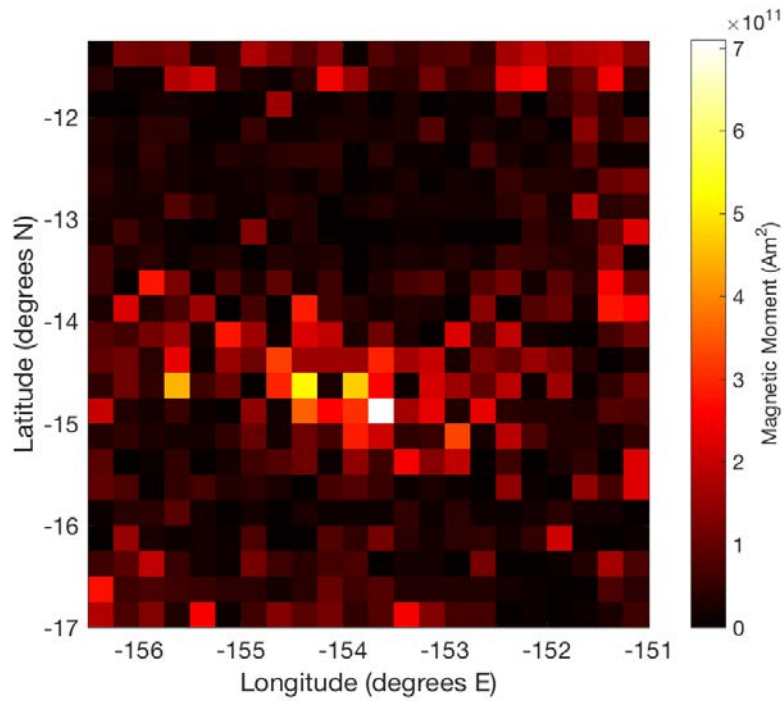


Figure 4.67. For Area 10, source model obtained with GD-VM algorithm. Details are as in Figure 4.58, except that the dataset is the same as in Figure 4.17.

Chapter 5

Phase-Dependent Atmospheric Retrievals on Gas Giant Planets in Reflected Light

This chapter is a modified reprint of M. Nayak, R. Lupu, M. Marley, J. Fortney, T. Robinson and N. Lewis (2016), Atmospheric Retrieval for Direct Imaging Spectroscopy of Gas Giants In Reflected Light II: Orbital Phase and Planetary Radius, accepted, Publications of the Astronomical Society of the Pacific.

5.1 Abstract

Future space-based telescopes, such as the Wide-Field Infrared Survey Telescope (WFIRST), will observe the reflected-light spectra of directly imaged extrasolar planets. Interpretation of such data presents a number of novel challenges, including accounting for unknown planet radius and uncertain stellar illumination phase angle. Here we report on our continued development of Markov Chain Monte Carlo retrieval methods for addressing these issues in the interpretation of such data. Specifically we explore how the unknown planet radius and potentially poorly known observer-planet-star phase angle impacts retrievals of parameters of interest such as atmospheric methane abundance, cloud properties and surface gravity. As expected,

the uncertainty in retrieved values is a strong function of signal-to-noise ratio (SNR) of the observed spectra, particularly for low metallicity atmospheres, which lack deep absorption signatures. Meaningful results may only be possible above certain SNR thresholds; for cases across a metallicity range of 1-50 times solar, we find that only an SNR of 20 systematically reproduces close to the correct methane abundance at all phase angles. However, even in cases where the phase angle is poorly known we find that the planet radius can be constrained to within a factor of two. We find that uncertainty in planet radius decreases at phase angles past quadrature, as the highly forward scattering nature of the atmosphere at these geometries limits the possible volume of phase space that relevant parameters can occupy. Finally, we present an estimation of possible improvement that can result from combining retrievals against observations at multiple phase angles.

5.2 Introduction

Transit and radial velocity (RV) surveys have been highly successful in detecting short-period exoplanet systems, and have allowed the compilation of a statistical picture of the bulk properties of inner planetary systems. However, the next frontier in exoplanet studies is space-based direct imaging and spectroscopy using optical-wavelength telescopes, coronagraphs and integral field spectrographs. Such instruments will allow the characterization of colder or self-luminous planets that orbit farther from their parent star. The upcoming Wide-Field Infra-Red Survey Telescope (WFIRST) space telescope will feature a space-based high-contrast

coronagraph for imaging and spectroscopic studies of planets around nearby stars (Spergel et al. 2013). It will perform spectroscopy of extrasolar planets in reflected light at spectral resolutions (R) of $R \sim 70$, in wavelengths ranging from ~ 600 - 970 nm. Unlike transit spectroscopy, which is able to probe to atmospheric pressures of ~ 1 mbar (Kreidberg et al. 2014), or ~ 1 bar in combination with emission spectra, direct imaging has the potential to probe deeper into the atmosphere, to the pressure at which atmospheric aerosols become optically thick [Morley et al., 2015].

To support the definition of future direct imaging missions and to enhance their science returns, we have been developing a set of tools to characterize gas giant planet atmospheric and physical properties using reflected light spectroscopy, given anticipated instrument parameters from WFIRST. In Lupu et al. (2016), the first in this series, retrievals of atmospheric methane abundances and basic cloud properties using Markov Chain Monte Carlo (MCMC) techniques were explored, assuming planets with known radii were observed at full phase. [Lupu et al., 2016] built on previous work by members of our group to create models of reflected light spectra, beginning with Marley et al. (1999) and leveraging albedo variations as a function of cloud structure, mass, metallicity, planet phase and star-planet separation by Cahoy et al. (2010). Other contributions in this field have included Sudarsky et al. (2000, 2003) and Burrows et al. (2004). All these studies of reflected light spectra of exoplanets modeled the planets at full phase [Marley et al., 1999; Lupu et al., 2016], an average phase [Sudarsky et al., 2003] or at a set of specified phase angles [Sudarsky et al.,

2005; Cahoy *et al.*, 2010] and implicitly assumed that the incident flux and planet size were known.

However during a real observation campaign, several factors that control the reflected flux will be poorly known. First, planets will be observed at a variety of different points along their orbits. Depending on the fidelity with which the orbit is constrained, the star-planet-observer angle (phase angle), and thus the illumination phase, may not be well known. The instantaneous distance of the planet from its star, and thus the incident flux, will almost certainly not be perfectly known. Likewise, planet radii will not be constrained, except by the observed brightness of the planet at a variety of wavelengths and the mass-radius relationship for those planets with masses constrained by radial velocity measurements. Any uncertainties in orbital phase will further obscure planet radius determination.

Figure 5.1 illustrates the degenerate nature of planet radius with increasing planet phase in scattered light; the brightness of a planet can decrease either with decreasing planet radius or increasing phase. In other words, a large planet at quadrature (phase angle $\alpha = 90^\circ$) and a smaller planet at full-phase ($\alpha = 0^\circ$) could not be distinguishable solely by their relative brightness. As we shall show, this degeneracy has a significant effect on the quality of the resulting retrievals on other parameters of interest, including methane abundance and cloud properties. In this work we explore the bounds of these mutually dependent parameters and determine signal-to-noise (SNR) requirements for scientifically interesting conclusions to be drawn.

The goal of the current work is therefore to characterize the effects of changing planet phase on retrievals of atmosphere molecular abundances, surface gravity and cloud properties when planetary radius is unknown. The paper is organized as follows: Section 5.3 provides background on our approach to modeling the phase angle and clouds, our MCMC formulation and our chosen exoplanet test cases of HD 99492c and HD 192310c; Section 5.4 details MCMC retrieval results and the use of posterior probability plots to extract 68% confidence intervals on parameters of interest. Section 5.5 contains our discussion of how planet radius, phase angle, methane abundance and cloud properties were constrained in the presence of planet phase and radius uncertainties; finally, Section 5.6 presents our conclusions.

5.3 Background

In this section, we provide a brief overview of some key concepts discussed in the paper. This work builds on previous work by several authors to create models of albedo spectra of extrasolar giant planets; a thorough description may be found in [Lupu *et al.*, 2016]. Our initial study reported in that paper represented the first time molecular abundances and cloud properties were simultaneously retrieved using Bayesian inference tools applied to simulated scattered light spectra of cool extrasolar giant planets. Similar applications of Bayesian methods to exoplanet studies include work by Irwin *et al.* (2008) and Benneke & Seager (2012), among others.

5.3.1 Albedo Model

To compute the thermal structure of each model planet's atmosphere, we use a 1D radiative-convective equilibrium model based on that developed for Titan (McKay et al. 1989) and solar system giant planets and exoplanets [Marley and McKay, 1999; Marley et al., 1999]. The methane opacity at optical wavelengths is taken from Karkoschka (1994) and collision-induced absorption from Freedman et al. (2008). In this paper our test planets are cold and we neglect H₂O opacity. Given a self-consistent model atmospheric profile, we compute an albedo spectrum following the methods described in Cahoy et al. (2010). Cloud scattering is treated with a two-term Heyney-Greenstein function, which captures moderate backscattering and high forward scattering as:

$$p_{TT-HG} = \left(1 - \frac{\bar{g}^2}{4}\right) p_{HG}(\bar{g}, \theta) + \frac{\bar{g}^2}{4} p_{HG}\left(-\frac{\bar{g}}{2}, \theta\right) \quad (5.1)$$

where:

$$p_{HG}(\bar{g}, \theta) = \frac{1 - \bar{g}^2}{(1 + \bar{g}^2 - 2\bar{g}\cos\theta)^{1.5}} \quad (5.2)$$

Here, \bar{g} is the scattering asymmetry factor, a measure of the preferred direction of light scattered by aerosol particles; this is a retrievable quantity. Integrating over the emergent intensity using Gaussian-Chebyshev quadrature ([Lupu et al., 2016], originally from Horak (1950) and Horak & Little (1965)) yields model albedo spectra for the planet. In this paper we treat the phase angle as fully unknown. We allow it to vary from full phase ($\alpha = 0^\circ$) to $\alpha = 135^\circ$, at which angle the flux for a Lambertian sphere is <5% of that at full phase. In reality, we will have some constraint on phase angle from radial velocity (RV) observations, which will improve

retrievals; our results may therefore be treated as a worst-case scenario (but see Section 4.5.2). Similarly, even though observations at full phase are not possible for direct imaging, we include that possibility to understand how the quality of retrievals at other phases may relate to those at zero phase, which were elucidated in [Lupu *et al.*, 2016].

5.3.2 MCMC Methodology

For our implementation of Markov Chain Monte Carlo (MCMC) methods, we follow the approach developed for massively parallel implementations by Lupu *et al.* (2016) and use *emcee*, an open-source affine invariant ensemble MCMC sampler (Foreman-Mackey *et al.* 2013; Goodman & Weare 2010). Given a set of well-chosen bounds on retrievable parameters (“priors”), this approach efficiently samples the parameter space and allows for massively parallel computation. For each retrievable parameter, this implementation employs multiple MCMC chains in parallel. Full details, and a comparison of *emcee* to another multimodal nested sampling algorithm (*MultiNest*), are discussed in [Lupu *et al.*, 2016].

Table 5.1. Description of retrievable parameters in two-layer cloud model [Marley *et al.*, 2014], as well as priors used for MCMC runs.

Quantity	Description	Priors	Descriptor
f_{CH_4}	Molecular abundance of Methane	-8 to -2	log space
g	Surface acceleration due to gravity	1 - 300	m/s ²
R	Planet Radius	0.1 - 100	Jupiter radius
dP_1	Pressure difference: Top of lower cloud to Bottom of upper cloud	-2 to 2	log, bar
dP_2	Pressure difference: Bottom of upper cloud to Top of upper cloud	-2 to 2	log, bar
τ	Total optical depth, upper cloud	-2 to 2	log, bar
ϖ_1	Single scattering albedo, upper cloud	0.01 to 0.9999	
\check{g}	Asymmetry Factor	0.01 to 0.9999	
P	Pressure, top of lower cloud	-2 to 1.5	log, bar
ϖ_2	Single scattering albedo, lower cloud	0.01 to 0.9999	
Φ	Planet phase angle	0 to 135	degrees

As also described in [Lupu *et al.*, 2016], we apply these methods to simulated spectral datasets, computed as in Section 4.3.1, to retrieve quantities of interest in the interpretation of exoplanet spectra. Table 5.1 lists all eleven retrievable quantities that are estimated by our Markov Chain Monte Carlo (MCMC) routine. It assumes that the atmosphere’s major absorber is solely methane, with H₂-He background gas. Priors are set to allow values to range across six orders of magnitude for methane abundance, 2.5 orders of magnitude for surface gravity and three orders of magnitude for planetary radius (Table 5.1). Of course, these are extremely large ranges; in reality better constraints are expected. For example, astrometry combined with RV constraints will likely determine the planet mass to within a factor of two. Likewise, the mass-radius relationship trivially demonstrates that a Jupiter mass planet would never have a radius of 100 R_J. However, the exploration of a large parameter space can be valuable in permitting a greater number of feasible solutions, enabling a better understanding of the degeneracies inherent in the problem. As an example, all else being equal, lower methane abundance at lower gravity can produce a similar absorption feature to a higher methane abundance at a higher surface gravity [Marley *et al.*, 2014; Lupu *et al.*, 2016]; the use of MCMC to explore this large parameter space may be useful to probabilistically distinguish between the two cases.

Also among the retrievable parameters, exoplanet cloud and haze aerosols are parameterized using an improved version of the simple two-layer cloud model first detailed in Marley *et al.* (2014). Using the two-layer cloud model, illustrated in Figure 5.2, we create a model cloud and a noise-free albedo spectrum (Marley *et al.* 2014).

These quantities are also used in [Lupu *et al.*, 2016], which contrasts the two-layer model against simpler one-layer and no cloud models.

To understand how instrumental and astrophysical parameters can affect observed spectra, and include these effects in our retrievals, we apply a noise model to the noise-free spectrum, which includes convolution with an instrument point spread function (PSF) to an appropriate spectral resolution, notionally representative of that expected for WFIRST. Parameters of the noise model are presented in Table 5.2 and the implementation follows Robinson *et al.* (2015). Each simulated data point is drawn from a normal distribution, with the mean given by the planet-star flux ratio and the standard distribution given by the noise model. This noisy spectrum then becomes the input to the MCMC retrieval code.

We make three notes here: firstly, at the time of this writing, the WFIRST coronagraph instrument parameters are still under active study and refinement [Harding *et al.*, 2015]. However, our adopted values (Table 5.2) are meant to be representative of the noise levels that the mission is expected capable of achieving, as it is understood to be in mid-2016. Secondly, the instrument-representative approach employed here differs from [Lupu *et al.*, 2016], which uses a general synthetic noise model. Finally, here we do not attempt to retrieve the atmospheric temperature-pressure profile, as the reflected light spectra are only weakly dependent on the profile. Variations in gravity do alter the scale height and atmospheric density and these effects are accounted for. A future paper in this series will explore atmospheric temperature profile retrievals.

Table 5.2. Parameters used in the notional WFIRST noise model. Details on implementation follow [Robinson et al., 2015]

Item	WFIRST representative value	Unit
Dark current	5.00E-04	s ⁻¹
Telescope diameter	2.4	m
Read noise	0.2	per pixel
System throughput	0.037	
Angular size of lenslet	0.017	arcsecond
Inner working angle	2.7	λ/D
Outer working angle	10	λ/D
Size of photometric aperture	1.5	λ/D
Contrast floor	1.00E-10	
Minimum wavelength	0.6	μm
Maximum wavelength	0.95	μm
Spectral resolution	R = 70	

Here we do not attempt to retrieve the atmospheric temperature-pressure profile, as the reflected light spectra are only weakly dependent on the profile. Variations in gravity do alter the scale height and atmospheric density and these effects are accounted for. Future work will explore atmospheric profile retrievals.

5.3.3 Test Cases: Synthetic HD 99492c (Planet A) and HD 192310c

Four test cases across two idealized exoplanets encompass our efforts to contrast the relative effects of changing planet mass. Represented in the retrievable parameters by surface gravity and planet radius, the planet mass in turn controls other retrieved properties. For a non-solar system test case, [Lupu et al., 2016] used HD 99492c [Marcy et al., 2005]; our first test case is also inspired by HD 99492c. The inferred mass of this planet is $0.36 \pm 0.02 M_J$ (Meschiari et al. 2010, Table 2); at a semi-major axis of 5.4 AU from its star, models from Fortney et al. (2007) suggest a radius for this planet of $\sim 0.9 R_J$. Kane et al. (2016) report that HD 99492c is in fact an artifact attributable to variability of the host star and not a planet. Therefore we treat

spectra generated for HD 99492c as a synthetic case study to baseline our results against, for a planet almost of Jupiter radius with a methane-dominated atmosphere. To permit observations at all phase angles to be above the WFIRST contrast floor (Table 5.2), we “relocate” our synthetic planet to 2 AU from its star and 5 parsecs from the telescope; the actual values for HD 99492c are 5.4 AU / 18 parsecs [Marcy *et al.*, 2005]. We refer to this synthetic HD 99492c analog as “Planet A” for the remainder of this work.

The second test case explores a planet with an order of magnitude smaller mass (Figure 5.3). HD 192310c, also known as Gliese 785 c, has $M \sin i$ of $0.076 \pm 0.016 M_J$ [Pepe *et al.*, 2011]. Using mass-radius relationships from Fortney *et al.* (2007) we infer a radius of $0.75 R_J$. Using the notional parameters in Table 5.2, this planet will be near the coronagraph inner working angle (IWA) at 600 nm. However, since the WFIRST coronagraphs are still under development, their in-flight performance may yet change. Thus, we choose not to relocate the planet as for HD 99492c / Planet A, and instead use HD 192310c as a test case for situations where a planet lies near enough to the coronagraph IWA to cause the noise to be dominated by stellar leakage. Using this approach, we produce three distinct models of HD 192310c at metallicities of 1x, 10x and 50x times solar abundance, which produce successively deeper methane features (see Figure 5.6). Figure 5.4 contrasts model spectra for Planet A and the 50x solar metallicity HD 192310c at $\alpha = 0^\circ$ and $\alpha = 90^\circ$.

5.4 Results

5.4.1 Retrieved best-fit spectra by MCMC

We generate model albedo spectra for Planet A (Figure 5.5) and HD 192310c (Figure 5.6) at varying phase angles similar to Figure 5.4; in this study we explore phase angles of 30° , 40° , 60° , 70° , 90° and 120° . Both resulting spectra are then combined with an instrument-specific model, in this case, the notional WFIRST noise model in Table 5.2 [Robinson *et al.*, 2015].

While [Lupu *et al.*, 2016] performs retrievals against an albedo spectrum, since this work is also concerned with planet radius, we retrieve against the planet-to-star flux ratio, or contrast spectrum. Contrast spectra are created for a range of signal-to-noise ratios (SNR) to explore observational limits and their effect on observations. Here we define the SNR to be centered at $\lambda = 0.6$ micron with an 8.6 nm wide bandpass. SNRs of 5, 10 and 20 are explored, as in [Lupu *et al.*, 2016]. To be clear, since SNR is wavelength-dependent, these values refer to the SNR at $0.6 \mu\text{m}$.

For each of the eleven retrievable parameters (Table 5.1), we employ twelve MCMC chains, or “walkers”, for a total of 132 chains. Each chain was then run for 2500 iterations for a final sample chain of 330,000 samples. Selected cases were run for 4000 iterations to ensure that the MCMC algorithm did not get stuck in a local minimum and was exploring the entire parameter space; returned ranges were found to be nearly identical to the 2500 iteration run, so we restrict ourselves to 2500 iterations for all the results presented here. We identified the best fit, 1σ and 2σ -range

of retrieved spectra for Planet A; the retrieved models match the “true” spectra well. Similar excellent fits are seen for phase angles between 30° and 120° despite decreasing contrast signals at larger phase angles (Figure 5.7).

We perform a similar study against HD 192310c using the same MCMC parameters as for Planet A. For this planet, we generate three separate test cases by constructing forward models and performing retrievals at three different metallicities, namely, one, ten and fifty times solar values (1x, 10x, 50x). For each metallicity case, we generate model albedo spectra at 30° , 40° , 60° , 70° , 90° and 120° phase angle and apply the notional WFIRST noise model to them.

The resulting spectra reveal a variety of methane absorption signatures (Figure 5.6). Notably, because of the relatively high cloud, the 1x solar case exhibits particularly subdued methane absorption features. Figure 5.8 - Figure 5.10 illustrate the corresponding spectral recoveries across three values of signal-to-noise (SNR) and three values of metallicity, at phase angles of 30° and 90° .

5.4.2 Inferring Phase-Dependent Relationships from Posterior Probability Distributions

We assemble retrieval results similar to those shown in Section 5.4.1 into posterior probability plots, which graphically show the marginal probability distribution between every retrieved parameter pair. Figure 5.11 is an example of this plot. Here, darker colors represent a higher probability of the solution lying in that

region, and the diagonal of the plot shows the marginalized probability distribution, to a 68% confidence interval, for each retrievable parameter in Table 5.1.

A broad distribution means that the parameter is largely unconstrained, as is the case for phase angle (Figure 5.11, marker a) or surface gravity. Conversely, a sharp peak in the distribution and small ranges on returned values means that the parameter can be well determined, such as planet radius (Figure 5.11, marker b). In other cases, more general relationships can be inferred, for example, lower limits to the albedo of the top cloud (Figure 5.11, marker c) and methane abundance. Such plots illuminate how variations in retrieved values vary with changes in the "true" planet phase, as well as interrelationships between other parameters. A brief discussion of general trends apparent in the relationships of phase angle with other retrievable parameters follows; though we use the Planet A case (Figure 5.11) to highlight these trends, they are also seen for HD 192310c.

Figure 5.12 focuses on selected panels from Figure 5.11. First, the relationship between radius and phase is in line with our conceptual understanding from Figure 5.1: for larger phase angles (i.e. a more crescent phase), a larger planet radius is favored. Even at a relatively high phase angle (60°) a clear detection of methane, with a lower limit to the atmospheric mixing ratio of larger than $10^{-3.5}$, is seen. Surface gravity appears essentially unconstrained, although as we will show later, a larger SNR or smaller phase angle does narrow the probable range. The difficulty in deriving meaningful constraints on gravity from reflection spectra is discussed in more detail in [Lupu *et al.*, 2016].

The MCMC analysis appears to constrain the top cloud well (quantity dP_2 , see Table 5.1), but is indeterminate on the pressure “gap” between the cloud layers (quantity dP_1). The pressure of the bottom cloud (quantity P_2) is not tightly constrained, but higher probability values are distributed around the true value. This could imply either that the bottom cloud is not well constrained, or perhaps that a one-layer cloud model is more suitable for this planet. Previous MCMC simulations on HD 99492c reach a similar conclusion [Marley *et al.*, 2014].

We generate marginalized probability distributions at seven phase angles (0° - 120°) and three SNR values (5, 10, 20). For the case of SNR = 20, Figure 5.13 shows the relationship between retrieved phase angle and planet radius for phase angles from 30° to 120° . While the probable ranges on retrieved planet phase angle are large, at both low and high phase angles, the MCMC algorithm retrieves best-fit values close to the true value. However, at phase angles between 45° and 90° , the probable phase angle values stretch across most of the phase angle solution space, making it more difficult to obtain good values. Observations with comparable SNR and multiple phase angles can therefore be extremely valuable in determining both orbital characteristics, if unknown or uncertain, and narrowing down planet radius.

Finally, we collate summary plots of the retrieved parameters at all seven phase angles (0° - 120°) and SNR values (5, 10, 20) for all four test cases. The retrieved values of methane abundance, surface gravity, planet radius, recovered phase angle and cloud pressures are respectively plotted against changing SNR and phase angle for Planet A (Figure 5.14), HD 192310c 1x (Figure 5.15), 10x (Figure

5.16) and 50x (Figure 5.17) cases. Colors represent the size of the 68% confidence interval values, seen for each parameter on the diagonal of probability distribution plots such as Figure 5.11.

Several trends are apparent from the summary figures. Generally speaking, we find that retrievals at higher SNR ratios (SNR = 20) place correct constraints on the atmospheric methane abundance, to within an order of magnitude. The low SNR=5 case identifies the presence of methane, but the abundance is highly uncertain (four orders of magnitude), as many combinations of cloud top pressure, phase angle, and gravity are able to adequately reproduce the noisy data.

In general, the high bright clouds found in this case seem to lead the retrievals to favor cloud tops deeper in the atmosphere than in the forward model, with lower brightness compensated by larger planetary radii. This is seen for all metallicities, particularly at low phase angles. The 1x metallicity case with the weakest methane features clearly presents a particular challenge, even at SNR of 10, as the methane abundance is nearly unconstrained. For all three metallicities considered, only the case with an SNR of 20 systematically reproduces close to the correct methane abundance at all phase angles. We discuss these findings further in the next section.

5.5 Discussion

In this section, we discuss how well the planet radius, phase angle, methane abundance and cloud properties were constrained in the presence of planet phase and radius uncertainties. We focus the discussion in this paper on the newly introduced

uncertain phase and radius determinations, as the abundance and cloud properties were the focus of [Lupu *et al.*, 2016].

5.5.1 Methane and Radius Retrieval

For the cases considered here we assumed that phase angle was almost completely unconstrained. While this is a situation unlikely to be encountered for a real planet, it is a difficult bounding case worthy of additional study. We find that phase angle is generally not well constrained from a single observed spectrum, since planet radius and cloud height trade against phase angle, resulting in large uncertainties in all parameters. Generally speaking, with no prior knowledge of orbital parameters from radial velocity, the most we can confidently tell about the phase angle from retrievals is whether it is *high* or *low* (above or below $\sim 90^\circ$).

One might expect the planet radius solution space to be similarly large, but this is not the case. Despite being given an impossibly large range of $0.1 - 100 R_J$, even at a low SNR of 5, the MCMC routine typically returns a solution within a factor of two of the true value ($\sim 1 R_J$). Regardless of true phase angle, the MCMC algorithm must match the observed flux from the planet. At more crescent phases, the atmosphere is highly forward scattering and molecular bands are weak. Since clouds are relatively less important at such scattering angles, this drastically reduces the number of free parameters. Consequently, we find the most accurate radius retrievals at the highest phase angles.

5.5.2 The impact of a known phase angle

Given the difficulty in retrieving the true phase angle from a single spectrum, we also explored the impact of a better-constrained phase angle, as might be expected during an observational campaign. To study this case we chose the 10x metallicity case for HD 192310c, at a favorable SNR of 20. Retrievals were performed on this case at multiple phase angles, given a $\pm 10^\circ$ restriction from the true value, on the possible values of the angle.

As seen in Figure 5.18, this does not significantly improve retrievals of gravity, cloud properties or the methane abundance. The only noticeable difference is that phase angle knowledge helps constrain the radius of the planet better, improving the radius determination by a factor of two. Given a proxy value for planet mass from radial velocity measurements ($M \sin i$), by improving knowledge of the planet radius, prior knowledge of the phase angle best helps improve the estimate of surface gravity (M/r^2), though this is not seen directly from gravity retrievals.

5.5.3 Applying an intersection criterion to multiple observations

It has been shown that planet radius retrievals, for example, improve with increasing phase angle, whereas retrievals for top cloud pressure improve with decreasing phase angle. Bounds on quantities such as methane abundance and cloud properties vary significantly with SNR. Simultaneous retrievals on observations taken at multiple phase angles would therefore likely hold promise for narrowing the solution space of best-fit models. While we did not perform simultaneous retrievals,

we present a preliminary investigation into their utility by imposing an intersection criterion.

The intersection criterion is defined as in set theory: for sets A and B , the intersection of sets ($A \cap B$) defines that set which contains only elements of A that also belong to B . For two observations taken at different phase angles, and separate retrievals, applying an intersection criterion means only those solutions that appear in both retrievals are considered valid. Here we use “observation” to refer to the integration time needed to produce one complete ~600-970 nm spectrum, at a given SNR. The intersection criterion is illustrated in Figure 5.19. While clearly an estimation, simultaneous retrievals against combined phase-varying datasets are planned as future work.

The underlying idea is that intersection of multiple observations at varying phase angles may determine a more likely range for parameters of interest. We begin by determining which combination of phase angles will be likely to improve retrievals the most. This analysis focuses on the lowest SNR case, as the uncertainty on retrieved results with one set of observed spectra is the highest, and multiple observations are likely to have the most impact. The HD 192310c 10x case is chosen again here, although a similar analysis may be conducted for any planet targeted as part of an observational campaign.

Figure 5.20 shows the improvement in 68% confidence intervals achieved by applying the intersection criterion to all phase angle solutions, for HD 192310c 10x, at an SNR of 5. Here, “improvement” denotes the difference between 1) confidence

intervals obtained using single observations and 2) intervals obtained by applying an intersection criterion to multiple observations taken at differing phase angles. A value of zero for improvement represents one of two cases; either 1) there is no overlap between retrieved values at different phases, and the solutions must be considered independently, or 2) returned solutions are completely identical at both phase angles. In either case, considering multiple observations does not represent an improvement over a single observation. Conversely, peaks represent cases where confidence intervals were tightened by applying an intersection criterion to multiple observations, i.e., we can estimate which combination of phase angles may be most helpful to reduce uncertainty in retrieved quantities. For example, for methane, if a first observation is taken at $\alpha=70^\circ$ (x-axis), a subsequent observation at $\alpha=30^\circ$ (yellow line) would improve the 68% confidence interval by approximately 1.4 orders of magnitude (y-axis).

Figure 5.20 shows that a steadily increasing improvement in estimates of planet radius can be expected with two observations at phase angles that exceed 45° . For example, for one observation at 70° and another at 120° , the estimate for planet radius can be improved by a factor of two, a significant improvement when considering that the best-fit solution from a single observation was already within a factor of two of the true solution. Similarly, confidence intervals on surface gravity may be improved by as much as $55 - 60 \text{ ms}^{-2}$ if observations are gathered at 0° and 70° phase angle, though gains of $>30 \text{ ms}^{-2}$ are possible with other combinations. Both these cases were also illustrated in Figure 5.19.

Similarly, the uncertainty in methane composition from retrievals against an observation taken at near-quadrature can be driven down by almost two orders of magnitude if combined with a low phase angle observation, but in the absence of such an observation, may still be reduced by 0.8 orders with an observation at 45° phase angle. The intersection criterion presents a way to estimate trends in phase-varying behavior; future simultaneous retrievals and joint probability distributions created from multiple observations will quantify the exact improvement.

Such improvements will of course be reduced with increasing SNR (smaller probability bounds, greater overlap), and with more than two observations. During an actual space-based observational campaign, operational or other constraints may limit the ability to observe a planet at a favorable viewing geometry. Therefore, we now estimate the likelihood of improvement in confidence intervals.

We randomly choose three phase-varying observations, and compare the intersection criterion result with that of a single observation, also randomly chosen. Figure 5.21 plots the improvement with the intersection criterion, for every possible three-observation combination of the seven phase angles studied here, for both Planet A and the 10x HD 192310c case. As expected, for either planet, the improvement generally does not exceed an order of magnitude for the $\text{SNR} = 20$ case. However for $\text{SNR} = 5$, the improvement is significant in all cases, even for largely invariant parameters such as gravity (marker d-e), but particularly for cloud parameters (marker f-g) and methane abundance. Up to 3.5 orders of magnitude in improvement for the methane abundance is seen for Planet A (marker h), depending on the phase angle

combinations; recall that for this case, we were unable to do much better than determine the presence of methane.

Similar results are seen for four and more observations. Such plots allow us to build an idea of trends for improvement in uncertainty estimates. These trends will be important for mission planning for WFIRST; these also present a starting point for estimating science return for realistic mission scenarios, where data is available from multiple observations at different phase angles and low SNR.

5.6 Conclusions

We have studied a number of retrievals on simulated phase-varying spectra, incorporating different metallicities, star-planet fluxes and signal-to-noise ratios. Specifically we presented results of how the unknown planet radius and potentially poorly known observer-planet-star phase angle can impact retrievals of atmospheric methane abundance, cloud properties and surface gravity, among others.

Given a varying planet phase, we find that the methane abundance can typically only be constrained to the correct order of magnitude at SNR of 20 or greater. For all three metallicities considered (1x, 10x, 50x solar), only the case with an SNR of 20 reproduces to the correct methane abundance at all phase angles. Low SNR cases merely identify the presence of methane, with the abundance being highly uncertain across several orders of magnitude, an important result for the design of future space-based missions such as WFIRST.

Surface gravity appears essentially unconstrained. The top cloud in a two-layer cloud model is well constrained, but is indeterminate on the pressure gap between cloud layers, indicating that a one-cloud model might be better suited to the examples in this paper. However our MCMC methods are able to return a solution for planet radius within a factor of two of the true value, even at low SNR values. Surprisingly, the confidence interval on the radius solution decreases with increasing phase angle. Since the atmosphere is highly forward scattering and molecular bands are weak at more crescent phases, clouds become less important. Retrievals for radius are consequently best at the highest phase angles.

We find that knowledge of the phase angle, and therefore its elimination as a free parameter, does not significantly improve estimates for methane abundance, cloud parameters or gravity. However it does improve the radius determination by a factor of two. On the other hand, with no prior knowledge of orbital parameters, the most we can confidently tell about the phase angle from retrieved results is whether it is high or low. Observations with comparable SNR and multiple phase angles can therefore be extremely valuable in determining both orbital characteristics, if unknown or uncertain, and narrowing down planet radius.

Finally, we find that simultaneous retrievals on observations taken at multiple phase angles holds promise for narrowing the solution space of best-fit models. We estimate this using an intersection criterion and find a steadily increasing improvement in estimates of all parameters, even for generally indeterminate parameters such as surface gravity and retrieved phase angle. For low SNR cases,

estimates for methane abundance can be improved by as much as 1-2 orders of magnitude if multiple observations at different phase angles are gathered, a fact of interest when planning future space-based observational campaigns. However, it is important not to assign too much importance to this, since even though bounds on the solution may decrease, this does not guarantee the *accuracy* of the solution. At low SNRs, the recovered methane solution is far separated from the true value at all phase angles. The best that multiple observations at low SNR can hope to accomplish is the information content of one observation at high SNR.

Our group is continuing to pursue MCMC methods for application to reflected-light spectral data in the context of a wide range of future missions, including WFIRST. Future work will focus on a continued improved treatment of clouds and hazes, as well as Raman scattering, although we expect this latter effect to be minimal, since Raman scattering features are weak in the visible wavelengths [Karkoschka, 1994]. We will also pursue retrievals to determine the planetary temperature-pressure profile via the reflection spectrum. Finally, we will perform simultaneous retrievals on observations taken at multiple phase angles, an improvement on the intersection criterion approximation investigated here.

5.7 Figures

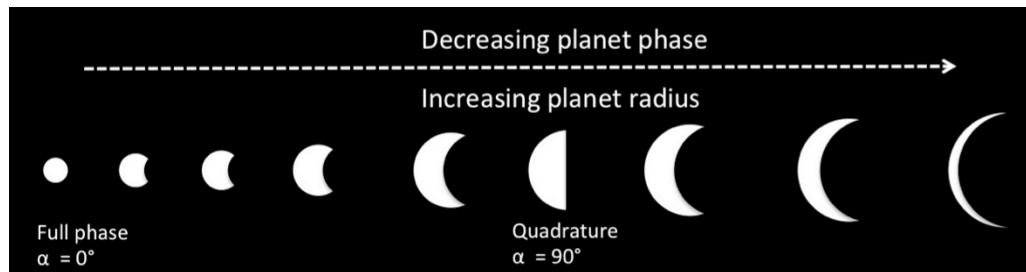


Figure 5.1. Illustration of the degenerate relationship between decreasing planet phase (increasing phase angle α) and increasing planet radius, in yielding an equivalent scattered flux. If the planet phase is unknown or uncertain, a larger planet at a crescent phase may reflect essentially the same amount of light as a smaller planet at a fuller phase.

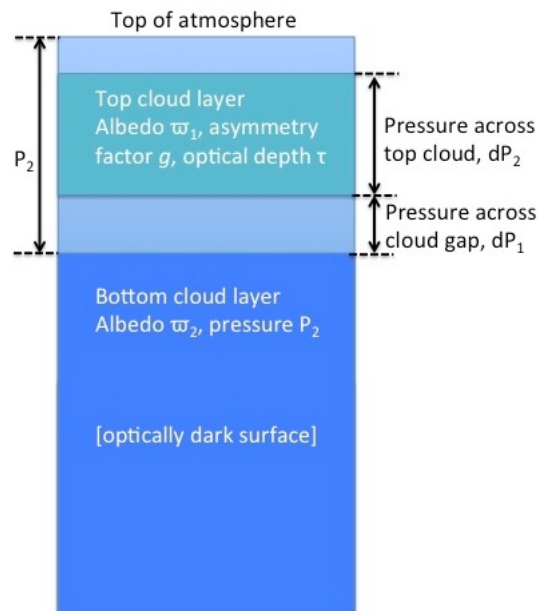


Figure 5.2. Illustrative representation of two-layer cloud model employed, after Marley et al. (2014).

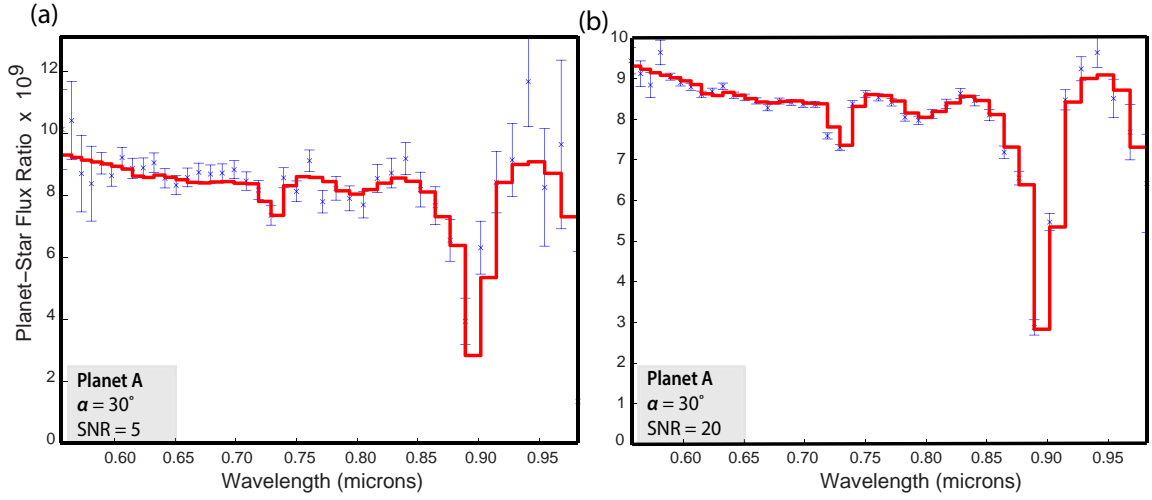


Figure 5.5. Contrast spectra for Planet A at SNR values of (a) 5 and (b) 20. Spectra are generated at a spectral resolution of $R = 70$ and a phase angle of 30° . Red represents the truth spectra and blue error bars represent notional instrument noise during observation [Robinson *et al.*, 2015].

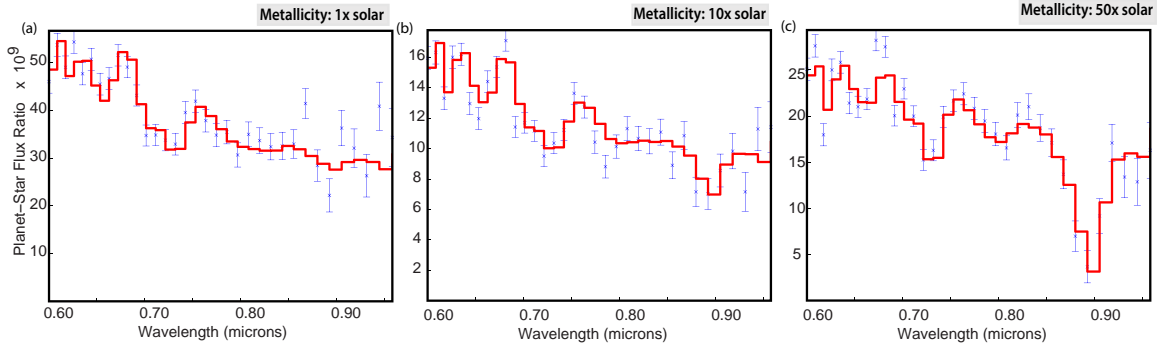


Figure 5.6. Contrast spectra for HD 192310c generated at metallicity values of (a) 1x, (b) 10x and (c) 50x that of the Sun. The difference in the methane absorption signature at ~ 0.9 micron is evident. Spectra are generated at phase angles of 0° , $\text{SNR} = 20$ and spectral resolution of $R = 70$.

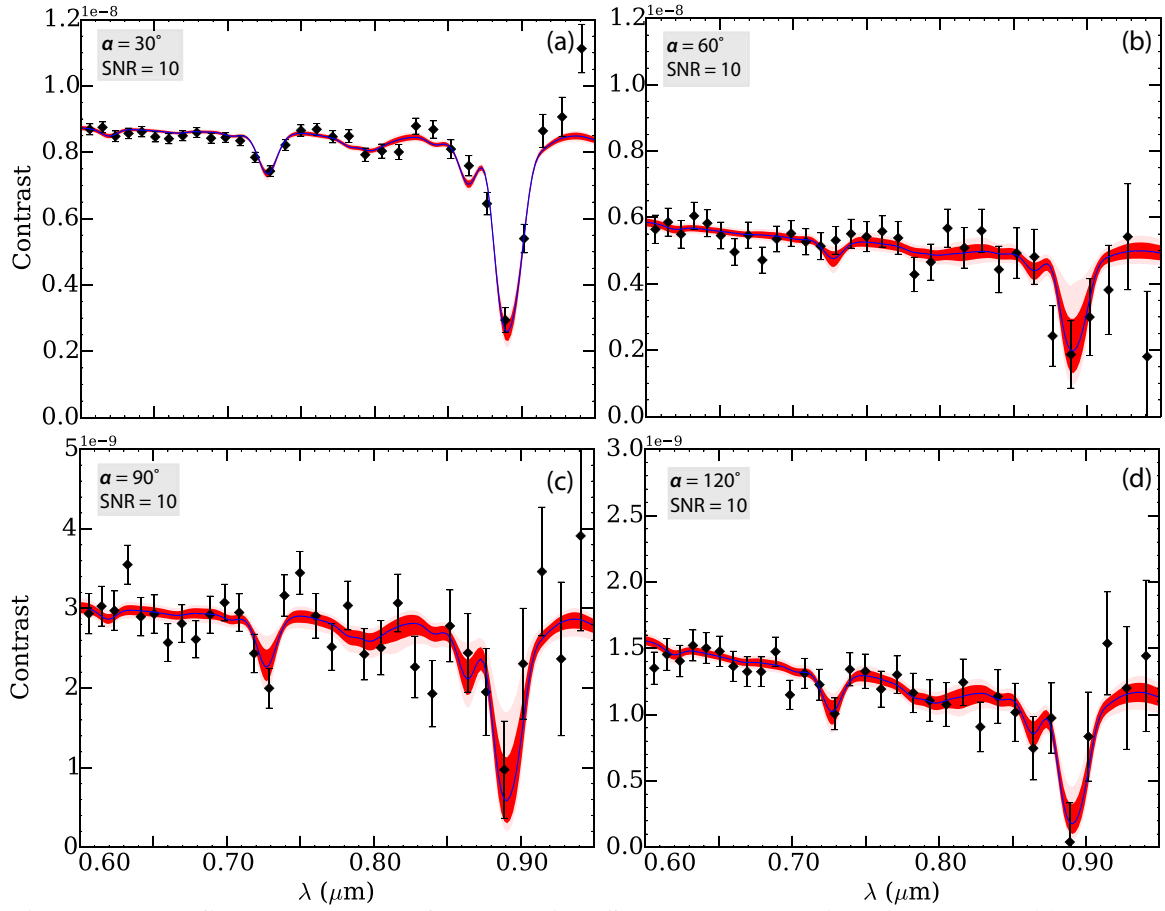


Figure 5.7. Best-fit contrast spectra for Planet A at SNR = 10 and varying phase angles: (a) 30°; (b) 60°; (c) 90°; (d) 120°. Model spectra are calculated from the best 198,000 samples (1500 iterations) of the 330,000 final sample chain (2500 iterations). The median spectrum (blue) matches well to the truth spectrum (black). 16-84% (dark red) and 4.5-95.5% (light red) percentile range of recovered solutions are also shown. Good matches to the model truth spectra are seen in all cases, even at relatively low contrast signals for large phase angles. Note the differing (smaller) vertical scales between (a) and (d).

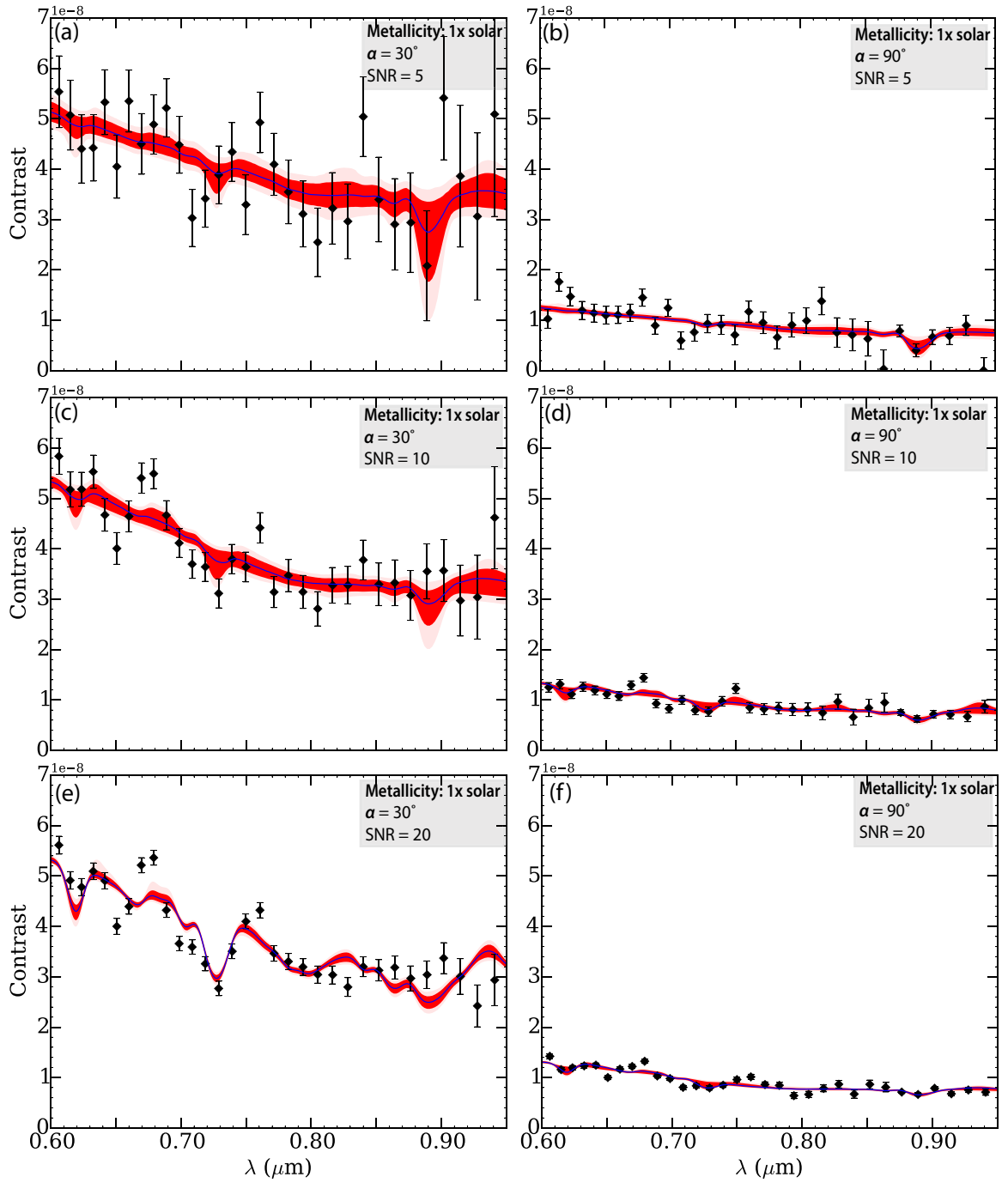


Figure 5.8. Best-fit contrast spectra for HD 192310c at a metallicity of 1x solar and varying SNR and phase angle: (a) SNR = 5, $\alpha = 30^\circ$; (b) SNR = 5, $\alpha = 90^\circ$; (c) SNR = 10, $\alpha = 30^\circ$; (d) SNR = 10, $\alpha = 90^\circ$; (e) SNR = 20, $\alpha = 30^\circ$; (f) SNR = 20, $\alpha = 90^\circ$. Note the lack of the characteristic methane absorption signal at 0.9 microns for high phase angles. Description of colors is as in Figure 5.7.

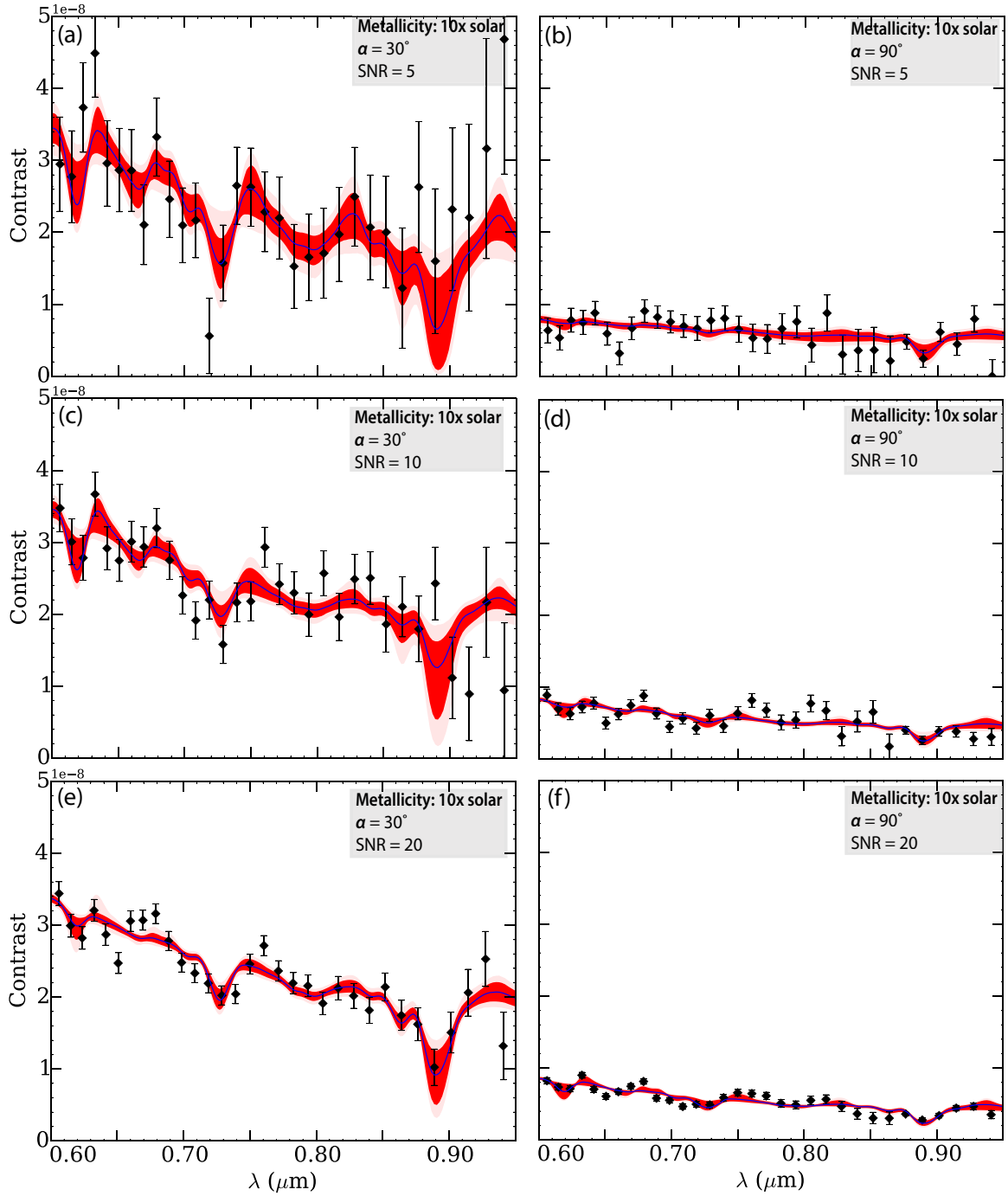


Figure 5.9. Best-fit contrast spectra for HD 192310c at a metallicity of 10x solar and varying SNR and phase angle: (a) SNR = 5, $\alpha = 30^\circ$; (b) SNR = 5, $\alpha = 90^\circ$; (c) SNR = 10, $\alpha = 30^\circ$; (d) SNR = 10, $\alpha = 90^\circ$; (e) SNR = 20, $\alpha = 30^\circ$; (f) SNR = 20, $\alpha = 90^\circ$. Good matches to the model truth spectra are seen in all cases, even at relatively low contrast signals for large phase angles. The improvement in recovered signal is evident with increasing SNR from (a) through (f). Description of colors is as in Figure 5.7.

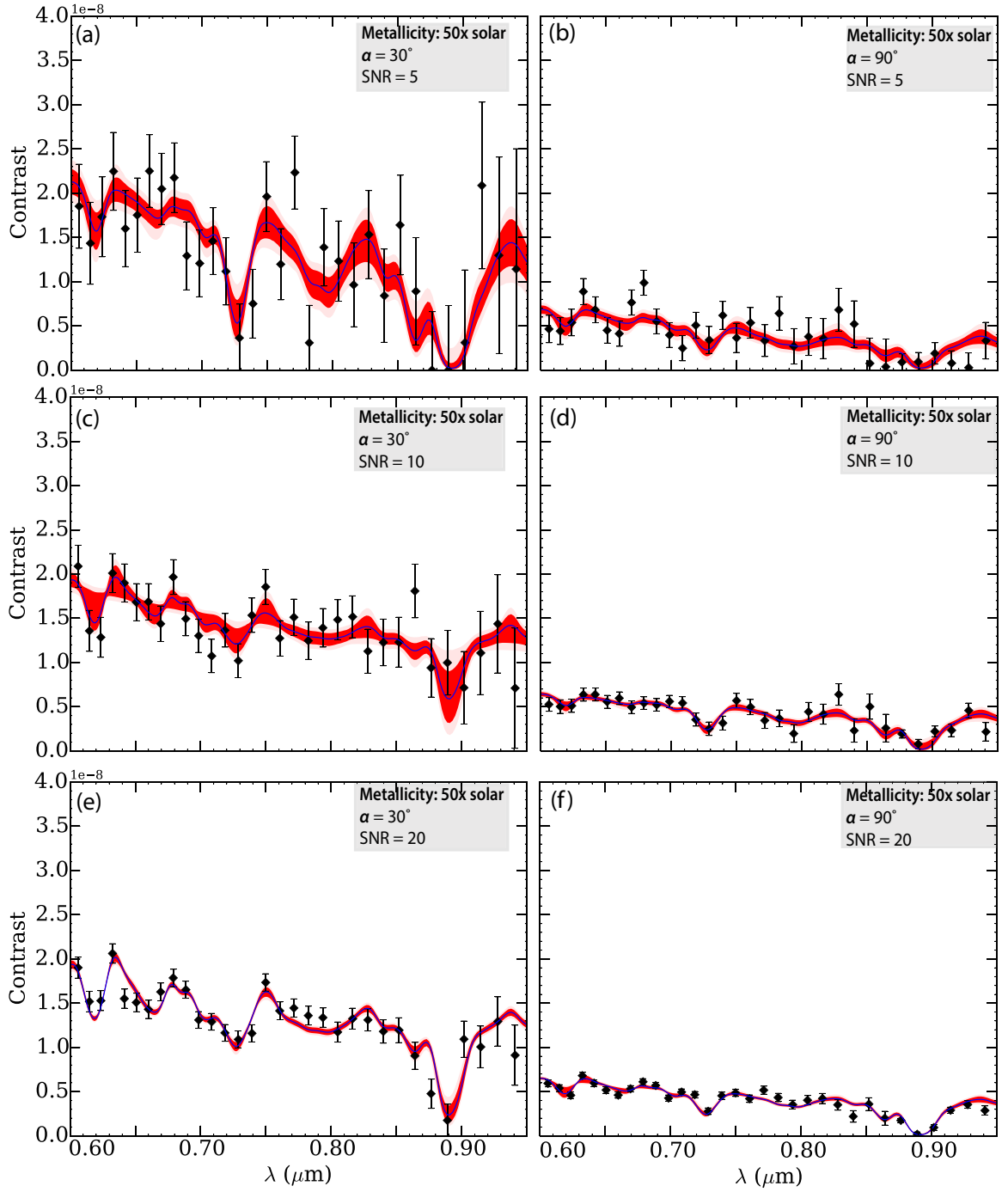


Figure 5.10. Best-fit contrast spectra for HD 192310c at a metallicity of 50x solar and varying SNR and phase angle: (a) SNR = 5, $\alpha = 30^\circ$; (b) SNR = 5, $\alpha = 90^\circ$; (c) SNR = 10, $\alpha = 30^\circ$; (d) SNR = 10, $\alpha = 90^\circ$; (e) SNR = 20, $\alpha = 30^\circ$; (f) SNR = 20, $\alpha = 90^\circ$. Good matches to the model truth spectra are seen in all cases, even at relatively low contrast signals for large phase angles. The improvement in recovered signal is evident with increasing SNR from (a) through (f). Description of colors is as in Figure 5.7.

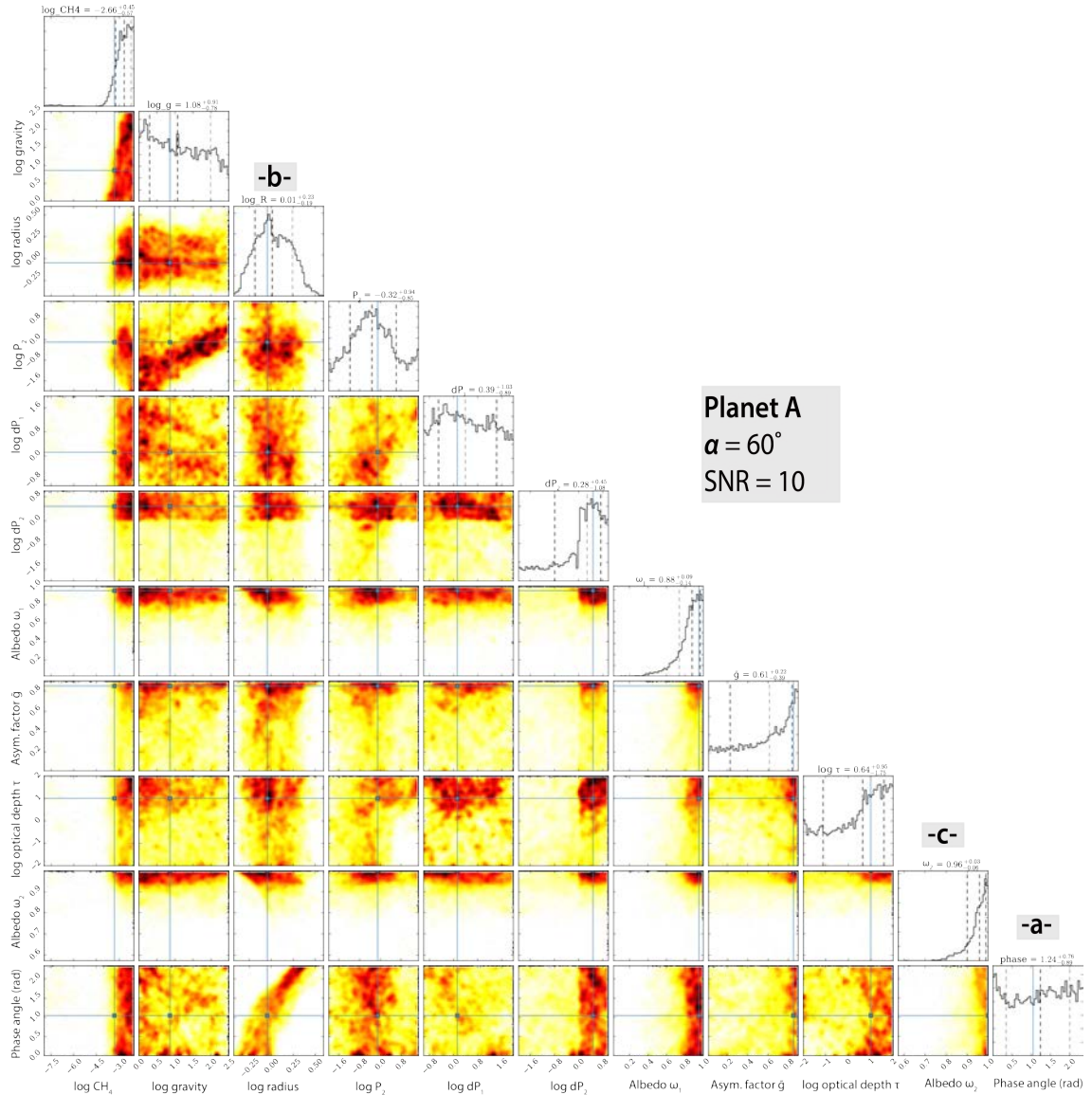


Figure 5.11. Posterior probability distribution plot for all eleven parameters retrieved by the MCMC algorithm (Table 5.1), for the case of Planet A at SNR = 10 and phase angle 60° (Figure 5.7c). Darker regions represent higher probability. Blue dots represent true values. The distributions are drawn from all remaining samples after the MCMC burn-in chains (first 1000 chains) are discarded. The diagonal of the plot represents the marginalized probability distributions for each parameter. Best-fit values in log space (except for phase angle) are shown. See text for references to text markers a-c. The error bars indicate (left to right) the 16%, 84% and 50% quantiles, i.e., this is the 68% confidence interval.

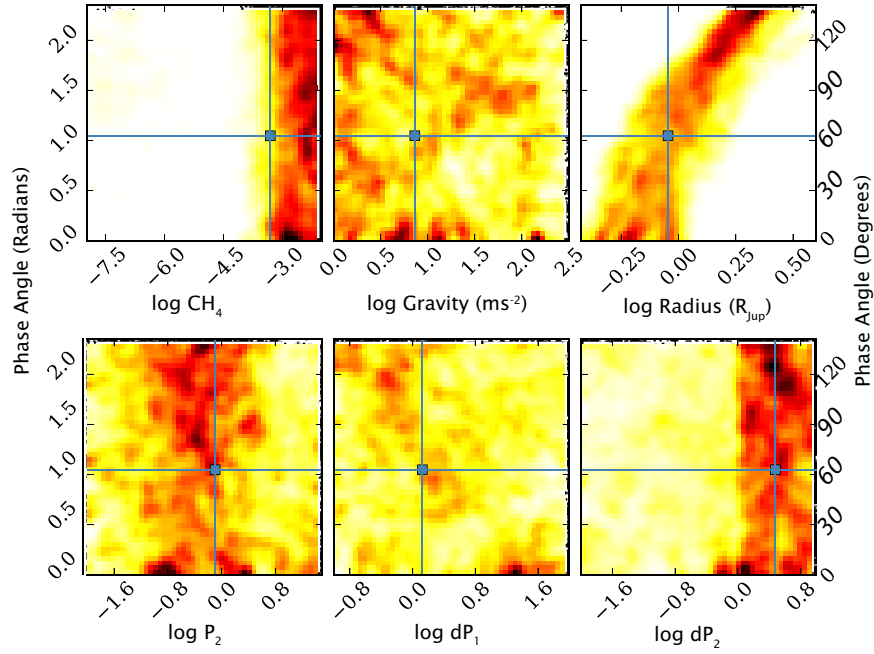


Figure 5.12. Highlight of pertinent parameter relationships with planet phase angle, excerpted from Figure 5.11. The top row shows probability distributions of phase angle against methane abundance, surface gravity and planet radius. The bottom row shows distributions of phase angle against, respectively, the pressure of the bottom cloud (P_2) in the two-layer model by Marley et al. (2014), the pressure difference between the two cloud layers (dP_1) and the pressure difference across the top cloud layer (dP_2). All parameters are in log space (except phase angle).

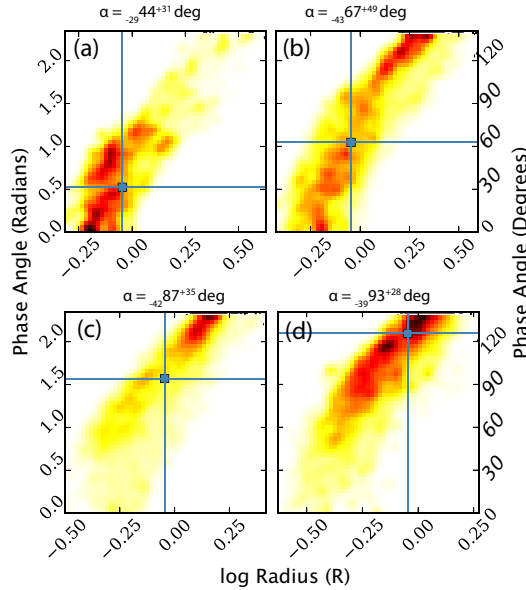


Figure 5.13. The relationship of planet radius with changing planet phase angle, for the Planet A test case, for an SNR of 20 and a truth phase angle (blue square) of: (a) 30° ; (b) 60° , (c) 90° and (d) 120° . The MCMC algorithm retrieves phase angle and radius values close to the true value for planet phases close to full phase and past quadrature. Best-fit values for each case are

indicated above the figure; superscripts and subscripts to this value indicate upper and lower bounds returned from the posterior probability plot diagonals (e.g. Figure 5.11).

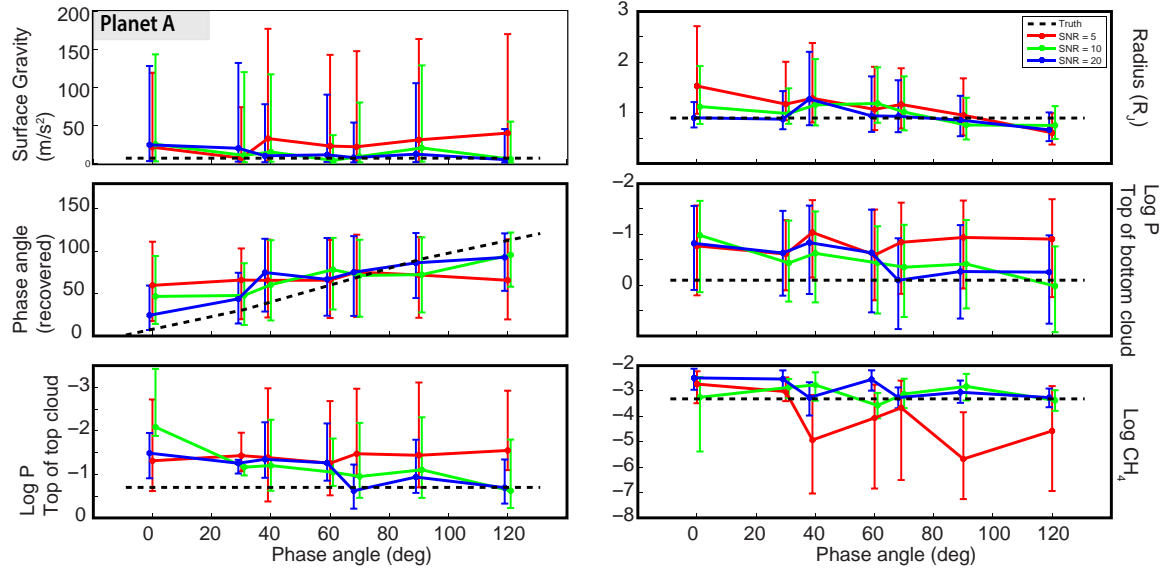


Figure 5.14. Summary of all results for Planet A test case. True phase angle varies from 0° to 120° . SNR varies between 5 (red), 10 (green) and 20 (blue). Error bars enclose the 68% confidence interval as defined by MCMC posterior probability distributions similar to Figure 5.11. Solid dots denote the best-fit values. A black dashed line denotes true values from the Planet A model.

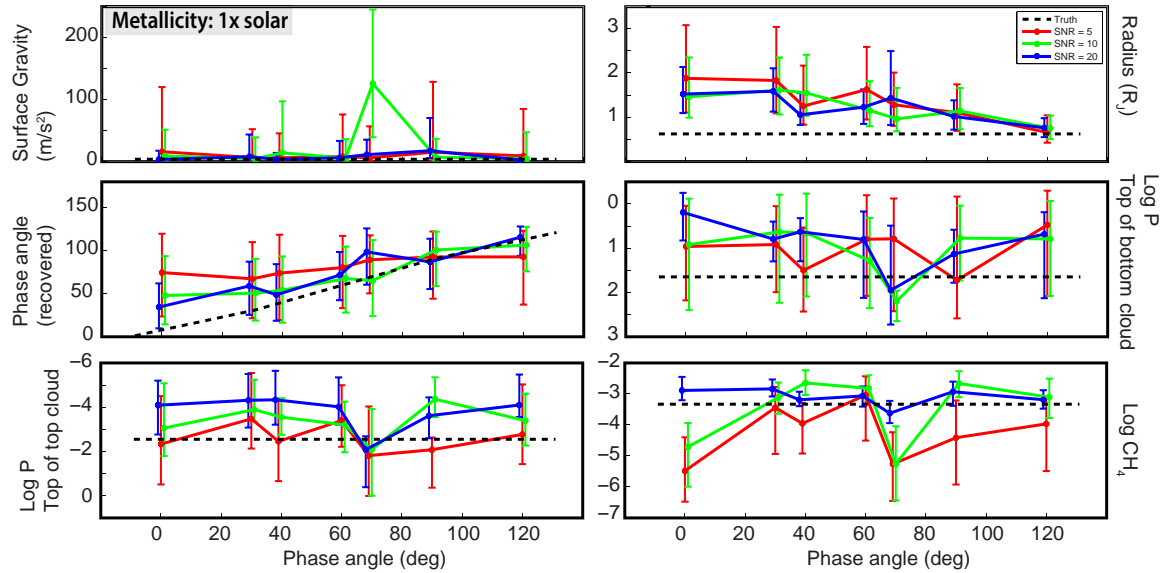


Figure 5.15. Summary of all results for the HD 192310c test case with 1x metallicity of the Sun. True phase angle varies from 0° to 120° . SNR varies between 5 (red), 10 (green) and 20 (blue). Error bars are as in Figure 5.14. Solid dots denote the best-fit values. A black dashed line denotes true values from the HD 192310c model.

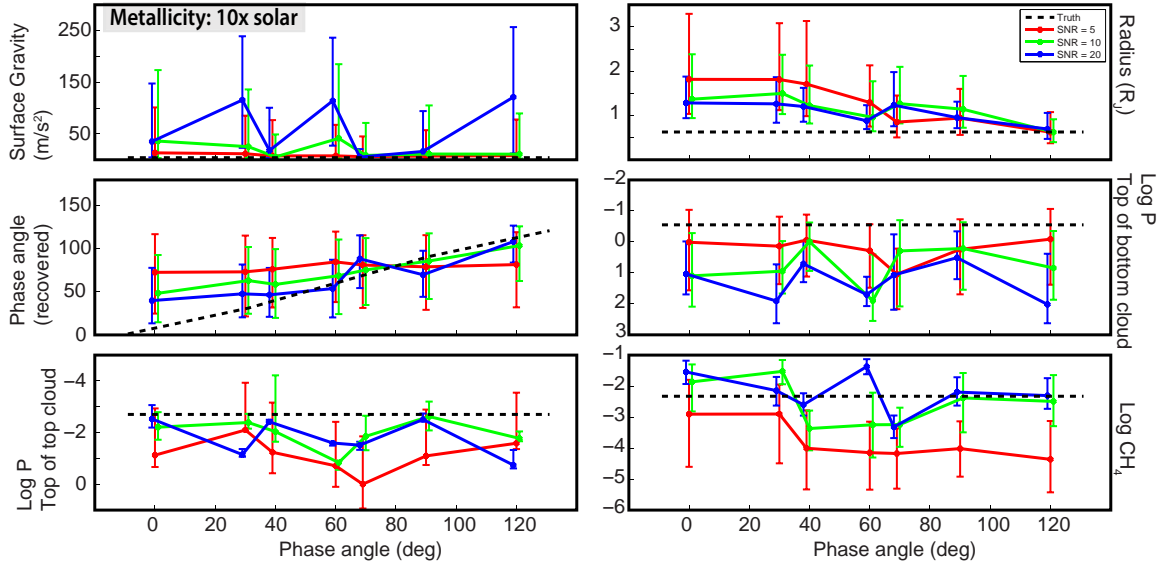


Figure 5.16. Summary of all results for the HD 192310c test case with 10x metallicity of the Sun. True phase angle varies from 0° to 120°. SNR varies between 5 (red), 10 (green) and 20 (blue). Error bars and solid dots are as in Figure 5.14. A black dashed line denotes true values from the HD 192310c model.

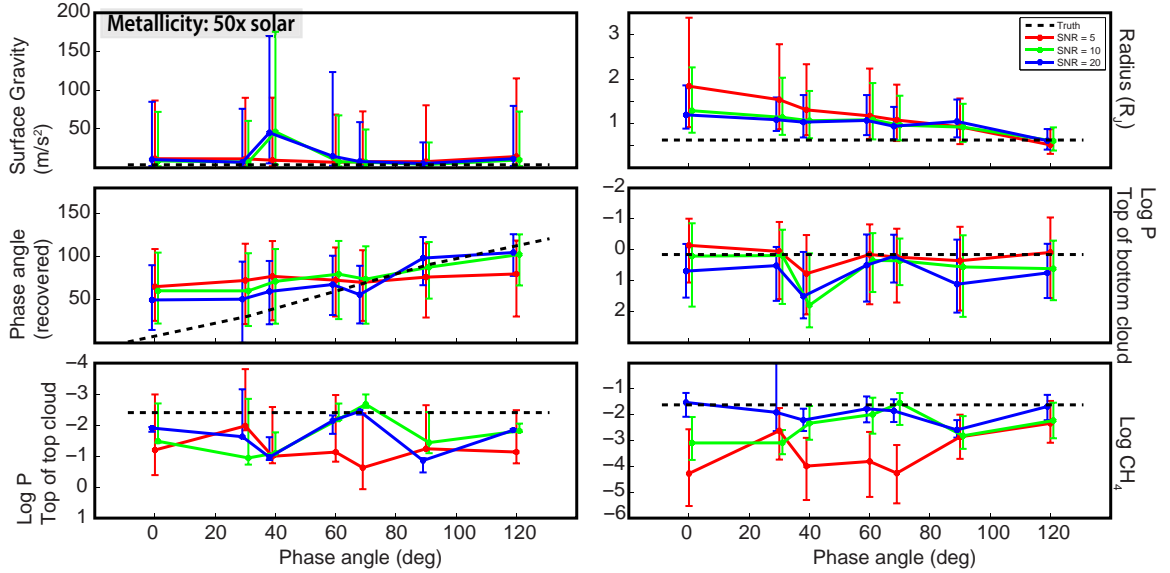


Figure 5.17. Summary of all results for the HD 192310c test case with 50x metallicity of the Sun. True phase angle varies from 0° to 120°. SNR varies between 5 (red), 10 (green) and 20 (blue). Error bars and solid dots are as in Figure 5.14. A black dashed line denotes true values from the HD 192310c model.

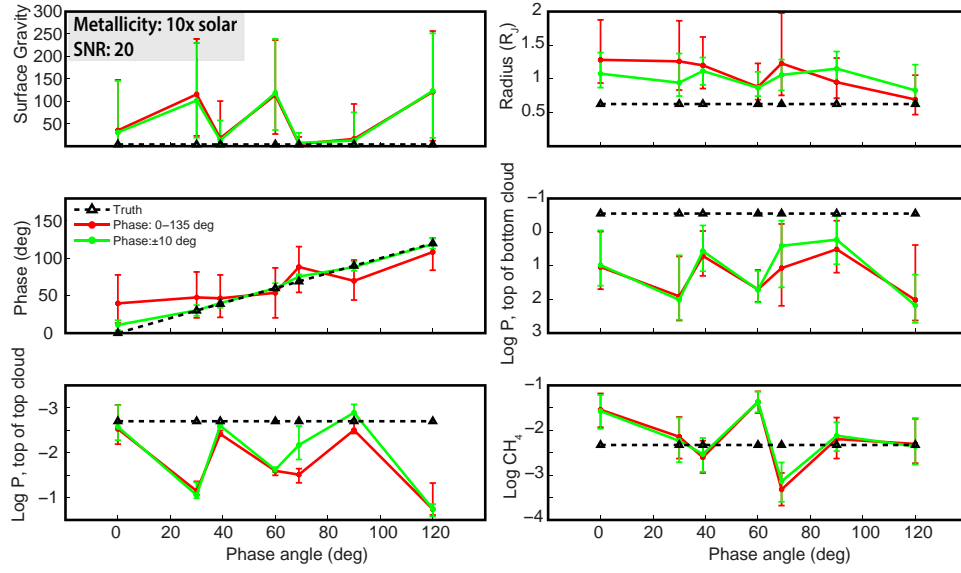


Figure 5.18. Results for the 10x metallicity case of HD 192310c, at SNR = 20, for an unbounded phase angle case (red) and a bounded case (green), where for the bounded case, the phase angle can vary by no more than 10° from the true value. No impact to cloud property or methane abundance retrievals are seen, however, the retrieved radius of the planet improves by a factor of two.

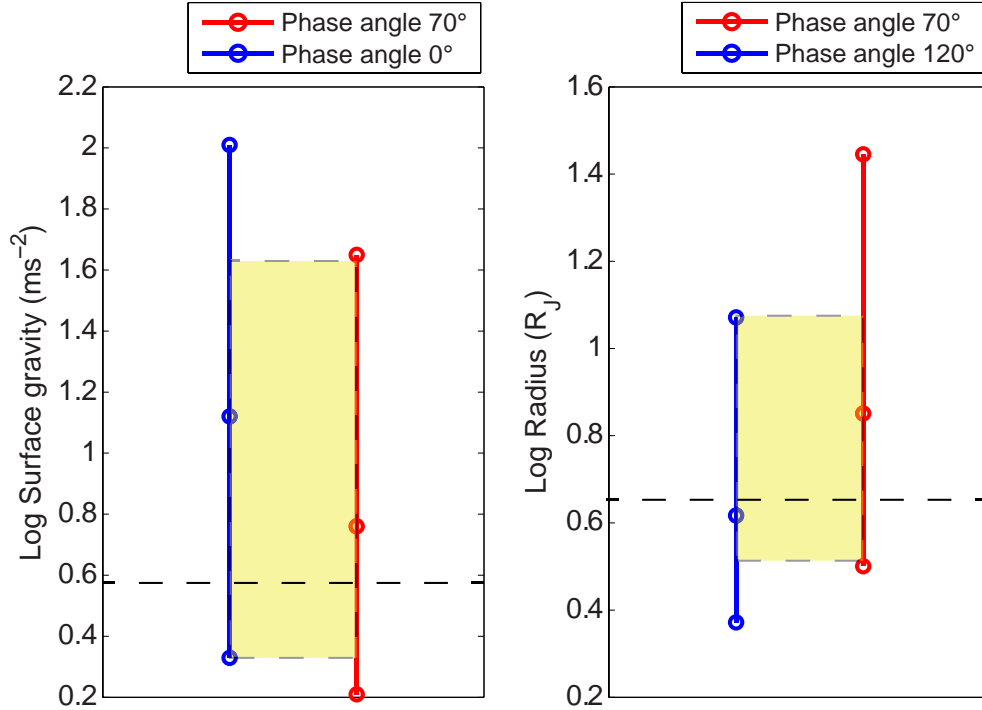


Figure 5.19. Illustration of the intersection criterion for surface gravity and planet radius (note log units for both). Data is from retrievals for HD 192310c, metallicity 10x solar and an SNR of 5. Phase angles are shown in the legend. The dashed black line indicates true values. The highlighted yellow area represents the region of solutions common to both retrievals (intersection criterion); it can be seen to visibly improve error bars on both cumulative solutions.

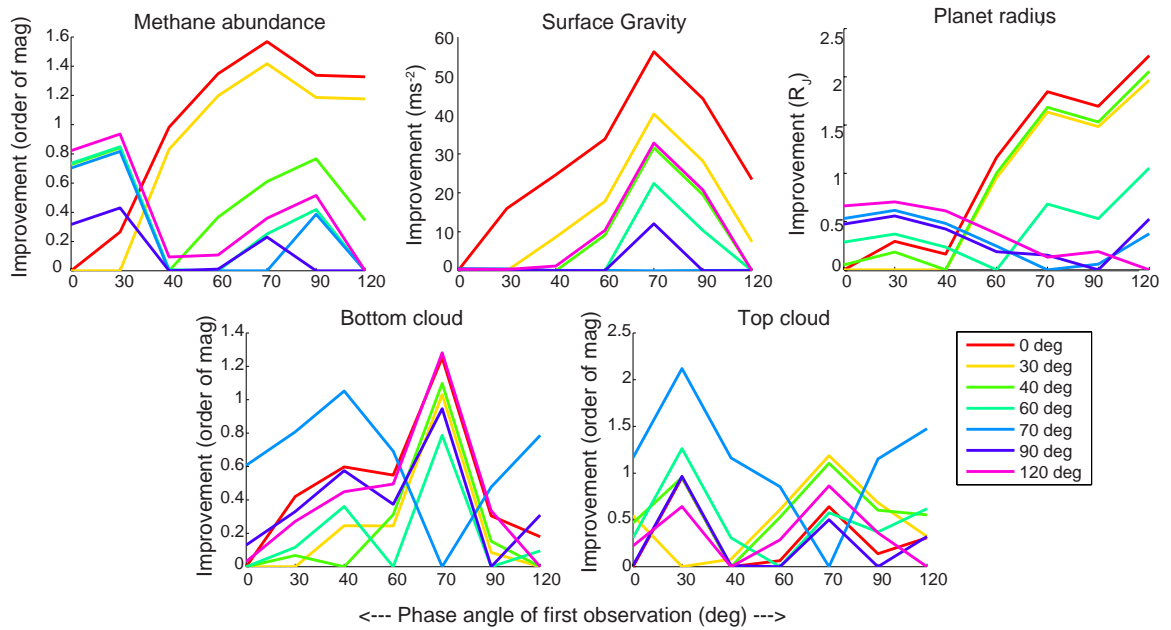


Figure 5.20. Improvement in 68% confidence interval ranges for methane abundance, surface gravity, planet radius, retrieved phase angle and two-cloud top pressures; peaks represent maximum improvement between two observations taken at different phase angles. Results are for HD 192310c (10x metallicity case) at SNR = 5. The first phase angle is represented on the x-axis; the second as colored lines (see figure legend). Units of the relative improvement are indicated in the figure titles.

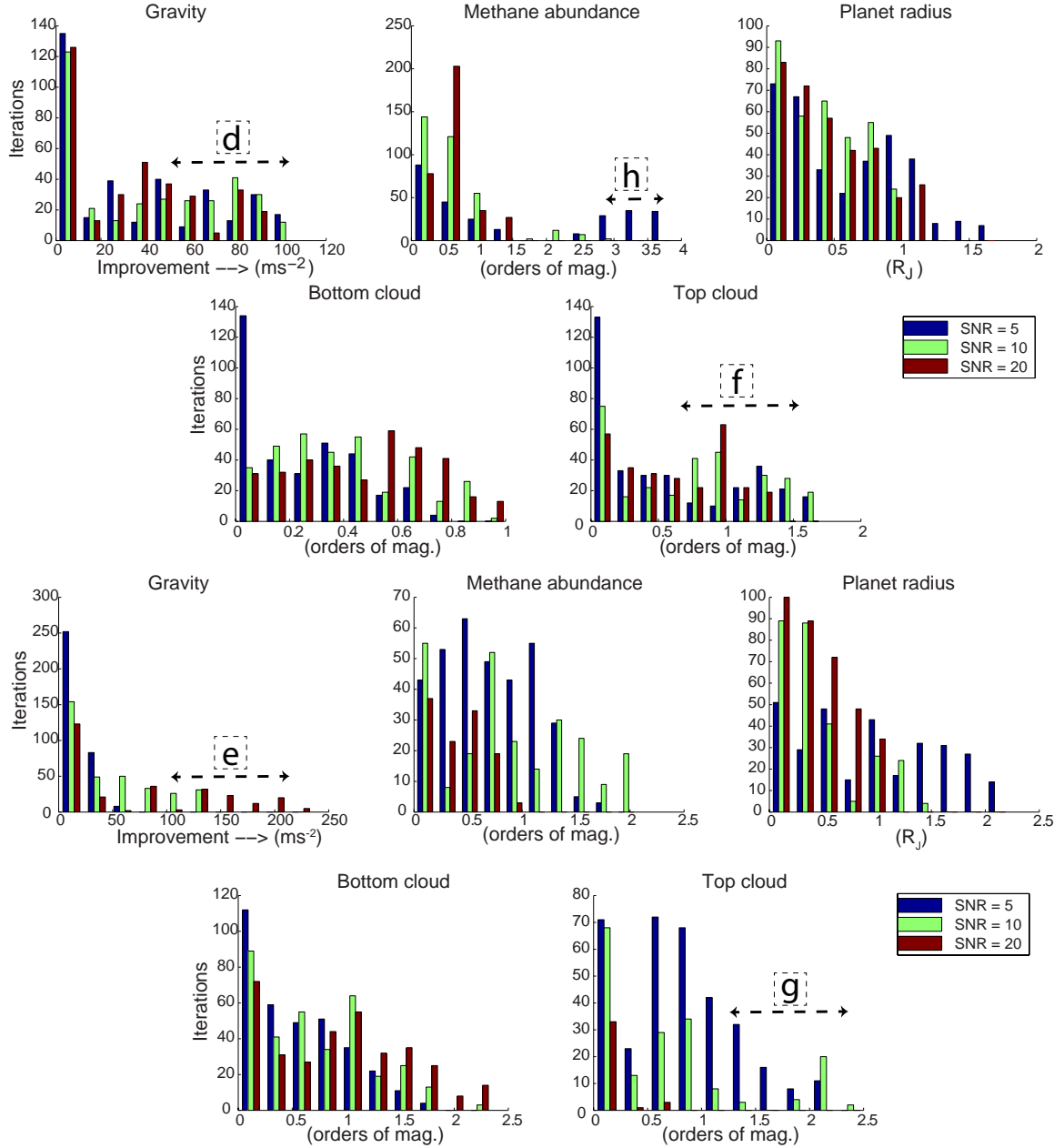


Figure 5.21. Improvement in 68% confidence intervals for an intersection criterion applied to three randomly chosen phase-varying observations of (A) Planet A and (B) HD 192310c, 10x metallicity case, compared to a randomly chosen single observation. SNR values of 5-20 are shown (blue: SNR 5, green: SNR 10, red: SNR 20). See text for references to text markers d-h. This plot may be used to determine trends for improvement in uncertainty estimates by retrieving against multiple datasets collected at differing phase angles. For example, for gravity, most cases show no improvement in gravity estimates (improvement clusters around 0 ms⁻²), regardless of SNR, when confidence intervals from multiple observations are stacked together, regardless of the phase angle of the single observation. However, for methane abundance, a significant number of SNR 5 cases (blue) show at 0.5-1 order of magnitude improvement when the intersection criterion is applied to multiple observations. A similar trend is noted for higher SNR cases, although the number of cases that note this improvement drops off as expected.

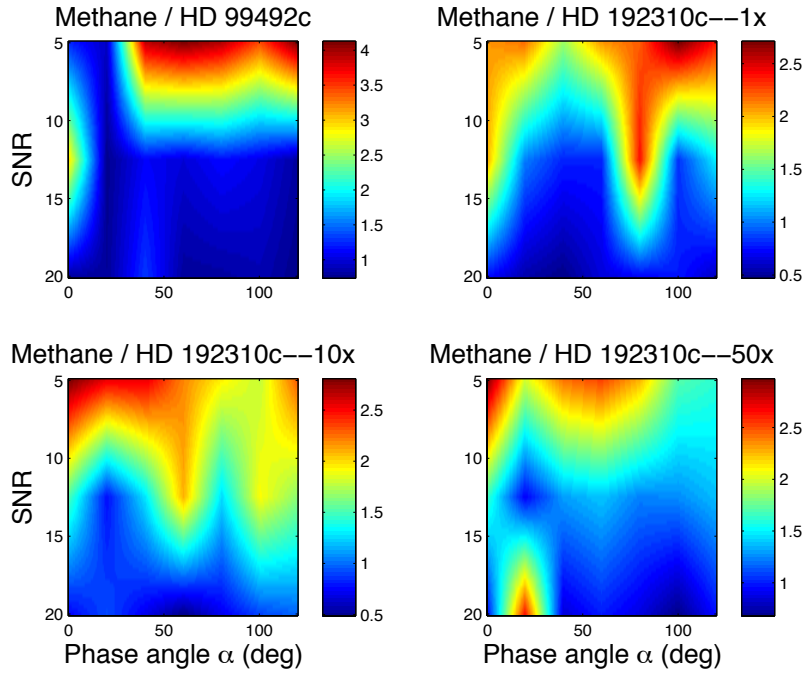


Figure 5.22. SNR versus phase angle relationships for all four test cases, with respect to methane abundance. Colors indicate the size of 68% confidence interval error bars in orders of magnitude. Values originate from posterior probability distributions similar to Figure 5.11. Blue colors indicate a tighter confidence interval, i.e., a better retrieval.

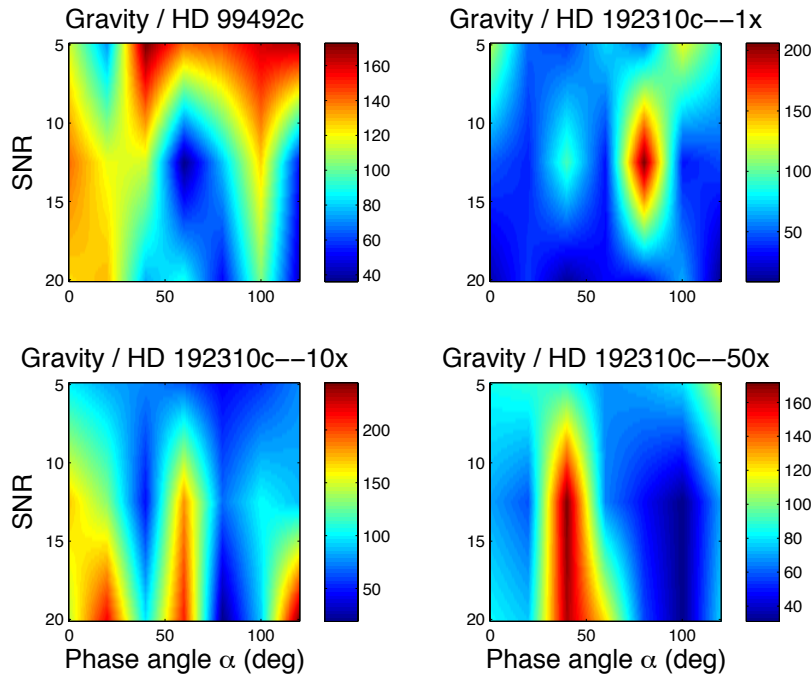


Figure 5.23. SNR versus phase angle relationships for all four test cases, with respect to surface gravity. Colors indicate the size of 68% confidence interval error bars in units of ms^{-2} . Values originate from posterior probability distributions similar to Figure 5.11. Blue colors indicate a tighter confidence interval, i.e., a better retrieval.

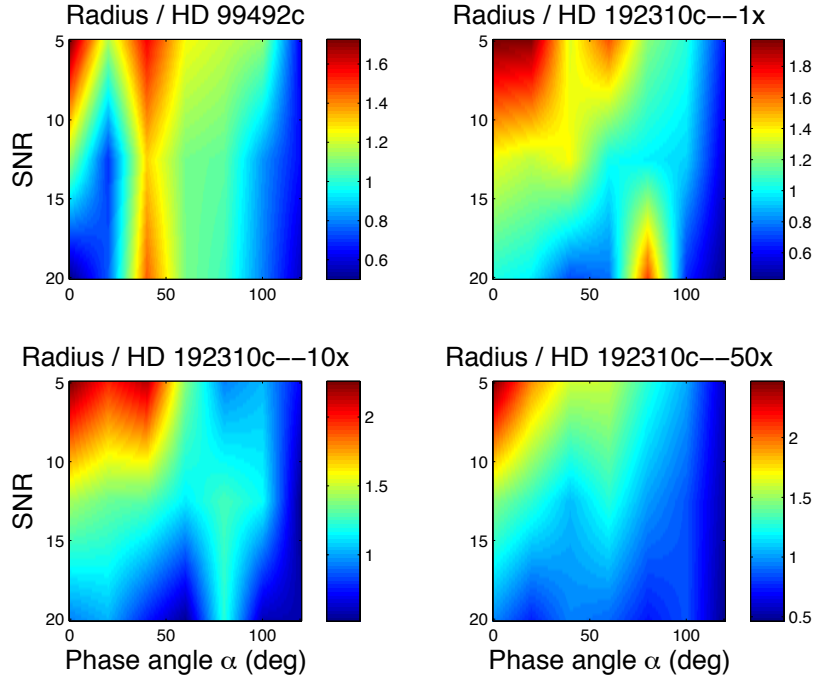


Figure 5.24. SNR versus phase angle relationships for all four test cases, with respect to planet radius. Colors indicate the size of 68% confidence interval error bars in units of R_J . Values originate from posterior probability distributions similar to Figure 5.11. Blue colors indicate a tighter confidence interval, i.e., a better retrieval.

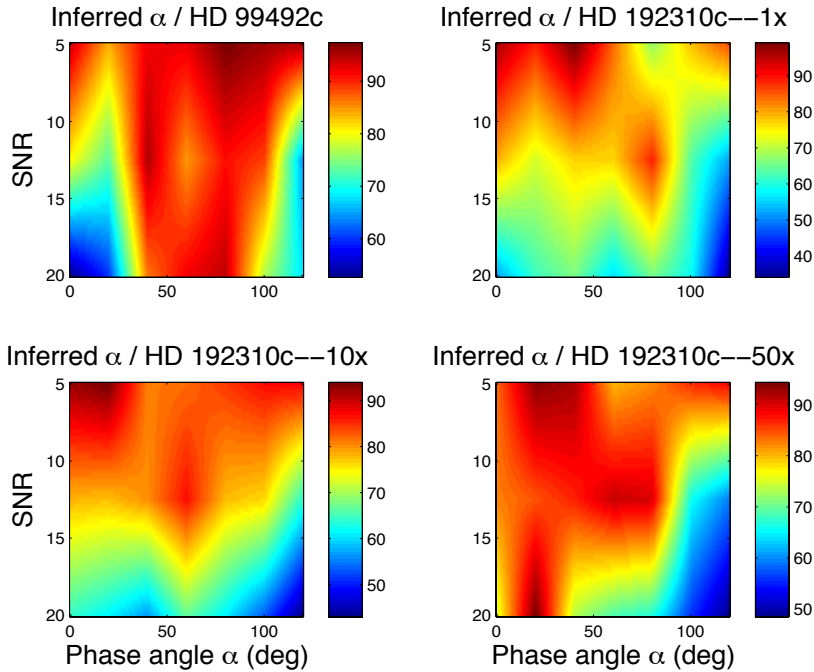


Figure 5.25. SNR versus phase angle relationships for all four test cases, with respect to inferred phase angle. Colors indicate the size of 68% confidence interval error bars in units of degrees. Values originate from posterior probability distributions similar to Figure 5.11. Blue colors indicate a tighter confidence interval, i.e., a better retrieval.

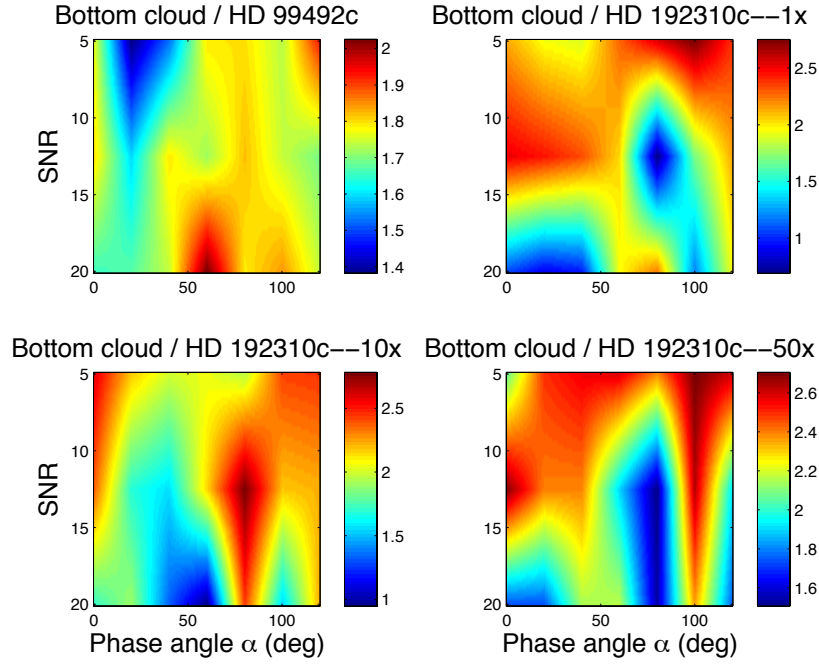


Figure 5.26. SNR versus phase angle relationships for all four test cases, with respect to the pressure at the top of the bottom cloud. Colors show size of 68% confidence interval error bars in orders of magnitude. Values originate from posterior probability distributions similar to Figure 5.11. Blue colors indicate a tighter confidence interval, i.e., a better retrieval.

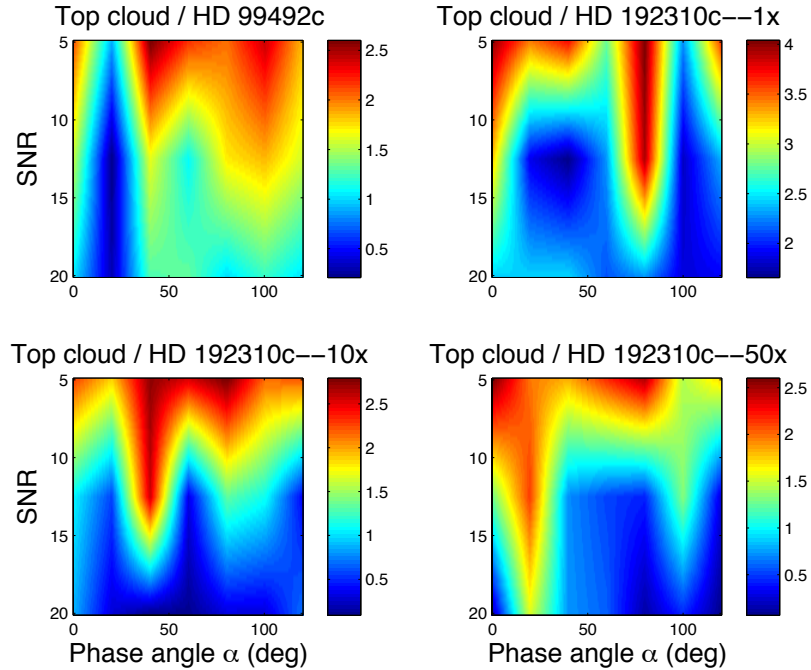


Figure 5.27. SNR versus phase angle relationships for all four test cases, with respect to the pressure at the top of the top cloud. Colors show size of 68% confidence interval error bars in orders of magnitude. Values originate from posterior probability distributions similar to Figure 5.11. Blue colors indicate a tighter confidence interval, i.e., a better retrieval.

Chapter 6

Bibliography

1. Acton, C., N. Backman, L. Elson, B. Semenov, F. Turner, and E. Wright (2002), Extending NASA's SPICE ancillary information system to meet future mission needs, in *2002 AIAA Space Operations Conference Proceedings*, pp. 8–11.
2. Alvarelos, J., K. J. Zahnle, A. R. Dobrovolskis, and P. Hamill (2002), Orbital Evolution of Impact Ejecta from Ganymede, *Icarus*, *160*(1), 108–123, doi:10.1006/icar.2002.6950.
3. Alvarelos, J. L., K. J. Zahnle, A. R. Dobrovolskis, and P. Hamill (2008), Transfer of mass from Io to Europa and beyond due to cometary impacts, *Icarus*, *194*(2), 636–646, doi:10.1016/j.icarus.2007.09.025.
4. Andrews, R. J. (1975), Origin and distribution of ejecta from near-surface laboratory-scale cratering experiments, *US Air Force Rep. AFWL-TR-74-314*.
5. Andrews-Hanna, J. C., J. Besserer, J. W. Head III, C. J. A. Howett, W. S. Kiefer, P. J. Lucey, P. J. McGovern, H. J. Melosh, G. A. Neumann, and R. J. Phillips (2014), Structure and evolution of the lunar Procellarum region as revealed by GRAIL gravity data, *Nature*, *514*(7520), 68–71.
6. Archinal, B. A. et al. (2010), Report of the IAU Working Group on Cartographic Coordinates and Rotational Elements: 2009, *Celest. Mech. Dyn. Astron.*, *109*(2), 101–135, doi:10.1007/s10569-010-9320-4.
7. Arkani-Hamed, J., and D. Boutin (2014), Analysis of isolated magnetic anomalies and magnetic signatures of impact craters: Evidence for a core dynamo in the early history of the Moon, *Icarus*, *237*, 262–277, doi:10.1016/j.icarus.2014.04.046.
8. Arkani-Hamed, J., and P. Olson (2010a), Giant impact stratification of the Martian core, *Geophys. Res. Lett.*, *37*(2), doi:10.1029/2009GL041417.
9. Arkani-Hamed, J., and P. Olson (2010b), Giant impacts, core stratification, and failure of the Martian dynamo, *J. Geophys. Res.*, *115*(E7), E07012, doi:10.1029/2010JE003579.
10. Arnold, J. R. (1975), Monte Carlo simulation of turnover processes in the lunar regolith, *Proc. Lunar Planet. Sci. Conf. 6th*, 2375–2395, doi:10.1051/0004-6361/200913596.
11. Asphaug, E., and H. J. Melosh (1993), The Stickney Impact of Phobos: A

- Dynamical Model, *Icarus*, 101, 144–164.
12. Asphaug, E., G. Collins, and M. Jutzi (2015a), *Global Scale Impacts*.
 13. Asphaug, E., T. Hurford, J. N. Spitale, D. Hemingway, A. R. Rhoden, W. G. Henning, B. G. Bills, and M. Walker (2015b), Tidal Disruption of Phobos as Cause of Surface Fractures, *Eur. Planet. Sci. Congr.*, EPSC2015–796.
 14. Avanesov, G., B. Bonev, and F. Kempe (1989), Television observations of Phobos, *Nature*, 341, 585–590.
 15. Barnhart, C. J., and F. Nimmo (2011), Role of impact excavation in distributing clays over Noachian surfaces, *J. Geophys. Res.*, 116(E1), E01009, doi:10.1029/2010JE003629.
 16. Le Bars, M., M. A. Wieczorek, Ö. Karatekin, D. Cébron, and M. Laneuville (2011), An impact-driven dynamo for the early Moon, *Nature*, 479(7372), 215–218, doi:10.1038/nature10565.
 17. Basilevsky, A. T., C. A. Lorenz, T. V. Shingareva, J. W. Head, K. R. Ramsley, and A. E. Zubarev (2014), The surface geology and geomorphology of Phobos, *Planet. Space Sci.*, 102, 95–118, doi:10.1016/j.pss.2014.04.013.
 18. Bierhaus, E. B., and L. Dones (2014), Craters and ejecta on Pluto and Charon: Anticipated results from the New Horizons flyby, *Icarus*, 246, 165–182, doi:10.1016/j.icarus.2014.05.044.
 19. Blewett, D. T., E. I. Coman, B. R. Hawke, J. J. Gillis-Davis, M. E. Purucker, and C. G. Hughes (2011), Lunar swirls: Examining crustal magnetic anomalies and space weathering trends, *J. Geophys. Res.*, 116(E2), E02002, doi:10.1029/2010JE003656.
 20. Britt, D. T., and C. M. Pieters (1988), The Origin of PHOBOS-Implication of Compositional Properties, *Sol. Syst. Res.*, 22, 143.
 21. Brown, P., R. E. Spalding, D. O. ReVelle, E. Tagliaferri, and S. P. Worden (2002), The flux of small near-Earth objects colliding with the Earth., *Nature*, 420(6913), 294–296, doi:10.1038/nature01238.
 22. Buczkowski, D. L., O. S. Barnouin-Jha, and L. M. Prockter (2008), 433 Eros lineaments: Global mapping and analysis, *Icarus*, 193(1), 39–52.
 23. Burns, J. A. (1972), Dynamical characteristics of Phobos and Deimos., *Rev. Geophys. Sp. Phys.*, 10(2), 463–483, doi:10.1029/RG010i002p00463.
 24. Burns, J. A. (1978), The dynamical evolution and origin of the Martian moons, *Vistas Astron.*, 22, 193–210, doi:10.1016/0083-6656(78)90015-6.
 25. Burns, J. A., D. P. Hamilton, F. Mignard, and S. Soter (1996), The Contamination of Iapetus by Phoebe Dust, *Physics, Chem. Dyn. Interplanet. Dust*, 104(ASP Conference Series).

26. Burrows, A., D. Sudarsky, and I. Hubeny (2004), Spectra and Diagnostics for the Direct Detection of Wide-Separation Extrasolar Giant Planets, *Astrophys. J.*, 609(1), 407–416, doi:10.1086/420974.
27. Butler, R. (1998), Paleomagnetism: Magnetic domains to geologic terranes, *Electron. Ed.*, (September), 319, doi:10.1006/icar.2001.6754.
28. Cahoy, K. L., M. S. Marley, and J. J. Fortney (2010), Exoplanet albedo spectra and colors as a function of planet phase, separation, and metallicity, *Astrophys. J.*, 724, 189–214, doi:10.1088/0004-637X/724/1/189.
29. Cazenave, A., A. Dobrovolskis, and B. Lago (1980), Orbital history of the Martian satellites with inferences on their origin, *Icarus*, 44(3), 730–744, doi:10.1016/0019-1035(80)90140-2.
30. Chappaz, L., H. J. Melosh, M. Vaquero, and K. C. Howell (2011), Transfer of Impact Ejecta Material from the Surface of Mars to Phobos and Deimos, in *AAS/AIAA Spaceflight Mechanics Meeting*.
31. Cintala, M., L. Berthoud, and F. Hörz (1999), Ejection-velocity distributions from impacts into coarse-grained sand, *Meteorit. Planet. Sci.*, 34, 605–623.
32. Cintala, M. J., and R. A. F. Grieve (1998), Scaling impact-melt and crater dimensions: Implications for the lunar cratering record, *Meteorit. Planet. Sci.*, 33, 889–912.
33. Coleman, P. J., G. Schubert, C. T. Russell, and L. R. Sharp (1972), Satellite measurements of the moon's magnetic field: A preliminary report, *Moon*, 4(3-4), 419–429, doi:10.1007/BF00562008.
34. Curtis, H. (2013), *Orbital mechanics for engineering students*, Butterworth-Heinemann.
35. Davis, D. R., R. Greenberg, and K. R. Housen (1981), The unusual dynamical environment of Phobos and Deimos, *Icarus*, 47, 220–233, doi:10.1016/0019-1035(81)90168-8.
36. Dobrovolskis, A. R., and J. A. Burns (1980), Life near the Roche limit - Behavior of ejecta from satellites close to planets, *Icarus*, 42, 422–441, doi:10.1016/0019-1035(80)90105-0.
37. Durda, D. D., W. F. Bottke, D. Nesvorný, B. L. Enke, W. J. Merline, E. Asphaug, and D. C. Richardson (2007), Size–frequency distributions of fragments from SPH/N-body simulations of asteroid impacts: Comparison with observed asteroid families, *Icarus*, 186(2), 498–516.
38. Dwyer, C. A., D. J. Stevenson, and F. Nimmo (2011), A long-lived lunar dynamo driven by continuous mechanical stirring, *Nature*, 479(7372), 212–214, doi:10.1038/nature10564.

39. Dyal, P., C. W. Parkin, and W. D. Daily (1974), Magnetism and the interior of the moon, *Rev. Geophys. Sp. Phys.*, 12(4), doi:10.1029/RG012i004p00568.
40. Farnocchia, D., S. R. Chesley, P. W. Chodas, P. Tricarico, M. S. P. Kelley, and T. L. Farnham (2014), Trajectory analysis for the nucleus and dust of comet C/2013~A1 (Siding Spring), , 1, 1–31, doi:10.1088/0004-637X/790/2/114.
41. Fisher, R. A. (1953), Dispersion on a sphere, *Proc. Roy. Soc. London, Series A* 2(295-305).
42. Fortney, J. J., M. S. Marley, and J. W. Barnes (2007), Planetary Radii across Five Orders of Magnitude in Mass and Stellar Insolation: Application to Transits, *Astrophys. J.*, 659, 1661, doi:10.1086/512120.
43. Freedman, R. S., M. S. Marley, and K. Lodders (2008), Line and mean opacities for ultracool dwarfs and extrasolar planets, *Astrophys. J. Suppl. Ser.*, 174(2), 504.
44. Fujiwara, A. (1991), Stickney-forming impact on phobos: Crater shape and induced stress distribution, *Icarus*, 89(2), 384–391, doi:10.1016/0019-1035(91)90185-V.
45. Garrick-Bethell, I. (2016), A Simple History of Lunar True Polar Wander, *Lunar Planet. Sci. Conf.*
46. Garrick-Bethell, I., and M. T. Zuber (2009), Elliptical structure of the lunar South Pole-Aitken basin, *Icarus*, 204(2), 399–408, doi:10.1016/j.icarus.2009.05.032.
47. Garrick-Bethell, I., V. Perera, F. Nimmo, and M. T. Zuber (2014a), The tidal rotational shape of the Moon and evidence for Polar Wander - supplementary information, *Nature*, 512(7513), 181–184, doi:10.1038/nature.
48. Garrick-Bethell, I., V. Perera, F. Nimmo, and M. T. Zuber (2014b), The tidal-rotational shape of the Moon and evidence for polar wander, *Nature*, 512(7513), 181–184, doi:10.1038/nature13639.
49. Gladman, B. J., J. A. Burns, M. J. Duncan, and H. F. Levison (1995), The dynamical evolution of lunar impact ejecta, *Icarus*, 118(2), 302–321, doi:10.1006/icar.1995.1193.
50. Goldreich, P., and A. Toomre (1969), Some remarks on polar wandering, *J. Geophys. Res.*, 74(10), 2555–2567, doi:10.1029/JB074i010p02555.
51. Gong, S., and M. A. Wieczorek (2016), Is the Lunar Magnetic Field Correlated with Gravity or Topography?, in *Lunar and Planetary Science Conference*, vol. 47, p. 2290.
52. Halekas, J. S., D. a. Brain, R. P. Lin, and D. L. Mitchell (2008), Solar wind

- interaction with lunar crustal magnetic anomalies, *Adv. Sp. Res.*, 41(8), 1319–1324, doi:10.1016/j.asr.2007.04.003.
53. Halekas, J. S., A. Poppe, G. T. Delory, W. M. Farrell, and M. Hor (2012), Solar wind electron interaction with the dayside lunar surface and crustal magnetic fields: Evidence for precursor effects, *Earth, Planets Sp.*, 64(2), 73–82, doi:10.5047/eps.2011.03.008.
 54. Hamelin, M. (2011), Motion of blocks on the surface of Phobos: New constraints for the formation of grooves, *Planet. Space Sci.*, 59(13), 1293–1307, doi:10.1016/j.pss.2010.05.023.
 55. Harding, L. K. et al. (2015), Technology advancement of the CCD201-20 EMCCD for the WFIRST coronagraph instrument: sensor characterization and radiation damage, *J. Astron. Telesc. Instruments, Syst.*, 2(1), 11007.
 56. Hemingway, D., and I. Garrick-Bethell (2012), Magnetic field direction and lunar swirl morphology: Insights from Airy and Reiner Gamma, *J. Geophys. Res.*, 117(E10), E10012, doi:10.1029/2012JE004165.
 57. Hermalyn, B., and P. Schultz (2013), New Insights Into the Ejecta Mass-Velocity Distribution: Experimental Time- Resolved Measurements and Applications To Cratering, *44th Lunar Planet. Sci. Conf.*
 58. Holsapple, K. A. (1993), The Scaling of Impact Processes in Planetary Sciences, *Annu. Rev. Earth Planet. Sci.*, 21, 333–373.
 59. Hood, L., and C. Williams (1989), The Lunar Swirls: Distribution and Possible Origins, *Lunar Planet. Sci. Conf.*, doi:1989LPSC...19...99H.
 60. Hood, L., A. Zakharian, J. Halekas, D. L. Mitchell, R. P. Lin, M. H. Acuna, and A. B. Binder (2001), Initial mapping and interpretation of lunar crustal magnetic anomalies using Lunar Prospector magnetometer data, *J. Geophys. Res.*, 106(E11), 27825–27839.
 61. Hood, L. L., and N. A. Artemieva (2008), Antipodal effects of lunar basin-forming impacts: Initial 3D simulations and comparisons with observations, *Icarus*, 193(2), 485–502, doi:10.1016/j.icarus.2007.08.023.
 62. Hood, L. L., and Z. Huang (1991), Formation of Magnetic Anomalies Antipodal to Lunar Impact Basins ' magnetic , 96(91), 9837–9846.
 63. Horak, H. G. (1950), Diffuse Reflection by Planetary Atmospheres., *Astrophys. J.*, 112, 445.
 64. Horak, H. G., and S. J. Little (1965), Calculations of Planetary Reflection., *Astrophys. J. Suppl. Ser.*, 11, 373.
 65. Horstman, K. C., and H. J. Melosh (1989), Drainage Pits in Cohesionless Materials : Implications for the Surface of Phobos, *J. Geophys. Res.*, 94(89),

433–441.

66. Housen, K. R., and K. A. Holsapple (2011), Ejecta from impact craters, *Icarus*, 211(1), 856–875, doi:10.1016/j.icarus.2010.09.017.
67. Hurford, T., and E. Asphaug (2015), Surface Evolution from Orbital Decay on Phobos, in *AAS/Division for Planetary Sciences Meeting Abstracts*, vol. 47.
68. Irving, E. (1964), *Paleomagnetism and its application to geological and geophysical problems*, 1st ed., John Wiley & Sons, Inc, New York, NY, USA.
69. Karkoschka, E. (1994), Spectrophotometry of the jovian planets and Titan at 300-to 1000-nm wavelength: The methane spectrum, *Icarus*, 111(1), 174–192.
70. Klacka, J. (2002), On Radiation Pressure and the Poynting-Robertson Effect for Fluffy Dust Particles, , 361, 349–361, doi:http://dx.doi.org/10.1006/icar.2002.6849.
71. Kramer, G. Y., J.-P. Combe, E. M. Harnett, B. R. Hawke, S. K. Noble, D. T. Blewett, T. B. McCord, and T. A. Giguere (2011), Characterization of lunar swirls at Mare Ingenii: A model for space weathering at magnetic anomalies, *J. Geophys. Res.*, 116(E4), E04008, doi:10.1029/2010JE003669.
72. Kurata, M., H. Tsunakawa, Y. Saito, H. Shibuya, M. Matsushima, and H. Shimizu (2005), Mini-magnetosphere over the Reiner Gamma magnetic anomaly region on the Moon, *Geophys. Res. Lett.*, 32(24), L24205, doi:10.1029/2005GL024097.
73. Lambeck, K. (1979), On the orbital evolution of the Martian satellites, *J. Geophys. Res.*, 84(B10), 5651, doi:10.1029/JB084iB10p05651.
74. Lee, P. (2009), *First International Conference on the Exploration of Phobos and Deimos: Summary and Recommendations*.
75. Lee, S. W., P. Thomas, and J. Veverka (1986), Phobos, Deimos, and the moon - Size and distribution of crater ejecta blocks, *Icarus*, 86, 77–86, doi:10.1016/0019-1035(86)90075-8.
76. Leimkuhler, B., and S. Reich (2004), *Simulating Hamiltonian Dynamics*, Cambridge., edited by P. G. Ciarlet, A. Iserles, R. V Kohn, and M. H. Wright, Cambridge University Press.
77. Leinhardt, Z. M., and S. T. Stewart (2012), Collisions Between Gravity-Dominated Bodies. I. Outcome Regimes and Scaling Laws, *Astrophys. J.*, 745(1), 79, doi:10.1088/0004-637X/745/1/79.
78. Lin, R. P., D. L. Mitchell, D. W. Curtis, K. A. Anderson, C. W. Carlson, J. McFadden, M. H. Acuna, L. L. Hood, and A. Binder (1998), Lunar Surface Magnetic Fields and Their Interaction with the Solar Wind: Results from Lunar Prospector, *Science (80-.)*, 281(5382), 1480–1484,

doi:10.1126/science.281.5382.1480.

79. Love, S. G., and T. J. Ahrens (1996), Catastrophic Impacts on Gravity Dominated Asteroids, *Icarus*, 124, 141–155, doi:10.1006/icar.1996.0195.
80. Lunine, J. I., G. Neugebauer, and B. M. Jakosky (1982), Infrared observations of Phobos and Deimos from Viking, *J. Geophys. Res.*, 87(B12), 10297, doi:10.1029/JB087iB12p10297.
81. Lupu, R. E., M. S. Marley, N. Lewis, M. Line, W. A. Traub, and K. Zahnle (2016), Developing Atmospheric Retrieval Methods for Direct Imaging Spectroscopy of Gas Giants in Reflected Light I: Methane Abundances and Basic Cloud Properties,
82. Marchi, S., C. Barbieri, M. Küppers, F. Marzari, B. Davidsson, H. U. Keller, S. Besse, P. Lamy, S. Mottola, and M. Massironi (2010), The cratering history of asteroid (2867) Steins, *Planet. Space Sci.*, 58(9), 1116–1123.
83. Marcy, G. W., R. P. Butler, S. S. Vogt, D. A. Fischer, G. W. Henry, G. Laughlin, J. T. Wright, and J. A. Johnson (2005), Five new extrasolar planets, *Astrophys. J.*, 619(1), 570.
84. Marley, M., R. Lupu, N. Lewis, and M. Line (2014), A Quick Study of the Characterization of Radial Velocity Giant Planets in Reflected Light by Forward and Inverse Modeling, *arXiv Prepr. arXiv ...*, 1–32.
85. Marley, M. S., and C. P. McKay (1999), Thermal Structure of Uranus' Atmosphere, *Icarus*, 138(2), 268–286, doi:10.1006/icar.1998.6071.
86. Marley, M. S., C. Gelino, D. Stephens, J. I. Lunine, and R. S. Freedman (1999), Reflected Spectra and Albedos of Extrasolar Giant Planets. I. Clear and Cloudy Atmospheres, *Astrophys. J.*, 513, 879, doi:10.1086/306881.
87. Maxwell, D., and K. Seifert (1974), Modeling of cratering, close-in displacements and ejecta, *Def. Nucl. Agency, Rep. #DNA-F-3628*.
88. Maxwell, D. E. (1977), Simple Z model for cratering, ejection, and the overturned flap, in *Impact and Explosion Cratering: Planetary and Terrestrial Implications*, vol. 1, pp. 1003–1008.
89. Melosh, H. J. (1989), Impact cratering: A geologic process, , 1–240.
90. Melosh, H. J., and P. Schenk (1993), Split Comets and the Origin of Crater Chains on Ganymede and Callisto, *Nature*, 365, 731–733, doi:10.1038/365731a0.
91. Meschiari, S., G. Laughlin, S. S. Vogt, R. P. Butler, E. J. Rivera, N. Haghighipour, and P. Jalowiczor (2010), The Lick-Carnegie Survey: Four New Exoplanet Candidates, *Astrophys. J.*, 117, 13, doi:10.1088/0004-637X/727/2/117.

92. Mitchell, D. L., J. S. Halekas, R. P. Lin, S. Frey, L. L. Hood, M. H. Acuña, and a. Binder (2008), Global mapping of lunar crustal magnetic fields by Lunar Prospector, *Icarus*, 194(2), 401–409, doi:10.1016/j.icarus.2007.10.027.
93. Moore, H. J., C. A. Hodges, and D. H. Scott (1974), Multiringed basins illustrated by Orientale and associated features, *Proc. 5th Lunar Planet. Sci. Conf.*, 1(Supplement 5, Geochimica et Cosmochimica Acta), 71–100, doi:1974LPSC....5...71M.
94. Morley, C. V, J. J. Fortney, M. S. Marley, K. Zahnle, M. Line, E. Kempton, C. Kerri, and N. Lewis (2015), Thermal Emission and Reflected Light Spectra of Super Earths with Flat Transmission Spectra, *Astrophys. J.*, 815(2), 110.
95. Morrison, S. J., P. C. Thomas, M. S. Tiscareno, J. A. Burns, and J. Veverka (2009), Grooves on small saturnian satellites and other objects: Characteristics and significance, *Icarus*, 204(1), 262–270.
96. Murchie, S. (2010), Mars Reconnaissance Orbiter Spherical Harmonics Binary Data Records, data set MRO-M-RSS-5-SDP-V1., *NASA Planet. Data Syst.*
97. Murchie, S., and S. Erard (1993), The spectrum of PHOBOS from PHOBOS 2 observations at 0.3-2.6 microns: Comparison to previous data and meteorite analogs, in *Lunar and Planetary Science Conference*, vol. 24, pp. 1025–1026.
98. Murchie, S., and S. Erard (1996), Spectral Properties and Heterogeneity of Phobos from Measurements by Phobos 2, *Icarus*, 123(1), 63–86, doi:10.1006/icar.1996.0142.
99. Murchie, S. L., D. T. Britt, J. W. Head, S. F. Pratt, P. C. Fisher, B. S. Zhukov, A. A. Kuzmin, L. V Ksanfomality, A. V Zharkov, and G. E. Nikitin (1991), Color heterogeneity of the surface of Phobos: Relationships to geologic features and comparison to meteorite analogs, *J. Geophys. Res. Solid Earth*, 96(B4), 5925–5945.
100. Murchie, S. L., P. C. Thomas, A. S. Rivkin, and N. L. Chabot (2003), Phobos and Deimos, *Asteroids III*, 2186–2224.
101. Murchie, S. L., T. Choo, D. Humm, A. S. Rivkin, J.-P. Bibring, Y. Langevin, B. Gondet, T. L. Roush, T. Duxbury, and C. Team (2008), MRO/CRISM observations of Phobos and Deimos, in *Lunar and Planetary Science Conference*, vol. 39, p. 1434.
102. Murray, E. J. B., J. C. Iliffe, J. A. L. Muller, G. Neu-, S. Werner, M. Balme, H. C. Team, G. St, F. Universität, and D. Building (2006), New Evidence on the Origin of Phobos' Parallel Grooves, *Lunar Planet. Sci. XXXVII*, 1, 3–4.

103. Murray, J. B., and D. C. Heggie (2014), Character and origin of Phobos' grooves, *Planet. Space Sci.*, 102, 1–25, doi:10.1016/j.pss.2014.03.001.
104. Nayak, M., and E. Asphaug (2015), Sesquinary Catenae on Phobos from Reaccretion of Ejected Material, *47th AAS Div. Planet. Sci. Meet.*, (2363941).
105. Nayak, M., I. Garrick-Bethell, and D. Hemingway (2016a), Diverse Lunar Paleopoles Inferred from South Pole-Aitken Basin Magnetic Anomalies, *Lunar Planet. Sci. Conf.*
106. Nayak, M., F. Nimmo, and B. Udrea (2016b), Effects of mass transfer between Martian satellites on surface geology, *Icarus*, 267, 220–231, doi:10.1016/j.icarus.2015.12.026.
107. Nayak, M. V., and E. Asphaug (2016), Sesquinary Catenae on the Martian Satellite Phobos from Reaccretion of Escaping Ejecta, *Nat. Commun.*, 7, 12591, doi:10.1038/NCOMMS12591.
108. Nicholas, J. B., M. E. Purucker, and T. J. Sabaka (2007), Age spot or youthful marking: Origin of Reiner Gamma, *Geophys. Res. Lett.*, 34(2), L02205, doi:10.1029/2006GL027794.
109. O'Keefe, J. D., and T. J. Ahrens (1985), Impact and explosion crater ejecta, fragment size, and velocity, *Icarus*, 62, 328–338, doi:10.1016/0019-1035(85)90128-9.
110. Parker, R. L. (1988), A statistical theory of seamount magnetism, *J. Geophys. Res.*, 93(B4), 3105, doi:10.1029/JB093iB04p03105.
111. Parker, R. R. L. (1991), A theory of ideal bodies for seamount magnetism, *J. Geophys. Res. Solid Earth* (...), 96(91), 101–112, doi:10.1029/91JB01497.
112. Peale, S. J. (1976), Excitation and relaxation of the wobble, precession, and libration of the Moon, *J. Geophys. Res.*, 81(11), 1813–1827, doi:10.1029/JB081i011p01813.
113. Pepe, F., C. Lovis, D. Segransan, W. Benz, F. Bouchy, X. Dumusque, M. Mayor, D. Queloz, N. C. Santos, and S. Udry (2011), The HARPS search for Earth-like planets in the habitable zone-I. Very low-mass planets around HD 20794, HD 85512, and HD 192310, *Astron. Astrophys.*, 534, A58.
114. Purucker, M. E. (2008), A global model of the internal magnetic field of the Moon based on Lunar Prospector magnetometer observations, *Icarus*, 197(1), 19–23, doi:10.1016/j.icarus.2008.03.016.
115. Purucker, M. E., and J. B. Nicholas (2010), Global spherical harmonic

- models of the internal magnetic field of the Moon based on sequential and coestimation approaches, *J. Geophys. Res.*, *115*(E12), E12007, doi:10.1029/2010JE003650.
116. Purucker, M. E., J. W. Head, and L. Wilson (2012), Magnetic signature of the lunar South Pole-Aitken basin: Character, origin, and age, *J. Geophys. Res.*, *117*(E5), E05001, doi:10.1029/2011JE003922.
 117. Ramsley, K. R., and J. W. Head (2013), Mars impact ejecta in the regolith of phobos: Bulk concentration and distribution, *Planet. Space Sci.*, *87*, 115–129, doi:10.1016/j.pss.2013.09.005.
 118. Richardson, J. E., H. J. Melosh, C. M. Lisse, and B. Carcich (2007), A ballistics analysis of the Deep Impact ejecta plume: Determining Comet Tempel 1's gravity, mass, and density, *Icarus*, *191*(2), 176–209, doi:10.1016/j.icarus.2007.08.033.
 119. Rivkin, A., R. H. Brown, D. E. Trilling, J. F. Bell III, and J. H. Plasmann (2002), Near-Infrared Spectrophotometry of Phobos and Deimos, *Icarus*, *156*(1), 64–75, doi:10.1006/icar.2001.6767.
 120. Robinson, T. D., K. R. Stapelfeldt, and M. S. Marley (2015), Characterizing Rocky and Gaseous Exoplanets with 2-meter Class Space-based Coronagraphs, *PASP*, *128*.
 121. Roddy, D. J. (1977), Large-scale impact and explosion craters-Comparisons of morphological and structural analogs, in *Impact and explosion cratering: Planetary and terrestrial implications*, vol. 1, pp. 185–246.
 122. Rosenblatt, P., S. Le Maistre, J. Marty, V. Dehant, M. Paetzold, and T. Van Hoolst (2008), Improvement of the Mass Determination of Both Martian Moons Using MEX, MGS, ODY and MRO Tracking Data, *AGU Fall Meet.*, *1*(Abstract #P41B-1377), 1377.
 123. Runcorn, S. K. (1983), Lunar magnetism, polar displacements and primeval satellites in the Earth–Moon system, *Nature*, *304*(5927), 589–596, doi:10.1038/304589a0.
 124. Schmedemann, N., G. G. Michael, B. a. Ivanov, J. B. Murray, and G. Neukum (2014), The age of Phobos and its largest crater, Stickney, *Planet. Space Sci.*, *102*, 152–163, doi:10.1016/j.pss.2014.04.009.
 125. Schmidt, R. M., and K. R. Housen (1987), Some recent advances in the scaling of impact and explosion cratering, *Int. J. Impact Eng.*, *5*(1), 543–560.
 126. Siegler, M. A., R. S. Miller, J. T. Keane, M. Laneuville, D. A. Paige, I.

- Matsuyama, D. J. Lawrence, A. Crotts, and M. J. Poston (2016), Lunar true polar wander inferred from polar hydrogen, *Nature*, 531(7595), 480–484, doi:10.1038/nature17166.
127. Smith, D. E. et al. (2010), Initial observations from the Lunar Orbiter Laser Altimeter (LOLA), *Geophys. Res. Lett.*, 37(18), 1–6, doi:10.1029/2010GL043751.
 128. Smith, H. D., P. Lee, and D. Hamilton (2015), Low Velocity Impacts on Phobos, *46th Lunar Planet. Sci. Conf.*, 8477–8478.
 129. Soter, S. (1971), Studies of the Terrestrial Planets, Cornell University.
 130. Soter, S. (1972), The Dust Belts of Mars, *Cornell Univ. Rep. CRSR* 462.
 131. Soter, S., and A. Harris (1977), Are striations on Phobos evidence for tidal stress?, *Nature*, (268), 421–422.
 132. Stöffler, D., D. E. Gault, J. Wedekind, and G. Polkowski (1975), Experimental hypervelocity impact into quartz sand: Distribution and shock metamorphism of ejecta, *J. Geophys. Res.*, 80(29), 4062–4077.
 133. Sudarsky, D., A. Burrows, and P. Pinto (2000), Albedo and Reflection Spectra of Extrasolar Giant Planets, *Astrophys. J.*, 538(2), 885–903, doi:10.1086/309160.
 134. Sudarsky, D., A. Burrows, and I. Hubeny (2003), Theoretical Spectra and Atmospheres of Extrasolar Giant Planets, *Astrophys. J.*, 588(2), 1121–1148, doi:10.1086/374331.
 135. Sudarsky, D., A. Burrows, I. Hubeny, and A. Li (2005), Phase Functions and Light Curves of Wide-Separation Extrasolar Giant Planets, *Astrophys. J.*, 627(1), 520–533, doi:10.1086/430206.
 136. Szeto, A. M. K. (1983), Orbital Evolution and Origin of the Martian Satellites, *Icarus*, (55), 133–168.
 137. Takahashi, F., H. Tsunakawa, H. Shimizu, H. Shibuya, and M. Matsushima (2014), Reorientation of the early lunar pole, *Nat. Geosci.*, 7(6), 409–412, doi:10.1038/ngeo2150.
 138. Thomas, N., R. Stelter, a. Ivanov, N. T. Bridges, K. E. Herkenhoff, and a. S. McEwen (2011), Spectral heterogeneity on Phobos and Deimos: HiRISE observations and comparisons to Mars Pathfinder results, *Planet. Space Sci.*, 59(13), 1281–1292, doi:10.1016/j.pss.2010.04.018.
 139. Thomas, P. (1979), Surface Features of Phobos and Deimos, *Icarus*, 40, 223–243.
 140. Thomas, P. (1998), Ejecta Emplacement on the Martian Satellites,

- Icarus*, 131(1), 78–106, doi:10.1006/icar.1997.5858.
141. Thomas, P., and J. Veverka (1980a), Crater densities on the satellites of Mars, *Icarus*, 41, 365–380, doi:10.1016/0019-1035(80)90221-3.
 142. Thomas, P., and J. Veverka (1980b), Downslope movement of material on Deimos, *Icarus*, (42), 234–250, doi:10.1016/0019-1035(80)90073-1.
 143. Thomas, P., J. Veverka, and T. Duxbury (1978), Origin of the grooves on Phobos, *Nature*, 273(5660), 282–284, doi:10.1038/273282a0.
 144. Thomas, P. C. (1993), Gravity, Tides, and Topography on Small Satellites and Asteroids: Application to Surface Features of the Martian Satellites, *Icarus*, 105(2), 326–344, doi:http://dx.doi.org/10.1006/icar.1993.1130.
 145. Thomas, P. C., D. Adinolfi, P. Helfenstein, D. Simonelli, and J. Veverka (1996), The Surface of Deimos : Contribution of Materials and Processes to Its Unique Appearance, *Icarus*, 123, 536–556.
 146. Tsunakawa, H., F. Takahashi, H. Shimizu, H. Shibuya, and M. Matsushima (2014), Regional mapping of the lunar magnetic anomalies at the surface: Method and its application to strong and weak magnetic anomaly regions, *Icarus*, 228, 35–53, doi:10.1016/j.icarus.2013.09.026.
 147. Udrea, B., M. Nayak, B. Allen, J. Bourke, G. Casariego, S. Gosselin, E. Hiester, M. Maier, J. Melchert, and C. Patel (2015), Mars Moons Prospector Mission with CubeSats, in *EGU General Assembly Conference Abstracts*, vol. 17, p. 7881.
 148. Udrea, B., M. V Nayak, F. J. Franquiz, and J. G. Bourke (2016), PIRARUCU: Mars Moons Prospector Mission with Cubesats, in *IEEE Aerospace Conference*, Big Sky, Montana.
 149. Vallado, D. A. (2013), *Fundamentals of Astrodynamics and Applications*, 4th ed., Microcosm Press.
 150. Veverka, J. (1978), The surfaces of Phobos and Deimos, *Vistas Astron.*, 22, 163–192, doi:10.1016/0083-6656(78)90014-4.
 151. Veverka, J., and T. C. Duxbury (1977), Viking observations of Phobos and Deimos: Preliminary results, *J. Geophys. Res.*, 82(28), 4213–4223, doi:10.1029/JS082i028p04213.
 152. Walsh, K. J., D. C. Richardson, and P. Michel (2008), Rotational breakup as the origin of small binary asteroids, *Nature*, 454(7201), 188–191.
 153. Weidenschilling, S. J. (1979), A possible origin for the grooves of Phobos, *Nature*, 282, 697–712.

154. Weiss, B. P., and S. M. Tikoo (2014), The lunar dynamo, *Science* (80-.), 346(6214), 1246753–1246753, doi:10.1126/science.1246753.
155. Wieczorek, M. A., and B. P. Weiss (2010), Testing the lunar dynamo hypothesis using global magnetic field data, in *41st Lunar and Planetary Science Conference.*, vol. 1625.
156. Wieczorek, M. A., B. P. Weiss, and S. T. Stewart (2012), An Impactor Origin for Lunar Magnetic Anomalies, *Science* (80-.), 335(6073), 1212–1215, doi:10.1126/science.1214773.
157. Williams, J., D. Boggs, C. F. Yoder, J. T. Ratcliff, and J. O. Dickey (2001), Lunar rotational dissipation in solid body and molten core, *J. Geophys. Res.*, 106(E11), 27933–27968, doi:10.1029/2000JE001396.
158. Wilson, L., and J. W. Head (2015), Groove formation on Phobos: Testing the Stickney ejecta emplacement model for a subset of the groove population, *Planet. Space Sci.*, 105, 26–42, doi:10.1016/j.pss.2014.11.001.
159. Witasse, O. et al. (2014), Mars Express investigations of Phobos and Deimos, *Planet. Space Sci.*, 102(December 2003), 18–34, doi:10.1016/j.pss.2013.08.002.
160. Yoder, C. F. (1982), Tidal rigidity of Phobos, *Icarus*, 346(49), 327–346, doi:10.1016/0019-1035(82)90040-9.
161. Zahnle, K., P. Schenk, H. Levison, and L. Dones (2003), Cratering rates in the outer solar system, *Icarus*, 163(2), 263–289, doi:10.1016/S0019-1035(03)00048-4.
162. Zahnle, K., J. L. Alvarellos, A. Dobrovolskis, and P. Hamill (2008), Secondary and sesquinary craters on Europa, *Icarus*, 194(2), 660–674, doi:10.1016/j.icarus.2007.10.024.
163. Zuber, M. T. et al. (2013), Gravity Field of the Moon from the Gravity Recovery and Interior Laboratory (GRAIL) Mission, *Science* (80-.), 339(6120), 668–671, doi:10.1126/science.1231507.